UNIVERSITY OF MESSINA

DEPARTMENT OF ENGINEERING

PHD. COURSE IN ENGINEERING AND CHEMISTRY OF MATERIALS AND CONSTRUCTIONS

XXXIII CYCLE

ENERGY METHODS FOR FRACTURE AND FATIGUE ASSESSMENT

Dario Francesco Santonocito

Tutor: Prof. Giacomo Risitano

SSD: ING/IND-14 – Progettazione meccanica e costruzione di macchine

2020

SUMMARY

The present Ph.D. thesis is the collection of three years of research activity in the fatigue field. The aim of the thesis was to apply Energy based methods to the assessment of the fatigue properties of materials.

The Risitano Thermographic Method and the novel Static Thermographic Method were extensively applied to a wide set of materials in order to validate them as rapid test procedures able to derive, in short amount of time and with few specimens, the fatigue properties of materials monitoring the energetic release.

Finite element simulations were carried out to applying the Strain Energy Density method as a local approach to predict the fatigue failure of notched mechanical components.

The Thermographic Method-s were applied to structural steel from an in-service component, plain and notched medium carbon steel specimens, high strength concrete under compressive loads, high density polyethylene for pressure pipe applications, 3D printed polyamide-12 specimens and short glass fiber reinforced composite PA66GF35.

The Strain Energy Density approach was applied to welded components, in particular cruciform welded joints, to compare the fatigue information provided by this method with the ones provided by the international welding standards.

The experimental activities were performed at the Laboratory of Mechanics of the University of Messina. Part of the research period was spent by the author at the University of Padova, under the supervision of Prof. Giovanni Meneghetti, and at the Norwegian University of Science and Technology (NTNU), under the supervision of Prof. Filippo Berto, to study local approaches techniques.

Several research perspectives have been opened by this thesis, that the author would to pursue in the future.

TABLE OF CONTENTS

INTRODUCTION

Fatigue properties are of fundamental importance in mechanical design, but they require a huge amount of time and material to be assessed.

A deep understating of the micro and macro failure mechanisms of the material show how the fatigue degradation is a process accompanied by energetic release. Several studies have shown how a large part of the input energy, provided to the material as mechanical work, is dissipated into heat, while a very small portion is stored within the material, leading to microstructural modifications, hence to fatigue failure [1].

Moving from this assumption, several energy based method have been developed to overcame the limitations of traditional fatigue tests. In particular, the Risitano Thermographic Method [2] has been proposed to derive the fatigue limit and the whole S-N curve of the material monitoring the superficial temperature of a specimen tested under fatigue loads.

A recent development has been introduced by Risitano and Risitano [3] with the Static Thermographic Method. By evaluating the specimen surface temperature during a monoaxial static tensile test, it is possible to obtain the fatigue limit as the macroscopic applied stress at which the temperature trend deviates from the linearity of the thermoelastic effect [4].

Dealing with notched components, it is difficult to take into account all the different parameters that may affect the fatigue behavior of the material. Under the assumption that fatigue failure is a local problem, Livieri and Lazzarin [5] proposed the Strain Energy Density approach to evaluate the averaged strain energy over a control volume and compare it to a critical value. This approach allows to compare the fatigue failures from different notch configurations.

The aim of this Ph.D. thesis is the adoption of the energy based methods to assess the fatigue properties of several materials in order to validate them. In particular, the Static Thermographic Method is extensively applied given its ability to assess the fatigue limit of several materials in a very short amount of time and with a simple static traction test.

The thesis is dived into two parts. In the first part, a theoretical background on the Risitano Thermographic Method, the Static Thermographic Method and the Strain Energy Density approach is proposed. In the second part, a series of experimental and numerical investigations is presented, carried out during the 3 years Ph.D. period. Each chapter of the second part presents a brief highlights of the experimental activity and the relative journal publication, as paper or procedia. At the end of the thesis a list of publication by the author is presented.

The chapter structure is as follow:

Part One – Theoretical background

In Chapter 1 "*Energy dissipation in fatigue test*", it is presented the engineering aspect of fatigue and the energy based approaches developed to assess it. Several aspects that may influence the fatigue behavior of the material are exposed. Moving from the micro and macro dissipative aspect of the fatigue degradation, the early study on the energetic release are presented. A deep insight on the Risitano Thermographic Method is presented, as well as a view on other energetic approaches.

In Chapter 2 "*Energetic release in static tensile test*", the fundamental relations of the coupling between the thermal and stress-strain field of a material is presented, as well as the thermoelasticity phenomenon. An insight on the early studies regarding the energetic release during a static tensile test is presented. Suddenly, the Static Thermographic Method approach is presented with the numerical temperature model, developed by the author, to predict the temperature trend during a static tensile test.

In Chapter 3 "*Local Approaches*", the basis of the local approaches are exposed. The Notch Stress Intensity Factor (NSIF) is presented in order to describe the asymptotic stress field near a notch tip. Suddenly, the Strain Energy Density approach is presented within its advantages over the NSIF approach. Lastly, the Peak Stress Method is exposed as a rapid numerical procedure to estimate the NSIF.

Part Two – Experimental activities

In Chapter 4 "*Structural Steel S355*", the Thermographic Method-s are applied to specimens retrieved from an in-service port crane. Traditional fatigue tests have been carried out to assess the fatigue limit and the S-N curve of the steel. The S-N curve predicted by means of the

Thermographic Method, as well as the fatigue limits estimated by both classical Thermographic and Static Thermographic Method are in good agreement with the traditional fatigue tests.

In Chapter 5 "*Medium carbon steel C45*", both the Thermographic Method-s are applied to a medium carbon steel to investigate its fatigue behavior. The fatigue limit assessed by them is in good agreement with the literature data and with the other fatigue limits assessed by several Italian Universities within the Energy Method group (MEAS) of the Italian society of Machine Design (AIAS). Numerical simulations have been carried out in order to estimate the energetic release and the beginning of irreversible plasticity during a static tensile test.

In Chapter 6 "*V-notched medium carbon steel AISI 1035*", the Static Thermographic Method is applied to notched specimens in order to estimate the deviation from the linearity of the thermoelastic effect. The corresponding applied stress has been compared with the one assessed by Thermographic Method showing good agreement. Numerical simulations have been carried out to assess the beginning of plastic effects near the notched region and the corresponding temperature trend. This activity is part of the collaboration between the University of Messina and the Norwegian University of Science and Technology (NTNU).

In Chapter 7 "*High Strength Concrete*", the Static Thermographic Method has been applied to cubic concrete specimens subjected to compressive loads, in order to monitor the evolution of the internal damage. Thermal image analysis and numerical finite elements simulations showed how it is possible to predict, by means of the infrared thermography, the beginning of micro failures that evolves in macroscopic failures of the material.

In Chapter 8 "*High-Density Polyehtilene*", for the first time Thermographic techniques have been applied to specimen of high density polyethylene (PE100). The temperature trend was monitored during static tensile and stepwise fatigue tests in order to predict the fatigue limit of the material. Traditional fatigue curve has been obtained showing good agreement between the traditional fatigue limit and the one by means of the Thermographic approaches.

In Chapter 9 "*3D-Printed Polyamide-12*", for the first time the Static Thermographic Method has been applied to 3D printed plastic material. The temperature trend was monitored by an infrared camera and the fatigue limit has been compared to the one from traditional constant amplitude fatigue test.

In Chapter 10 "*Composite material PA66GF35*", the Static Thermographic Method has been applied to composite material. The aim of the activity was to link the internal material microstructure and its microfailure mechanisms with the macroscopic energetic release. A micromechanical finite element system of the fiber-matrix system was modelled and the damage information retrieved from this model have been adopted to carried out finite element simulation on the specimen subjected to static tensile loading in order to predict the temperature trend.

In Chapter 11 "*Local approaches for welded structures*", the Notch Stress Intensity Factor, the Strain Energy Density Method and the Peak Stress Method have been applied to synthetize the fatigue data of welded joints, treated as notched mechanical component. This activity is part of the training period performed by the author at the University of Padova under the supervision of Prof. Giovanni Meneghetti.

In Chapter 12 "*Fatigue assessment of welded joint by means of SED approach and comparison with standards*", numerical finite element simulations have been carried out on cruciform welded joint applying the Strain Energy Density approach. The fatigue information retrieved from the SED method have been compared with the current international standards that prescribe the fatigue design of such components. This activity is part of the collaboration between the University of Messina and the Norwegian University of Science and Technology (NTNU), where the author spent a period of three months under the supervision of Prof. Filippo Berto.

PART I
THEORETICAL BACKGROUND

1. ENERGY DISSIPATION IN FATIGUE TEST

Fatigue assessment of material is of fundamental importance for a proper, reliable and safety design of mechanical components.

Historically, such tests have been performed on specimens under constant amplitude stress or strain, requiring a very large amount of time and of tested specimens, i.e. adopted material. Nowadays, this testing approach is not competitive in the industry field where it is necessary to obtain useful information on materials and components to develop new devices or improve it in a rapid way.

Studies have shown that the fatigue degradation is a dissipative phenomenon where only a portion of the external energy, provided as work on the mechanical component, is stored within the material to activate microstructural change. A very large amount of energy is dissipated into the surrounding environment as heat. Moving from this consideration, many researchers have developed experimental methods to assess the fatigue behavior of the material evaluating the dissipative aspect during a fatigue test.

Despite some researchers measured the energy dissipation of a specimen subjected to fatigue loading, the first, who adopts the Infrared Thermography to monitor the specimen surface temperature and link it to the fatigue behavior of the material, was Risitano in 1983. In this chapter, it is presented a broad view on fatigue of materials and the energy based method to assess it.

In section 1.1 are exposed briefly several aspects that may influence the fatigue behavior of the materials, in particular the fatigue regime, the mean stress effect, the load history and the stress state.

In section 1.2, some preliminary studies on the fatigue behavior of the material are presented, moving from the microscale to the macroscale effects, that take into account energetic aspect of the fatigue process.

In section 1.3, it is presented the Risitano Thermographic Method as a rapid procedure to estimate the fatigue limit and the S-N curve of the material evaluating the temperature trend during a fatigue test.

In section 1.4 are presented some energetic approach defined to overcome the problems that may arise from the direct evaluation of the fatigue properties from the temperature evolution of the material. Starting from the first thermodynamic law applied to an elementary volume of material, some parameters, independent from the test boundary condition, are adopted to evaluate the fatigue properties of the material.

1.1. Fatigue in materials

Fatigue assessment of engineering materials is still an open challenge for researchers all around the world, due to the difficulties encountered in modelling such a complex phenomenon. The material behavior, the environmental condition and the load type may severally influence the resistance of mechanical components to stress, or strain, that change during time. Nevertheless, the material response at micro scale can be severally different from that at macroscale.

Defects in material are the main reason of fatigue failure. They develop at atomic scale, due to microslip of dislocation, and grow up to microscopic fatigue damage that may evolve in macrocracks. The application of a cyclic load leads to the formation and accumulation of microcracks and their growth onto macrocracks [6]. The macrocracks can propagate and became irreversible plastic deformation till the mechanical component failure. Usually, fatigue failure results in a catastrophic failure due to the rapid propagation of the cracks, hence it is necessary, mainly for safety reason, to predict such phenomenon.

Fatigue failure can be influenced by several parameters. For example, the fatigue regime (Low Cycle Fatigue LCF, High Cycle Fatigue HCF) leads to different failure mechanism of the component, as wells as the stress state (uniaxial or multiaxial) and the load history (amplitude and sequence).

1.1.1. Fatigue regimes

The fatigue life of mechanical component can be described by the S-N curve (Stress vs. Number of cycle) or Wohler curve [7] (Figure 1.1), which report the number of cycles to failure

versus the applied maximum stress under different stress ratio R, defined as the ratio between the minimum applied stress and the maximum one, considering a sinusoidal stress function (Figure 1.2). As the applied stress increases, the resistance of the component, i.e. the number of cycles, decreases; on the other hand, as the applied stress is reduced, the number of cycles increases. The S-N curve are usually reported in a bi-log diagram and, depending on the number of cycles range, it is possible to define several fatigue regimes. The Low Cycle Fatigue regime is defined for a number of cycles from 10^3 to 10^4. In this regime, the main fatigue failure mechanism is due to the stress that arises at the surface of the specimen and large plastic strain of the material is observed. In the High Cycle Fatigue regime, ($N>10^6$) the stress and strain are within the elastic region. Other regions of interest in the S-N curve are the Intermediate Cycle Fatigue (ICF, 10^5-10^6); the very low cycle fatigue (VLCF, $<10^3$) and the very high cycle fatigue (VHCF, $>10^8$).

Some materials (steel or titanium alloys), for an applied stress level lower than a certain value, do not show fatigue failure. This stress level is defined as the "endurance limit" or "fatigue limit" of the material σ_0. Other materials, such as nonferrous metals and plastic, do not show a fatigue limit, so the S-N curve continue to decrease.

Usually, for a number of cycle of $1x10^6$ or $2x10^6$ for metals, it is conventionally assumed that the material has an infinite life. Some studies show how, despite lower stresses than the fatigue limit are applied, for a very high number of cycle fatigue failure can occur [8–12].

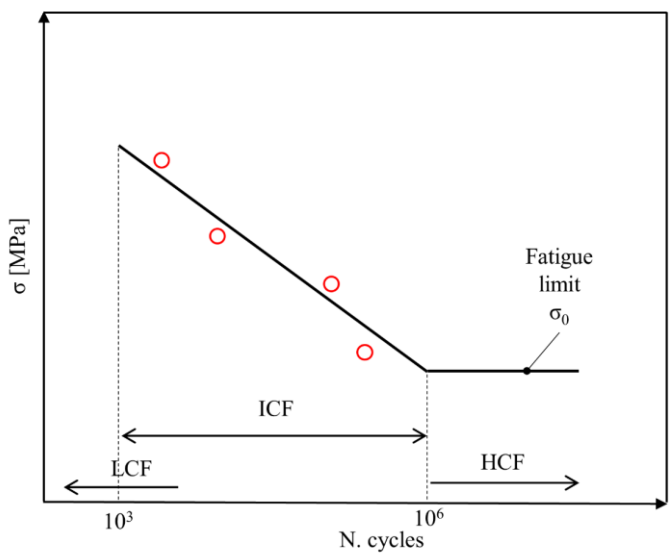

Figure 1.1: Typical fatigue (S-N) curve for a material with fatigue limit.

To model the S-N curve several models have been developed. One of the most adopted is the Basquin's model, where a linear correlation in bi-log terms between the stress amplitude σ and the number of cycle to failure N_f is assumed. The terms a and b are constant evaluated from experimental results.

$$\sigma = a \cdot \left(N_f\right)^b \tag{1.1}$$

1.1.2. Mean stress effect

Another parameter to take into account for fatigue assessment is the effect of the mean stress. A sinusoidal load (Figure 1.2), hence the corresponding stress, may defined by the following parameters:

$$\sigma_m = \frac{\sigma_{max} + \sigma_{\min}}{2} \tag{1.2}$$

$$\Delta\sigma = \frac{\sigma_{max} - \sigma_{\min}}{2} \tag{1.3}$$

$$\mathrm{R} = \frac{\sigma_{\min}}{\sigma_{max}} \tag{1.4}$$

Several authors developed fatigue models that take into account the effect of the mean stress. Each of them present some limitations in its application compared to other models. Three of the most adopted models are the ones proposed by Goodman, Gerber and Sodemberg [13–15].

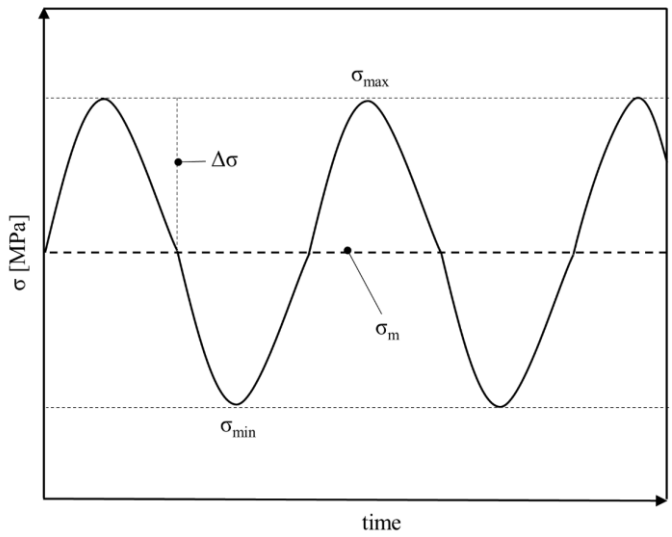

Figure 1.2: Parameters of a cyclic fatigue load.

1.1.3. Load history

The S-N curve are defined for a constant stress amplitude sinusoidal condition. However, in real applications mechanical components experience a wide range of stresses, with variable amplitude, frequencies and sequence in a randomly way. Hence, the stress amplitude and also the mean stress can vary during the fatigue life of a component. Palmgren [16], for the first time, evaluating the fatigue life of ball bearing, proposed a linear rule for the damage assessment. Its work was later extended by Miner [17] and Manson [18]. The Palmgreen-Miner cumulative damage criterion defines the damage fraction D_i for a stress level S_i, equal to the cycle ratio performed by the specimen n_i and the theorical number of cycle to failure for that stress level N_{fi}. The sum of each partial damage must be equal to 1:

$$\sum \frac{n_i}{N_{fi}} = 1 \tag{1.5}$$

This linear damage rule does not consider the loading sequence effect and it is independent from the stress level and its amplitude. Several study have shown its limitations [19,20]; however it is still an adopted criterion due to its simplicity.

1.1.4. Stress state

In real application, mechanical components are subjected to complex stress state where the principal strain are non-proportional and may change their direction during a load sequence. Generally, mechanical components can be subjected to multiaxial stress state. Several class of model have been developed and they can be categorized as: stress based, strain based and energy-based [21]. One of the most popular multiaxial criterion is the "critical plane approach" proposed by Stenfield [22]and later by Socie [23]. It is based on the concept that cracks initiate and propagate in the critical plane across the material. This critical planes are the ones where the combination of the shear and normal stress reaches the maximum value. On the hand, one of the most adopted criterion, that reduces a multiaxial stress state into an equivalent monoaxial equivalent stress, is the von Mises criterion [24]. This criterion can be adopted in mutiaxial conditions where the maximum shear and normal stresses are in phase (proportional multiaxial loading). In case where the maximum of both loading is not in phase (non-proportional loading), other multiaxial model, such as the critical plane one, have to be adopted.

1.1.5. Some consideration about the test time

Generally, fatigue tests are really expensive, both in terms of time and specimens required to obtain the full fatigue curve of the material. For metallic materials they are usually conducted at frequencies in the range of 10-20 Hz and, for example, considering a run-out number of cycle of $2x10^6$, a single test may require about 27 hours. This number of hour must be multiplied for a minimum number of 6 specimens (2 specimens per 3 stress level) to obtain the fatigue curve of the material.

For plastic or composite materials, the test frequency may play an important role. In fact it is not possible to perform fatigue tests with high frequencies in order to prevent the self-heating phenomena that may arise in such kind of materials [25]. The material properties may be severally influenced by high temperature during the fatigue test. This limitation leads to an increase in terms of test time.

To overcome such problems, researchers have been developed (and they are still developing), rapid test methods to assess the fatigue properties of materials and mechanical components.

1.2. From microstructure to macroscopic dissipative effect in fatigue

As previously stated, fatigue is a high dissipative phenomenon that involves several energetic transformations. In particular, the plastic energy dissipation is a manifestation of the failure mechanisms that happens within the material, firstly at microscale, secondly at macroscale, when subjected to fatigue loading.

The dislocations are assumed as the responsible to dissipation at atomic scale. In a pioneristic work, Eshelby [26] apply the notion of dislocation to assess the energy dissipation in metals. He describes the mechanism of mechanical damping in vibrating metals considering also the movement of dislocations. Eshelby observed that in addition to the thermoelastic damping, adopted by Zener [27], there was an additional energy loss due to the oscillation of the dislocations. The movement of the dislocation lead to a redistribution of the stress field within the material and hence to a change in the temperature distribution which, governing the heat flow, causes the mechanical damping. Such a phenomenon is strictly dependent on the applied stress and on the dislocation density.

From a macroscopic point of view, the strain energy dissipated in a cyclic loop may be a useful aid to predict the fatigue failure of materials. In a work of 1965, Morrow [28] developed a model to evaluate the plastic strain energy from the hysteresis loop in terms of stress and strain. He noticed how the plastic strain energy released per cycle is almost constant during the fatigue test and varies with the strain level and the cyclic properties of the material (i.e. cyclic strain hardening, cyclic ductility and fatigue strength coefficient).

The consideration of the dynamic hysteresis loop method have been adopted by Kaleta [29] and coworkers to measure the energy stored in specimens of carbon steel under alternating fatigue loading at a stress equal to the fatigue limit of the material. The stored energy was estimated as difference of the mechanical energy spent in the specimen and the external released energy into the surrounding environment.

Several studies [30,31] have shown that under different strain rates, about the 90% of the generated plastic strain energy is converted into heat. Under this consideration it is possible to say that fatigue is a dissipative phenomenon; hence, measuring the energy dissipation can provide useful information regarding the fatigue life of the material.

1.2.1. Temperature trend during a fatigue test

During a fatigue test, the temperature variation of the specimen may be decomposed into two contributes (Figure 1.3): one given by the elastic strain energy and the other to the plastic strain energy. The first effect is associated with a cyclic recoverable change in temperature (thermoelastic effect), while the latter is associated with an increase in the average value of the temperature.

The variation of the specimen temperature can be performed adopting thermocouples or by means of Infrared Thermography (IR), a full field technique. Thanks to its rapid growth, IR thermography allows to capture very small variations in the temperature of a body due to elastic deformations, compared to thermocouples that may also alter the measurement.

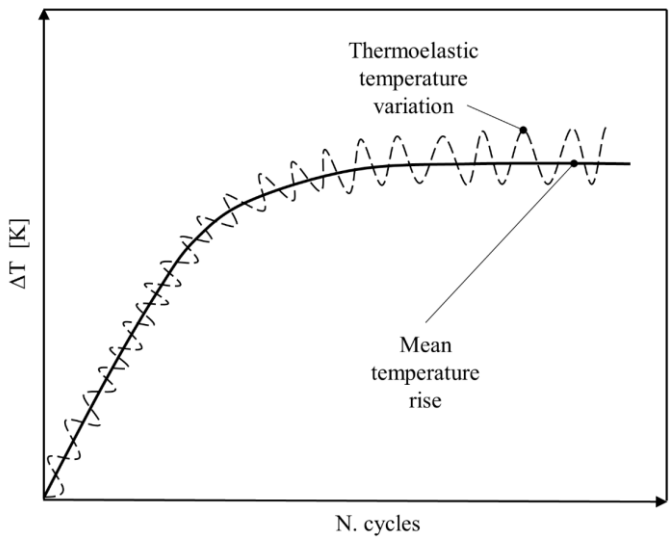

Figure 1.3: Temperature trend during a fatigue test with elastic and plastic contribution.

La Rosa and Risitano [2], applying the IR thermography to monitor the superficial temperature of a plain specimen under constant amplitude fatigue loading conditions, observed three different phases (Figure 1.4). In the first phase (Phase I), the temperature increases and in the second phase (Phase II) it reaches a plateau region, where the temperature has an almost constant value defined as the stabilization temperature ΔT_{st}. Finally, in the third phase (Phase III), the temperature experiences a very high further temperature increment till the specimen failure.

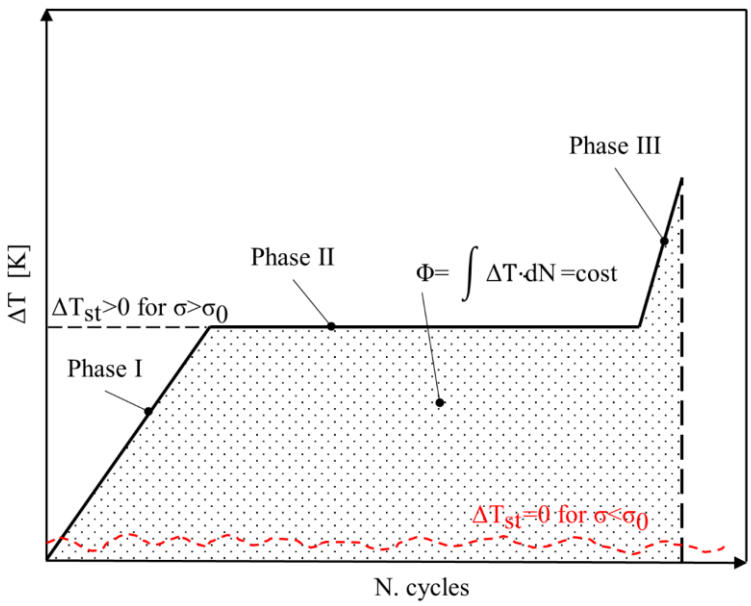

Figure 1.4: Temperature evolution during a fatigue test.

As already observed by Kaleta [29], if the applied stress is below the fatigue limit of the material, the increase in temperature ΔT, evaluated as the difference between the initial temperature and the instantaneous temperature, is very limited and it can be considered null or as noise. On the other hand, if the applied stress is above the fatigue limit of the material the three phases of the temperature trend, as previously described, are shown.

For stresses above the fatigue limit the temperature gradient in terms of number of cycles (ΔT/ΔN) of the Phase I was higher the higher the applied stress. The same consideration is valid also for the stabilization temperature: the greater the applied stress, the greater the stabilization temperature value.

The duration of Phase I and III, i.e. respectively the number of cycles required to reaches the stabilization temperature of Phase II and the phase prior to failure, respect the whole fatigue life of the specimen vary widely. For applied stresses near the fatigue limit of the specimen it is expected that fatigue life is almost covered by Phase II; conversely for applied stresses near the yielding strength of the material, Phase II is very short. Generally, for stresses not near the yielding strength of the material, the Phase I is in the order of the 10% of the whole fatigue life.

Increasing the fatigue test frequency increases also the temperature gradient and considering that the test is very short, the influence of the ambient temperature is negligible.

1.3. Risitano Thermographic Method

Considering the observations on the temperature trend in section 1.2.1, La Rosa and Risitano [2] proposed the Thermographic Method (TM) or the Risitano Thermographic Method, after the researcher who first used thermography to explore the thermal distribution on a specimen, hence determining the fatigue limit.

Since 1983 [32], Risitano proposed the adoption of the IR thermography as a contactless technique to overcome the problem of detection systems, such as thermocouples, that may influence the measurements. An experimental program to validate the adoption of IR thermography was performed and the first results were presented in 1986 [33] at the national congress of the Italian society of machine design (AIAS). In this work, the traditional method for the construction of the S-N curve was paired with the analysis of the temperature over the specimen surface.

Several works of Risitano and coworkers and of other authors validated the TM over a large set of materials: steels [32–36], aluminum alloys [37], cast iron [38–41] and composites [42,43]. On the basis of this observations, Risitano proposed the thermographic analysis as a rapid procedure to estimate the fatigue limit of materials. The fatigue limit can be defined macroscopically as the stress value for which the temperature of the material increases.

Monitoring the specimen surface temperature during a constant amplitude fatigue test by means of an IR camera, it is possible to assess the stabilization temperature ΔT_{st} (or the thermal gradient $\Delta T/\Delta N$) for each applied stress. Reporting in a graph the recorded stabilization temperature versus the applied stress or its square (Figure 1.5), by performing the linear regression it is possible to evaluate the fatigue limit as the intersection of the regression line with the abscissa axis. In a work of 2005, Curti and Curà [44] proposed an iterative method in order to assess the fatigue limit considering also the possible small temperature increments for stresses below the fatigue limit.

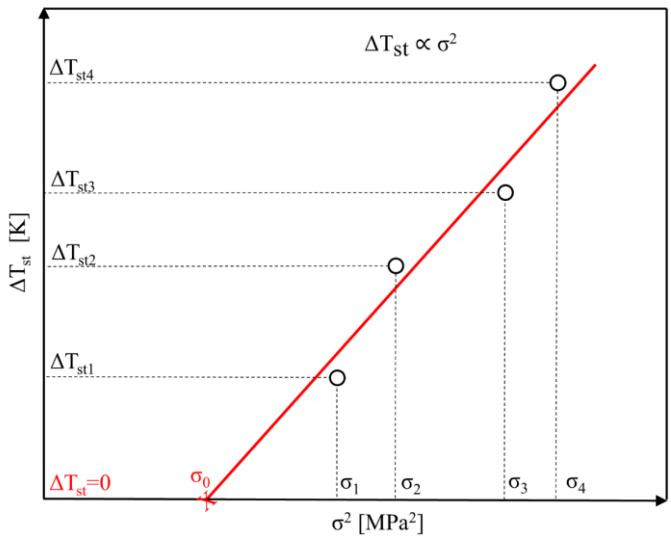

Figure 1.5: Determination of the fatigue limit by means of the TM.

The Thermographic Method can be considered an effective non-destructive method, valid in practical applications where the fatigue limit of a mechanical component is required [45].

The stabilization temperature is reached in a few number of cycles, hence it is possible to reuse the same specimen to apply other stress levels, particularly if loaded at stress level very far from the yielding strength of the material. In this case the specimen experiences very little damage due to the limited number of cycles needed to determine ΔT_{st} or the thermal gradient $\Delta T/\Delta N$.

Moving from the previous consideration, Fargione et al. [46], proposed a rapid procedure to estimate the entire S-N curve from a very limited number of specimens (even one). It is assumed that the fatigue failure occurs when the energy of plastic deformations reaches a constant critical value E_c, characteristic of each material and equal to the energy to failure per unit volume. Considering E_p as the plastic energy per unit volume, the cumulative residual lifetime of the specimen after a number of cycle N_0 can be evaluated as:

$$E_r = E_c - \int_0^{N_0} E_p dN \tag{1.6}$$

The energy of plastic deformation per cycle E_p is proportional to the energy liberated as heat Q by the specimen and, considering that the stored energy in the specimen is very low compared to Q, it is possible states that Q is proportional to the limit energy of the material ($Q \propto E_c$).

From experimental tests it is possible to evaluate the liberated energy Q and a parameter Φ, the Energy Parameter, as the integral of the temperature trend versus the number of cycles (Figure 1.4 and Figure 1.6). The Energy Parameter, as well as the liberated energy Q, is proportional to the limit energy of the material (equation (1.7)).

$$\Phi = \int_0^{N_0} \Delta T \cdot dN \ \propto E_c \tag{1.7}$$

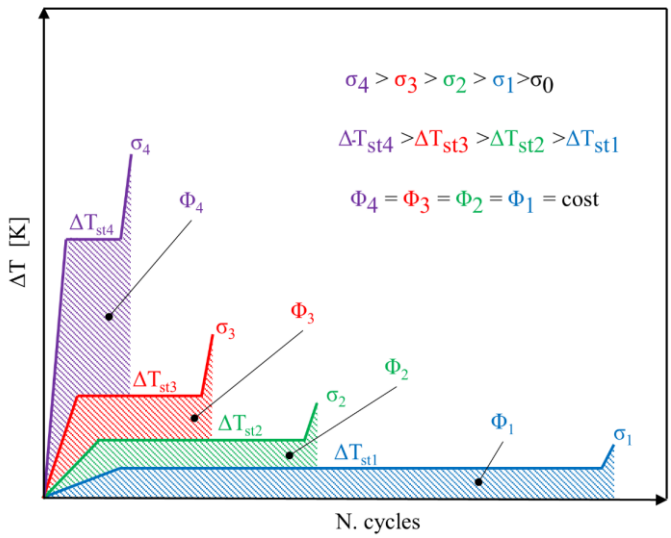

Figure 1.6: Temperature trend during a constant amplitude fatigue test as function of the applied stress level.

As the applied stress is higher compared to the fatigue limit of the material, the higher is the stabilization temperature, but, on the other hand, the subtended are of the temperature vs. number of cycle curve, equal to the Energy Parameter Φ, can be considered constant, given a fixed stress ratio R and test frequency. To estimate Φ, it is convenient to discard the stress levels for which it is difficult to identify the three phases (near the yielding strength of the material.

It is possible to evaluate the whole fatigue curve of the material adopting a very limited number of specimens. Given the fact that the stabilization temperature is reached in short number of cycle, it is possible to apply in a stepped way a stress level sequence, recording the stabilization temperature, till the failure of the specimen (Figure 1.7). The Energy Parameter can be estimated

as the integral of the temperature curve and, by the experience of the Authors, it can be evaluated, for a constant amplitude test, in a simple way as:

$$\Phi \approx \Delta T_{st} \cdot N_f \tag{1.8}$$

Where it is assumed that Phase I and Phase III are negligible compared to the Phase II (valid for stress levels near the fatigue limit). On the basis of equation (1.8), it is possible to evaluate the number of cycles at which the specimen would break if it were stressed only at stress level σ_i. The points represented by the abscissa and ordinate, respectively, equal to the number of cycles and the stress level, can be reported in a S-N diagram to obtain the whole fatigue curve of the specimen (Figure 1.8).

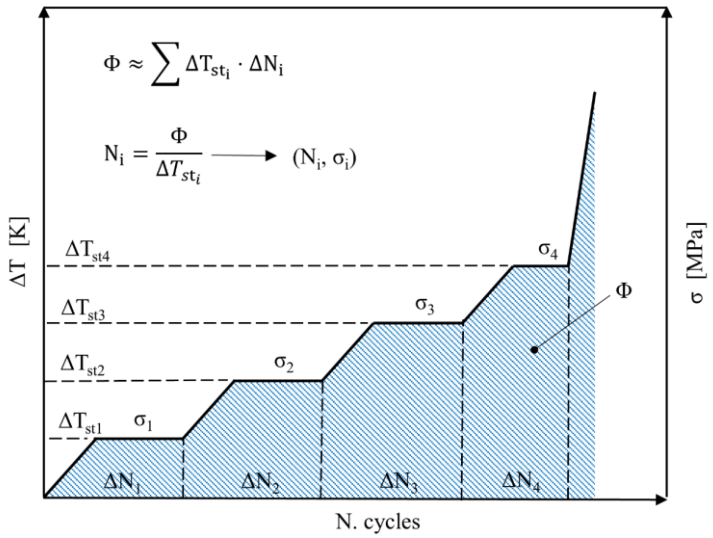

Figure 1.7: Stepwise fatigue test to obtain the stabilization temperature and the Energy Parameter Φ.

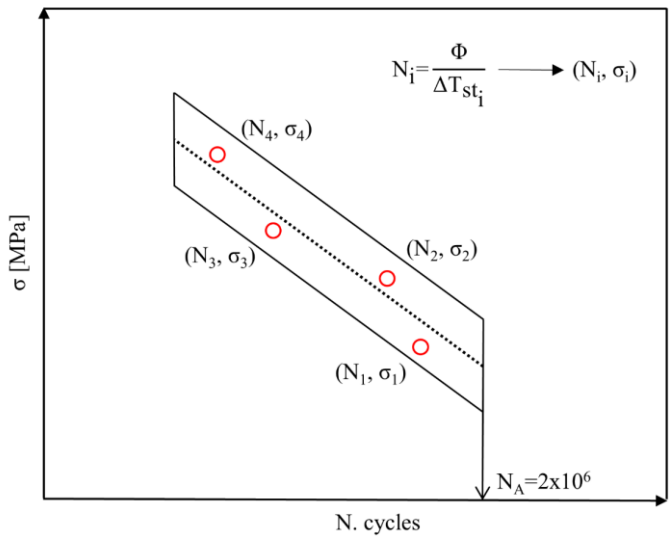

Figure 1.8: S-N curve as evaluated by mean of the stepwise fatigue test.

Several studies have been performed on different materials and applications by many researchers, validating the Thermographic Method [10,19,47–58].

The Thermographic Method, proposed by Risitano and coworkers, is a rapid test procedure able to derive, in a very short amount of time and with a limited number of specimens, the fatigue properties of the material evaluating its temperature evolution.

1.4. Energy based approach

The temperature measurement, if no precautions are taken into account, may be affected by the boundary conditions; for example, room temperature, reflecting sources and heat exchange with the grip section of the testing machine. Based on the classical continuum mechanics, some researchers [59,60], developed energy based approaches to overcome the previously mentioned problem.

The energy balance equation (first principle of thermodynamics) has been reported in terms of power per unit volume, introducing the Helmotz free energy as a thermodynamics potential [60,61]:

$$\rho c \frac{\partial \bar{T}}{\partial t} - \lambda \nabla^2 \bar{T} = \frac{\partial \bar{W}}{\partial t} - \frac{\partial \overline{E_s}}{\partial t} \tag{1.9}$$

The power quantities of equation (1.9) are averaged over one cycle of fatigue loading, according to [62]. The term W represent the plastic energy, E_s the stored energy, T is the material temperature, λ the thermal conductivity of the material and ρ the material density and c the specific heat.

As previously stated in section 1.2, only a part of the total energy spent in the material, introduced by fatigue loading, is stored into the material as internal energy and leading to fatigue failure. A very large amount is dissipated into the form of heat, leading to an increase of the specimen temperature.

In equation (1.9), the contribution of the thermoelastic effect has been neglected, due it reversibility that not lead to an energy dissipation. In addition, the dependence of the material from the temperature variation has been also neglected.

It is possible to define the internal energy rate as stated by Roussellier [63]:

$$\frac{\partial U}{\partial t} = \rho c \frac{\partial T}{\partial t} + \frac{\partial E_s}{\partial t} \tag{1.10}$$

If the average heat rate per cycle is defined as:

$$\frac{\partial \bar{Q}}{\partial t} = \lambda \cdot \nabla^2 \bar{T} \tag{1.11}$$

It is possible to write equation (1.9) as:

$$\frac{\partial \bar{U}}{\partial t} = \frac{\partial \bar{W}}{\partial t} + \frac{\partial \bar{Q}}{\partial t} \tag{1.12}$$

The previous equation represents an energy balance where the mechanical energy W and the dissipated heat energy Q, taken as average value over a cycle, are involved (Figure 1.9).

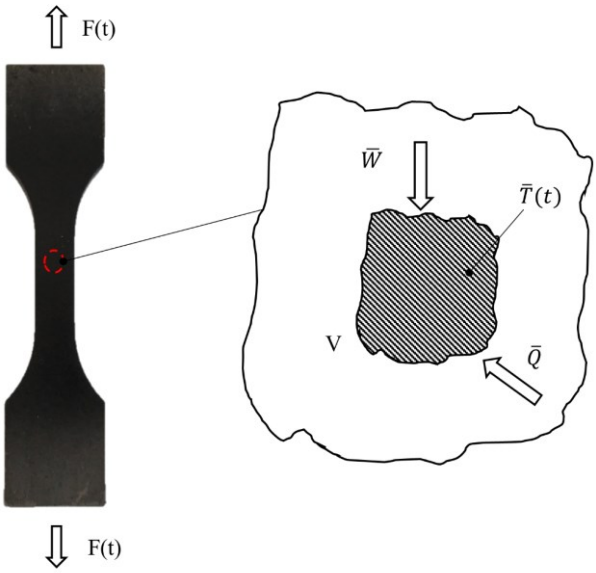

Figure 1.9: Energy balance for a material undergoing fatigue loading.

Equation (1.9), since all the quantities are averaged over a cycle, represent the average evolution of the temperature per cycle. According to this equation, the temperature can be related to the thermal energy dissipated in an elementary volume of material, but the temperature is severally affected by the experimental (thermal and mechanical) boundary conditions (specimen geometry, room temperature and test frequency). On the other hand, the energetic quantities W and Q are independent of the thermal and mechanical boundary conditions [59,64–66].

According to Meneghetti [67], during a fatigue test, when the temperature stabilizes, its thermal average derivate becomes null, hence equation (1.12), considering the relation between the internal energy rate and the stored energy (equation (1.10)), becomes:

$$\frac{\partial \overline{E_s}}{\partial t} = \frac{\partial \bar{W}}{\partial t} + \frac{\partial \bar{Q}}{\partial t} \tag{1.13}$$

If during a fatigue test the external work is removed suddenly (W= 0) at a time t^*, then the internal stored energy become zero, hence equation (1.13) can be rewritten as:

$$\frac{\partial \bar{Q}}{\partial t} = \rho c \frac{\partial T}{\partial t} \tag{1.14}$$

Where the energy heat rate Q dissipated to the surrounding ambient is continuous in terms of time. It is possible to assess the thermal energy release in a unit of volume per cycle. It can be estimated in an easy way taking into account the test frequency f:

$$\bar{Q} = \frac{\frac{\partial \bar{Q}}{\partial t}}{f} = \frac{\rho c \left.\frac{\partial T}{\partial t}\right|_{t>t^*}}{f} \tag{1.15}$$

By means of equation (1.15) it is possible to perform measurements of the specific heat loss at any point over the specimen surface (e.g. notched region [68]), during a fatigue test simply stopping the test after that the stabilization temperature has been reached (Figure 1.10).

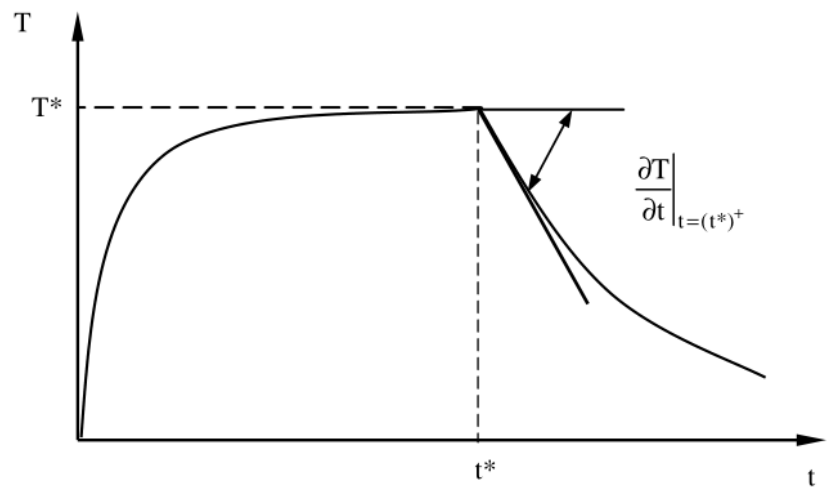

Figure 1.10: Determination of Q by measuring the experimental thermal cooling gradient. From [67]

Compared to the Thermographic Method, where it is possible to perform temperature measurement at a coarse sample rate, even in the order of 1 image per minute for HCF regimes; the evaluation of the temperature cooling curve requires a very high frame rate to perform a good estimation of the cooling gradient.

A comparison of the experimental thermal methods on stainless steel specimen has been reported in the work of Ricotta et al. [69].

2. ENERGETIC RELEASE IN STATIC TENSILE TEST

In the present chapter, the energetic release of a specimen under static tensile test condition is presented. From 1985, thanks to the development of thermocouples and infrared thermography, it has been possible to evaluate the temperature trend of specimen during monotonic tensile test. Nowadays the analysis of the energetic release in static test condition can provide useful information also on the fatigue behavior of the material.

In section 2.1 and 2.2, are presented the constitutive relation between the thermal field and the stress-strain field. Such relations are derived for isotropic and orthotropic material, considering that this two material models are the most adopted in practical application (isotropic model for metal and plastic material, orthotropic for many composite material). The fundamental relation that link the stress field to the thermal field under elastic condition, as observed by Lord Kelvin [70] in 1853, is presented. This relation describes the thermoelastic effect.

In section 2.3 are presented the early studies on the energetic release of metallic and composites specimens. Caglioti suggested to adopt the temperature analysis as a useful aid to assess some material properties difficult to evaluate only by means of the stress and strain fields. Melvin, for the first time, correlated the energetic release under static tensile test to the internal microstructure of the material. The presence of internal micro defect, hence the rise of micro plasticization phenomena, severally affect the temperature trend, showing a deviation from the linearity of the thermoelastic effect, as the applied stress increases.

In section 2.4, the Static Thermographic Method is presented. Moving to the previous studies, Risitano and Risitano defined the end of the thermoelastic effect as the limit stress of the material, where the first micro plasticization arises within the material. They linked this stress value to the conventional fatigue limit of the material. In the same section, two model to predict the temperature trend are presented. The first model requires an experimental calibration and it is able to predict with good agreement the experimental temperature trend of metallic material. The

second model is proposed by the author, and is suitable to be adopted with finite element simulation, as is done in further chapters of Part II of this thesis.

2.1. Stress-Strain-temperature constitutive relationship

Prior to describe the fundamental aspect of the Static Thermographic Method, it is necessary to provide an inside on the constitutive relationship between the stress-strain field and thermal field within the material. In the most general form of constitutive relations, proposed by Duhamel and Neuman [71,72], the effect of thermal and hygroscopic strains is taken into account:

$$\{\sigma\} = [C]\{\varepsilon\} - [\beta](T - T_0) - [\phi](M - M_0) \tag{2.1}$$

Where [C] represent the fourth-order elastic isothermal stiffness tensor with 21 independent components, [β] is the second-order thermal expansion tensor, T_0 is the reference temperature and M_0 is the reference humidity. The humidity effect in thermoelastic analysis could be neglected for sake of simplicity, hence the equation (2.1) could be formulated as [71]:

$$\{\sigma\} = [C](\{\varepsilon\} - \{\alpha\}\Delta T) \tag{2.2}$$

$$[\beta] = [C]\{\alpha\} \tag{2.3}$$

The term {α} is the second-order coefficient of thermal expansion tensor. Under the hypothesis of homogeneous isotropic bodies, equation (2.2) can be reformulated adopting the Lamè constant [71], here reported in expanded form:

$$\sigma_{11} = (2\mu + \lambda)\varepsilon_{11} + \lambda\varepsilon_{22} + \lambda\varepsilon_{33} - \gamma\Delta T \tag{2.4}$$

$$\sigma_{22} = \lambda\varepsilon_{11} + (2\mu + \lambda)\varepsilon_{22} + \lambda\varepsilon_{33} - \gamma\Delta T$$

$$\sigma_{33} = \lambda\varepsilon_{11} + \lambda\varepsilon_{22} + (2\mu + \lambda)\varepsilon_{33} - \gamma\Delta T$$

$$\sigma_{12} = 2\mu\varepsilon_{12}$$

$$\sigma_{23} = 2\mu\varepsilon_{23}$$

$$\sigma_{31} = 2\mu\varepsilon_{31}$$

Or in a condensed form:

$$\sigma_{ij} = 2\mu\varepsilon_{ij} + (\lambda\varepsilon_{kk} - \gamma\Delta T)\delta_{ij} \tag{2.5}$$

Where δ_{ij} the Kronecker's symbols (1 if i=j; 0 if i≠j). The following expressions are adopted for the Lamè constants, where α is the linear thermal expansion coefficient for isotropic material:

$$\mu = \frac{E}{2(1+\nu)}, \qquad \lambda = \frac{\nu E}{(1+\nu)(1-2\nu)} \tag{2.6}$$

$$G = \mu\,, \quad E = \frac{\mu(3\lambda + 2\mu)}{\lambda + \mu}\,, \qquad \nu = \frac{\lambda}{2(\lambda+\mu)}, \qquad \gamma = (3\lambda + 2\mu)\alpha = \frac{E\alpha}{1-2\nu}$$

2.1.1. First stress invariant and first strain invariant

Considering equations (2.4) or (2.5) it is possible to obtain a relation between the first stress invariant (sum of the hydrostatic pressure or sum of the principal stress) and the first strain invariant. By summing the first three terms of equation (2.4), it is possible to obtain the following expression for the first stress invariant:

$$\Delta I_{1,\sigma} = (2\mu + 3\lambda)(\varepsilon_{11} + \varepsilon_{22} + \varepsilon_{33}) - 3\gamma\Delta T = (2\mu + 3\lambda)\Delta I_{1,\varepsilon} - 3\gamma\Delta T \tag{2.7}$$

From the previous equation it is possible to retrieve the first strain invariant as:

$$\Delta I_{1,\varepsilon} = \frac{1}{(2\mu + 3\lambda)} \Delta I_{1,\sigma} + 3\gamma\Delta T = \frac{\alpha}{\gamma} \Delta I_{1,\sigma} + 3\gamma\Delta T \tag{2.8}$$

Where the relation between the Lamè constant γ and α of equation (2.6) has been considered. The same expression can be formulated considering the elastic modulus and the Poisson ratio of the material:

$$\Delta I_{1,\varepsilon} = \frac{1 - 2\nu}{E} \Delta I_{1,\sigma} + 3\alpha\Delta T \tag{2.9}$$

2.1.2. Plane stress condition

Under the hypothesis of a plane stress field, equations (2.5) can be written in an easier form, given the fact that σ_{33}= σ_{23}= σ_{31}= 0. By substituting equation (2.6) into σ_{11} stress of equation (2.4) the following expression is obtained:

$$\sigma_{11} = \frac{E}{(1+\nu)(1-2\nu)} [(1-\nu)\varepsilon_{11} + \nu(\varepsilon_{22} + \varepsilon_{33}) - (1+\nu)\alpha\Delta T] \tag{2.10}$$

From the expression of σ_{33} of equation (2.9), imposing the equality to 0, the expression of ε_{33} as a function of ε_{11} and ε_{22} could be obtained and then it can be substituted to equation (2.10).

$$\varepsilon_{33} = \frac{1+\nu}{1-\nu} \alpha\Delta T - \frac{\nu}{1-\nu} (\varepsilon_{11} + \varepsilon_{22}) \tag{2.11}$$

$$\sigma_{11} = \frac{E}{1-\nu^2} (\varepsilon_{11} + \nu\varepsilon_{22}) - \frac{E}{1-\nu} \alpha\Delta T \tag{2.12}$$

Adopting the same procedure, an equivalent expression for σ_{33} and for the in-plane shear stress can be obtained. The stress-strain-temperature relation in the case of a plane stress field can be expressed as follows:

$$\sigma_{11} = \frac{E}{1-\nu^2}(\varepsilon_{11} + \nu\varepsilon_{22}) - \frac{E}{1-\nu}\alpha\Delta T \tag{2.13}$$

$$\sigma_{22} = \frac{E}{1-\nu^2}(\varepsilon_{22} + \nu\varepsilon_{11}) - \frac{E}{1-\nu}\alpha\Delta T$$

$$\sigma_{12} = \frac{E}{1+\nu}\varepsilon_{12}$$

2.2. Thermodynamics of the elastic continuum

The general expression of the thermoelastic law in the more general case of an anisotropic material was developed by Potter and Graves [73]. They developed a formulation were the temperature variation of a solid material were bind to its deformation field under adiabatic conditions. The first principle of thermodynamics can be expressed in the following form, linking the internal energy of the system u with the work applied w and the heat provided to it q.

$$du = \delta w + \delta q \tag{2.14}$$

The internal energy differential is expressed as an exact differential, with letter d, because it is a state variable (i.e. independent on the transformation path followed by the system), while the applied work and heat differential are expressed with inexact differential symbol δ, because they are dependent on the transformation path followed by the system to move from one state to another. The elementary work needed to deform a material volume unit, considering the stress and strain tensors is:

$$\delta w = \{\sigma\}^T\{d\varepsilon\} \tag{2.15}$$

Substituting equation (2.15) into (2.14), the first principle of thermodynamics could be expressed as:

$$du = \{\sigma\}^T\{d\varepsilon\} + \delta q \tag{2.16}$$

Under the hypothesis of reversible transformation, the second principle of thermodynamics states that:

$$dS = \frac{\delta q'}{T} \tag{2.17}$$

Where T is the absolute temperature, S the mass entropy of the system and q' the provided heat per mass unit. Combining equations (2.16) and (2.17), and introducing the density of the material ρ in order to refer equation (2.17) to the volume unit, equation (2.18) is obtained:

$$du = \{\sigma\}^T\{d\varepsilon\} + \rho T dS \tag{2.18}$$

The Helmotz's free energy is another state variable expressed as:

$$H = u - \rho T S \tag{2.19}$$

The total differential expression of this state variable can be developed taking into account the conservation of the mass and imposing a constant density:

$$dH = du - \rho T dS - \rho S dT \tag{2.20}$$

Substituting (2.18) into (2.20) the following expression is obtained:

$$dH = \{\sigma\}^T\{d\varepsilon\} - \rho S dT \tag{2.21}$$

Considering the constitutive law of the material, in this case a perfectly solid linear elastic material, the link between the stress tensor, strain tensor and temperature can be expressed as:

$$\{\sigma\} = [C](\{\varepsilon\} - \{\alpha\}\Delta T) \tag{2.22}$$

In this expression, only two within the variables {σ}, {ε} and T are independent, hence the state of the material could be identified adopting, for example {ε} and T. Given the fact that the Helmotz's free energy is a state variable, it depends only by the strain tensor and temperature; hence it can be derived respect this two independent variables:

$$dH = \left\{\frac{\partial H}{\partial\{\varepsilon\}}\right\}^T d\{\varepsilon\} + \frac{\partial H}{\partial T} dT \tag{2.23}$$

Comparing equations (2.21) and (2.23), the following expression for the partial derivate of the Helmotz's free energy can be obtained:

$$\left\{\frac{\partial H}{\partial\{\varepsilon\}}\right\}^T = \{\sigma\}^T \; ; \qquad \frac{\partial H}{\partial T} = -\rho S \tag{2.24}$$

Entropy is also a state variable, hence it depends from the strain tensor and temperature. Its differential can be expressed as:

$$dS = \left\{\frac{\partial S}{\partial\{\varepsilon\}}\right\}^T d\{\varepsilon\} + \frac{\partial S}{\partial T} dT \tag{2.25}$$

Taking into account the previous equation,

$$\rho dS = \left\{\frac{\partial^2 H}{\partial\{\varepsilon\}\partial T}\right\}^T d\{\varepsilon\} + \frac{\partial^2 H}{\partial T^2} dT \tag{2.26}$$

The next step is to delete di entropy and Helmotz's free energy from the previous equation; hence it is useful to derive to respect the temperature the first expression of equation (2.24).

$$\left\{\frac{\partial^2 H}{\partial\{\varepsilon\}\partial T}\right\}^T = \frac{\partial\{\sigma\}^T}{\partial T} \tag{2.27}$$

This expression, together with equation (2.17), can be substitute into (2.27):

$$\rho\frac{\delta q'}{T} = -\frac{\partial\{\sigma\}^T}{\partial T}\, d\{\varepsilon\} - \frac{\partial^2 H}{\partial T^2} dT \tag{2.28}$$

It is possible to obtain a useful expression of the second derivative of the Helmotz's free energy in equation (2.28), by substituting in the same equation the differential operator *d* with the partial derivative operator:

$$\frac{\rho}{T}\left(\frac{\delta q'}{\partial T}\right)_\varepsilon = -\frac{\partial\{\sigma\}^T}{\partial T}\left(\frac{\partial\{\varepsilon\}}{\partial T}\right)_\varepsilon - \frac{\partial^2 H}{\partial T^2}\left(\frac{\partial T}{\partial T}\right)_\varepsilon \tag{2.29}$$

Bearing in mind that the partial derivate is performed under the constant deformation hypothesis, the previous equation became:

$$\frac{\rho}{T}\left(\frac{\delta q'}{\partial T}\right)_\varepsilon = -\frac{\partial^2 H}{\partial T^2} \tag{2.30}$$

Introducing the heat mass capacity related to constant deformation:

$$\frac{\partial^2 H}{\partial T^2} = -\frac{\rho C_\varepsilon}{T} \tag{2.31}$$

Considering the equation (2.29) and substituting the previous equation:

$$\frac{\rho}{T}\left(\frac{\delta q'}{\partial T}\right)_\varepsilon = -\frac{\partial\{\sigma\}^T}{\partial T}\, d\{\varepsilon\} - \frac{\rho C_\varepsilon}{T} dT \tag{2.32}$$

It is possible to excise the stress tensor from equation (2.32), adopting the material constitutive equation (2.22), derived respect the temperature under constant deformation:

$$\left(\frac{\partial\{\sigma\}}{\partial T}\right)_{\varepsilon} = \left(\frac{\partial[C]}{\partial T}\right)_{\varepsilon}(\{\varepsilon\} - \{\alpha\}\Delta T) - [C]\left(\{\alpha\} + \Delta T\left(\frac{\partial\{\alpha\}}{\partial T}\right)_{\varepsilon}\right) \tag{2.33}$$

If the constant deformation index is omitted:

$$\frac{\partial\{\sigma\}^T}{\partial T} = (\{\varepsilon\}^T - \{\alpha\}^{\mathrm{T}}\Delta T)\frac{\partial[C]}{\partial T} - [C]\left(\{\alpha\}^T + \Delta T\,\frac{\partial\{\alpha\}^T}{\partial T}\right) \tag{2.34}$$

The previous equation could be introduced in equation (2.32), hence writing:

$$\frac{\rho}{T}\frac{\delta q'}{\partial T} = -\left[(\{\varepsilon\}^T - \{\alpha\}^{\mathrm{T}}\Delta T)\frac{\partial[C]}{\partial T} - [C]\left(\{\alpha\}^T + \Delta T\,\frac{\partial\{\alpha\}^T}{\partial T}\right)\right]d\{\varepsilon\} + \frac{\rho C_{\varepsilon}}{T}dT \tag{2.35}$$

That, under adiabatic condition, given that δq' is null:

$$\frac{\rho C_{\varepsilon}}{T}dT = \left[(\{\varepsilon\}^T - \{\alpha\}^{\mathrm{T}}\Delta T)\frac{\partial[C]}{\partial T} - [C]\left(\{\alpha\}^T + \Delta T\,\frac{\partial\{\alpha\}^T}{\partial T}\right)\right]d\{\varepsilon\} \tag{2.36}$$

Assuming that the reference temperature respects which the constitutive equation has been written is the average temperature of the sinusoidal stressed material, hence ΔT is the temperature excursion caused by the cyclic deformation $\Delta\{\varepsilon\}$. The previous equation can be rewritten as:

$$\rho C_{\varepsilon}\frac{\Delta T}{T} = \left[(\{\varepsilon\}^T - \{\alpha\}^{\mathrm{T}}\Delta T)\frac{\partial[C]}{\partial T} - [C]\left(\{\alpha\}^T + \Delta T\,\frac{\partial\{\alpha\}^T}{\partial T}\right)\right]\Delta\{\varepsilon\} \tag{2.37}$$

This expression is at the base of the stress thermoelastic analysis. It is written in a general form, taking into account the material characteristics variation with the temperature and directions, i.e. anisotropic materials.

2.2.1. Isotropic material

Under the hypothesis of an isotropic material, some simplifying assumptions can be made in order to excise some terms and to obtain a simplified formulation that link directly the thermoelastic signal with the first stress invariant. For an isotropic material the stiffness matrix [C] has only two independent parameters (E and ν) and the thermal expansion vector has only one coefficient α, for normal deformation contribute; zero for the shear contribute. Another simplifying hypothesis is that is possible to neglect the variation of the elastic characteristic and of the expansion coefficient with the temperature.

$$\{\alpha\}^T = \{\alpha, \alpha, \alpha, 0,0,0\} \tag{2.38}$$

$$\frac{\partial[C]}{\partial T} = 0 \qquad \frac{\partial\{\alpha\}^T}{\partial T} = 0 \tag{2.39}$$

Under these assumption, equation (2.37), became:

$$\rho C_\varepsilon \frac{\Delta T}{T} = -\{\alpha\}^{\mathrm{T}}[C]\Delta\{\varepsilon\} \tag{2.40}$$

Developing the second member of the previous equation:

$$\rho C_\varepsilon \frac{\Delta T}{T} = -\alpha \frac{E}{(1+\nu)(1-2\nu)}\{(1+\nu),(1+\nu),(1+\nu)\}^T\Delta\{\varepsilon\} \tag{2.41}$$

$$\rho C_\varepsilon \frac{\Delta T}{T} = -\alpha \frac{E}{(1-2\nu)}\left(\Delta\varepsilon_{xx} + \Delta\varepsilon_{yy} + \Delta\varepsilon_{zz}\right) = -\alpha \frac{E}{(1-2\nu)}\Delta I_{1,\varepsilon} \tag{2.42}$$

Instead of the first deformation invariant, it is convenient to rewrite the equation (2.42) adopting the first stress invariant (equation (2.9)):

$$\rho C_\varepsilon \frac{\Delta T}{T} = -\alpha\Delta \mathrm{I}_{1,\sigma} - 3\alpha^2 \frac{E}{1-2\nu}\Delta T \tag{2.43}$$

That can be rearranged as:

$$\rho\left(C_\varepsilon + \frac{3\alpha^2 T}{\rho}\frac{E}{1-2\nu}\right)\frac{\Delta T}{T} = -\alpha\Delta \mathrm{I}_{1,\sigma} \tag{2.44}$$

This equation is formally similar to the previous one and more useful from a practical point of view, given that a link between the specific heat at constant deformation and constant stress exist. It is well known that in solid materials, as well as in liquid ones, it is difficult to estimate the specific heat at constant deformation due to the high stress field that rise when the deformations are locked [74]. Despite this, a relation between the two specific heat exist, evaluated on the basis of the heat amount provided to the solid and the temperature variation at zero stress. Under these hypotheses it is possible to write [75]:

$$\delta q = \rho C_\sigma dT \qquad \delta q' = C_\sigma dT \tag{2.45}$$

Inserting equation (2.45) in equation (2.35), taking into account all the simplifying hypotheses adopted here, the following equation can be write:

$$\rho C_\sigma \frac{\mathrm{d}T}{T} = \alpha\frac{E}{(1-2\nu)}\Delta I_{1,\varepsilon} + \frac{\rho C_\varepsilon}{T}dT \tag{2.46}$$

Under the hypothesis of constant stress, it is possible to insert the first strain invariant. The following expression that link the specific heat at constant deformation with constant stress:

$$C_\sigma = 3\frac{\alpha^2 T}{\rho}\cdot\frac{E}{1-2\nu} + C_\varepsilon \tag{2.47}$$

This relation allow to rewrite equation (2.44) as:

$$\rho C_\sigma \frac{\Delta T}{T} = -\alpha\Delta I_{1,\sigma} = -\alpha\cdot(\Delta\sigma_{\mathrm{xx}} + \Delta\sigma_{yy} + \Delta\sigma_{zz} = -\alpha\cdot\Delta(\sigma_1 + \sigma_2 + \sigma_3) \tag{2.48}$$

The previous equation states that the local temperature variation is directly proportional to the first stress invariant variation of the local stress state, i.e. the variation of the hydrostatic stress component or the sum of the principal stresses. For an elastic homogeneous isotropic solid, neglecting the variation of the mechanical and thermal material properties with the temperature, it is possible to write:

$$\Delta T = -\frac{\alpha}{\rho C_\sigma} \cdot T \Delta I_{1,\sigma} = -K_m T \cdot \Delta I_{1,\sigma} \tag{2.49}$$

The K_m constant in equation (2.49) is the thermoelastic constant of the material. Some materials present negative values of the thermoelastic constant (rubber, carbon fiber, some plastic material), but in general it is positive. The typical value for this constant for steel alloys is about 3.3×10^{-12} Pa^{-1}, while for aluminum alloys 9.5×10^{-12} Pa^{-1}. This constant can be assumed constant only if the variation with temperature of the thermal expansion coefficient, the density and the specific heat can be neglected.

The thermoelastic effect is due to the interconnection between the mechanical work made on the material in the elastic field and the variation of its thermodynamics characteristics, i.e. stress-strain vs. entropy and temperature. Under an isentropic (reversible) process, the variation of the internal energy of the deformed body is due only to the mechanical work done, as stated by the first and second thermodynamics principles. For an elastic homogeneous isotropic material under uniaxial stress, equation (2.49) simplify in:

$$\left(\frac{\partial \mathrm{T}}{\partial \sigma_1}\right)_S = -K_m \cdot T \tag{2.50}$$

According to this equation, a traction stress in elastic regime lead to a temperature decrement, while a compression increases it. As a general rule, a crystalline material tends to cool itself when undergoes to traction condition; however, if the load velocity is extremely slow, the material absorb heat from the surrounding environment and its temperature remain constant, i.e. the process is isotherm.

2.2.2. Orthotropic material

For an anisotropic material with orthotropic properties, the thermal expansion coefficient vector and the stiffness matrix of the material assume the form of equation (2.51).

$$\begin{Bmatrix} \sigma_{ii} \\ \sigma_{jj} \\ \sigma_{kk} \\ \sigma_{ij} \\ \sigma_{ik} \\ \sigma_{jk} \end{Bmatrix} = \begin{bmatrix} C_{iiii} & C_{iijj} & C_{iikk} & 0 & 0 & 0 \\ C_{iijj} & C_{jjjj} & C_{iikk} & 0 & 0 & 0 \\ C_{kkii} & C_{kkjj} & C_{kkkk} & 0 & 0 & 0 \\ 0 & 0 & 0 & C_{ijij} & 0 & 0 \\ 0 & 0 & 0 & 0 & C_{ikik} & 0 \\ 0 & 0 & 0 & 0 & 0 & C_{jkjk} \end{bmatrix} \cdot \left(\begin{Bmatrix} \varepsilon_{ii} \\ \varepsilon_{jj} \\ \varepsilon_{kk} \\ \varepsilon_{ij} \\ \varepsilon_{ik} \\ \varepsilon_{jk} \end{Bmatrix} - \begin{Bmatrix} \alpha_{ii} \\ \alpha_{jj} \\ \alpha_{kk} \\ \alpha_{ij} \\ \alpha_{ik} \\ \alpha_{jk} \end{Bmatrix} \Delta T \right) \tag{2.51}$$

In order to define the stiffness matrix, nine independent parameters are required: the three normal elastic modulus, the three tangential elastic modulus and the three Poisson coefficient. If the reference system is not the same of the orthotropic axes, all the terms of the stiffness matrix and of the thermal expansion coefficient are different from zero.

For a thin lamina of material, the stress state can be assumed as planar, where three of the six independent are equal to zero (e.g. σ_{ii}, σ_{jj}, σ_{ij}). As regards the deformations, ε_{ik} and ε_{jk} are null, while ε_{kk} is equal to:

$$\varepsilon_{kk} = -\frac{C_{kkii}\varepsilon_{ii} + C_{kkjj}\varepsilon_{jj}}{C_{kkkk}} \tag{2.52}$$

In an arbitrary reference system, the thermoelastic equation (2.37) for an anisotropic material, hence also for orthotropic material, under plane stress state is:

$$\rho C_{\sigma} \frac{\Delta T}{T} = -(\alpha_{xx}\Delta\sigma_{xx} + \alpha_{yy}\Delta\sigma_{yy} + \alpha_{xy}\Delta\sigma_{xy}) \tag{2.53}$$

And, if the principal stress reference system is taken into account, which directions in general do not coincide with the principal directions of the deformations and material orthotropic principal directions, the thermoelastic equation (2.48) simplifies in:

$$\rho C_\sigma \frac{\Delta T}{T} = -(\alpha_{11}\Delta\sigma_1 + \alpha_{22}\Delta\sigma_2) \tag{2.54}$$

Where in the principal reference system the following expression are valid:

$$\{\sigma\} = \begin{Bmatrix} \sigma_1 \\ \sigma_2 \\ 0 \end{Bmatrix} \qquad \{\alpha\} = \begin{Bmatrix} \alpha_{11} \\ \alpha_{22} \\ \alpha_{12} \end{Bmatrix} \tag{2.55}$$

Equation (2.54) does not allow an easy assessment of the temperature value due to the fact that the principal stress direction varies locally and are unknown a priori; in addition, it is not possible to assign the thermal expansion coefficient values in these directions. On the other hand, if the reference orthotropic reference system is taken into account, the stress and thermal expansion coefficient became:

$$\{\sigma\} = \begin{Bmatrix} \sigma_{ii} \\ \sigma_{jj} \\ \sigma_{ij} \end{Bmatrix} \qquad \{\alpha\} = \begin{Bmatrix} \alpha_{ii} \\ \alpha_{jj} \\ 0 \end{Bmatrix} \tag{2.56}$$

That are known, given that the thermal expansion coefficient are defined along the orthotropic directions. The thermoelastic equation (2.48) became:

$$\Delta T = -\frac{T}{\rho C_\sigma}(\alpha_{\mathrm{ii}}\Delta\sigma_{\mathrm{ii}} + \alpha_{jj}\Delta\sigma_{jj}) \tag{2.57}$$

Considering the temperature variation, it is possible to write in analogy to the isotropic solid equation (2.57) as:

$$\Delta T = -K_m T\left(\Delta\sigma_{\mathrm{ii}} + \alpha_m \Delta\sigma_{jj}\right) \qquad K_m = -\frac{\alpha_{ii}}{\rho C_\sigma} \qquad \alpha_m = \frac{\alpha_{jj}}{\alpha_{ii}} \tag{2.58}$$

Compared to the coefficient α11 and α22 in equation (2.54), the coefficient ii and jj or the Km constant and αm ratio, can be univocally determined knowing the principal directions respect to which estimate the thermal expansion coefficient.

2.3. Thermal behavior under static tensile test

2.3.1. Early study of the change in the temperature trend during tensile test

In a work of 1982, Caglioti [76] studied the behavior of a material that undergoes to elastic deformation towards the "thermoelastic instability". According to Caglioti, any mechanical transformation can be considered as an irreversible thermodynamics transformation, hence all the state variables (e.g. strain, stress and temperature) and the coupling between them must be taken into account for a clear understanding of the mechanical transformation. The consideration of the thermal behavior during mechanical tests, in particular during fatigue tests, has been taken into account recently. Assuming that entropy change measures the quality of a system transformation, when a deformation is applied to a material, it promotes two different entropy changes: a thermal entropy change and a configurational entropy change. They are of the same importance and must compensate each other during an ideally adiabatic and isentropic transformation. For example, the reason for thermoelastic cooling of metallic specimen under adiabatic tension [70]. As the applied deformation increases, the adiabatic cooling of the specimen proceeds up to a state where the deformation field promotes a positive change in the temperature field.

Caglioti proposed to adopt the whole thermoelastic region, thanks to the coupling between the thermal and mechanical transformation, as a very fine probe of the state of the material. The thermoelastic behavior can be adopted for an accurate determination of several thermal and mechanical properties of the materials itself and to predict eventually change in its mechanical behavior.

One of the main reason why the thermoelastic behavior has been neglected is due to the small temperature variation during an adiabatic elastic transformation. For example, the order of magnitude of the temperature decrement for a metal under adiabatic conditions is of the order of 0.2K, a value that in practical application has been always neglected due to the difficult to assess it. Nowadays, thanks to the development of infrared sensors, it is possible to apply the infrared thermography in an easy way on a large set of materials, even under working conditions.

Caglioti observed that when the metallic material is elastically strained, the temperature tend change in a remarkable way as the yielding stress is approaching Figure 2.1. This temperature behavior might help to identify the thermoelastic limit between the elastic and the incipient

plastic regime. In the work of Caglioti, the temperature versus stress diagram (ΔT-σ) for a steel sample during a monoaxial tensile test in order to determine the yielding stress of the material.

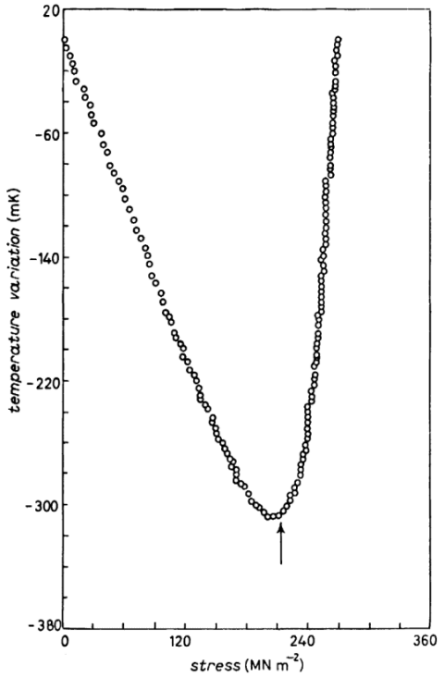

Figure 2.1: Temperature dependence on the stress reacting to the deformation imposed to a steel sample [76].

The yielding stress has been defined as the corresponding stress for which the temperature tangent is horizontal and then the temperature trend experience an increment.

2.3.2. Correlation between the energetic release and the material microstructure

Melvin et al. studied in detail the heat generated during mono axial tensile test of several types of steel [77] and composite materials [78]. Melvin developed a model taking into account microscopic considerations on the macroscopic thermal behavior of the material. The microscopic approach involves the analysis of the atomic source of plastic strain, i.e. dislocations. On the other hand, the macroscopic approach models the material as a continuum, considering only its average properties.

Focusing on the microscopic scale, when a tensile stress is applied on a crystalline structure, such as metals, a corresponding elastic dilation is observable. The applied external work, at atomic level, is adopted to raise the interatomic potential of the vibrating body in thermal equilibrium and hence increase the mean interatomic separation. In order to oppose to the

deformation, the material, given also the fact that cannot increase the atomic population, cool down. If the applied stress is removed, the resumes its previous average interatomic separation without showing effect of the previous deformation. This ability is limited if the load is increased beyond an elastic limit.

The plastic deformations begin when the elastic response of the crystal reaches its limit. This kind of deformation is due to the slipping of the crystalline structure to release internal stress. The consequence of this slip result in a micro frictional heating generation which is of opposite sign respect the thermoelastic cooling.

According to the study of Brown (1968) [79], three types of deformation can operate before the macroplastic behavior: elastic (linear or nonlinear); inelastic and microplastic. In the first stage, the elastic one, no energy dissipation is present during a load-unload cycle. In the second stage, some plastic strain, but recoverable, are present with some energy dissipation during a loading-unloading cycle, due to the movement of the dislocation that return in their original configuration. In the last stage, energy dissipation is present with irreversible dislocation motion.

At a microscopic scale, dislocation contains kinks which tends to move from a minimum energetic level to another. The application of a low stress allows the movement and hence the minimization of the energy level. Microplasticity has been observed at stresses lower than the macroscopic yielding stress in bcc metals and fcc alloys [80]. The yielding first occurs in isolated grains but, as the load increases, thanks to the stress concentration generated in neighbors' crystals, it spread from one grain to another and lead to macroscopic breakdown. The yielding, as observed by Caglioti, is associated with a sudden increase in the temperature trend of the specimen, compensating the thermoelastic cooling of the specimen.

Melvin developed a mathematical model applying the thermodynamics theory, evaluating the entropy of the phenomena as the sum of the thermodynamics forces and the fluxes:

$$\frac{\partial T}{\partial t} - \chi \nabla^2 T = -\gamma \frac{T_0}{E}(1 - 2\nu)\frac{d\sigma}{dt} \tag{2.59}$$

Where χ is the thermal diffusivity of the material and γ the Gruneisen parameter, expression of the anharmonicity of the interatomic potential [76].

In the case of mono axial static tensile stress for homogeneous material and under the adiabatic hypothesis, i.e. laplacian term equal to zero, equation (2.59) can be solved becoming:

$$\mathrm{T(z,t)} = T_0 - \frac{4}{\pi^3}\gamma T_0 \dot{\varepsilon}(1-2\nu)\frac{L^2}{x}\cdot\sum_{n=1}^{\infty}\left(\frac{1-e^{-\frac{n^2}{\tau_d}}}{n^3}\cdot\sin\left(n\pi\frac{z}{L}\right)\right) \quad n\ odd \tag{2.60}$$

Valid for a cylindrical sample with a constant stress rate (stress/time), not fast enough to neglect the viscous effect. The terms τ_d is the time constant or characteristic heat diffusion time, evaluated as:

$$\tau_d = \frac{L^2}{\pi^2\chi} \tag{2.61}$$

L is the length of the reduced area of the specimen.

If during a tensile test performed at constant strain rate, the time to reach the thermo elasto-plastic limit is much lower than the characteristic heat diffusion time τ_d, the test can be considered as performed under adiabatic conditions.

Beyond the elastic limit, additional terms should be adopted in order to model the dissipative phenomena represented by inelastic and plastic deformation. Beghi et al. [81] defined a function for the entropy generation due to plasticity in the form of dissipated mechanical power.

$$\mathrm{s_{pl}} = f\frac{\sigma\dot{\varepsilon}_{pl}}{T} \tag{2.62}$$

The empirical coefficient f is the fraction of the plastic power immediately dissipated and it depends of the stress history of the body.

Adding the effect of equation (2.66) into equation (2.59), always under adiabatic assumption, the following equation can be derived:

$$\frac{\partial T}{\partial t} = -\gamma \frac{T_0}{E}(1-2\nu)\frac{d\sigma}{dt} + f\frac{\sigma}{C_v}\frac{d\varepsilon_{pl}}{dt} \tag{2.63}$$

The coefficient f is strictly dependent of the stress, strain and temperature condition. For sake of simplicity it can be assumed equal to one, as no energy is stored by the microstructure and hence is all dissipated. Energy storage is due to the dislocation interaction in the form of work hardening. This process is not expected to be preponderant till the material begun to yield.

Melvin proposed a constitutive equation for the material in order to represent the deformation range from zero up to the initiation of macroplastic flow:

$$\sigma \doteq E\dot{\varepsilon} + M\dot{\varepsilon_{pl}} \tag{2.64}$$

Where ε is the total strain and M is defined as the plastic modulus, similar to the elastic modulus E of the material. The plastic strain rate can be assumed as equal to:

$$\dot{\varepsilon}_{pl} = b\rho_m \frac{\nu^*}{S}\sigma \tag{2.65}$$

Where ρ_m is the mobile dislocation density, ν^* the dislocation velocity (i.e. the speed of sound in the material), S is the coupling stress that acts across the glide plane and b is the Burges vector.

It is assumed that the tensile test is performed at constant total stress rate, chosen fast enough to assure adiabatic conditions, but not so rapid as viscous effects become significant. After substitution of equations (2.64) and (2.65) into (2.63), the integration can be performed between t_0 and t, with $\sigma_0=\varepsilon_0=t_0= 0$ and T_0 as the room temperature.

$$\Delta T = K_m T_0 \sigma_m - B\frac{\sigma_m^2}{3c_v E} \tag{2.66}$$

Where B is the drag coefficient, linked to the Burges vector b ($B= Mb\rho_m\nu^*/S$). the solution of equation (2.66) is composed by a first elastic component and a second plastic component, whose

contribute to a positive temperature change due to microplasticity, since the drag coefficient B is negative.

The mathematical model proposed by Melvin is difficult to apply in practical applications due to the uncertainty in the assessment of the coefficient. In Figure 2.2 is reported the temperature trend for an AISI 316L steel specimen with the predicted curve applying the mathematical model, with different B values. The inversion of the temperature trend ($dT/d\sigma = 0$) is defined as the Thermal Elasto-Plastic Limit (TELP). The correlation seems adequate up to the TEPL. The earlier deviation from the theoretical trend of the experimental temperature signal may be due to the invalidity of one or more assumptions concerning the f value, the mobile dislocation density or the stress dependence of the dislocation velocity.

In composites materials, such as carbon/epoxy, the theoretical curve shows the deviation from the linearity of the thermal signal from the thermoelastic phase. This can be addressed to the arises of internal defect within the composite material (Figure 2.3).

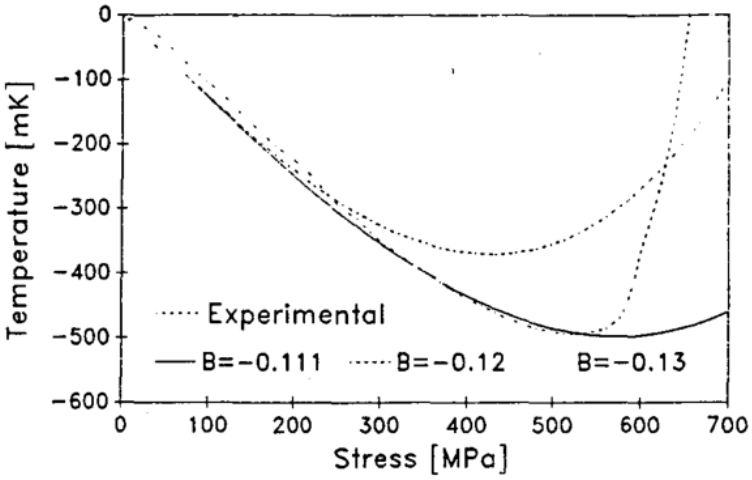

Figure 2.2: Temperature change versus stress for 316L tested in tension. Theoretical and experimental temperature trend from [77].

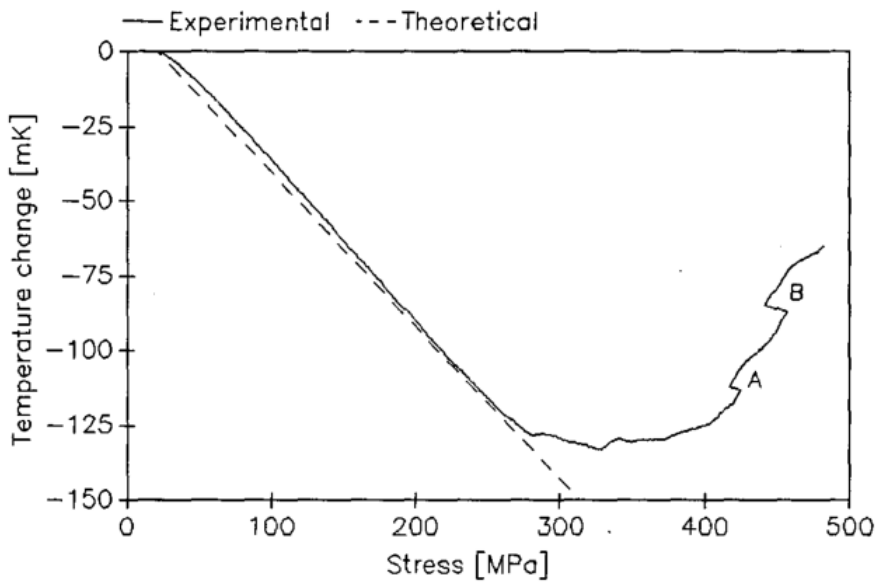

Figure 2.3: Temperature change-stress response to a ensile test on carbon/epoxy with theoretical elastic response from [78].

2.4. The Static Thermographic Method

In the last twenty years, several authors have investigated by means of infrared thermography the surface temperature of a specimen during a static tensile test. In 2000, Chrysochoos and Louche [82] developed a processing technique for infrared images to analyze the thermal manifestation due to the elastoplastic evolution of the material during a static tensile test. In 2009, Plekhov and Naimark [83] examined the propagation of heat waves over the specimen surface. Studies conducted at the University of Catania by Geraci et al. [84] involved the analysis of the surface temperature of steel specimens during static traction tests with an infrared camera. Observing the hottest point of the thermal frames, Geraci and coworkers detected the end of the thermoelastic effect and the beginning of the thermoplastic one, regardless of the applied stress rate. Taking place from the previous study of Chrysochoos and Geraci, Risitano et al. [85] in 2010 analyzed the energy dissipation during a static traction test of a specimen to better identify the end of the thermoelastic phase, due to its deviation from the linearity of the temperature versus stress signal. In the same year, Clienti et al. [86] performed a series of experiments on plain and notched polyvinyl chloride (PVC) specimens in order to identify the end of the thermoelastic phase and assess the thermal behavior, hence the plasticity evolution, as a function of the distance from the notch. The obtained results in terms of “limit stress”, i.e. the stress level at which the deviation from the linearity of the thermoelastic trend is noticed, were compared to

the results in terms of fatigue limit on the same specimens, retrieved using the Thermographic Method (section 1.3).

In 2013, Risitano and Risitano [3] on the basis of the previous work, proposed the Static Thermographic Method (STM) as a rapid test procedure to the derive the fatigue limit of the material by monitoring the superficial temperature during a simple static traction test.

The proposed procedure starts from the assumption according to which fatigue failures occurs at points where the local stress condition is amplified by structural micro defects within the material. These local stress fields are able to produce plastic deformation in the material structure. The internal defects act as stress raisers compared to the average nominal stress at which the specimen is loaded. If the same average stress is applied under fatigue test conditions, the specimen will fail. According to Risitano and Risitano, the fatigue limit can be defined as "the average value of the stress at which, at some point of the material stress-strain curve, local and irreversible plastic conditions are achieved". This may be addressed to the possible start from local slip surface that under cyclic stress spread into fatigue cracks. A static tensile test can be thought as the first positive half cycle of a tension-compression fatigue test. During the static tensile part, a deviation from the linearity is due to the rise of heat generation sources as a consequence of irreversible micro plastic deformations.

As observed by Melvin, the micro plasticization process is represented by several phases (Figure 2.4). The first phase, where the average stress is enough low and all the crystals are stressed into the elastic field (segment OA). In the second phase the majority of the crystal are elastically stressed, but a fraction of it is plastically deformed (segment AB). As the stress level increases, in the third phase, all the crystals are plastically deformed (segment BU).

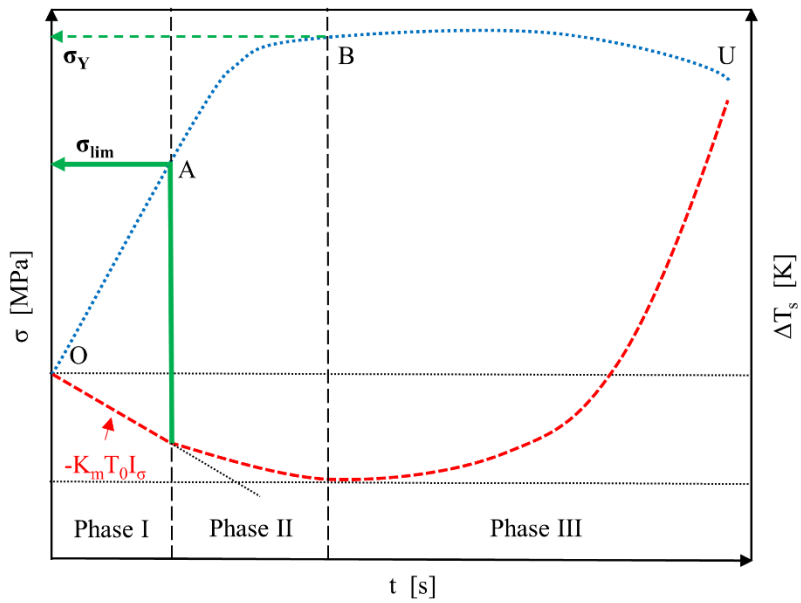

Figure 2.4: Temperature trend during a static tensile test.

The thermal behavior can be also distinguished in three phases linked to the previous crystal states. In the first phase (Phase I), where all the crystals are elastically stressed, the temperature trend follows the linear thermoelastic law; in the second phase (Phase II), where some crystals are plastically deformed, a deviation from the linearity is noticed. Finally, in the third phase (Phase III), all the crystals contribute to the rise in temperature till the failure of the specimen.

As seen in section 2.2.1, under adiabatic test conditions for an isotropic material, neglecting the plastic contribution of equation (2.66), it is possible to write the expression already seen in equation (2.49):

$$\Delta T = -\frac{\alpha}{\rho C_\sigma} \cdot T_0 \sigma_m = -K_m T_0 \cdot \sigma_m \tag{2.67}$$

During the perfect thermoelastic phase, the temperature detected on the specimen surface temperature exhibits a linear decrease as the load increases. If a plasticization condition is reached locally, near a defect zone of infinitesimal volume dV_p, under an average stress σ_p (lower than the yielding stress), equation (2.67) is no longer valid and the plastic deformation is the reason of the infinitesimal heat generation dQ_p that lead to a deviation from the linear trend. Therefore, while a portion $V\text{-}dV_p$ of the material volume has an elastic trend, obeying to equation

(2.67), the fraction dV_p adds heat. The dissipated heat is equal, under perfect plastic conditions, to:

$$dQ_p = \beta \sigma_p d\varepsilon_p \tag{2.68}$$

The terms β is the Taylor-Quinney coefficient, i.e. the percentage of plastic deformation energy dissipated into heat. The heat amount generated strictly depends on the local deformation law, the increase in deformation time and the distribution of the plasticization process within the volume V over the duration of the plastic behavior phase. If the average stress σ_p is applied to the specimen in a tension-compression fatigue test (stress ratio R= -1), the change of the internal structure may become persistent, even if the macroscopic deformation belongs to phase II. The specimen will fail before the defined run-out number of cycles. On the other hand, the specimen never breaks for an applied stress lower than σ_p.

The novelty of the proposed method consists on a rapid procedure, even faster than the other fatigue energy based methods, in order to estimate the fatigue limit of the material. The individuation of the first local plasticization, followed by heat release during a static traction test, can be defined as the "limit stress" σ_{lim}, transition stress from Phase I to Phase II. It is the stress at which the released heat modifies the linear temperature trend during a monoaxial static tensile test. The value of the limit stress can be adopted as an estimation of the fatigue limit of the material.

2.4.1. Simplified model of surface temperature of a static tensile test

In their work, Risitano and Risitano [3] proposed a simplified model to predict the temperature trend during a static tensile test of metallic specimens. It is assumed that the test is performed with a constant load value and a test speed v_c (in N/s) and some assumptions are adopted. The internal transmission heat into the material volume is very high compared with the overall test duration; in addition, given the small specimen thickness, the heat developed within the volume is immediately displayed on the specimen lateral surface. The crystal spent a very rapid amount of time to plasticize compared to the test time. At the end, the density ρ of the material is constant during the test and the radiation heat can be neglected.

The energetic balance equation over a duration dt from t_0 for the specimen thermodynamic system, following the first principle of thermodynamics, and a volume $V= V_e+dV_p$, can be written as:

$$V_e \rho c_\varepsilon dT_e + \beta \sigma_0 \varepsilon_p dV_p + k_c S_l dT = V \rho_1 c_\sigma dT \tag{2.69}$$

The first term is the energy stored in the elastic volume; the second term is the energy due to plastic deformations; the third term is the convective heat exchanged with the surrounding environment and, lastly, the fourth tem is the variation of internal energy of the specimen. given the small temperature variation, it is possible to assume that the density of the material, prior of the deformation and after, is equal ($\rho=\rho_1$) and the specific heat at constant strain and constant stress are equal ($c_\varepsilon=c_\sigma$). It is possible to integrate equation (2.69):

$$\int \left(V \rho c_\varepsilon + k_c \frac{V}{h} \right) dT = -\int V_e \rho c_\varepsilon K_m T_a E d\varepsilon + \int \beta \sigma_0 \varepsilon_p dV_p \tag{2.70}$$

It is possible to define the time dependence of the following parameters, as determined by the experimental behavior during the metal complete plastic phase:

$$\varepsilon = \varepsilon_0 + t \cdot \frac{\varepsilon_0}{t_0} \tag{2.71}$$

$$\varepsilon_p = \frac{\Delta l_p}{l_0} = v_c \frac{t_r}{l_0} \tag{2.72}$$

$$v_c = \sigma_r \frac{S}{t_r} \tag{2.73}$$

Where σ_r is the fracture stress and t_r is the time duration where the specimen exhibits thermoplastic behavior during the test. According to the fracture mechanics theory, it can be assumed that the plasticization volumes varies with a quadratic law respect the time, hence it is possible to write:

$$V_p = t^2 \frac{V}{t_r^2} \tag{2.74}$$

$$V_e = V - t^2 \frac{V}{t_r^2} \tag{2.75}$$

Solving the integrals of equation (2.70), the temperature T can be written as:

$$\mathrm{T} = -\mathrm{K_m} T_a \sigma_r \frac{t}{t_r} + \frac{\beta m \sigma_0 \varepsilon_p \left(\frac{t}{t_r}\right)^2}{\rho c_\varepsilon} + \frac{K_m T_a \sigma_r \left(\frac{t}{t_r}\right)^3}{3} \tag{2.76}$$

After a calibration test, it is possible to apply this temperature model. In Figure 2.5, it is reported the temperature evolution during a static traction test of a notched Fe360 specimen. As it is possible to note, the theoretical temperature trend evaluated adopting equation (2.76) is able to predict in a good way the experimental temperature.

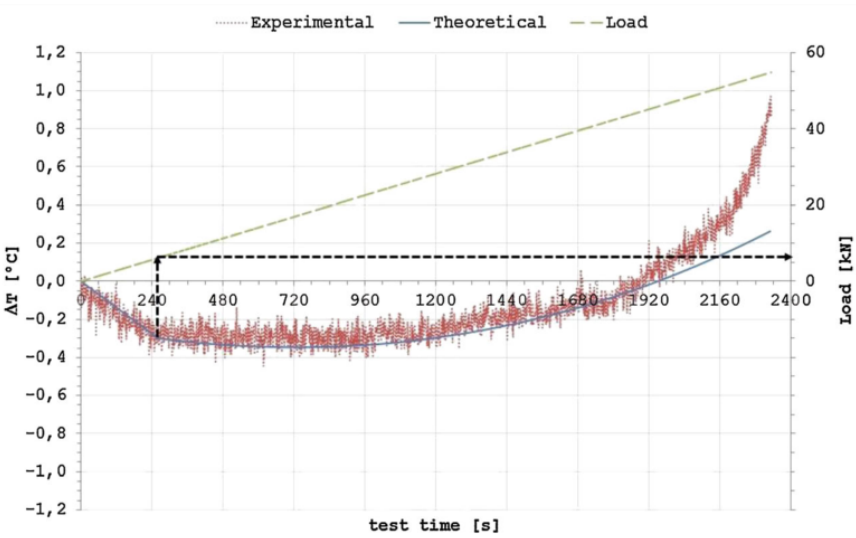

Figure 2.5: Observed experimental and theoretical temperature evolution for a point of the specimen near the hole during the monoaxial static traction test from [3].

2.4.2. Numerical model for predicting the temperature trend from FE analysis

Several authors have investigated2 the temperature evolution of the material during fatigue loading conditions [87,88], but no studies regarding the modelling of the temperature evolution during a static tensile test have been conducted.

In this section, the author proposed a simplified temperature model for engineering materials under static tensile condition. It is based on the fundamental assumption that fatigue failures occur within the material where the local stress distribution, amplified by structural or superficial micro defects, is capable of producing local micro plastic deformation [3]. The local stress state can be linked to a macroscopic nominal stress value (load/area) that introduce in the material the first micro plasticization.

The relationship between the applied stress, or strain, and the corresponding temperature change in solid material consist of two contributions due to a thermoelastic and a thermoplastic effect [88]:

$$\Delta T = \Delta T_e + \Delta T_p \tag{2.77}$$

The thermoelastic effect is a well know phenomenon (section 2.2.1) adopted in stress analysis to evaluate the distribution of the first invariant stress tensor, i.e. the sum of the principal stresses [89,90]. Under adiabatic conditions and for a linear isotropic homogeneous material, the variation of the material temperature, follows the Lord Kelvin's law (equation (2.49)), that here is reported for simplicity:

$$\Delta T = -\frac{\alpha}{\rho C_\sigma} \cdot T \Delta I_{1,\sigma} = -K_m T \cdot \Delta I_{1,\sigma} \tag{2.78}$$

Where K_m is the thermoelastic coefficient.

After the material locally reaches a stress condition beyond its yielding stress, the irreversible plastic deformations lead to an increase in temperature. From the first principle of thermodynamics (energy conservation), the rise in internal energy could be addressed to the heat generated by plastic deformation:

$$\rho c \frac{\partial T}{\partial t} = \frac{\partial Q}{\partial t} \tag{2.79}$$

The generated heat due to plastic deformation can be linked to the mechanical energy by means of the Taylor-Quinney coefficient, defined as the percentage of plastic deformation energy dissipated into heat ($Q = \beta W_p$). Despite this coefficient varies in different metallic materials [91], for sake of simplicity it can be assumed constant and equal to 0.9. the irreversible mechanical energy per unit volume per one loading cycle is given by:

$$\mathrm{W_p} = \frac{1}{\beta}\int Q dt = \frac{1}{\beta}\int \sigma_p d\varepsilon_p \tag{2.80}$$

Under these hypothesis, the temperature increment due to plastic deformation for a cyclic loading condition can be estimated as [88]:

$$\Delta T_p = \frac{1}{\rho c_p}\left(\int_{\varepsilon_1}^{\varepsilon_2} \sigma_l d\varepsilon - \int_{\varepsilon_1}^{\varepsilon_2} \sigma_u d\varepsilon\right) \tag{2.81}$$

Where ε_1 and ε_2 are the minimum and maximum strain of the hysteresis loop, σ_l and σ_u the stresses, respectively, at loading and unloading part of the hysteresis loop. Considering a static tensile test as a positive part of a fully reversed fatigue test performed at very low frequency, it is possible to take into consideration only the loading part of equation (2.81), obtaining:

$$\Delta T_p = \frac{1}{\rho c_p}\int_{\varepsilon_1}^{\varepsilon_2} Q dt = \frac{\beta}{\rho c_p}\int_{\varepsilon_1}^{\varepsilon_2} \sigma_p d\varepsilon \tag{2.82}$$

In the elastic phase the temperature experiences a linear decrease due to the thermoelastic effect. If a plasticity condition is reached locally in some internal defect point of the material, equation (2.78) is no longer valid and a heat amount leads to a deviation from the linear trend.

The present model is suitable to be adopted in finite element simulations where the material curve is defined considering some plasticity criteria (e.g. isotropic hardening, kinematic hardening, etc.). In fact, from a non-linear structural finite element simulation it is possible to

derive for each node, in an easy way, the first stress invariant, as the sum of the three principal stresses, and the plastic work per volume unit, a quantity directly evaluated by a large part of FE software. By knowing the thermomechanical properties of the material, such as linear expansion coefficient α, density ρ and specific heat c, it is possible to evaluate the temperature decrement due to the thermoelastic effect adopting equation (2.78). The temperature rise due to the plastic phenomena can be estimated multiplying the plastic work per unit volume for the Taylor-Quinney coefficient, adopting equation (2.82).

Further development of this model can be its implementation on custom FE elements for coupled thermo-structural analysis. Actually, as the author is aware, FE software, such Ansys, show the possibility to perform coupled thermo-structural analysis adopting a special class of elements (SOLID226, SOLID227, etc.), but the coupling is directed only from the thermal field to the structural one, not vice versa. It means that the FE elements are able to model the plastic phase, but they are unable to properly model the thermoelastic effect.

Despite all, the model has been applied by the author to model the temperature trend of several experimental tests adopting non-linear finite element simulations.

3. LOCAL APPROACHES

In this chapter, the theoretical background of several local approaches is presented: Notch Stress Intensity Factor (NSIF), average Strain Energy Density (SED) and Peak Stress Method (PSM).

Dealing with mechanical notched components, several fatigue tests have to be performed in order to obtain the S-N curve. This huge amount of tests is due to the large differences in the geometrical configuration and the loading mode. For example, in welded joints, for the same configuration (cruciform of T), the plate dimensions can vary in a very large range. On the other hand, the fatigue life of such components is severally affected by the local configuration of the notched regions. It is possible to say that fatigue life is a local problem, regardless the whole geometrical configuration and loading mode.

Moving from this assumption, several "local approaches" have been historically developed to overcame the previously mentioned problems and to obtain a synthesis of the fatigue data of a large amount of mechanical components, especially welded components. They are useful approaches in order to obtain only one S-N curve with scatter band to properly design such components.

In section 3.1, the NSIF approach is illustrated. Moving from the concept of the fracture mechanics for cracks, the NSIFs represent an extension of such concept to generally V-notched component with notch opening angle $2\alpha \geq 0°$. The stress field around the notch tip is analyzed in terms of its singularities under mode I and mode II loading conditions.

In section 3.2, the averaged SED method is proposed. This local approach is based on the estimation of the strain energy density over a control volume. The obtained finite value, nevertheless the stress field is singular, is compared to a critical value to determine the failure of the component. The SED approach can be used to determine the fatigue life of notched component by performing a linear elastic finite element simulation and comparing it to the SED

based S-N curve. This approach overcomes the difficulties of the NSIF approach, but requires the modelling of the control volume.

In section 3.3, the Peak Stress Method is presented. This approach is able to obtain the NSIF in a rapid way, evaluating the elastic peak stress at notch tip node thanks to a calibration procedure of the finite element software, finite element type and mesh configuration. The PSM approach, moving from the SED definition, can be adopted to synthetize the fatigue data of notched components in a short amount of type, overcoming the difficulties encountered in the NSIF approach and also in the SED approach, avoiding the modelling of the control volume. However, it requires a preliminary calibration of the model.

3.1. Linear Elastic Fracture Mechanics for sharp V-Notches

Assuming a mechanical component with the presence of a sharp V-notch (Figure 3.1), it is possible to extended the concepts of the linear elastic fracture mechanics (LEFM) to such a component. V-notches are considered as sharp when the notch fillet radius is equal to zero (ρ= 0). Under fatigue loadings, even notches with non-zero fillet radius behaves like the sharp case if $\rho \leq 4\ a_0$ (e.g. for a structural steel a_0= 0.1 mm, hence $\rho \leq$ 0.4 mm). these evidences are reported in the work of Smith and Miller (1978) [92].

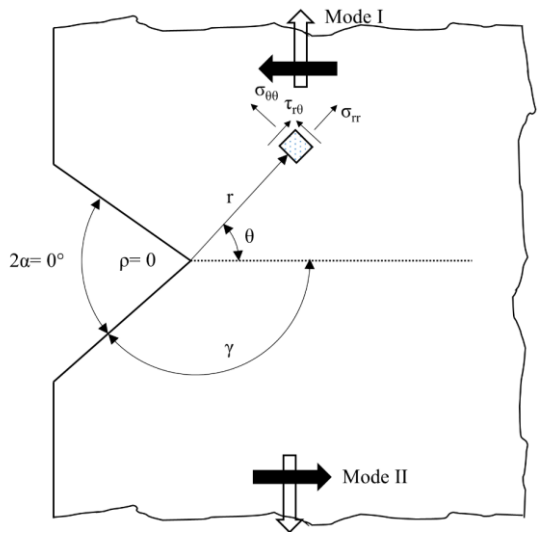

Figure 3.1: Polar reference system for V-notch and Mode I and II loading.

Under plane stress condition is possible to define two loading mode, Mode I and Mode II, in a similar way as done for the crack case. We are considering a V-notch and assuming that it may

be stressed in mode I and/or mode II; the notch is sharp ($\rho \leq 4\ a_0$) and the plastic zone at the tip is small enough (i.e. the linear equations are valid). Under these hypotheses the stress distribution around the tip is expressed by the following equations:

$$\begin{Bmatrix} \sigma_{\theta\theta} \\ \sigma_{rr} \\ \tau_{r\theta} \end{Bmatrix} = \frac{K_1}{r^{1-\lambda_1}} \cdot \begin{Bmatrix} \tilde{\sigma}_{\theta\theta}(\theta) \\ \tilde{\sigma}_{rr}(\theta) \\ \tilde{\tau}_{r\theta}(\theta) \end{Bmatrix}_{mode\ I} + \frac{K_2}{r^{1-\lambda_2}} \cdot \begin{Bmatrix} \tilde{\sigma}_{\theta\theta}(\theta) \\ \tilde{\sigma}_{rr}(\theta) \\ \tilde{\tau}_{r\theta}(\theta) \end{Bmatrix}_{mode\ II} \tag{3.1}$$

The previous equation is expressed for a polar reference system at the notch tip and takes into account both the contribution of mode I and mode II. The stress fields are singular for $r \rightarrow 0$ and $\sigma \rightarrow \infty$. The parameter $1-\lambda_1$ and $1-\lambda_2$ are the singularity grades [93]. The values of λ, the Williams eigenvalues, are functions of the opening angle as reported in Figure 3.2. The Williams eigenvalues are solution of the following equations:

$$\sin(\lambda_1 q\pi) + \lambda_1 \sin(q\pi) = 0 \tag{3.2}$$

$$\sin(\lambda_2 q\pi) + \lambda_2 \sin(q\pi) = 0 \tag{3.3}$$

The parameter q is linked to the notch opening angle according to the following relation:

$$2\alpha = \pi(2 - q) \tag{3.4}$$

It is possible to observe that the stress field due to the mode I is always singular, regardless the opening angle values; on the other hand, the stress field due to the mode II is singular only if the opening angle is lower than 102°. When $2\alpha = 0°$, the maximum singularity grade is equal to 0.5 that is the case of the LEFM.

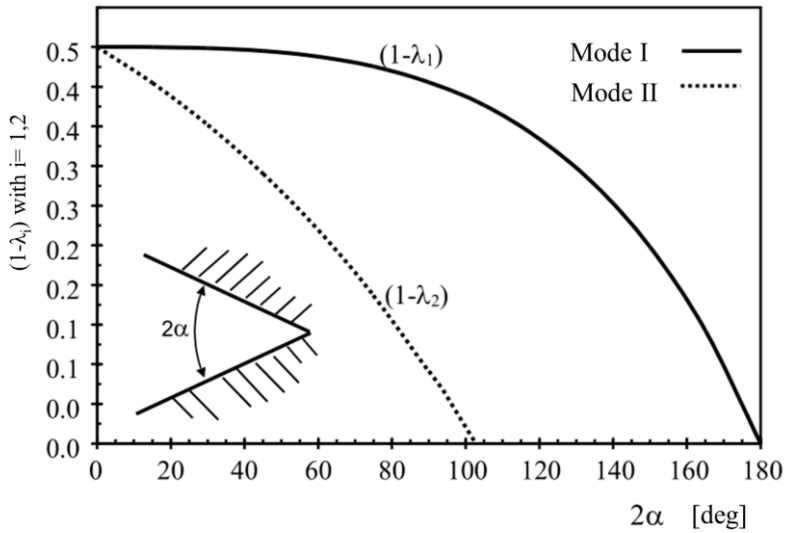

Figure 3.2: Williams eigenvalues vs. the notch opening angle for mode I and mode II.

The parameter K_1 and K_2 of equation (3.1) are the linear elastic Notch Stress Intensity Factor (NSIF). Such parameters are equals to the asymptotic stress field at a distance r= 1/2π from the notch tip. Gross and Mendelson [94] define them as:

$$K_1 = \sqrt{2\pi} \lim_{r \to 0^+} r^{1-\lambda_1} \sigma_{\theta\theta}(r, \theta = 0) \tag{3.5}$$

$$K_2 = \sqrt{2\pi} \lim_{r \to 0^+} r^{1-\lambda_2} \tau_{r\theta}(r, \theta = 0) \tag{3.6}$$

It is to point out that the K_1 expression for 2α= 0° is equal to the SIF of the LEFM K_I (crack case). In a similar way respect K_I, the NSIF K_1 and K_2 express the fatigue life of the notched component.

Considering two notched components with the same opening angle 2α, thanks to the NSIF approach, it is not necessary to know the whole geometries of the components. In fact, if the loading conditions generates the same NSIF range ΔK_1 (maximum K1 minus minimum K1), the two components will have the same fatigue life. It is necessary to know only ΔK_1 and the nominal stresses under the hypothesis that they generate locally a mode I load.

An important application of the NSIF approach is the study of the fatigue life of welded joints with failures both from weld root or toe region. The geometric profile of the toe region of the

welding bead can be associated to a V-notch with an opening angle of $2\alpha = 135°$. The fatigue life of this components is affected by the welding process and its geometries, hence it is not important to consider the whole stresses of the joints but only the stress field near the toe or root regions. On the other hand, the welding standard (e.g. Eurocode 3 and British Standard) evaluates the fatigue strength of the welded joints adopting the nominal stress approach. If we consider the fatigue strength in terms of nominal stress for a welded joint and report them respect to the number of cycles to failure [95], the experimental data are within a very large scatter band (Figure 3.3). In order to design this kind of joints it is necessary to adopt several S-N curves depending on the joint geometry. The large scatter band is due the high differences between the applied remote stress and the local stress field that arises in toe and root regions. As pointed out by Lazzarin and Tovo [95], if we adopt the NSIF approach, it is possible to overcame such difficulty and the experimental data are redistributed within a narrow scatter band. The fatigue life of several geometries, but with the same notch geometry, is well synthetized by the ΔK_1 parameter. The geometry effect and also the scale effect are already included within the ΔK_1 parameter.

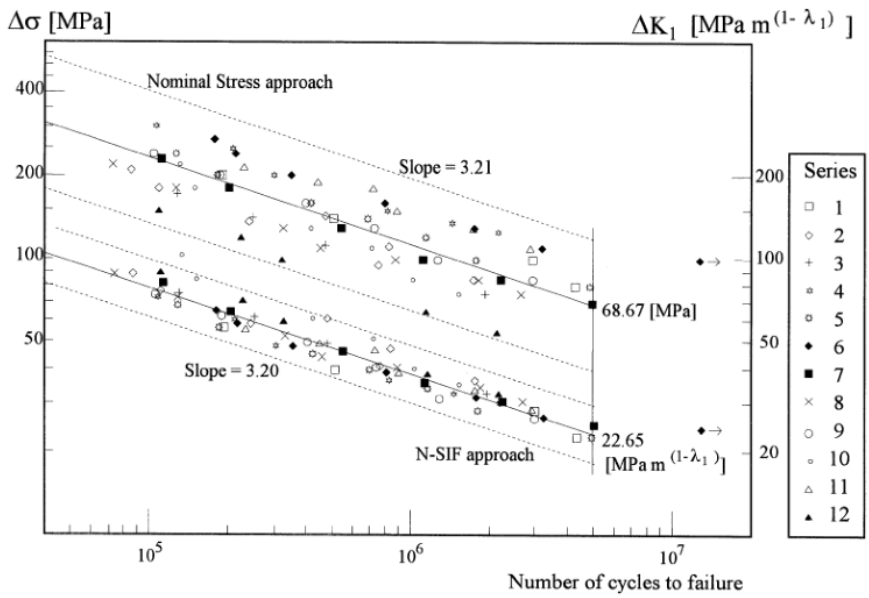

Figure 3.3: S-N curves based on the nominal stress approach and NSIF approach from [95]

The main advantage of a local approach in terms of NSIF respect to a nominal one is that it is possible to adopts only one design S-N curve with a given probability of survival, regardless the joint geometry, but with the same notch condition.

In addition, the NSIF approach is well suited for numerical assessment (e.g finite element methods), of large and complex structures. It is possible to assess it by FE model adopting the definition of equations (3.5) and (3.6). In order to estimate the NSIF value at weld toe region, it is required a very high mesh density. Near the singularity point the element dimension must be in the order of 10^{-5}mm to properly catch the gradient of the local stress field (Figure 3.4). it is necessary a good expertise in the FE modelling technique, as well as in the post processing of the data. In Chapter 11 an estimation of the ΔK_1 parameter by means of the Gross and Mendelson definition is performed.

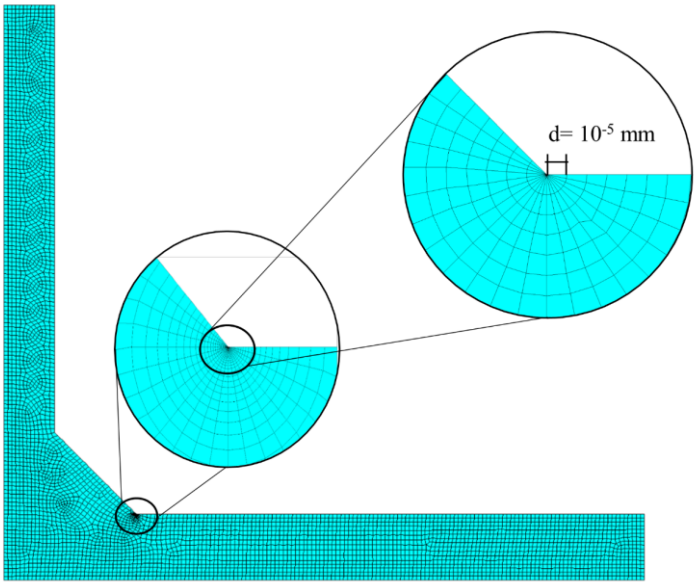

Figure 3.4: NSIF mesh refinement for the estimation of K_1

One of the main disadvantages of the NSIF approach in terms of fatigue data summarization is that it not allows to synthetize the fatigue data from different notch geometries. In other words, it is not possible to compare the fatigue failures from different notch type, e.g. weld root and toe regions. To overcome this limitation, an approach based on the estimation of the average strain energy density value over a control volume has been proposed by Livieri and Lazzarin [5].

3.2. Strain Energy Density approach

The local Strain Energy Density (SED) approach as proposed by Lazzarin and coworkers [5,96–98] is a validated method to investigate fracture of materials both under static and fatigue failure. Considering a brittle material with a sharp V-notch, the fracture occurs when the local SED W, averaged over a defined control volume, reaches a critical value W_c, regardless the

notch opening angle and the loading type. For an ideal brittle material, the critical SED value can be evaluated as:

$$W_c = \frac{\sigma_t^2}{2E} \tag{3.7}$$

Where σ_t is the ultimate tensile strength.

The basic idea of the SED approach is reminiscent of the Beltrami hypothesis [99] and the concept of elementary material volume as proposed by Neuber [100]. Many researchers investigated the brittle fracture. Considering cracked plates under mode I and mode II loading, the basic idea is the mode I dominance, as suggested by Erdogan and Sih [101], to investigate the fracture and predict the crack kinking angle. The crack, under this hypothesis, grows in the direction perpendicular to the maximum tangential stress in radial direction from its tip. This approach can be used also to investigate the case of blunt V-notches under mixed-mode loading. In a work, Sih [102] defined the strain energy density factor S as the product of the strain energy density by a critical distance from the notch tip. Even in this case the fracture is governed by a critical value S_c of the S factor. The crack propagation direction is predicted defining a minimum condition on S. This theory includes in its treatise blunt V-notch [103] and notched component made of ductile material [104]. Glinka and Molski [105] proposed a local-SED criterion based on the constancy of such parameter near the notch tip. It has been applied to sharp V-notches in plain strain condition and small yielding [98].

Under the hypothesis of linear elastic isotropic material and according to the Beltrami formulation, the total strain energy density can be expressed as:

$$W(r,\theta) = \frac{1}{2E}\left(\sigma_{11}^2 + \sigma_{22}^2 + \sigma_{33}^3 - 2\nu(\sigma_{11}\sigma_{22} + \sigma_{11}\sigma_{33} + \sigma_{22}\sigma_{33}) + 2(1+\nu)\sigma_{12}^2\right) \tag{3.8}$$

For a sharp V-notch, the stress distribution for mode I and mode II around the notch tip can be expressed in the following way expanding the terms of equation (3.1), in terms of the Williams eigenvalues can be expressed as:

$$\begin{Bmatrix}\sigma_{\theta\theta}\\ \sigma_{rr}\\ \tau_{r\theta}\end{Bmatrix}_I = \frac{1}{\sqrt{2\pi}}\frac{r^{\lambda_1-1}K_1}{(1+\lambda_1)+\chi_1(1-\lambda_1)} \cdot \left[\begin{Bmatrix}(1+\lambda_1)\cos(1-\lambda_1)\,\theta\\ (3-\lambda_1)\cos(1-\lambda_1)\,\theta\\ (1-\lambda_1)\sin(1-\lambda_1)\,\theta\end{Bmatrix} + \chi_1(1-\lambda_1)\cdot\begin{Bmatrix}\cos(1+\lambda_1)\,\theta\\ -\cos(1+\lambda_1)\,\theta\\ \sin(1+\lambda_1)\,\theta\end{Bmatrix}\right] \tag{3.9}$$

$$\begin{Bmatrix}\sigma_{\theta\theta}\\ \sigma_{rr}\\ \tau_{r\theta}\end{Bmatrix}_{II} = \frac{1}{\sqrt{2\pi}}\frac{r^{\lambda_2-1}K_2}{(1-\lambda_2)+\chi_2(1+\lambda_2)} \cdot \left[\begin{Bmatrix}-(1+\lambda_2)\sin(1-\lambda_2)\,\theta\\ -(3-\lambda_2)\sin(1-\lambda_2)\,\theta\\ (1-\lambda_2)\cos(1-\lambda_2)\,\theta\end{Bmatrix} + \chi_2(1+\lambda_2) \cdot \begin{Bmatrix}-\sin(1+\lambda_2)\,\theta\\ \sin(1+\lambda_2)\,\theta\\ \cos(1+\lambda_2)\,\theta\end{Bmatrix}\right] \tag{3.10}$$

Where K_1 and K_2 are the NSIF (equation (3.5) and (3.6)), which express the intensities of the asymptotic stress field. The parameter χ_1 and χ_2 are two auxiliary parameters that depends on the notch opening angle. They can be evaluated, recalling equations (3.2) and (3.3), as:

$$\chi_1 = -\frac{\sin\left(\frac{(1-\lambda_1)q\pi}{2}\right)}{\sin\left(\frac{(1+\lambda_1)q\pi}{2}\right)} \qquad \chi_1 = -\frac{\sin\left(\frac{(1-\lambda_1)q\pi}{2}\right)}{\sin\left(\frac{(1+\lambda_1)q\pi}{2}\right)} \tag{3.11}$$

It is possible to adopt the superposition principle in order to obtain the stress distribution close to the notch tip in mixed-mode I+II loading condition:

$$\begin{Bmatrix}\sigma_{\theta\theta}\\ \sigma_{rr}\\ \tau_{r\theta}\end{Bmatrix} = r^{1-\lambda_1}K_1\begin{vmatrix}\tilde{\sigma}_{\theta\theta}^{(1)} & \tilde{\tau}_{r\theta}^{(1)} & 0\\ \tilde{\tau}_{r\theta}^{(1)} & \tilde{\sigma}_{rr}^{(1)} & 0\\ 0 & 0 & \tilde{\sigma}_{zz}^{(1)}\end{vmatrix} + r^{1-\lambda_2}K_2\begin{vmatrix}\tilde{\sigma}_{\theta\theta}^{(2)} & \tilde{\tau}_{r\theta}^{(2)} & 0\\ \tilde{\tau}_{r\theta}^{(2)} & \tilde{\sigma}_{rr}^{(2)} & 0\\ 0 & 0 & \tilde{\sigma}_{zz}^{(2)}\end{vmatrix} \tag{3.12}$$

Where the terms in the matrix can be derived from equations (3.9) and (3.10) as function of the notch opening angle 2α and the polar coordinate θ. Equation (3.12) describes the grade of

singularity of the stress field under mode I and II. In equation (3.8), as the stresses tends toward infinity, also the strain energy tends towards infinity. However, the strain energy density over a local finite volume around the notch tip has a finite value which can be considered to control failure.

Substituting the expression (3.12) of the stresses in equation (3.8), it is possible to express the strain energy density as:

$$W(r,\theta) = W_1(r,\theta) + W_2(r,\theta) + W_{12}(r,\theta) \tag{3.13}$$

Where the three terms of the previous equation are:

$$\begin{aligned} W_1(r,\theta) = \frac{1}{2E}\, r^{2(\lambda_1-1)} K_1^2 \Big(& \tilde{\sigma}_{\theta\theta}^{(1)^2} + \tilde{\sigma}_{rr}^{(1)^2} + \tilde{\sigma}_{zz}^{(1)^2} \\ & - 2\nu\Big(\tilde{\sigma}_{\theta\theta}^{(1)}\tilde{\sigma}_{rr}^{(1)} + \tilde{\sigma}_{\theta\theta}^{(1)}\tilde{\sigma}_{zz}^{(1)} + \tilde{\sigma}_{rr}^{(1)}\tilde{\sigma}_{zz}^{(1)}\Big) + 2(1+\nu)\tilde{\tau}_{r\theta}^{(1)^2}\Big) \end{aligned} \tag{3.14}$$

$$\begin{aligned} W_2(r,\theta) = \frac{1}{2E}\, r^{2(\lambda_2-1)} K_2^2 \Big(& \tilde{\sigma}_{\theta\theta}^{(2)^2} + \tilde{\sigma}_{rr}^{(2)^2} + \tilde{\sigma}_{zz}^{(2)^2} \\ & - 2\nu\Big(\tilde{\sigma}_{\theta\theta}^{(2)}\tilde{\sigma}_{rr}^{(2)} + \tilde{\sigma}_{\theta\theta}^{(2)}\tilde{\sigma}_{zz}^{(2)} + \tilde{\sigma}_{rr}^{(2)}\tilde{\sigma}_{zz}^{(2)}\Big) + 2(1+\nu)\tilde{\tau}_{r\theta}^{(2)^2}\Big) \end{aligned} \tag{3.15}$$

$$\begin{aligned} W_{12}(r,\theta) = \frac{1}{E}\, r^{\lambda_1+\lambda_2-2} K_1 K_2 \Big(& \tilde{\sigma}_{\theta\theta}^{(1)}\tilde{\sigma}_{\theta\theta}^{(2)} + \tilde{\sigma}_{rr}^{(1)}\tilde{\sigma}_{rr}^{(2)} + \tilde{\sigma}_{zz}^{(1)}\tilde{\sigma}_{zz}^{(2)} \\ & - \nu\Big(\tilde{\sigma}_{\theta\theta}^{(1)}\tilde{\sigma}_{rr}^{(2)} + \tilde{\sigma}_{\theta\theta}^{(1)}\tilde{\sigma}_{zz}^{(2)} + \tilde{\sigma}_{rr}^{(2)}\tilde{\sigma}_{zz}^{(1)} + \tilde{\sigma}_{\theta\theta}^{(2)}\tilde{\sigma}_{rr}^{(1)} + \tilde{\sigma}_{\theta\theta}^{(2)}\tilde{\sigma}_{zz}^{(1)} \\ & + \tilde{\sigma}_{rr}^{(1)}\tilde{\sigma}_{zz}^{(2)}\Big) + 2(1+\nu)\tilde{\tau}_{r\theta}^{(1)}\tilde{\tau}_{r\theta}^{(2)}\Big) \end{aligned} \tag{3.16}$$

To evaluate the average value of the strain energy density it is adopted a cylinder-shaped area of radius R_0. This is called “control volume” and its radius, the “critical radius”, is dependent only by the material type (Figure 3.5). The higher the brittleness, the lower the R_0 value. For plane problems, the control volume becomes a circular sector of radius R_0.

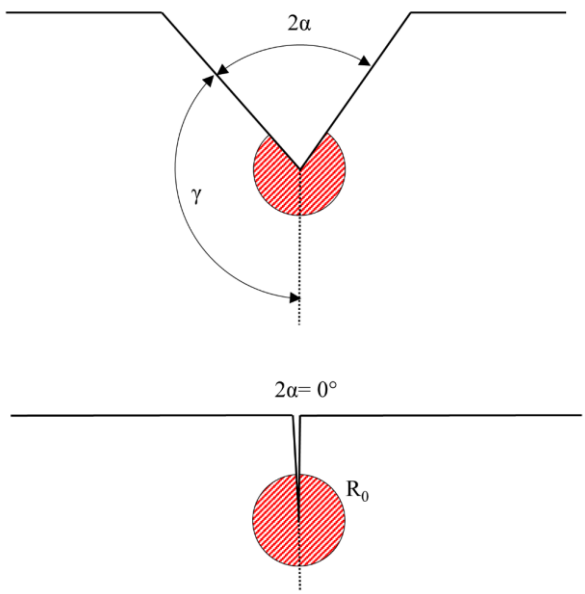

Figure 3.5: Control volume with critical radius for the SED approach.

If the notch under study is a crack (2α= 0°), under plain strain and plain stress conditions the control radius can be estimated as:

$$R_0 = \frac{(1+\nu)(5-8\nu)}{4\pi}\left(\frac{K_{IC}}{\sigma_t}\right)^2 \qquad plane\ strain \tag{3.17}$$

$$R_0 = \frac{(5-3\nu)}{4\pi}\left(\frac{K_C}{\sigma_t}\right)^2 \qquad plane\ stress \tag{3.18}$$

In the case of a sharp V-notch, the critical radius can be assessed as:

$$R_0 = \left[\frac{I_1 K_{IC}^2}{4\lambda_1(\pi-\alpha)EW_c}\right]^{\frac{1}{2(1-\lambda_1)}} = \left[\frac{I_1}{2\lambda_1(\pi-\alpha)}\left(\frac{K_{IC}}{\sigma_t}\right)^2\right]^{\frac{1}{2(1-\lambda_1)}} \tag{3.19}$$

The value of λ and I_1 depends on the notch opening angle 2α, the stress field and on the material properties. In the case of mode I loading, the K_{1C} equals the fracture toughness K_{IC}.

The elastic deformation energy within the control volume can be derived integrating the strain energy density over the area:

$$E_R = \int_A W \cdot dA = \int_0^R \int_{-\gamma}^{+\gamma} [W_1(r,\theta) + W_2(r,\theta) + W_{12}(r,\theta)] \cdot r dr d\theta \tag{3.20}$$

Given the fact that the integration field is symmetric compared to the notch bisector, the mixed mode contribution W_{12} can be set to zero, hence:

$$E_R = E_{1R} + E_{2R} = \frac{1}{E} \cdot \frac{I_{1\gamma}}{4\lambda_1} K_1^2 R^{2\lambda_1} + \frac{1}{E} \cdot \frac{I_{2\gamma}}{4\lambda_2} K_2^2 R^{2\lambda_2} \tag{3.21}$$

Where the terms $I_{1\gamma}$ and $I_{2\gamma}$ are equal to:

$$I_{1\gamma} = \int_{-\gamma}^{+\gamma} \left({\tilde{\sigma}_{\theta\theta}^{(1)}}^2 + {\tilde{\sigma}_{rr}^{(1)}}^2 + {\tilde{\sigma}_{zz}^{(1)}}^2 - 2\nu\left(\tilde{\sigma}_{\theta\theta}^{(1)}\tilde{\sigma}_{rr}^{(1)} + \tilde{\sigma}_{\theta\theta}^{(1)}\tilde{\sigma}_{zz}^{(1)} + \tilde{\sigma}_{rr}^{(1)}\tilde{\sigma}_{zz}^{(1)}\right) + 2(1+\nu){\tilde{\tau}_{r\theta}^{(1)}}^2 \right) d\theta \tag{3.22}$$

$$I_{2\gamma} = \int_{-\gamma}^{+\gamma} \left({\tilde{\sigma}_{\theta\theta}^{(2)}}^2 + {\tilde{\sigma}_{rr}^{(2)}}^2 + {\tilde{\sigma}_{zz}^{(2)}}^2 - 2\nu\left(\tilde{\sigma}_{\theta\theta}^{(2)}\tilde{\sigma}_{rr}^{(2)} + \tilde{\sigma}_{\theta\theta}^{(2)}\tilde{\sigma}_{zz}^{(2)} + \tilde{\sigma}_{rr}^{(2)}\tilde{\sigma}_{zz}^{(2)}\right) + 2(1+\nu){\tilde{\tau}_{r\theta}^{(2)}}^2 \right) d\theta \tag{3.23}$$

The area on which the integration is performed can be estimated as:

$$A_R = \int_0^R \int_{-\gamma}^{+\gamma} r dr d\theta = R_0^2 \gamma \tag{3.24}$$

It is possible to estimate the average elastic deformation energy on the control volume area as:

$$\overline{W} = \frac{E_R}{A_R} = \frac{1}{E} \cdot e_1 \cdot K_1^2 \cdot R_0^{2(\lambda_1 - 1)} + \frac{1}{E} \cdot e_2 \cdot K_2^2 \cdot R_0^{2(\lambda_2 - 1)} \tag{3.25}$$

Where e_1 and e_2 are function of the notch opening angle, according to:

$$e_1(2\alpha) = \frac{I_{1\gamma}}{4\lambda_1\gamma} \tag{3.26}$$

$$e_2(2\alpha) = \frac{I_{2\gamma}}{4\lambda_2\gamma} \tag{3.27}$$

Considering the contribution of all the three modes of loading (I, II and III), the value of the strain energy density is given by:

$$\bar{W} = \frac{e_1}{E}\left[\frac{K_1}{R_0^{1-\lambda_1}}\right]^2 + \frac{e_2}{E}\left[\frac{K_2}{R_0^{1-\lambda_2}}\right]^2 + \frac{e_3}{E}\left[\frac{K_3}{R_0^{1-\lambda_3}}\right]^2 \tag{3.28}$$

From equation (3.28), it is evident how the SED approach allows to evaluate the NSIF a posteriori, avoiding the creation of a fine mesh near the notch tip. Another advantage of the SED method compared to the NSIF is that its dimensions are constant (Nmm/mm^3), while for the NSIFs they strictly depend on the notch opening angle (MPamm$^{1-\lambda}$). As regard the computational time, the SED approach is able to provide reliable solutions even with a coarse mesh of the control volume, compared to the very fine mesh required to estimate the NSIFs. This is due to its direct dependence from the stiffness matrix and of the nodal displacement. Compared to other approaches, the SED method allows also the possibility to include three dimensional effect and out of plane singularities that are not evaluable by the Williams theory.

As regard this effect, the torsional loading conditions lead to the an out of plane singularity with mode III. Studies have shown how the material behavior is different compared to the other mode of loading. Test conducted on PMMA specimens [106,107], showed a considerable plastic behavior and a major contribution of the net resistance area. This required a non-conventional approach that consider the apparent linear elastic SED to overcome the presence of different fracture mechanism under mode III.

A broad view of the SED approach has been described by Lazzarin and Berto in 2014 [108].

3.2.1. Blunt notches

The SED approach has been originally developed under the assumption of sharp V-notch, but, thanks to a semi-empirical procedure proposed by Filippi et al. [109], it has been extended also to blunt V-notches and U-notches. This procedure has been validated through numerical simulations [109,110].

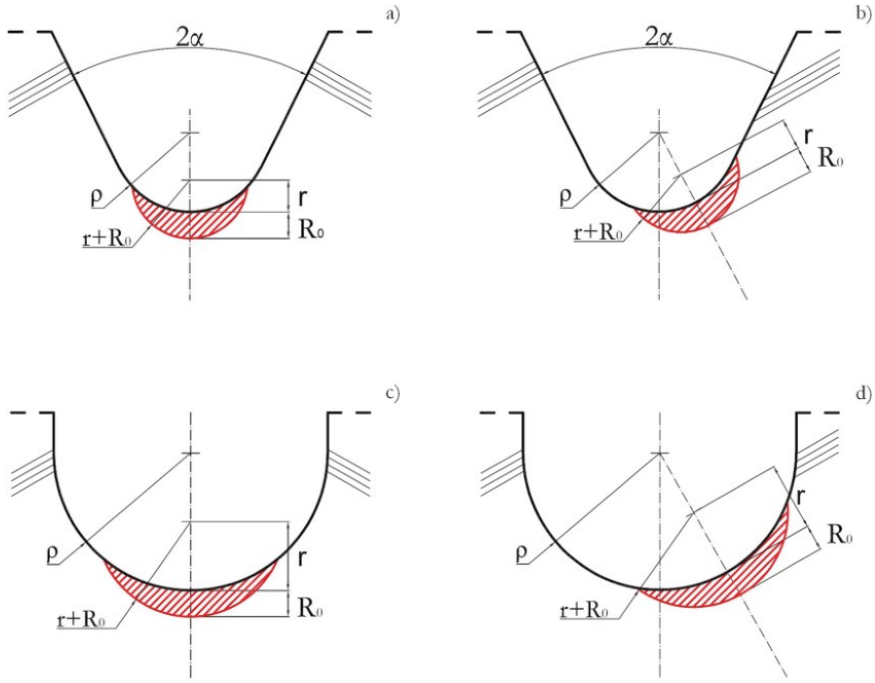

Figure 3.6: Control volume for: a) blunt V-notch under mode I loading; b) blunt V-notch under mixed mode loading; c) U-notch under mode I loading; d) U-notch under mixed mode loading. From [111].

In such notch conditions the control volume assumes a modified shape depending on the loading mode. In mode I loading mode it assumes a crescent shape with R_0 beings the maximum width along the notch bisector line. The control volume is the intersection between the component and a circle of radius $r+R_0$ centered at the notch bisector, at a distance r from the notch edge. For mixed mode loading conditions, it has been noted that the maximum elastic stress is out of the notch bisector line. Its position along the notch edge is strictly dependent on the distribution of stresses due to mode I and II. Compared to the pure mode I, the control volume center not belongs to the notch bisector, but rigidly rotated with respect to it and centered in a point where the SED reaches its maximum value [112,113].

As regards the loading case of Figure 3.6a-b, the following expression for the radius r is valid:

$$r = \rho \cdot \frac{\pi - 2\alpha}{2\pi - 2\alpha} \tag{3.29}$$

For the loading case of Figure 3.6c-d, the following expression of r is valid:

$$r = \frac{\rho}{2} \tag{3.30}$$

This procedure requires to perform several finite element simulations in order to find the maximum SED value and hence the right position of the control volume.

3.2.2. Fatigue assessment by SED

Considering that the high cycle fatigue failure exhibits brittle fractures, hence they happen in the linear elastic regime, it is possible to apply the SED method in order to estimate the fatigue strength of mechanical components. The fatigue life can be expressed in terms of the cyclic average SED of the notch.

Taking into account a mechanical component with sharp V-notch angle large enough to assure the mode II non singularity (2α≥ 102.6°), for example a welded joint, the radius of the control volume can be estimated by the following relation:

$$R_0 = \left(\frac{\sqrt{2e_1} \Delta K_{1A}^N}{\Delta \sigma_A} \right)^{\frac{1}{1-\lambda_1}} \tag{3.31}$$

According to equation (3.31), in order to estimate the value of the critical radius, the fatigue strength of the butt welded joint, extrapolated from its fatigue curve with a probability of survival of 50% at run-out number of cycle, is required. In addition, the NSIF based fatigue strength for the welded joint component is required too.

Considering the welded toe region as a sharp V-notch, Livieri et al. [5], obtained the scatter band in terms of cyclic average SED analyzing more than 900 fatigue failure data with different failure area (toe or root region), under different loading conditions (Figure 3.7). They obtained a synthesis of the fatigue strength of welded component where the geometry varies in a great

range (main plate thickness, transverse plate and bead flank). The average SED is reported versus the number of cycles to failure.

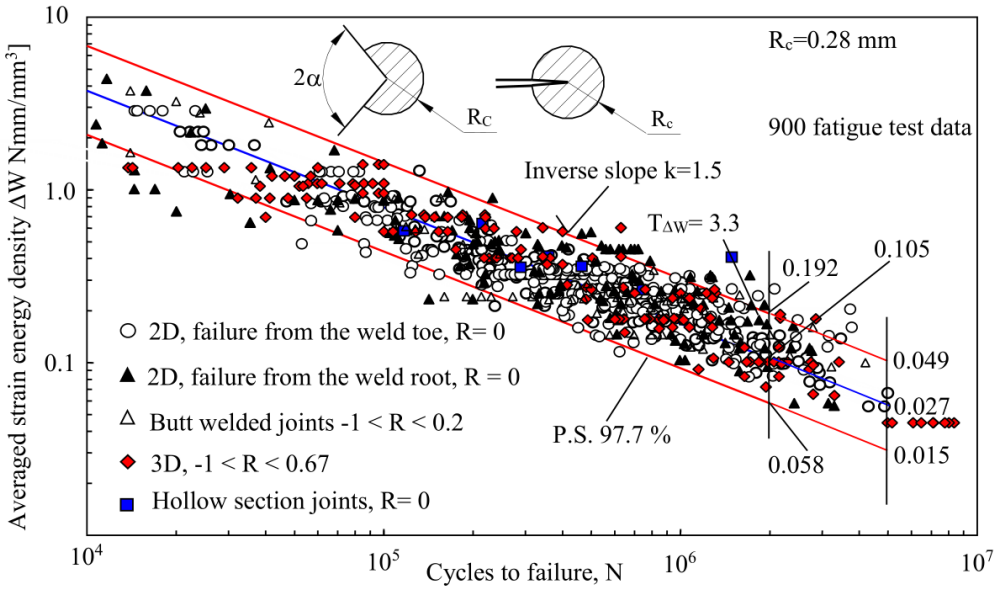

Figure 3.7: Fatigue strength of steel welded joints as a function of the averaged SED. From [114].

The procedure required to evaluate the fatigue strength by means of the SED method consist in the calculation of the mean SED at weld toe or root region for a nominal tensile stress $\Delta\sigma_1$ through a linear elastic finite element simulation. Adopting equation (3.32), valid only under the hypothesis of linear elastic behavior, it is possible to evaluate the remote tensile load that represent the fatigue limit of the component with a given probability of survival, being ΔW_L the critical value of the mean SED that corresponds to the fatigue limit.

$$\Delta\sigma_L = \Delta\sigma_i \left(\frac{\Delta W_L}{\Delta W_i}\right)^{0.5} \tag{3.32}$$

For steel welded joints, according to the scatter band of Figure 3.7, the critical value for the SED at PS= 97.7% is equal to 0.058 Nmm/mm^3.

3.3. Peak Stress Method

In 2007, Meneghetti and Lazzarin [115] proposed the Peak Stress Method (PSM) as a rapid FE technique, adopting coarse meshes, in order to estimate the NSIFs. Compared to the estimation of the NSIFs performed with the Gross and Mendelson's definition (equations (3.5) and (3.6)), it is possible to adopt coarse meshes, with elements several order of magnitude higher, and it is adopted the elastic peak stress at V-notch tip (Figure 3.8) respect the stress distribution over a distance. Its simplicity in the application is due to a high calibrated procedure; in fact, it is necessary to know the FE software adopted, the element type and the mesh pattern. The PSM allows to estimate in a rapid way the NSIFs value adopting the elastic peak stress σ_{peak} of the node at notch tip evaluated with an elastic FE analysis.

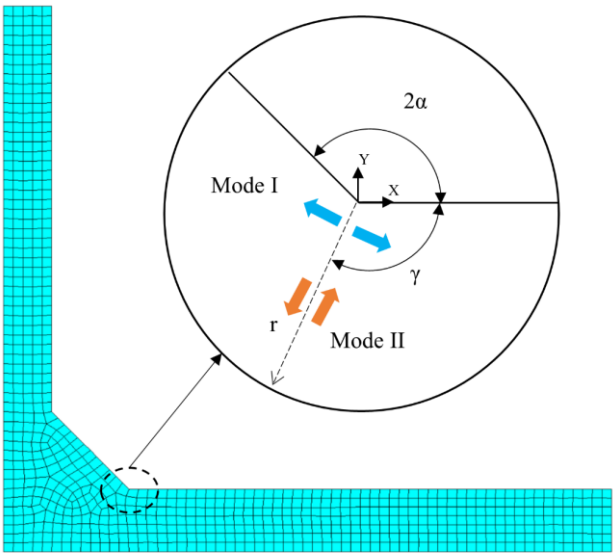

Figure 3.8: Polar reference system at notch tip for a welded joint.

Nisitani and Teranishi [116] presented a numerical procedure suitable for estimating the K_I for a crack emanating from an ellipsoidal cavity. This procedure is based on the estimation of the linear elastic peak stress σ_{peak} calculated at the crack tip from FE model with mesh pattern with constant element size. They showed how the ratio K_I/σ_{peak} depends only to the element size. Hence the elastic peak stress could be adopted to assess in a rapid way the K_I value considering mesh patterns calibrated on geometries where the exact K_I value is known. This criterion can be extended to sharp V-notches [117] components and the element size required to evaluate K_I from σ_{peak} is some order of magnitude greater than that required to directly evaluate K_I from the Gross and Mendelson's definition. The following expression has been validated:

$$K_1 = K_{FE}^{*} \cdot \sigma_{peak} \cdot d^{1-\lambda_1} \tag{3.33}$$

Where K_{FE}^{*} is a constant and d is the average finite element size imposed to the mesher. The K_{FE}^{*} constant depends by the adopted software, element typology and mesh pattern.

Originally calibrated for Ansys FE software, recently it has been also calibrated for other FE software [118] (Abaqus, Straus7, MSC Patran/Nastran, etc.). It has been calibrated also on plane elements (PLANE42 and PLANE182 with "simple enhanced strain") and solid elements (SOLID45, SOLID185 and SOLID187 with "simple enhanced strain"). A state of the art about the PSM has been reported by Meneghetti and Campagnolo in 2020 [119].

As regards the mesh pattern (Figure 3.9), after have defined the average element size, the free mesh generation algorithm has to create a mesh where four elements must share the tip node if the opening angle 2α≤90°, otherwise two elements must share the tip node if the opening angle is 2α >90°.

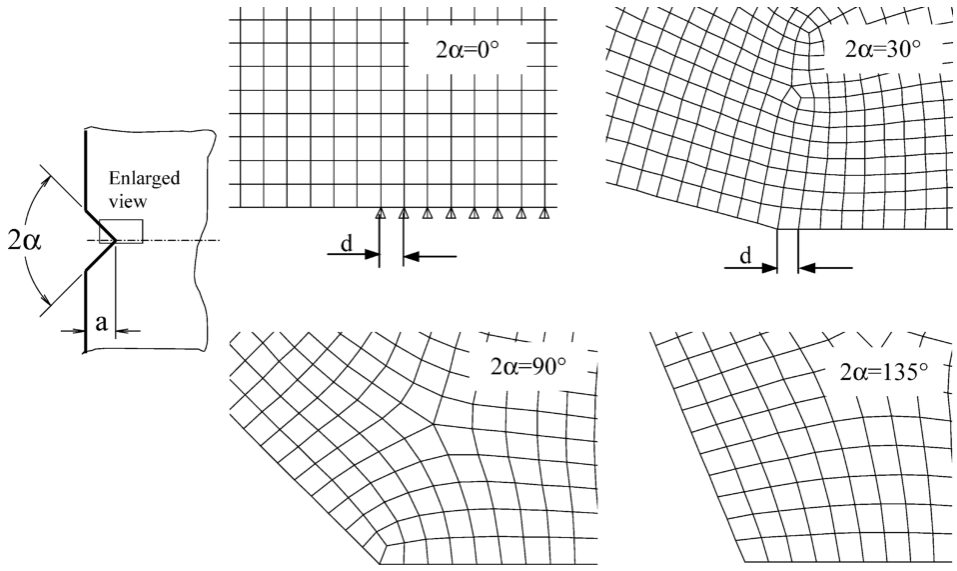

Figure 3.9:Mesh patterns adopted in numerical analysis obtained by Ansys mesher with global element size of 1 mm. From [115].

Under such conditions, it is possible to assume the value of K_{FE}^{*}= 1.38. this value has been retrieved after a calibration procedure considering several notch opening angle values and element size values. Reporting the dimensionless value K_{FE}^{*} vs. the a/d ratio, where a is a characteristic length of the model (e.g. for welded joint it is equal to the loaded plate), it has been

shown Figure 3.10 that the scatter band is restricted to 6% with an average value of 1.38. Hence for engineering application the previous value for K_{FE}^* can be adopted.

The element size value can be chosen arbitrary but within a range of applicability [115,118]. For example, for mode I load the mesh density ratio a/d should be greater than 3 in order to obtain K_{FE}^*= 1.38±5%.

The procedure to follow in order to estimate the NSIF with the PSM approach is the following. A finite element analysis has been performed adopting plane strain 4-node elements. The mesh density ratio a/d has been chosen in order to obtain a ratio greater than 3, hence the global element size d is defined. The peak stress is equal to the elastic peak stress of the node at notch tip.

Recently the PSM has been applied also to 3D finite element model of tube welded joints adopting tetra elements [120,121].

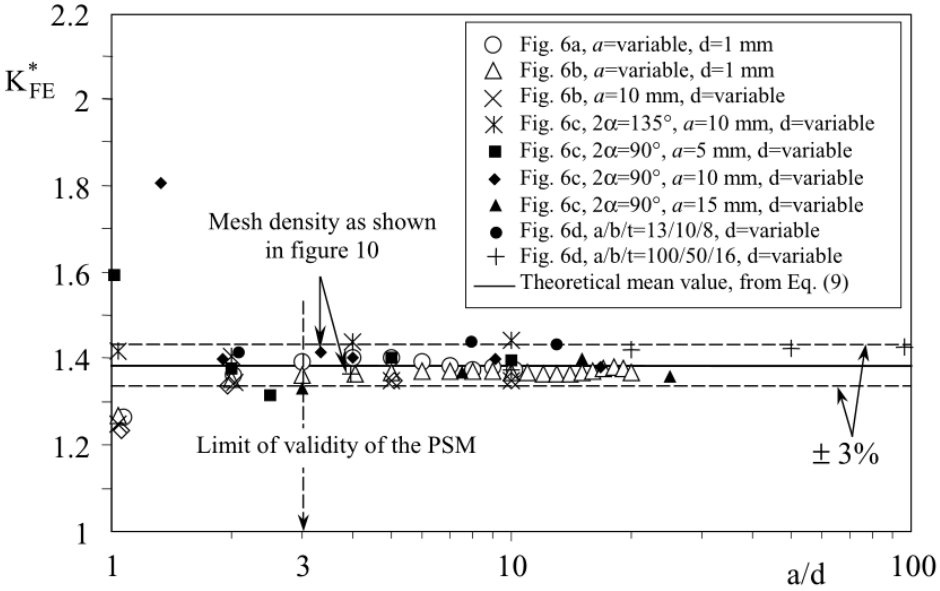

Figure 3.10: Non-dimensional K_{FE}^* ratio as evaluated from 61 FE analyses with scatter band. From [115].

3.3.1. PSM for welded joint

Meneghetti and Lazzarin [115] proposed to summarize the fatigue strength of welded joints in terms of an equivalent peak stress. Considering a sharp V-notch geometry loaded in the more general form under mode I and mode II, and taking into account the PSM relation (equation (3.33)), the average SED expression (equation (3.28)) can be rewritten in terms of the peak stress

σ_{peak} evaluated according to the PSM approach. In addition, under the hypothesis of plane strain state, it is possible to evaluate an equivalent peak stress from the following expression [122]:

$$\Delta\overline{W} = \frac{e_1}{E}\left[K_{FE}^{*} \cdot \Delta\sigma_{peak} \cdot \left(\frac{d}{R_c}\right)^{1-\lambda_1}\right]^2 + \frac{e_2}{E}\left[K_{FE}^{**} \cdot \Delta\tau_{peak} \cdot \left(\frac{d}{R_c}\right)^{1-\lambda_1}\right]^2 = \frac{1-\nu^2}{2E} \cdot \Delta\sigma_{eq,peak}^2 \tag{3.34}$$

It is possible to estimate the K_2 NSIF in the same way as the K_1. The shear peak stress evaluated at the node tip can be expressed as [123]:

$$K_2 = K_{FE}^{**} \cdot \tau_{peak} \cdot d^{1-\lambda_2} \tag{3.35}$$

The equivalent peak stress can be expressed as:

$$\Delta\sigma_{\mathrm{eq,peak}} = \sqrt{f_{w1}^2 \cdot \Delta\sigma_{peak}^2 + f_{w2}^2 \cdot \Delta\tau_{peak}^2} \tag{3.36}$$

The corrective coefficients f_{w1} and f_{w2} are obtained comparing equation (3.34) and (3.36):

$$\mathrm{f_{w1}} = K_{FE}^{*} \cdot \sqrt{\frac{2e_1}{1-\nu^2}} \cdot \left(\frac{d}{R_c}\right)^{1-\lambda_1} \tag{3.37}$$

$$\mathrm{f_{w2}} = K_{FE}^{**} \cdot \sqrt{\frac{2e_2}{1-\nu^2}} \cdot \left(\frac{d}{R_c}\right)^{1-\lambda_2} \tag{3.38}$$

Compared to the SED approach, it is not necessary to model the control volume to estimate the average SED and the average element size d can be greater than the dimension of the control volume radius R_c, where it is necessary to have $d<R_c$.

The conditions of applicability of equation (3.35) are the same for the mode I. For the constant K_{FE}^{**} an average value of 3.38 can be assumed, however a greater mesh density is required under

the presence of mode II. The mesh density ratio a/d must be greater than 14 in order to obtain K_{FE}^{**}=3.38±5%.

Adopting the equivalent peak stress of equation (3.36), it is possible to obtain a synthesis of the fatigue data of steel welded joint breakage from root or weld bead toe regions in a similar way as previously seen for the SED approach.

According to the PSM formulation of the SED approach, the fatigue failures are predicted in the points that exhibits the higher equivalent peak stress $\Delta\sigma_{eq,peak}$. By knowing the equivalent peak stress, it is possible to predict the fatigue life by means of the scatter band of Figure 3.11 for steel welded joints.

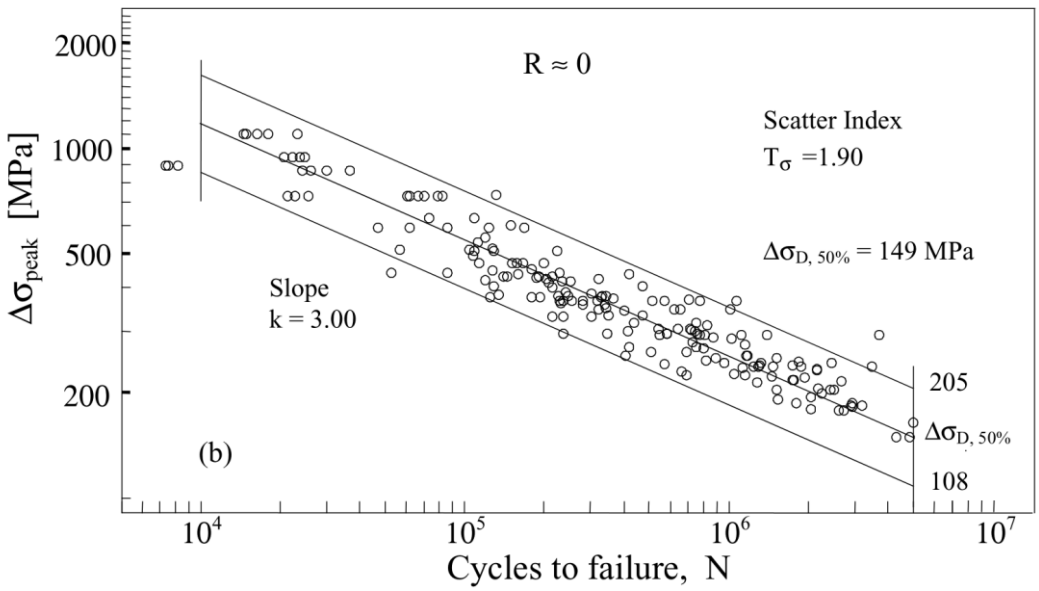

Figure 3.11: Fatigue strength of fillet-welded joints made of structural steels in terms of the equivalent elastic peak stress from [115].

PART II
EXPERIMENTAL ACTIVITIES

4. STRUCTURAL STEEL S355

Corigliano P, Cucinotta F, Guglielmino E, Risitano G, Santonocito D. Fatigue assessment of a marine structural steel and comparison with Thermographic Method and Static Thermographic Method. Fatigue Fract Eng Mater Struct 2020;43:734–43. doi:10.1111/ffe.13158.

Corigliano P, Cucinotta F, Guglielmino E, Risitano G, Santonocito D. Thermographic analysis during tensile tests and fatigue assessment of S355 steel. Procedia Struct Integr 2019;18:280–6. doi:10.1016/j.prostr.2019.08.165.

Highlights

Fatigue properties are of fundamental importance and extremely time consuming to be assessed. The aim of this research activity is to apply the Thermographic Method (TM) and the Static Thermographic Method (STM) during fatigue and tensile tests in order to correlate the temperature trend to the fatigue properties of an S355 steel.

The material was retrieved from an existing marine structure: an in-service port crane. Traditional fatigue tests were performed in order to evaluate the S-N curve with a scatter band. Step Load tests were carried out deriving the fatigue limit and the Energy Parameter of the material. Static tensile tests were performed in order to obtain the stress at which the temperature trend deviates from the thermoelastic behavior. The fatigue properties obtained by means of the thermal methods were compared to the traditional ones showing a good agreement.

Nomenclature

c	specific heat capacity of the material [J/kg.K]
E	Young's Modulus [MPa]
f	test frequency [Hz]
k	inverse slope of the scatter band
K_m	thermoelastic coefficient [MPa^{-1}]
n	work hardening exponent (Hollomon's equation)
N, N_f	number of cycle, number of cycle to failure

R	stress ratio
R^2	coefficient of determination
R_f	stress at rupture [MPa]
$R_{m\ tech}$	maximum technical stress [MPa]
$R_{m\ true}$	maximum true stress [MPa]
R_{p02}	yield stress, stress which produces the 0.2% residual plastic long. strain [MPa]
t	test time [s]
T, T_i	instantaneous value of temperature [K]
T_0	initial value of temperature estimated at time zero [K]
T_σ	scatter index of the scatter band
α	thermal diffusivity of the material [m^2/s]
ΔN_i	number of cycle block length
ΔT	absolute surface temperature variation during a fatigue test [K]
ΔT_s	absolute surface temperature variation during a static tensile test [K]
ΔT_{st}	stabilization temperature for fatigue tests [K]
ΔT_1	estimated value of temperature for the first set of temperature data [K]
ΔT_2	estimated value of temperature for the second set of temperature data [K]
ε_r	strain at rupture [%]
ε_u	strain at maximum load [%]
ε_y	strain evaluated along the specimen's longitudinal direction [%]
ν	Poisson's ratio
Φ	Energy Parameter [Cycles·K]
Φ_{ave}	average value of the Energy Parameter [Cycles·K]
ρ	density of the material [kg/m^3]
σ	stress level [MPa]
σ_D	critical macro stress that produces irreversible micro-plasticity [MPa]
σ_{lim}	fatigue limit estimated with the Static Thermographic Method [MPa]

σ_0	fatigue limit estimated with the Thermographic Method [MPa]
$\sigma_{0,5\%}$	value of the fatigue limit with a probability of survival of 5%
$\sigma_{0,50\%}$	value of the fatigue limit with a probability of survival of 50%
$\sigma_{0,95\%}$	value of the fatigue limit with a probability of survival of 90%
σ_1	uniaxial stress [MPa]
$\dot{\sigma}$	stress rate [MPa/min]

4.1. Introduction

The traditional methods of fatigue assessment of materials are extremely time consuming, so an innovative approach, based on thermographic analyses of the temperature evolution during the fatigue tests, has been proposed for a rapid prediction of the fatigue limit and the S-N curve, using a very limited number of tests: the Thermographic Method (TM) [2]. In a recent work, Risitano and Risitano [3] proposed the Static Thermographic Method (STM) as a rapid procedure to derive the fatigue limit of the material evaluating the temperature evolution during a static tensile test.

Many studies showed as the thermal analysis applied to steel [69,124,125] and composite [126,127] components allow the estimation of the fatigue limit of the material with a limited number of specimens. The thermal analysis by means of IR sensor has been also applied to estimate the fatigue behavior on welded joints used in marine structures [128]. Full-field measurement techniques have been applied in literature for the experimental investigation of metallic and composite materials subjected to mechanical and thermal loading [129–133].

The Infrared Thermography was applied for the analysis of different materials subjected to different loading conditions: notched steel specimens under tensile static tests [3,134], short glass fibre-reinforced polyamide composites under static and fatigue loading [132], high cycle [2,44,50,64,135,136]and very high cycle [10,12] fatigue regimes. The determination of the Energy Parameter by means of Infrared Thermography has been also used to evaluate the causes of failure of in service mechanical components [45].

The aim of this research activity is the application of the Static Thermographic Method (STM) and of the Thermographic Method (TM) during static tensile and fatigue tests for the rapid

fatigue assessment of S355 steel. This kind of steel is widely used in mechanical construction, especially in shipbuilding and marine structures. The tested material has been retrieved from the arm of an in-service port crane. Tensile tests were carried out adopting full-field techniques, such as Digital Image Correlation (DIC) and Infrared Thermography (IR). From infrared thermography relevant information about the energetic behavior of the material have been derived. Moreover, classic fatigue tests were performed and the S-N curve was evaluated. The predictions of the fatigue limit and of fatigue life, obtained by the analysis of the specimen surface temperature evolution during step load tests and static tests, were compared with the predictions obtained from the traditional fatigue tests.

4.2. Materials and methods

Static tensile tests and fatigue tests were carried out on specimens made of S355 steel. The specimens were obtained cutting *in situ* seven metal sheets from different sections of the support part of a port crane fixed arm. Each of these metal sheets were named with “T” letter followed by the cut and specimen numbers (e.g. “T2-6”, metal sheet no. 2, specimen no. 6). From each of the metal sheet, eight dog bone shaped specimens were cut (Figure 4.1a) with a nominal cross section of 15 mm x 10 mm. All the tests were performed with a servo-hydraulic axial load machine INSTRON 8854 with maximum load capacity of 250 kN. A total number of three static tests were conducted: one test was performed under displacement control in order to assess the mechanical properties of the material, with a velocity of 2 mm/min; while the other two static tests were performed under load control, adopting a stress rate of 183 MPa/min. Two kind of fatigue tests were performed, both with stress ratio R= -1 and frequency f= 20Hz. A first series of test was conducted on eighteen specimens at different stress level with constant amplitude, ranging from 160 to 260 MPa, in order to obtain the S-N curve of the material. A second series of fatigue tests was performed on nine specimens with a step increase of the stress amplitude, ranging from 95 MPa up to 285 MPa.

Full-field techniques are a powerful aid in the assessment of the mechanical behavior of the material and they can also speed-up the overall test time. The use of Digital Image Correlation is useful for determining the mechanical characteristics of the material such as Young's Modulus, Poisson's ratio and yielding strength. The DIC is a full-field non-contact measurements method which allows the detection of displacement and strain fields. For the application of this technique, two cameras with a resolution of 4000 x 3000 pixels, focal length of 50 mm, were used. The system accuracy for the strain measurement is up to 0.01%, and the images were

acquired at 1 Hz. The ARAMIS 3D 12 M system was used to analyze the strain field of the specimen surface. Infrared Thermography was used to monitor the evolution of the surface temperature of the specimen and to apply Thermographic Method and Static Thermographic Method during tensile and fatigue test. The infrared camera FLIR A40 was used, with a sample rate of 1 Hz and a temperature measurement range between -40°C and +120°C. During all the tests the maximum temperature value of a rectangular measurement area, placed on the entire length of the specimen's reduced section, has been recorded. Before starting the tests, the specimens were coated with a black-white speckle pattern on one surface, in order to allow the assessment of the strain field, while they were coated with black paint on the other surface to increase the thermal emissivity of the material up to 0.98. The experimental setup is showed in Figure 4.1b, where the DIC system and IR camera are placed on the two different faces of the specimen.

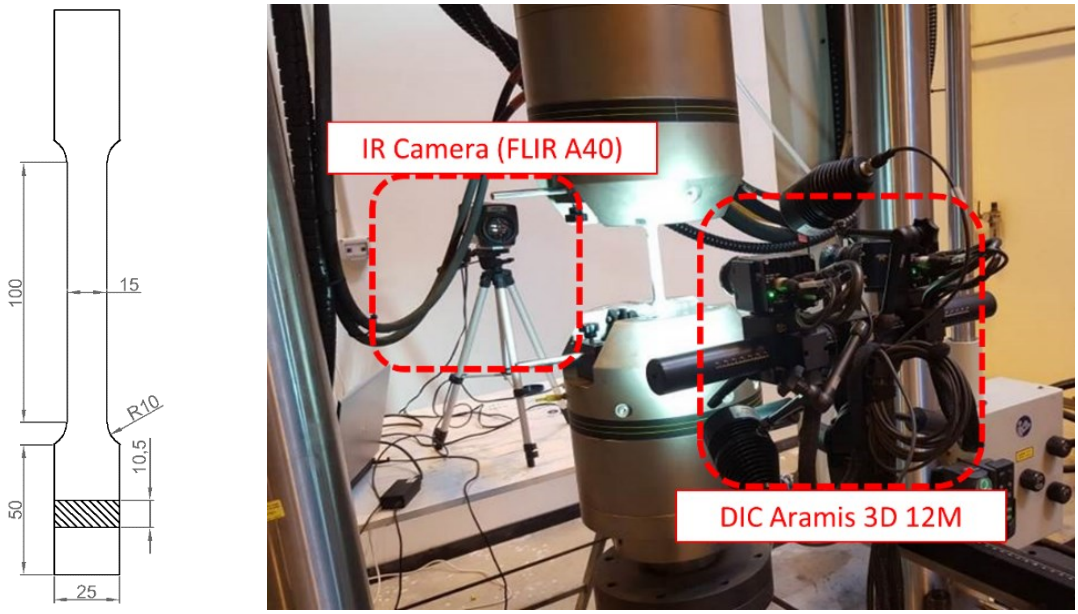

(a) (b)

Figure 4.1: a) dogbone specimen geometry; b) experimental setup with DIC system and IR camera.

The load and temperature data coming from the tests were analyzed adopting an algorithm implemented via Matlab® scripts. For both the static and fatigue tests, the specimen rupture instant has been taken as the reference time for synchronizing the data. In order to clean the temperature signal from outliers and to enhance the trend of the thermoelastic effect during static

tests, a locally weighted scatter plot smooth filter (*rlowess*), already implemented in Matlab®, was chosen. This kind of filter uses locally linear regression to smooth data defining a span in which each data point assumes a weight depending on its distance from the data to be smoothed. Evaluating the median absolute deviation of the residuals, it is also possible for the filter to assign a zero weight to the outlier points, hence excluding them from the smooth procedure. For all of the analyzed static test a data span equals to the 7% of the whole data set was adopted. Numerical integration via the trapezoidal method of the absolute temperature variation of the specimen surface vs. the number of cycle was carried out until the maximum value of temperature, for the analysis of the energetic release during the fatigue tests and the estimation of the Energy Parameter.

4.3. Results and Discussions

4.3.1. Material properties

In order to assess the properties of the S355 steel under investigation, a static test was carried out under displacement control adopting an elongation rate of 2 mm/min. The DIC technique allowed a complete analysis of the displacements and strains of the whole surface of the specimen, as well as the detection of local strain concentrations during the tests. Once the test data has been acquired with the DIC system, it automatically estimates several mechanical properties of the material, both for the elastic and plastic field. Starting from the displacement field, the longitudinal strains are calculated as the ratio between the absolute variation of the elongation of two spot and their initial distance. In Figure 4.2a are reported the stress vs. longitudinal elongation curves. The technical curve takes into account the nominal stress, i.e. load over the nominal cross sectional area, while the true curve is estimated as the ratio between the load and the instantaneous cross sectional area. In Figure 4.2b the calculation procedure of the Young's modulus and the yield strength is reported. The Young's modulus is evaluated as the linear regression of the first 67 points of the technical stress curve, with a coefficient of determination R^2= 0.9996, while the yielding strength R_{p02}, defined as the value of the stress which produces the 0.2% residual plastic longitudinal strain, is obtained as the intersection between the technical curve and the straight line with the same slope of the elastic modulus shifted by a strain value of 0.2%. The values obtained with the aid of the DIC technique are reported in Table 4.1. As is possible to note, the yield strength and the maximum technical stress of the steel under examination are compliant with the nominal material characteristics (R_{p02}≥355 MPa, R_m=450÷600 MPa).

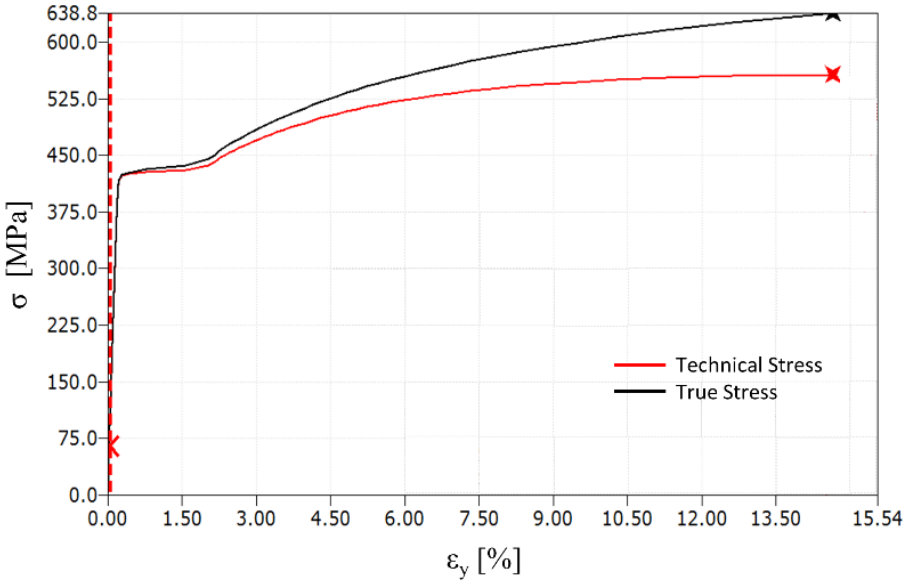

(a)

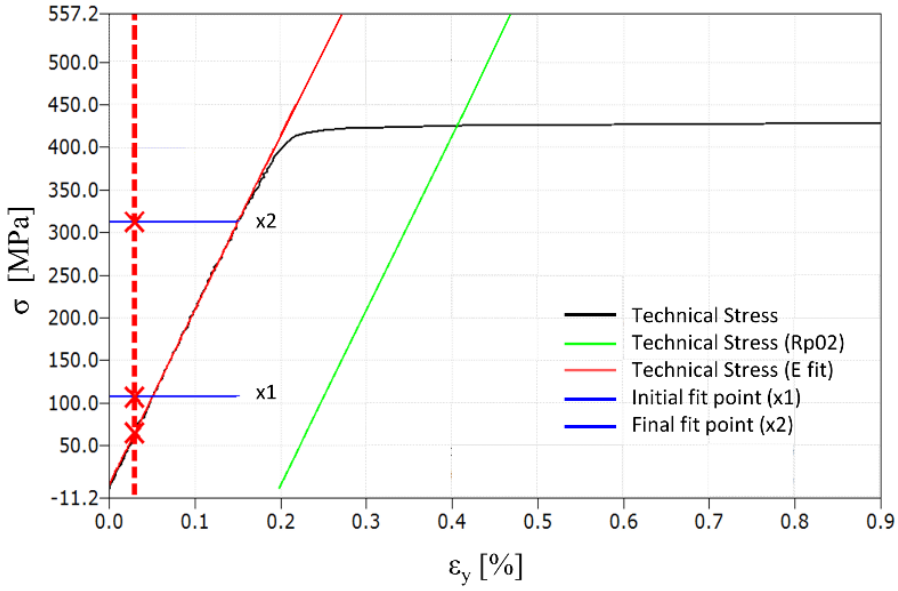

(b)

Figure 4.2: a) Technical and real stress-strain curves evaluated by the DIC technique; b) Evaluation of the Young's Modulus and yielding strength by the DIC technique.

Table 4.1: Mechanical properties of the investigated S355 steel.

S355 steel		
Young's Modulus	E	205315 MPa
Poisson ratio	ν	0.29
Yield Stress	R_{p02}	425 MPa
Work hardening exponent	n	0.165
Maximum technical stress	$R_{m\ tech}$	557 MPa
Maximum true stress	$R_{m\ true}$	639 MPa
Strain at maximum load	ε_u	14.64 %
Stress at rupture	R_f	514 MPa
Strain at rupture	ε_r	15.55 %

4.3.2. Fatigue tests and Thermographic Method

A series of fatigue tests at constant amplitude were carried out by imposing different values of the maximum stress, with a stress ratio R= -1, setting the run-out, i.e. the number of cycles that have theoretically infinite life, to $2x10^6$ cycles and adopting a load frequency of 20 Hz. In Figure 4.3 are reported in a double logarithmic plot, the experimental fatigue data with a scatter band of 95% and 5% probability of survival and inverse slope k= 6.95. The values of the fatigue limit, derived from the stress amplitude-number of cycle to failure curve at $2x10^6$ cycle and estimated at the different probabilities of survival of 95%, 50% and 5%, are respectively 143 MPa, 173 MPa and 209 MPa. The value of the fatigue limit present in literature [20] for the same steel falls in this range. The scatter index T_σ, evaluated as the ratio between the fatigue limit at 5% probability of survival and the same value at 95% probability of survival, is equal to 1.46, a typical value for structural steels.

During the traditional fatigue tests, the IR camera has been used to monitor the temperature evolution over the number of cycle. In Figure 4.4, for two different tests with constant amplitude, the three temperature phases, as reported by La Rosa and Risitano [2], are clearly visible. The temperature data are represented as the absolute difference between the current value of the temperature and the value at the initial cycle. The stabilization temperature has been evaluated as the average with standard deviation of the temperature point of the second phase, not taking into account the point of the first and third phases. As expected, the higher the stress, the higher the stabilization temperature, but, on the other hand, the energetic parameter presents the same order of magnitude for all the tests ($\Phi \approx 5.7x10^5$ Cycles·K).

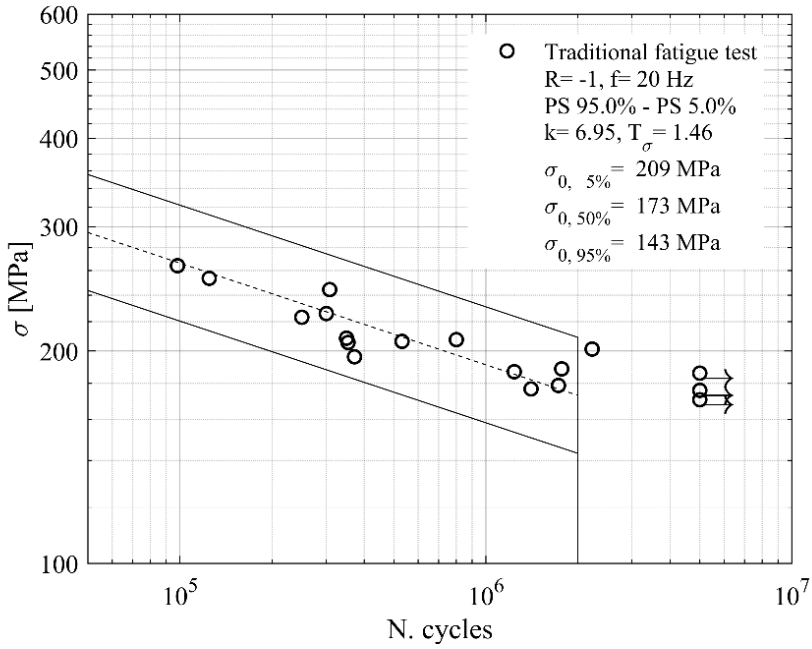

Figure 4.3: Stress amplitude-number of cycle to failure curve with scatter band obtained from traditional fatigue tests.

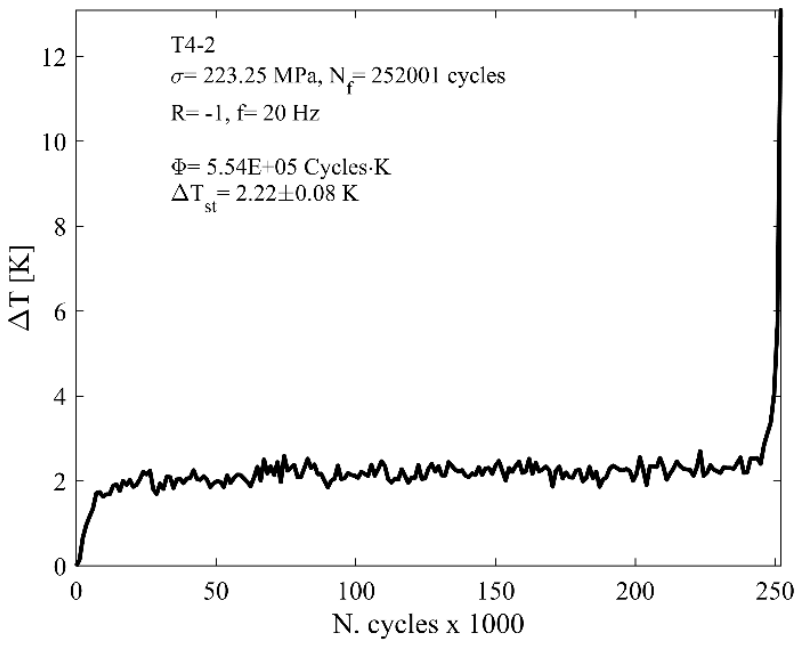

(a)

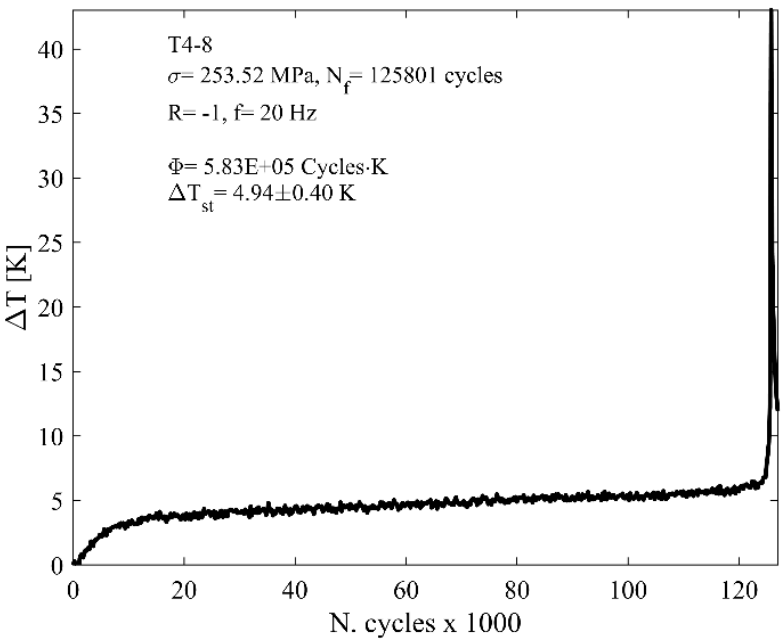

(b)

Figure 4.4: Temperature trend and evaluation of the Energy Parameter Φ during traditional fatigue tests.

Besides traditional fatigue tests which require a relevant number of specimens to be tested, the Thermographic Method allows the rapid assessment of the fatigue properties of the material with a few number of specimens. A series of stepped tests with increasing stress and with the same load ratio and frequency of the traditional one were carried out. In Figure 4.5, the temperature evolution vs. number of cycle vs. stress level are represented for two of the nine stepped tests. As for the traditional case, the temperature data are represented respect to the absolute difference from the initial cycle. For each stress level, the stabilization temperature has been evaluated as the average value and standard deviation of the temperature data of that stress level, excluding the points in the transition from one stress level to the other. Generally, these temperature points are within a span of 30% in the initial part and of 10% in the final part of the stress level block. For stress levels below the fatigue limit the value of the stabilization temperature are lower compared to the last stress level and sometimes it is not possible to assess a stabilization temperature due to the noise of the temperature signal (Figure 4.5a). For higher stress levels the temperature never reaches a stabilization, therefore it increases until the specimen failure. As is possible to note, the increase in the stabilization temperature values experience a sudden change

moving from 133 MPa to 210 MPa, passing through the 171 MPa stress level, therefore the fatigue limit is expected to be located in this stress range.

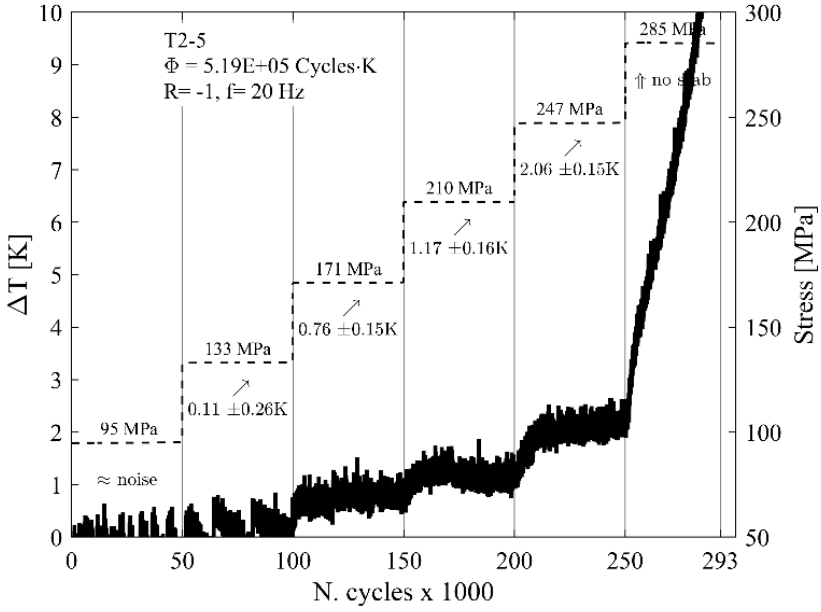

(a)

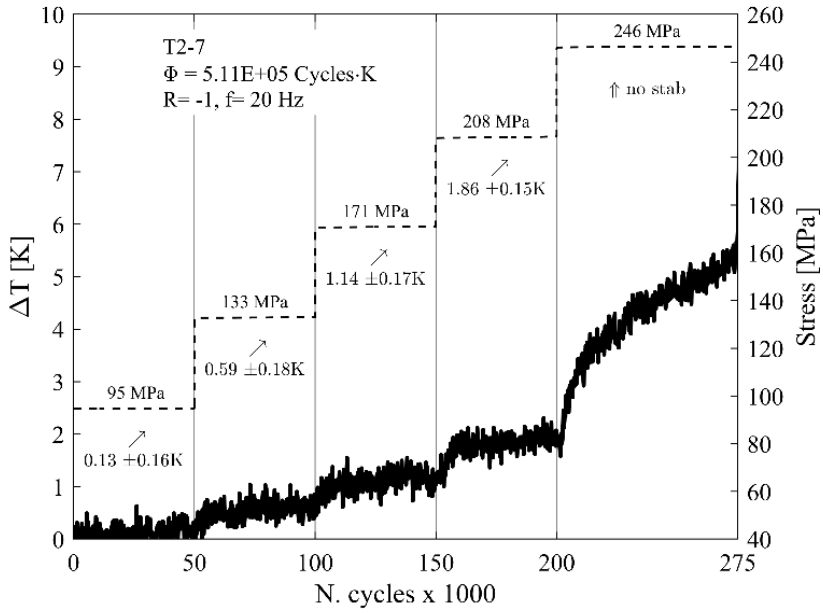

(b)

Figure 4.5: Temperature evolution vs. number of cycle vs. stress level during step load tests.

As regards the energetic release during the step tests, in Figure 4.6 are reported the different values of the Energy Parameter evaluated as the integral of the area subtended by the surface

temperature vs. the number of cycle of each test until failure. The order of magnitude for all the stepped test is the same and the average value of this parameter seems to be in good agreement with the values calculated for the traditional fatigue tests.

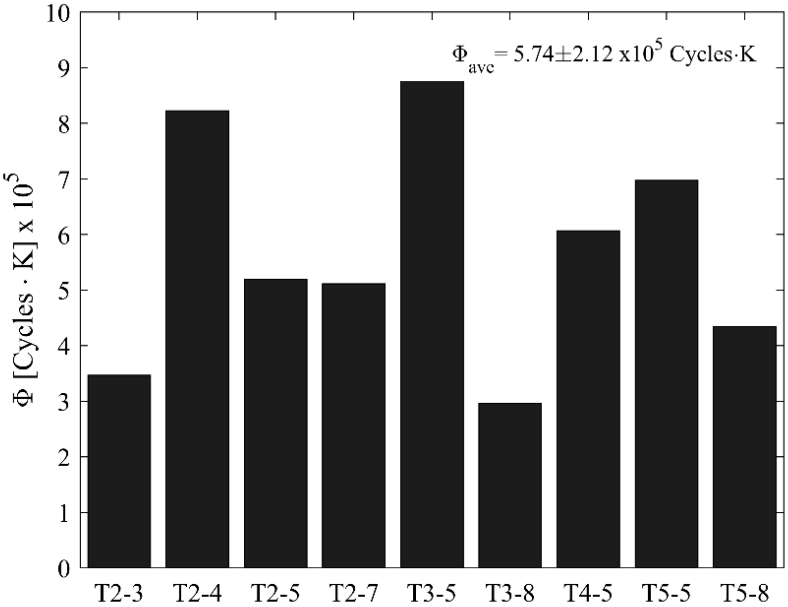

Figure 4.6: Comparison between the Energy Parameter of the step load tests.

By knowing the stabilization temperature of the different stress level for each of the nine step tests, it is possible to plot them against the relative applied stress (Figure 4.7). The data set presents a knee for a stress range between 160 MPa and 200 MPa. It is possible to subdivide the temperature data set into two groups: the first below the knee (ΔT_1 estimated with stress level between 90 and 160 MPa) and the second above it (ΔT_2 estimated with stress level between 200 and 260 MPa). By making a linear regression for the two set of temperature point, it is possible to evaluate the fatigue limit as the intersection between the two straight line. For the whole step tests, a value of 179.5 MPa for the fatigue limit has been found. As it is possible to observe in Figure 4.5 and in a more clearly way in Figure 4.7, the stabilization temperatures experience a sudden increase for stress level above the fatigue limit. The value of the fatigue limit assessed by the Thermographic Method is in line with that found by means of traditional fatigue test evaluated at a probability of survival of 50%.

It is possible to compare the S-N data coming from the Thermographic Method step tests with the scatter band of the fatigue data obtained with conventional tests. The Energy Parameter for each step test has been evaluated and the values of the number of cycles to failure have been

obtained as the ratio between the Energy Parameter and the stabilization temperature of each stress level. The stress levels below the fatigue limit of $\sigma_{0,\,50\%}$= 173 MPa have not been taken into account because the stabilization temperature of those stress level are lower compared to the stabilization temperature of the stress level above the fatigue limit. As is possible to observe in Figure 4.8, the data points obtained by means of the Thermographic Method fall entirely within the scatter band of traditional fatigue tests, hence the Thermographic Method is able to predict, with a very low number of specimens, the entire S-N curve of the material.

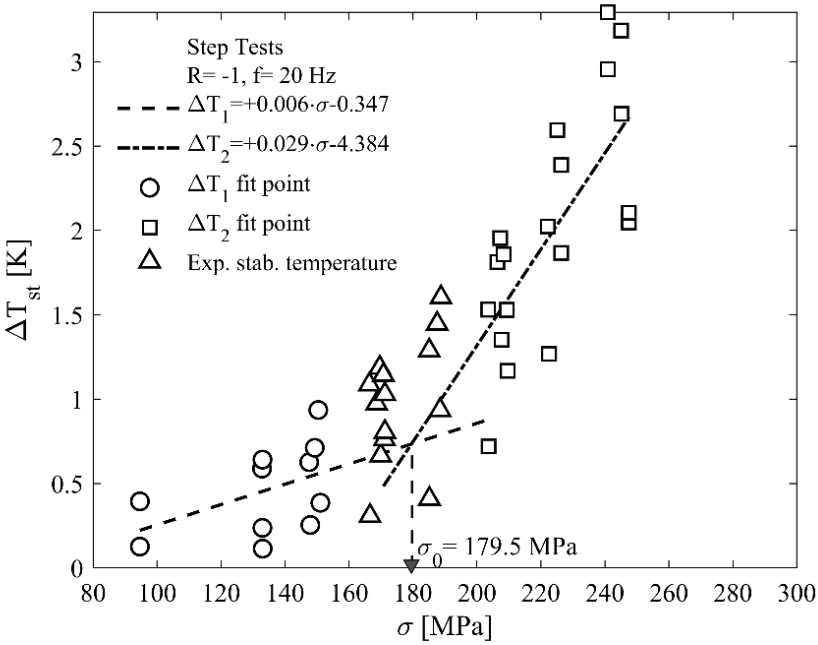

Figure 4.7: Evaluation of the fatigue limit by means of the Thermographic Method reporting the stabilization temperature vs. the relative stress level.

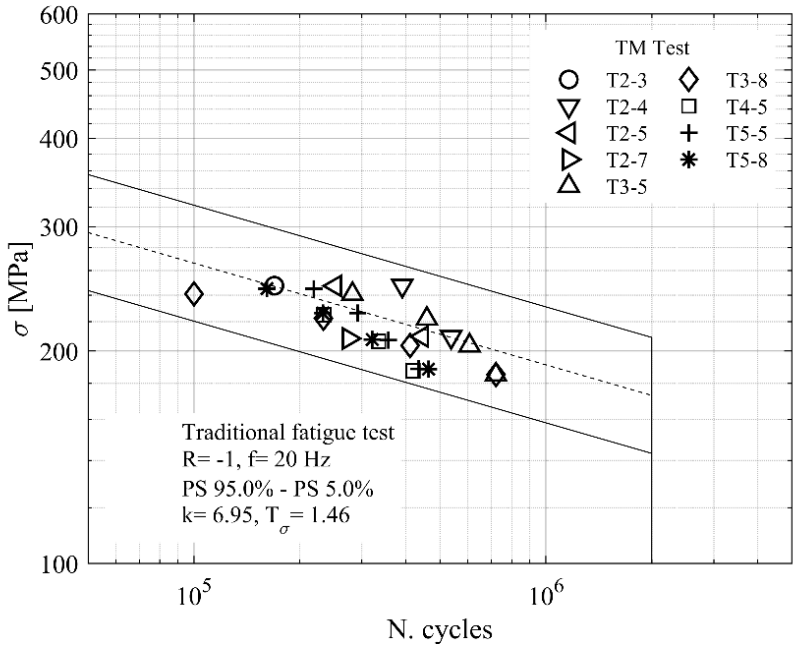

Figure 4.8: Comparison between the S-N value obtained by Thermographic Method step tests and the scatter band from traditional fatigue tests.

4.3.3. Static Thermographic Method

A second series of static tests has been conducted on two specimens using a stress rate of 183 MPa/min. The stress rate has to be choose properly in order to assure adiabatic test condition, i.e. when the "characteristic heat diffusion time" of the specimen is more and more less than the whole test time. In Figure 4.9 are reported the trend of the applied stress and the experimental temperature variation ΔT during the tensile test, calculated as the difference of the instantaneous temperature of the specimen surface minus the initial surface temperature ($\Delta T = T_i - T_0$). The temperature data reported has been filtered with a *rlowess* filter in order to reduce the outliers and highlight the thermoelastic trend.

It is clearly visible that there is an initial phase in which the temperature variation has an almost constant slope, which identify the thermoelastic phase, and then tends to stabilize during a second phase. The first deviation from linearity, which corresponds to the end of the first phase, can be correlated to the damage limit, very close to traditional fatigue limit. The change in the slope of the temperature increment can be easily find as the intersection between the straight line of regression of the thermoelastic region (early stage of the temperature trend, ΔT_1 fit point series) and the straight line of the nearly zero derivative flex region (last stage before the sudden increase in temperature trend, ΔT_2 fit point series). The corresponding average stress value coming from

the two test is 181.2 MPa. The values obtained using the three different approaches, traditional fatigue tests, Thermographic Method and Static Thermographic Method, seem to be in good agreement, as the obtained scatter is normal for structural steels also during traditional fatigue tests.

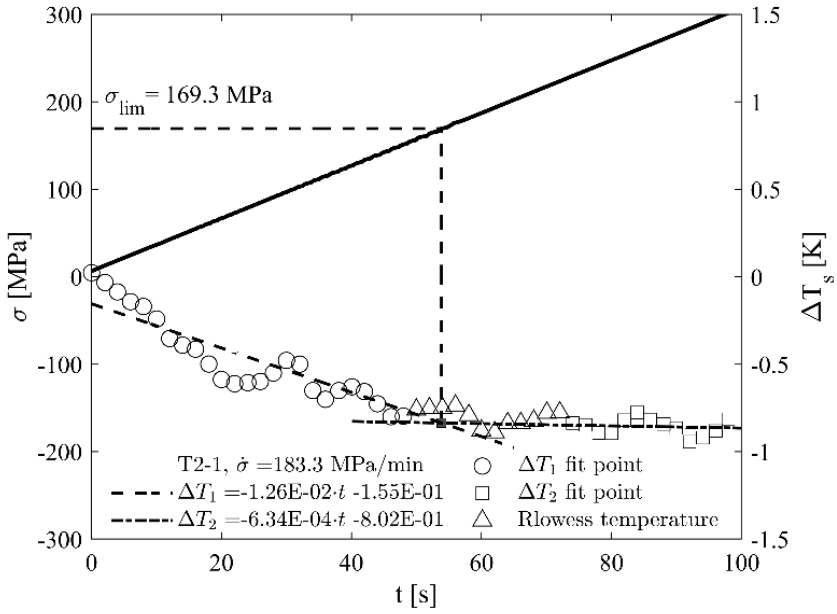

(a)

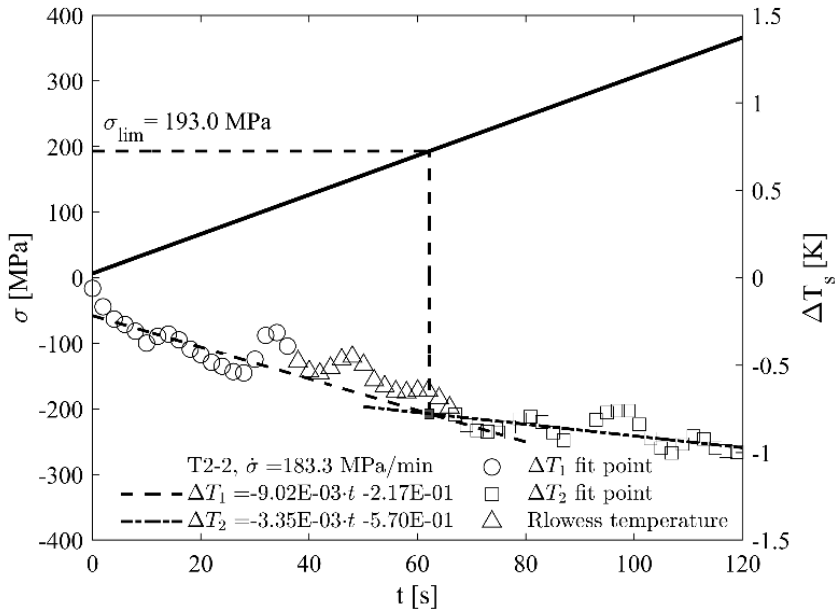

(b)

Figure 4.9: Temperature evolution vs. applied stress during static tensile test.

4.4. Conclusion

In this study the fatigue properties of a widely used structural steel of the S355 type, taken by an in service marine structure, have been evaluated. Three different approaches have been adopted to assess the fatigue limit of the material: traditional fatigue test, Thermographic Method (TM) and Static Thermographic Method (STM).

Full-field techniques (DIC and IR thermography) were applied for the mechanical properties and energetic release evaluation under both fatigue and static traction tests.

The predictions of the fatigue life obtained by means of the two thermographic methodologies were compared with the value obtained by the traditional procedure. In particular:

- From the traditional fatigue tests the fatigue limits evaluated at a number of cycle to failure equals to $2x10^6$ and at different probability of survival are $\sigma_{0,\,95\%}$= 143 MPa, $\sigma_{0,\,50\%}$= 173 MPa and $\sigma_{0,\,5\%}$= 209 MPa. The Energy Parameter has a value of about $\Phi \approx 5.7x10^5$ Cycles·K.
- From the step load tests, applying the TM the fatigue limit has been estimated, with a value equals to 179.5 MPa, and the Energy Parameters have been evaluated (Φ= $5.74 \pm 2.12\ x10^5$ Cycles·K). The S-N data obtained from the same step tests have been compared with the scatter band of traditional fatigue tests, showing how all the TM points fall within the scatter band.
- From the two static tensile tests, applying the STM, the stress limit of the material has been evaluated (σ_{lim}= 181.2 MPa).

The predicted values by means of the two thermographic methods are in good agreement with the experimental values obtained with traditional fatigue tests. The TM and STM are able to estimate, even with a limited number of specimens, the fatigue life of the material. The Energy Parameter could give interesting information for the development of a residual fatigue life prediction model of structural components.

5. MEDIUM CARBON STEEL C45

Guglielmino E, Risitano G, Santonocito D, Guglielmino E, Risitano G, Santonocito D. A new approach to the analysis of fatigue parameters by thermal variations during tensile tests on steel. Procedia Struct Integr 2020;24:651–7. doi:10.1016/j.prostr.2020.02.057.

Highlights

The aim of this research activity is to apply the Static Thermographic Method (STM) and the Thermograhic Method (TM) during static tensile tests in order to correlate the surface temperature trend to the fatigue properties of a C45 steel. Full-field techniques are a powerful aid in the evaluation of the mechanical behaviour of the material and they can also accelerate the overall test time.

This research activity is part of the collaboration between the University of Messina and other several Italian universities within the Italian National Machine Design Society (AIAS) group on Energetic Methods (MEAS).

In this chapter, results about the influence of the applied stress rate on the thermal release of a medium carbon steel has been evaluated and a series of fatigue test has been carried out on the same material. In addition, numerical simulations have been performed in order to assess the end of the thermoelastic effect during a static tensile test. The obtained limit stress has been compared with the fatigue limit coming from other energetic method and conventional fatigue tests showing good agreement.

Nomenclature

c	specific heat capacity of the material [J/kg.K]
$I_{1\sigma}$	First stress invariant [MPa]
K_m	thermoelastic coefficient [Pa^{-1}]
R	stress ratio
t	test time [s]
T, T_i	instantaneous value of temperature [K]

T_0	initial value of temperature estimated at time zero [K]
W_p	Plastic work per volume unit [Nmm/mm^3]
α	thermal diffusivity of the material [m^2/s]
ΔT_s	absolute surface temperature variation during a static tensile test [K]
ΔT_1	estimated value of temperature for the first set of temperature data [K]
ΔT_2	estimated value of temperature for the second set of temperature data [K]
ρ	density of the material [kg/m3]
Φ	Energy Parameter [Cycles·K]
σ	stress level [MPa]
σ_{lim}	fatigue limit estimated with the Static Thermographic Method [MPa]

5.1. Introduction

Traditional fatigue tests are extremely time consuming and require a huge number of specimens in order to obtain the fatigue properties of the material. An innovative approach, based on thermographic analyses of the temperature evolution during the fatigue tests, has been proposed for a rapid prediction of the fatigue limit and the S-N curve, using a very limited number of tests: the Thermographic Method (TM) [2]. In a recent work, Risitano and Risitano [3] proposed the Static Thermographic Method (STM) as a rapid procedure to derive the fatigue limit of the material evaluating the temperature evolution during a static tensile test.

In the last twenty years, the Infrared Thermography (IR) has been applied for the analysis of different materials subjected to several loading conditions: notched and plain steel specimens under static and fatigue tests [19,68,69], laminated composites under tensile static loading [134], polyethylene under static and fatigue loading [137], short glass fiber-reinforced polyamide composites under static and fatigue loading [132], steels under high cycle [44,50,64] and very high cycle fatigue regimes [10,12].

The aim of this research activity is the application of the Static Thermographic Method (STM) and of the Thermographic Method (TM) during static tensile and fatigue tests for the assessment of the fatigue life of a medium carbon steel of the class C45. Tensile tests were carried out and infrared thermography has been adopted during all static tests in order to assess the influence of

the stress rate on the energetic release of the material. In addition, stepwise fatigue tests are carried out and the obtained value of the fatigue limit is compared with the one obtained by STM. This research activity is part of the collaboration between the University of Messina and several others Italian universities within the AIAS group on Energetic Methods, made on the same material. A comparison of the found fatigue limit is performed at the end of the chapter in order to highlights the differences between the several energy based method for fatigue assessment.

5.2. Materials and Methods

5.2.1. Experimental tests

Static tensile tests and stepwise fatigue tests were carried out on specimens made of C45 steel. The specimens have a dog bone shape (Figure 5.1a) with a nominal cross section of 12 mm x 6 mm. All the tests were performed with a servo-hydraulic load machine MTS 810 (Fig. 2b). In order to assess the influence of the load velocity on the energetic release of the specimen, the static tests were conducted under load control adopting three different stress rate: 200 MPa/min, 400 MPa/min and 800 MPa/min. For each stress rate a number of three specimens was tested. The stepwise fatigue tests were conducted on two specimens with a stress ratio R= -1 and a test frequency f= 20 Hz. An increasing value of the maximum applied stress was adopted, ranging from 180 MPa up to 320 MPa, with a stress step $\Delta\sigma$= 20 MPa and a number of cycles per block equal to 20000.

The infrared camera FLIR A40 was used to monitor the specimen's surface temperature. For the static tensile tests, a sample rate of 2 image per second was adopted with a temperature measurement range between -40°C and +120°C, while for the stepwise fatigue tests a sample rate of 2 image per minute was adopted with a temperature measurement range between 0°C and +500°C. The specimen surface was deeply cleaned from rolling oil by means of absorbent paper; then it was coated with high-emissivity black paint (emissivity up to 0.98). During all the tests the maximum temperature value of a rectangular measurement area, placed on the entire length of the specimen's reduced section, has been recorded.

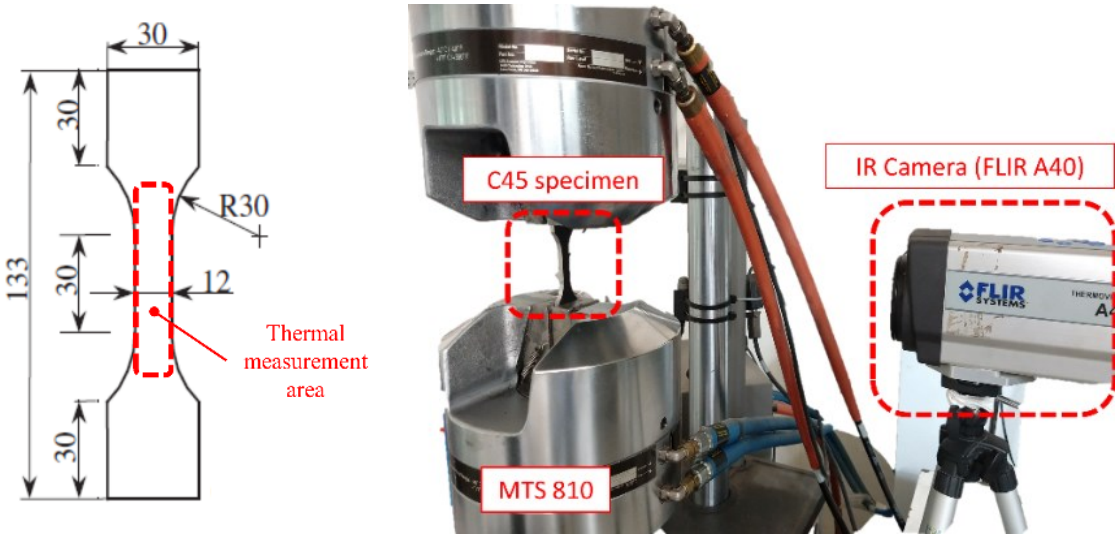

(a) (b)

Figure 5.1: a) dog-bone specimen geometry; b) experimental setup.

The load and temperature data coming from the tests were analyzed adopting an algorithm implemented via Matlab® scripts. The specimen rupture instant has been taken as the reference time for synchronizing the data. In order to clean the temperature signal from outliers and to enhance the trend of the thermoelastic effect during static tests, a locally weighted scatter plot smooth filter (rlowess) with a data span of 10%, already implemented in Matlab®, was chosen. This kind of filter uses locally linear regression to smooth data defining a span in which each data point assumes a weight depending on its distance from the data to be smoothed. In order to find the limit stress, two linear regressions were performed on the temperature data set of the Phase 1 (thermoelastic trend) and Phase 2 (plateau region). The limit stress could be find as the relative stress level of the intersection point between these two straight line.

For the stepwise fatigue tests, the stabilization temperature was estimated as the average value with one standard deviation of the temperature signal for each block, excluding the point in the transition from one stress level to the other. Generally, these temperature points are within a span of 30% in the initial part and of 10% in the final part of the stress level block. The specimen's surface temperature variation ΔT was estimated as the difference between the instantaneous temperature and the initial value of temperature recorded at time zero.

5.2.2. Numerical simulation

A nonlinear finite element model was implemented on Ansys® APDL, adopting $1/8^{th}$ of the specimen geometry (Figure 5.2), according to the model developed in section 2.4.2. The elasto-

plastic material behavior of C45 steel was modelled adopting a multilinear isotropic hardening plasticity model with true stress-strain data from [138], given the fact that they were estimated for the same batch of material. The thermo- mechanical material properties of C45 are reported in Table 5.1.

Hexahedral 20-node SOLID186 elements were chosen and, after a calibration procedure, a number of 3584 elements were adopted. Symmetric boundary conditions were applied to the geometry, locking the nodal displacement along the first axis and the rotations respect the other two remaining axes of the symmetry faces. The maximum tensile force was equally distributed on the grip section nodes and gradually ramped over a number of 1000 substeps.

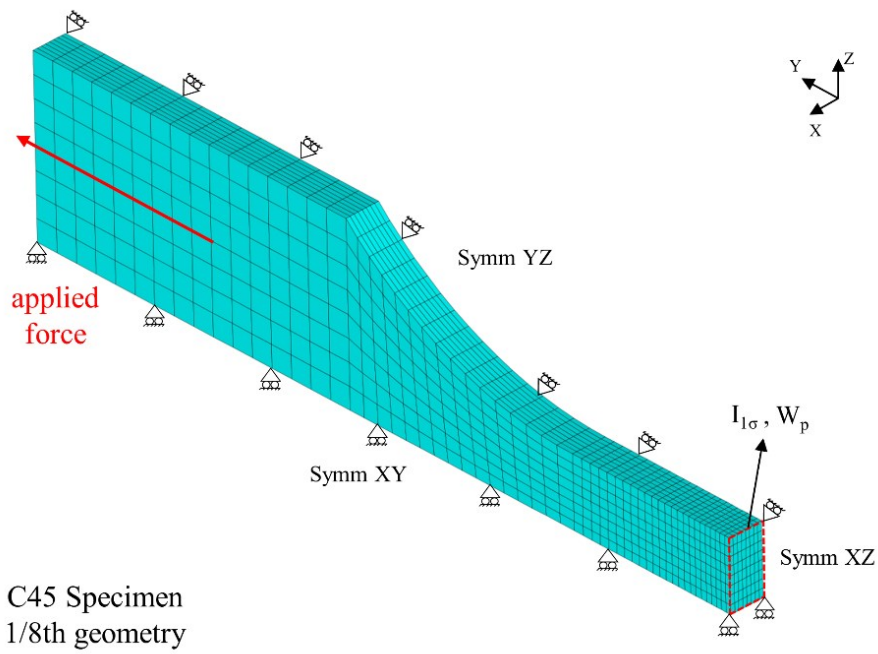

Figure 5.2: Finite element model.

Table 5.1: C45 mechanical and thermal properties.

Tensile Stress at Yield	Tensile Modulus	Poisson's ratio	Density	Specific heat	Linear expansion coefficient	Thermoelastic coefficient
σ_y [MPa]	E [GPa]	ν	ρ [kg/m^3]	c [J/kg.K]	α [K^{-1}]	K_m [Pa^{-1}]
435	210	0.33	7860	480	12 x 10^{-6}	3.17x10^{-12}

In the post-processing of the results, the first stress invariant $I_{1\sigma}$ and the plastic work per volume unit W_p of the resistance section have been evaluated, according to the fact that all the tested specimens were broken at their midsection.

5.3. Results and Discussion

5.3.1. Static tensile tests

A series of static tensile tests has been conducted on three specimens per stress rate, for a total number of nine tensile tests. In this kind of test, the stress rate has to be choose properly in order to assure adiabatic conditions. The applied stress is reported versus the specimen's surface temperature variation, estimated as the difference between the instantaneous temperature and the initial temperature of the surface recorded at time zero ($\Delta T = T_i - T_0$). The temperature data has been filtered with a *rlowess* filter in order to reduce the outliers and highlight the thermoelastic trend. For all of the adopted stress rate is reported only one graph as an example, considering that the other tests exhibit the same thermal behavior.

For the first applied stress rate of 200 MPa/min, the temperature trend has been reported in Figure 5.3. It is not easy to distinguish the different phases and the change in the slope of the temperature signal. A possible explanation could be addressed to the slow test velocity which allows the specimen to exchange heat with the surrounding environment, i.e. the energetic release is not adiabatic.

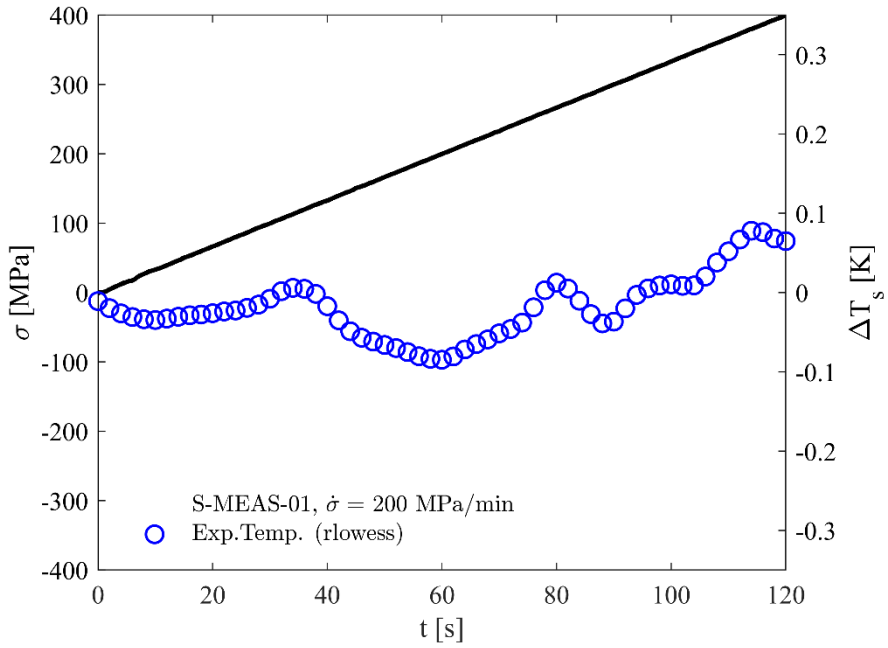

Figure 5.3: Temperature evolution vs. applied stress during static tensile test, with a stress rate of 200 MPa/min.

Considering an applied stress rate of 400 MPa/min (Figure 5.4), in the initial part of the ΔT-t curve it is possible to distinguish the linear trend of the temperature, then it deviates from the linearity reaching a plateau region. It is possible to draw two linear regression line, the former for the first linear phase (early stage of the temperature signal, ΔT_1 fit point series) and the latter for the second phase (last stage before the sudden increase in the temperature signal, ΔT_2 fit point series), not taking into account the temperature values near the slope change (Experimental Temperature series). Solving the system of equations, it is possible to determine the intersection point of the two straight lines. The corresponding value of the applied stress could be related to the macroscopic stress that leads to the irreversible plasticization phenomena in the material. For the stress rate of 400 MPa/min, the limit stress has been evaluated on three tests, obtaining a value equals to 222.2±4.0 MPa.

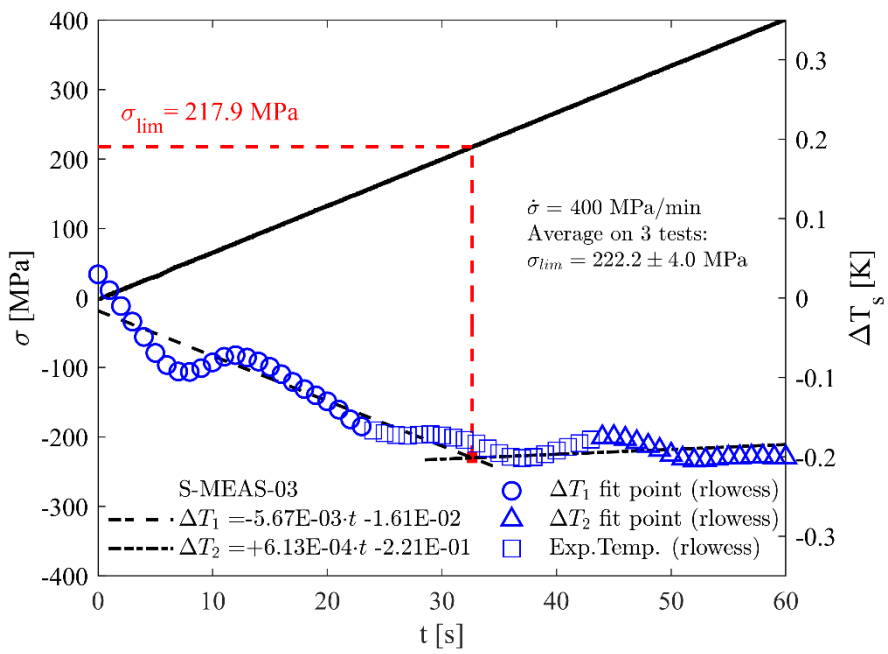

Figure 5.4: Temperature evolution vs. applied stress during static tensile test, with stress rate of 400 MPa/min.

Considering a stress rate of 800 MPa/min (Figure 5.5), the energetic release is faster than the previous two cases and it is difficult to distinguish in a clear way the two different temperature phases (ΔT_1 and ΔT_2 fit point series), although it is possible to draw two regression lines and make their intersection. The value of the limit stress found on the three tests is equals to 220.2±7.4 MPa.

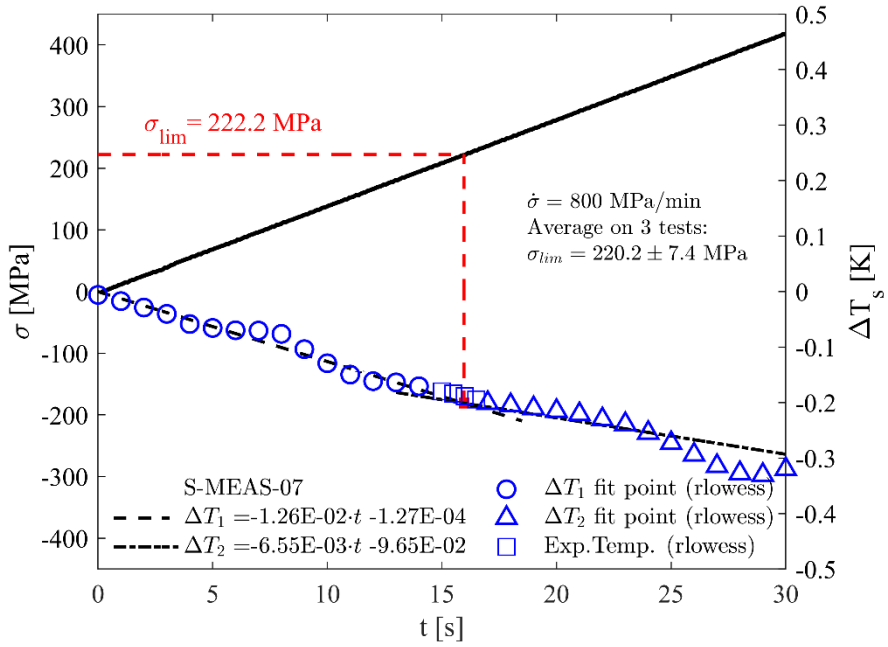

Figure 5.5: Temperature evolution vs. applied stress during static tensile test, with stress rate of 800 MPa/min.

The limit stress obtained by means of the Static Thermographic Method, in particular for the two stress rate of 400 MPa/min, which ensure the best adiabatic test conditions could be assumed equal to 222.2±4.0 MPa. It is important to observe how this value has been obtained by means of a simple static traction test and in a very short amount of time (~5 minutes per test).

5.3.2. Numerical analysis

From the finite element simulations according to the temperature model developed in section 2.4.2, the first stress invariant and the plastic work per unit of volume of the cross section area have been evaluated during the load increment. In Figure 5.6 are reported the experimental superficial temperature of the specimen (not filtered) and the estimated FEM temperature vs. the applied nominal stress. The experimental temperature trend experiences a deviation from the linearity of the thermoelastic effect for a stress value below the yielding stress of the material (~435 MPa). After the yielding stress has been reached, the temperature experiences a high further temperature increment till the specimen breakage. The FE simulated temperature trend shows a perfect linear trend up to the yielding point, then the plastic work per unit of volume suddenly increases, leading to an abrupt positive change in temperature, reaching asymptotically the final ultimate stress.

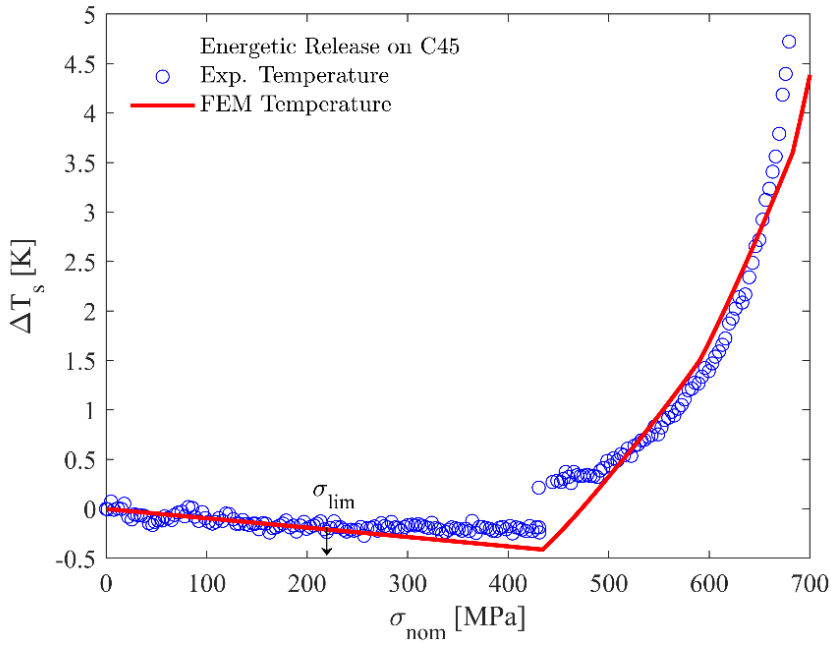

Figure 5.6: Energetic release during a static traction test of C45, experimental and numerical trend.

Focusing on the first part of the temperature trend (Figure 5.7), it is evident how the experimental temperature deviates from the linearity for a nominal macroscopic stress level approximately equal to the limit stress. It is easy to distinguish the two phases: the first where both experimental and simulated temperature show a linear trend and the thermoelastic coefficient K_m is able to properly fit it, and the second, where the experimental and simulated temperature have different trends.

The reason of the different temperature trends (experimental and simulated) may reside in the presence within the material of local defects that lead to local plastic condition, hence to a temperature rise. Actually it not easy to properly simulate such micro-defects adopting the FE techniques.

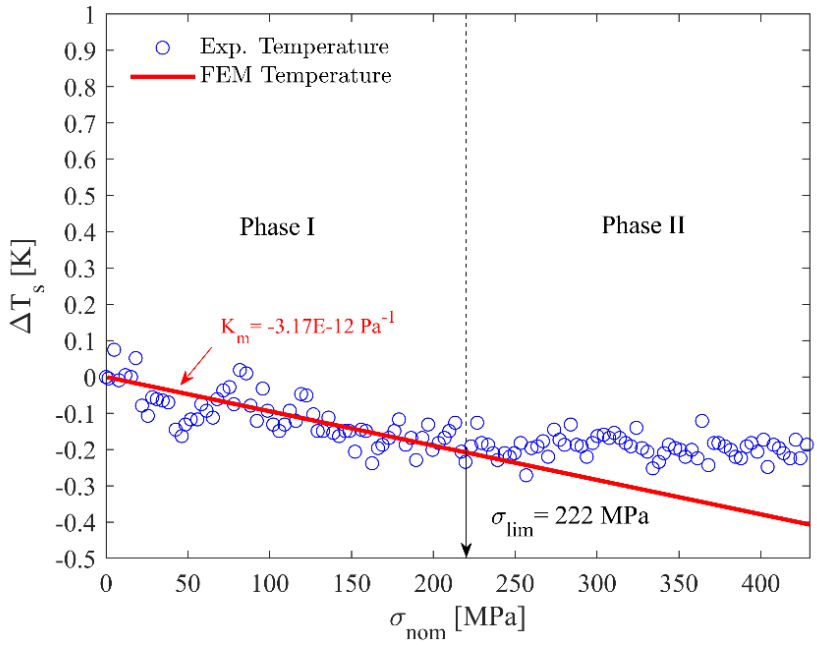

Figure 5.7: Energetic release during a static traction test. Deviation from the linearity of the thermoelastic trend.

5.3.3. Stepwise fatigue test

A second series of test was performed on two specimens adopting a step increment of the maximum applied stress with R= -1 and test frequency f= 20 Hz. In Figure 5.8 the superficial temperature evolution is reported versus the number of cycles and the applied stress. The temperature has been evaluated as the difference between the instantaneous temperature and the temperature at the beginning of the fatigue test. For stress levels equal to 180 and 200 MPa it is not possible to assess in a clear way a temperature increment. As the stress level increases from 200 MPa to 220 MPa, it is possible to observe a temperature rise with stabilization of the trend. With higher stress level (>240 MPa) the temperature experiences a very high further increment without plateau region till the specimen failure. Both of the tested specimen never reached stress level higher than 280 MPa. The Energy Parameter Φ has been estimated for the two tests as the numerical integral of the subtend area of the temperature curve vs the number of cycles, showing value with the same order of magnitude (~$2x10^6$ Cycles·K).

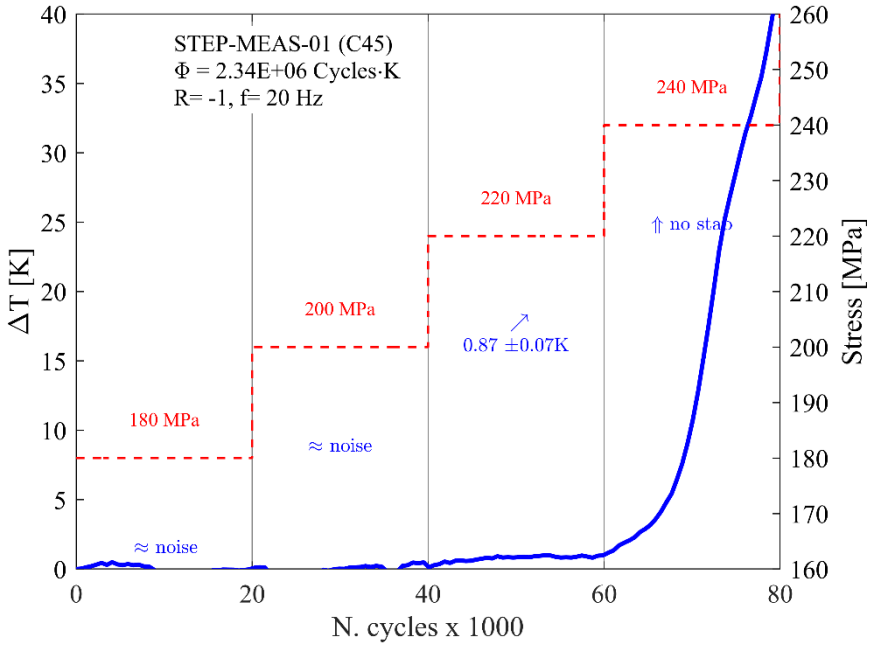

(a)

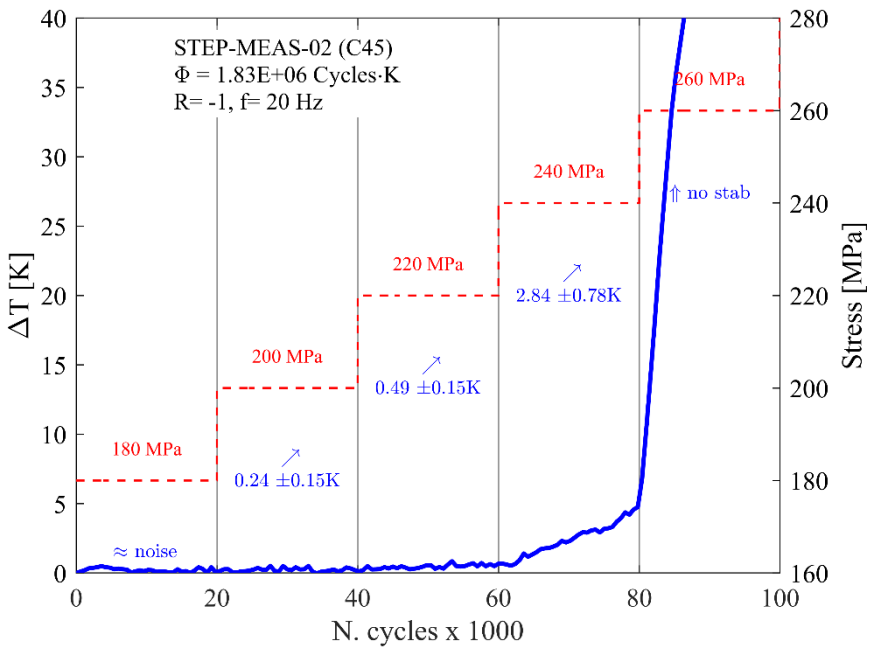

(b)

Figure 5.8: Stepwise fatigue test on C45 applying the Thermographic Method

Due to the sudden higher temperature increment it has not been possible to evaluate the S-N curve of the material with the procedure proposed by Fargione et al. [46]. On the other hand, it has been possible to evaluate how the temperature experiences an increment for stress level in the stress range between 200 and 220 MPa. This indicates that fatigue damage begin for those

stress levels and it is in agreement with the value of the limit stress found by means of static traction test applying the STM.

5.3.4. Comparison with other test

The limit stress obtained by means of the STM could be compared with the fatigue limit obtained with alternate traction-compression tests in literature, conceivable as the more damaging dynamic load condition for the material. In a work by Szala and Ligaj [139], the S-N curve of a C45 steel, obtained with constant load tests and load ratio R= -1, has been reported. The fatigue limit evaluated with a 50% probability of survival at $2x10^6$ cycles is equals to 210 MPa. Curà and Gallinatti [140] for the same steel report a fatigue limit, obtained by means of Stair Case procedure with R= -1, equals to 239±9 MPa.

Within the Energy Method group of the Italian National Machine Design Society (AIAS), a round robin has been performed between several Universities. The aim of this round robin was to compare the different energetic test procedures available for the rapid estimation of the fatigue limit of materials. The adopted procedure includes the Static Thermographic Method, as well as the Thermographic Method (with the adoption of the temperature gradient over the number of cycles dT/dN and the stabilization temperature T_{stab}), the analysis of the thermoelastic signal (E-mode and D-mode) and the lost energy per cycle Q. In addition, traditional Staircase procedure for evaluate the fatigue limit has been performed. All the tests were performed on the specimens of Figure 5.1a, made of the same C45 steel, except for the geometry of the Staircase procedure by the University of Pisa. In Table 5.2 are reported the different values of the fatigue limit assessed with different techniques for a stress ratio of R= -1. It is possible to observe how the predicted value of the fatigue limit by means of the STM is well below the values estimated with other experimental techniques. Compared to the fatigue limit estimated by means of the traditional Staircase procedure of the University of Pisa, the limit stress is below the fatigue limit with a probability of survival PS of 90%, hence the limit stress could be adopted as a more conservative design parameter compared to the other values. It is important also to point out that the different specimen preparations performed by the Universities, cleaning and/or machining, may severally affect the final value of the fatigue limit. In particular, the Staircase procedure by the University of Pisa was performed on different specimen geometries adopting a resonant fatigue test machine which may lead the specimen to a higher bulk temperature during the fatigue tests. Compared to the classical fatigue tests, but also to the other energetic approaches, the Static

Thermographic Method was the most rapid procedure which required the lowest number of specimens.

Table 5.2: Comparison of the different experimental techniques for the fatigue limit assessment (in MPa) for R= -1.

Test procedure	University of Messina	University of Catania	Politechnic of Milan	University of Padova	University of Pisa
STM	222	205			
TM (dT/dN)			316		
TM (T_{stab})	200÷220	310	309		
E-mode (ω)			301		
D-mode (2ω)			305		
Q			308	295	
					261 (PS 10%)*
Staircase				274	245 (PS 50%)*
					229 (PS 90%)*

**procedure performed with resonant fatigue test machine and with different specimen geometry.*

5.4. Conclusion

In this chapter the energetic release during a tensile test of a C45 steel has been evaluated. This research activity is part of the collaboration between the University of Messina and other several Italian Universities within the AIAS group on Energetic Methods. The IR camera allowed the application of the Static Thermographic Method and of the Thermographic Method monitoring the specimen's surface temperature.

The influence of the applied stress rate on the energetic release has been evaluated, showing how the choice of a proper stress rate assure adiabatic test conditions. Considering a stress rate of 400 MPa/min the limit stress has been evaluated as the stress level at which the temperature deviates from its linear trend, obtaining a value of 222.2±4.0 MPa. Numerical analysis was performed in order to assess the end of the thermoelastic effect compared to a finite element model.

Stepwise fatigue tests adopting the TM were performed showing how a temperature increment is present for stresses in the range of 200÷220 MPa. This indicates that fatigue damage begin for those stress levels.

The obtained values of the limit stress have been compared with fatigue limits taken from literature for the same steel showing good agreement. Comparisons with other energetic methodologies and with traditional Staircase tests have been performed, showing how the assessed limit stress value could be adopted as a more conservative fatigue design parameter.

The Static Thermographic Method is a rapid test methodology able to predict the fatigue properties of the materials from a static tensile test, even with a limited number of specimens and in a short amount of time.

6. V-NOTCHED MEDIUM CARBON STEEL AISI 1035

Foti P, Santonocito D, Ferro P, Risitano G, Berto F. Determination of Fatigue Limit by Static Thermographic Method and Classic Thermographic Method on Notched Specimens. Procedia Struct Integr 2020;26:166–74. doi:10.1016/j.prostr.2020.06.020.

Foti P, Risitano G, Berto F, Santonocito D. Evaluation of the Energetic Release During Tensile Tests in Notched Specimens by Means of Experimental and Numerical Techniques. Under review (presented at national machine design conference AIAS2020, Energetic Method Session)

Highlights

The aim of the present chapter is to investigate the fatigue limit of notched mechanical components through several energy based approach: Thermographic Method (TM) and Static Thermographic Method (STM).

Fatigue tests have been carried out on blunt V-notch specimens, made of medium carbon steel AISI 1035, in order to apply the TM and evaluate the fatigue limit of the notched material. Static tensile tests at different stress rate have been carried out on the same specimen geometry in order to evaluate the energetic release of the material during a traction test and applying the STM. A numerical finite element analysis has been performed to predict the temperature trend during a tensile test and compared to the experimental trend.

The limit stress values assessed by the energy based methods are in good agreement, suggesting how they can be adopted to assess in a rapid way the fatigue limit of mechanical components.

This research activity is part of the collaboration between the University of Messina and the Norwegian University of Science and Technology NTNU.

Nomenclature

c	specific heat capacity of the material [J/kg.K]
E	Young's Modulus [MPa]
f	fatigue test frequency [Hz]
$I_{1\sigma}$	First stress invariant [MPa]

K_m	thermoelastic coefficient [Pa^{-1}]
N_f	number of cycle at failure
R	stress ratio
t	test time [s]
T, T_i	instantaneous value of temperature [K]
T_0	initial value of temperature estimated at time zero [K]
W_p	Plastic work per volume unit [Nmm/mm^3]
2α	notch opening angle [°]
α	thermal diffusivity of the material [m^2/s]
ΔN	number of cycles per block of a stepwise fatigue test
ΔT_s	absolute surface temperature variation during a static tensile test [K]
ΔT_1	estimated value of temperature for the first set of temperature data [K]
ΔT_2	estimated value of temperature for the second set of temperature data [K]
$\Delta\sigma$	stress step increase for a stepwise fatigue test[MPa]
ε_f	strain at failure
ρ	density of the material [kg/m^3], notch fillet radius [mm]
ν	Poisson coefficient
σ	stress level [MPa]
$\sigma_{0\ TM}$	fatigue limit assessed by Thermographic Method
σ_y	yielding stress [MPa]
σ_U	ultimate stress [MPa]
σ_{lim}, $\sigma_{lim\ FEM}$	limit stress estimated with the Static Thermographic Method [MPa] experimental, simulated

6.1. Introduction

In the field of mechanical design, the determination of the material mechanical properties is particularly time consuming especially dealing with fatigue properties whose obtainment through traditional fatigue tests requires a large number of specimens for its assessment.

The infrared thermography (IR) techniques could be used to determine the material fatigue properties especially when a limited set of specimens are available or when there is the need to decrease costs and tests time. Due to these peculiarities, the IR techniques are very attractive for many researchers who face the problem of fatigue of materials.

Their use has already shown that the thermal analysis allows the estimation of the fatigue limit of the material with a very small number of specimens dealing with plain and notched steel specimens under static and fatigue tests [3,49,50,68,69,124,125,141,142], laminated composite under tensile static loadings [126,134,143], polyethylene under static and fatigue loadings [137], short glass fiber-reinforced polyamide composites under static and fatigue loadings [132], steels under high cycle [44,50,64,142] and very high cycle fatigue regimes [10,141] and additive manufactured components [144].

Among the IR techniques, in the present chapter the Thermographic Method (TM), proposed in 1989, has been adopted to evaluate the fatigue limit of the material in a short amount of time. The Static Thermographic Method (STM), proposed in 2013 [3] as a rapid and economic procedure to estimates the fatigue limit of such a material analyzing the surface temperature trend of specimens subjected to static loads has been adopted. By side of these experimental techniques, the thermal behavior of the material during a static tensile test has been simulated by finite element analysis.

6.2. Materials and Methods

The material under study was a medium carbon steel AISI 1035 and two kind of specimen geometries were adopted (Figure 6.1a): a plain geometry and a blunt V-notched geometry with opening angle $2\alpha = 120°$ and fillet radius $\rho = 2$ mm. All the tests were performed with a servo-hydraulic axial load machine INSTRON 8854 with maximum load capacity of 250 kN.

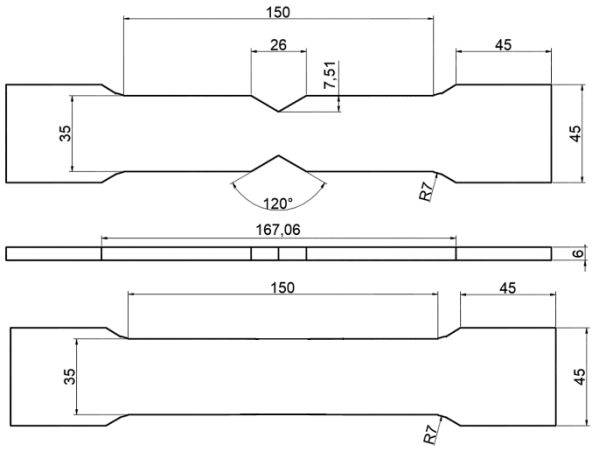

(a)

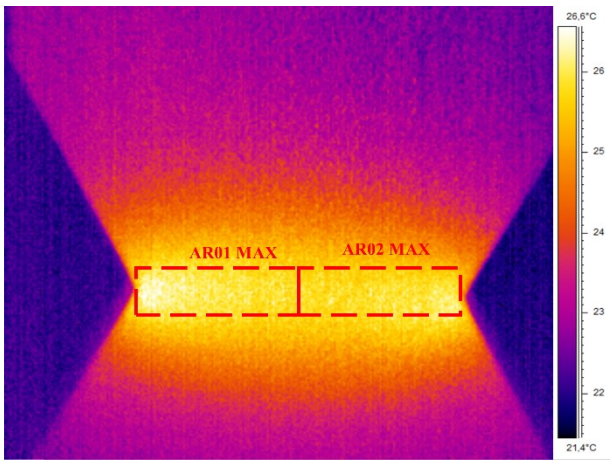

(b)

Figure 6.1: a) specimen geometries; b) IR camera spot on the specimen V-notch area.

In order to apply the TM and STM during fatigue and tensile tests, infrared thermography was adopted to monitor the evolution of the specimen surface temperature. During all the tests, the maximum temperature value of a rectangular measurement area, placed in the vicinity of the two specimen notched section (Figure 6.1b), has been recorded. The infrared camera FLIR A40, with a temperature measurement range between -40°C and +120°C was used. The specimens were coated with a black paint to increase the thermal emissivity of the material up to 0.98. A static tensile test under displacement control (5 mm/min) was performed in order to obtain the material true stress-strain curve adopting the plain specimen geometry (Figure 6.2a).

. The Digital Image Correlation (DIC) technique was adopted to monitor the superficial deformation of the specimen with two cameras (resolution of 4000 x 3000 pixels, focal length of 50 mm). The system accuracy for the strain measurement is up to 0.01%, and the images were acquired at 1 Hz. The ARAMIS 3D 12 M system was used to analyze the strain field of the specimen surface (Figure 6.2b).

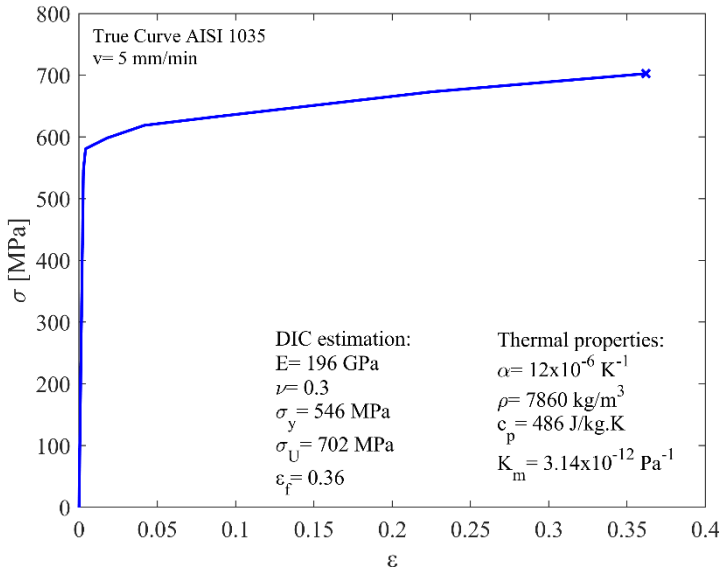

(a)

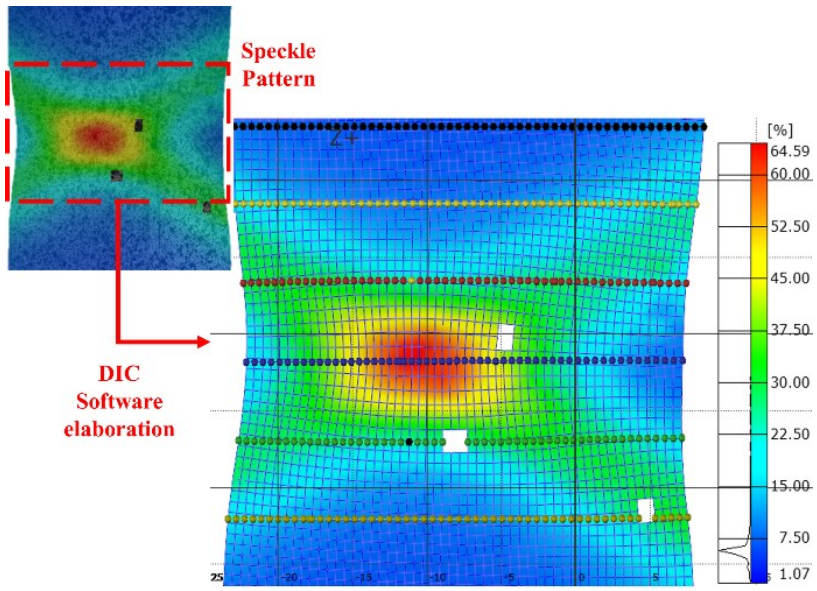

(b)

Figure 6.2: a) True stress-strain curve and thermo-mechanical properties for AISI 1035; b) DIC software elaboration.

A series of three fatigue tests was performed on the notched geometry adopting a stress ratio R= -1 and a frequency f= 20 Hz. A fatigue test was performed adopting a step-wise increase of the stress (Δσ= 42 MPa), ranging from 42 MPa up to 250 MPa with a number of cycle per block ΔN= 20000. The other two fatigue test were performed under constant amplitude stress, respectively of 200 MPa and 260 MPa. The sample rate of the infrared camera was set to 1 image per minute.

A second series of static tensile tests was performed on the notched specimens under stress control in order to assess the influence of the stress rate on the energetic release of the material. Three different load application speeds were considered: 60, 120 and 180 MPa/min. The infrared camera sample rate was set to 1 image per second a total number of 5 test were performed.

A nonlinear finite element models was implemented adopting Ansys APDL in order to estimate the thermal behavior under a static tensile test of the notched specimens (section 2.4.2). The elasto-plastic material behavior was modelled adopting a multilinear isotropic hardening plasticity model with true stress-strain data from experimental tests. For the notched specimen (Figure 6.3), only 1/8th of the geometry was modelled, taking advantage of the specimen symmetries. Hexahedral 20-node SOLID186 elements were chosen and, after a calibration procedure, a number of 10.000 elements were adopted. Symmetric boundary conditions were applied to the geometry, while the tensile force was equally distributed on the grip section nodes. The first stress invariant and the plastic work per unit volume of the node belonging to the blunt V-notch volume were considered in order to evaluate the energetic release of the specimen.

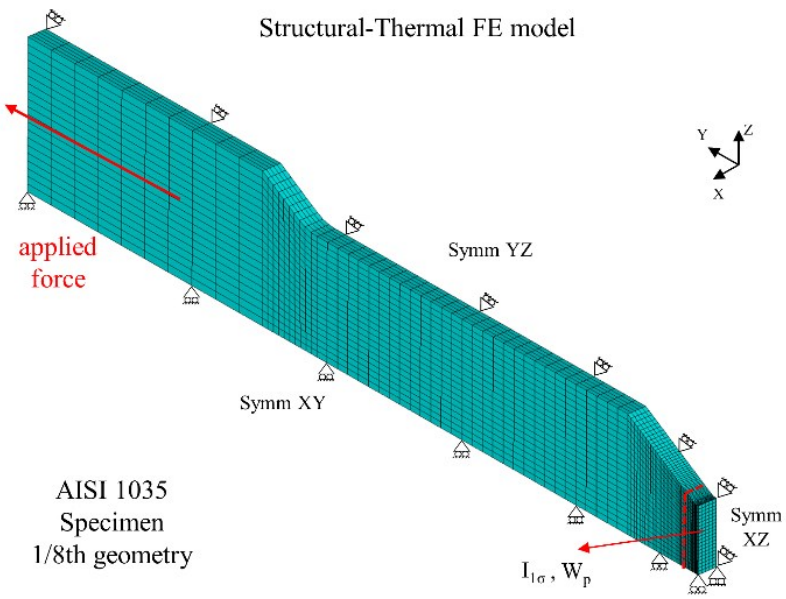

Figure 6.3: FE model for predicting the thermal behavior of the specimen.

6.3. Results and discussion

6.3.1. Fatigue tests

During the fatigue tests, the evolution of the specimen surface temperature has been analyzed in order to apply the TM. Given the fact that the temperature trend during all the tests does not show a stabilization phase, in the following analysis the initial thermal gradient ΔT/ΔN has been considered. The first fatigue test was performed with a stepwise increase of the stress level Δσ under fully reversed load condition. In Figure 6.4 the temperature trend vs. the number of cycles and the stress level has been reported. For stress level below 208 MPa no significant increase in the temperature trend can be appreciated. As the stress level reaches 208 MPa, a rapid temperature increment can be noticed, with a thermal gradient of 5.7×10^{-5} K/cycle. For the higher stress level of 250 MPa a very high further temperature increment is exhibited, with a thermal gradient of 2.1×10^{-4} K/cycle, until the specimen failure.

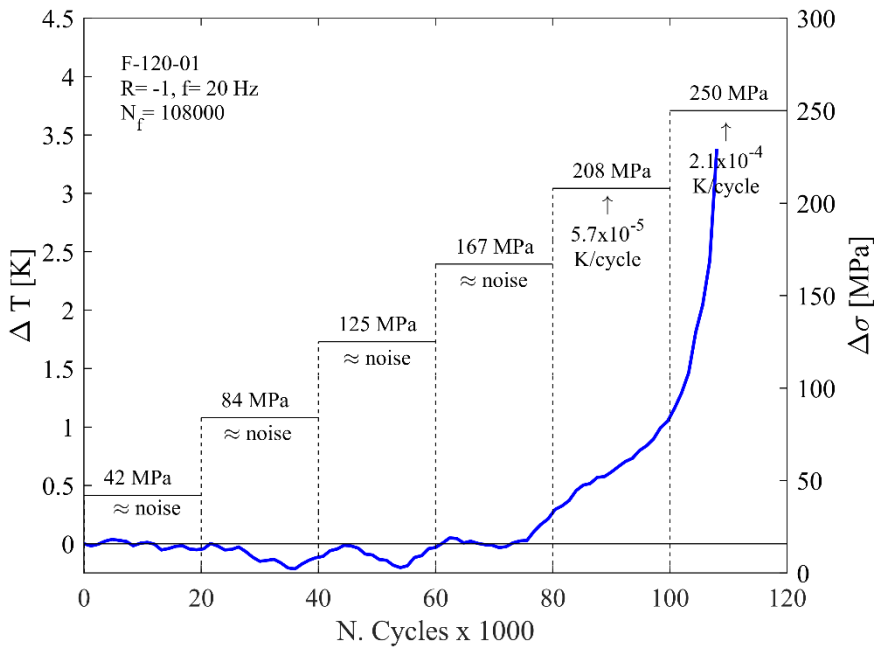

Figure 6.4: Stepwise fatigue test.

Considering that the temperature trend of the stepwise fatigue test has been shown a significant increment moving from 167 MPa and 208 MPa, it is reasonable to think that the fatigue limit of the material under study falls within this stress levels. According to the previous argument, the remaining two fatigue tests have been performed under constant amplitude stress levels above 200 MPa. The first constant amplitude fatigue test carried out with a stress level of 260 MPa

(Figure 6.5a). Even in this case the temperature signal did not shown a stabilization phase, hence the thermal gradient has been estimated ($1.2x10^{-4}$ K/cycle). The second constant amplitude fatigue test has been carried out with a stress level of 200 MPa (Figure 6.5b), showing a thermal gradient of $3.41x10^{-5}$ K/cycle. Generally, the higher the stress, the higher the thermal gradient during a fatigue test.

In order to estimate the fatigue limit by means of the TM, the thermal gradients of the three fatigue test have been reported vs. the square of their corresponding stress level (Figure 6.6). It is possible to evaluate the fatigue limit performing the linear regression of the data and making the intersection of it with the stress axis. A value of $\sigma_{0\ TM}$=174.6 MPa has been found for the fatigue limit assessed by the TM.

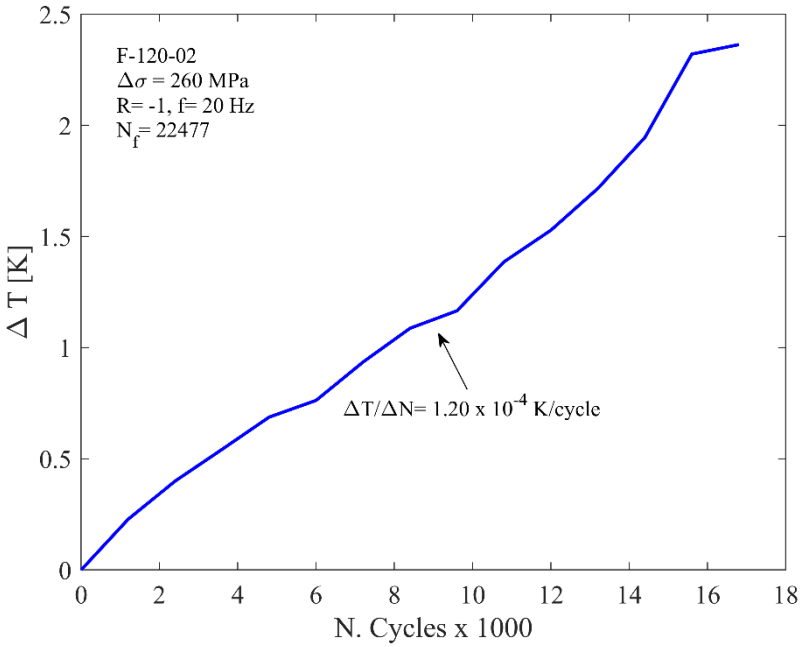

(a)

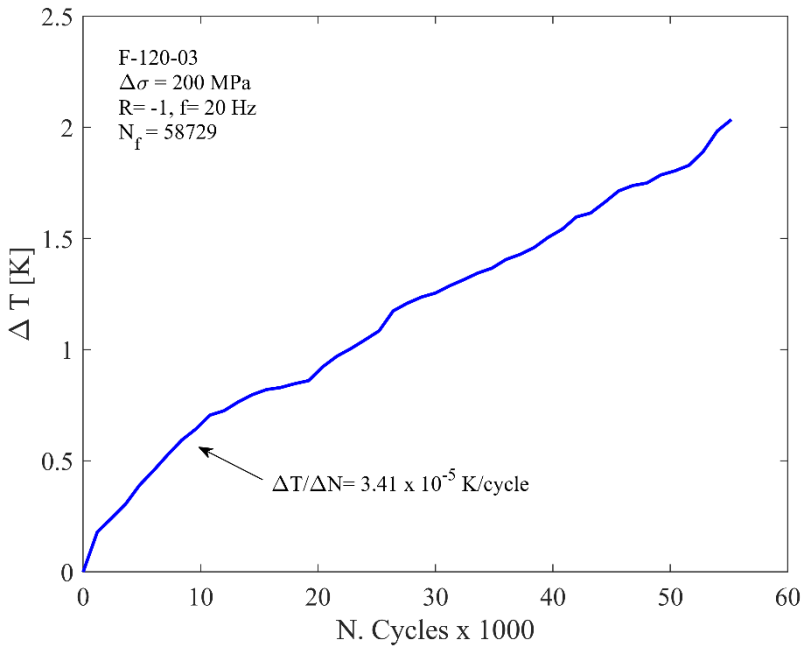

(b)

Figure 6.5: Constant amplitude fatigue test: a) 260 MPa; b) 200 MPa.

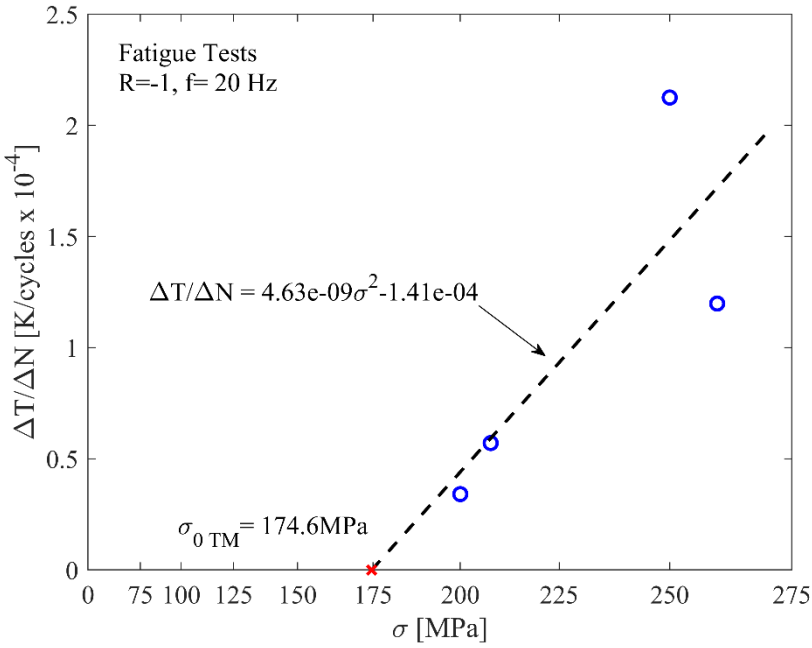

Figure 6.6: Fatigue limit assessed by TM.

6.3.2. Energetic release during tensile tests

The specimen surface temperature evolution during static tensile tests has been recorded by means of an IR camera in order to apply the STM. The difference between the instantaneous temperature and the initial temperature of the surface at time zero ($\Delta T = T_i - T_0$) has been related with the applied stress synchronizing the load data from the servo-hydraulic axial load machine with the one from the IR camera. The instant of failure of the specimen has been taken as the reference. In order to better identify the different phases of the surface temperature evolution and highlight the thermoelastic trend, a *rlowless* filter has been used to process the data, considering a data span of 10%.

The first three static tests have been carried out at three different applied stress rates in order to find out the best test parameter to meet the adiabatic condition. From the data acquired, the best results are achieved with an applied stress rate of 120 MPa/min, which has been chosen to carry out the remaining two static tests. In Figure 6.7 are reported the temperature trend of the two tests performed under constant stress rate of 60 MPa/min and 180 MPa/min. As regard the first stress rate of 60 MPa/min, in the initial part of the ΔT-t curve the thermoelastic behavior is distinguishable, as well as the plateau region. It is possible to draw a linear regression line to interpolate the data referred to the thermoelastic region, designated in the diagram as ΔT_1, and another one to interpolate the data referred to the second phase, ΔT_2 in the diagram.

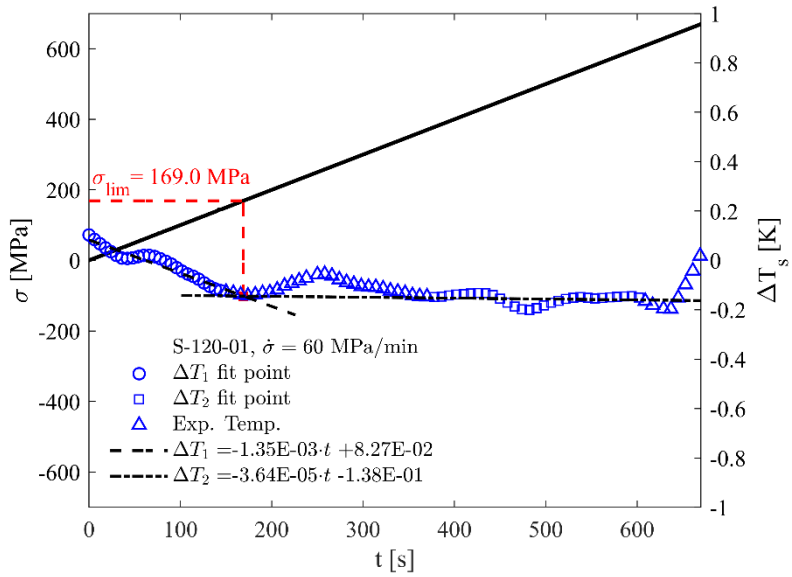

(a)

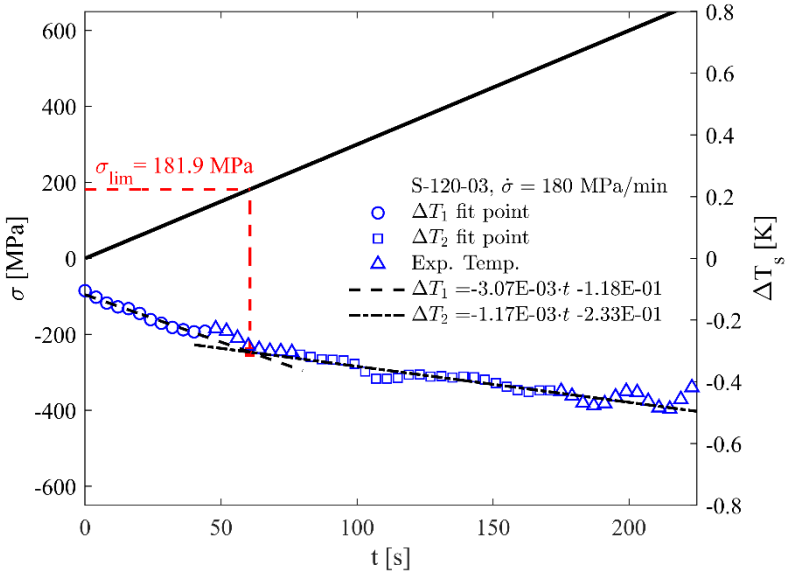

(b)

Figure 6.7: Temperature trend during static tensile test at a) 60 MPa/min; b) 180 MPa/min.

It is worth underlining that, in the interpolations explained above, the temperature values near the transition between the thermoelastic and the thermoplastic regions have not been considered (Experimental Temperature series). Solving the system of equations, it is possible to determine the intersection point of the two straight lines, whose time coordinate allows to determine the corresponding value of the applied stress, namely σ_{lim}. For the stress rate of 60 MPa/min, a value of 169 MPa for the limit stress has been found. Triple the stress rate, from 60 MPa/min to 180 MPa/min, it became difficult to distinguish the two temperature phases. However, it is still possible to draw two linear regressions and make their intersection with the same procedure previously explained. For a stress rate of 180 MPa/min, a value of 181.9 MPa for the limit stress has been found. For the other two applied stress rates the effect in terms of decrease in surface temperature seems to be mitigate. This can be addressed, for the lowest rate, to the possible exchanged heat with the surrounding environment due to the longer test time while, for the faster rate, the excessive reduced time of the test do not allow the material to manifest the temperature evolution clearly in each one of its phases.

As previously stated, the best adiabatic condition for the static tensile tests has been reached adopting a stress rate equal to 120 MPa/min. In Figure 6.8 are reported the temperature trends of the three tensile tests. The thermoelastic phase is clearly distinguishable as well as the deviation from the linearity entering in the thermoplastic region and the further rapid temperature increment before the final failure. For each test, it has been possible to draw the linear regressions

and make their intersection evaluating the limit stress. The average value of the limit stress evaluated on the three tests is σ_{lim}= 177.4±0.6 MPa. According to the considerations already done in section 2.4, this stress value can be thought as the macroscopic stress that lead to the first plasticization phenomena in the material. The limit stress value found by means of the STM is really close to the fatigue limit assessed by the TM.

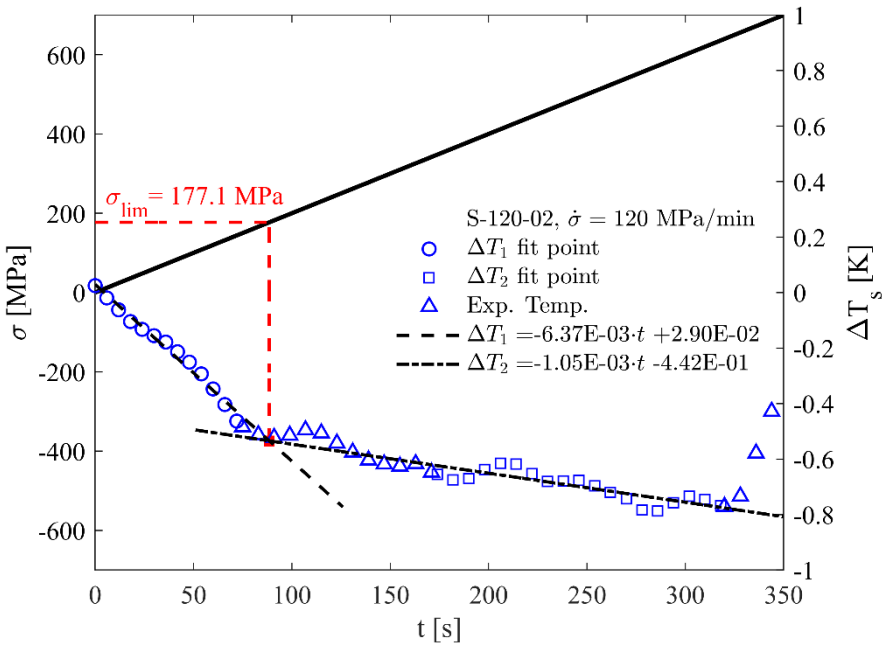

(a)

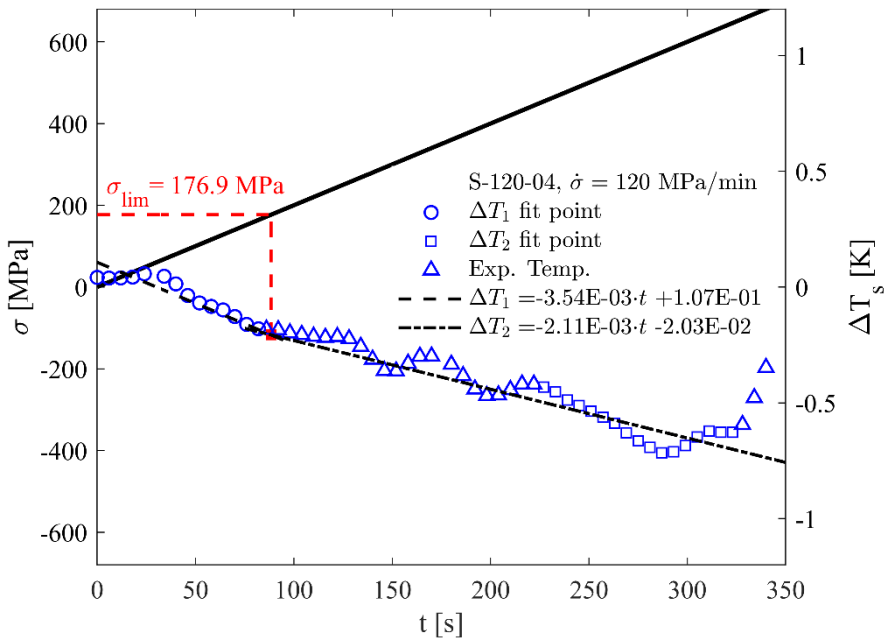

(b)

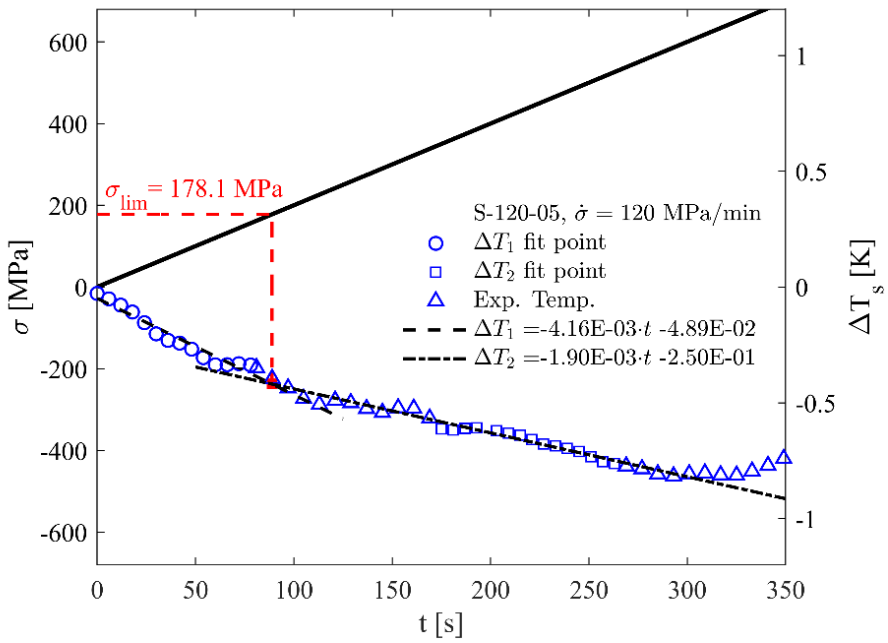

(c)

Figure 6.8: Temperature trend for applied stress rate of 120 MPa/min.

6.3.3. Prediction of the temperature trend

The thermal behavior of the notched specimens during a static tensile test has been modelled through a 3D elasto-plastic FE analysis. For each node of the volume surrounding the notch, the first stress invariant $I_{1\sigma}$, i.e. the sum of the three principal stresses, and the plastic work per unit volume have been evaluated. The results coming from the structural analysis have been adopted as input for the temperature model presented in section 2.4.2, evaluating the thermal contribution due to the elastic and plastic material behavior, and averaging it. The experimental and FE temperature trends have been reported in Figure 6.9 vs. the stress level, referred to the specimen reduced section, for the three static tensile tests performed with a stress rate of 120 MPa/min. For the FE temperature model, the thermoelastic constant K_m as calculated by literature data has been adopted. Generally, the simulated thermal trend follows the experimental temperature behavior, especially near the failure stress, where it experiences a rapid increment till breakage. For the first and last tensile tests (Figure 6.9a, c), the FE simulations overestimates the temperature trend, while for the second tensile test (Figure 6.9b) the simulated temperature trend well fit the experimental behavior.

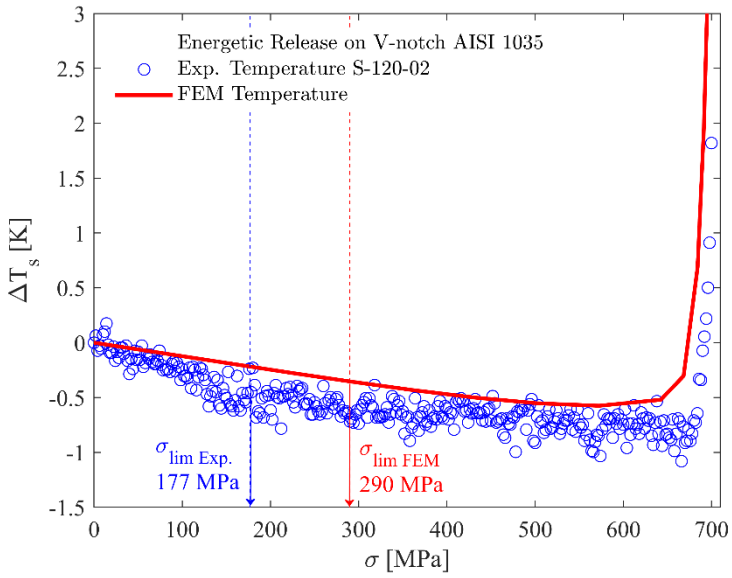
Energetic Release on V-notch AISI 1035
Exp. Temperature S-120-02
FEM Temperature
ΔT_s [K]
σ [MPa]
σ lim Exp.
177 MPa
σ lim FEM
290 MPa

(a)

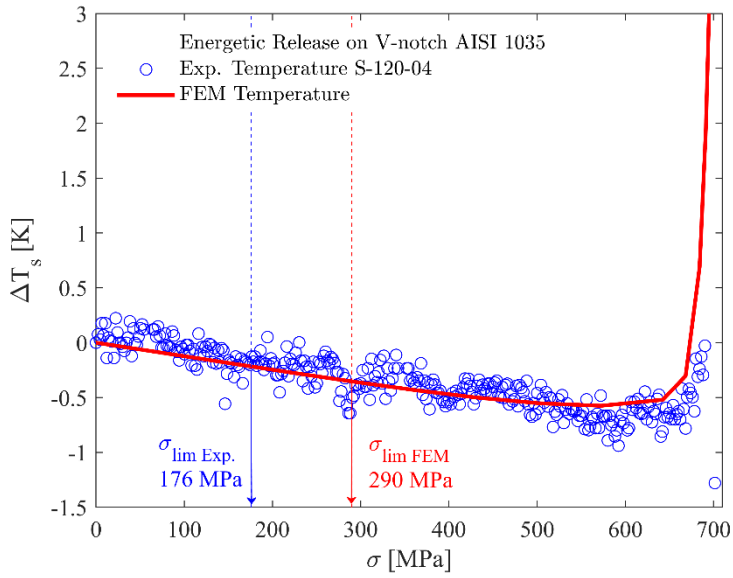
Energetic Release on V-notch AISI 1035
Exp. Temperature S-120-04
FEM Temperature
ΔT_s [K]
σ [MPa]
σ lim Exp.
176 MPa
σ lim FEM
290 MPa

(b)

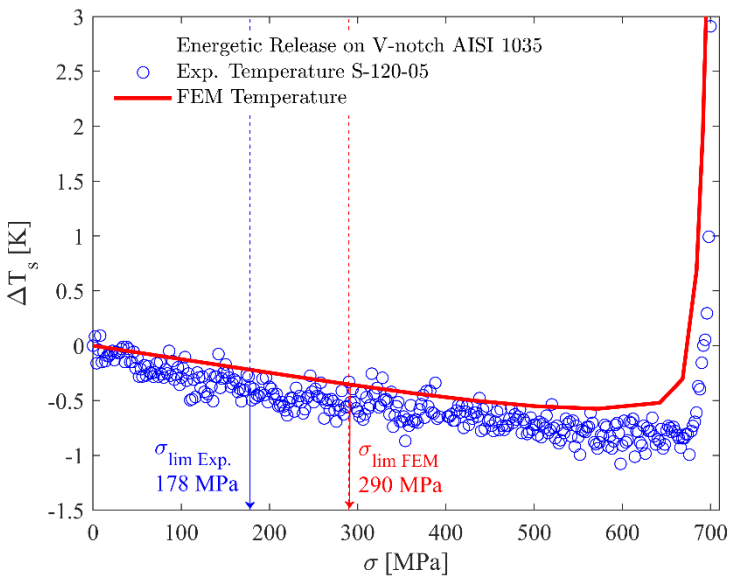

(c)

Figure 6.9: Experimental vs. FE thermal behavior of notched AISI 1035 specimens during a static tensile test.

Table 6.1: Thermoelastic constant for the static tensile tests.

Test	S-120-02	S-120-04	S-120-05
K_m [Pa^{-1}]	9.06×10^{-12}	2.28×10^{-12}	9.00×10^{-12}

As regard the experimental thermoelastic constant K_m, it has been evaluated on the three notched geometries. The linear regression of the experimental temperature data vs. the nominal stress up to 100 MPa, where the temperature trend is expected to be perfectly linear, has been performed and the value have been reported in Table 6.1. The thermoelastic constant values for the first and third tests are nearly similar. On the other hand, the second tensile test thermoelastic constant shows a different value compared to the previous two tests.

Discrepancies are also present for the limit stress, indeed the first plasticization in the FE model appear for a nominal stress level of 290 MPa, higher compared to the experimental value of 177 MPa. These differences in the rise of plastic phenomena, as well as of the thermoelastic coefficient may be addressed to the presence of local micro defect within the material near the notch area (i.e. inclusion or machining defects) that may alter the local mechanical behavior and, hence, also the thermal behavior of the material.

6.4. Conclusion

In the present chapter, the fatigue assessment of medium carbon steel AISI 1035 blunt V-notch specimens has been performed adopting several energy based methods: Thermographic Method and Static Thermographic Method.

Experimental fatigue tests have been performed monitoring the specimens surface temperature in order to estimate in a rapid way the fatigue limit of the material by means of the TM. Static tensile tests have been performed adopting several stress rate to assure adiabatic test condition, in order to evaluate the first deviation from the thermoelastic trend of the temperature signal. Elasto-plastic numerical simulations have been performed in order to predict the specimen thermal behavior under static tensile test and compare it to the experimental temperature trend, showing how the local defect on the notch area can severally affect the fatigue strength of the material.

The energy based methods can be adopted in order to estimate and predict in a rapid way the fatigue life of notched mechanical components.

7. HIGH STRENGTH CONCRETE

Cucinotta F, D'Aveni A, Risitano A, Risitano G, Santonocito D. Thermal emission analysis to predict damage in specimens of high strength concrete. Under submission.

Highlights

In this paper thermal analysis was applied to determine the "Critical Stress" of concrete, different from its ultimate strength, able to produce the first damage in the structures under compressive loads. The Critical Stress can be thought as the stress able to produce the beginning of fatigue rupture within the material.

Several specimens of high strength concrete were tested in order to define the incipient crack phenomena also in internal part of the specimen, not accessible by direct inspections, with the aid of infrared thermography. A finite element analysis completes the study and compares, for the same static loading conditions, the stress state with the experimental thermographic images.

The final results show as the coupling of normal compressive test and the acquisition of the thermal images can be an useful aid to estimate a security stress value, indeed the Critical Stress, before the Ultimate Serviceability Limit (SLU) of the structure, defined as the maximum load condition before its failure.

Nomenclature

b	Burges vector (depending on the characteristics of the material)
B	$= Mb\rho_m v^*/S$
c_v	Specific heat at constant volume [J/kg.K]
E	Tangent modulus of elasticity [MPa]
f_{ck}	Cylindrical compressive strength of concrete at 28 days [MPa]
R_c	Cubic compressive strength of concrete at 28 days [MPa]
K_m	Thermoelastic coefficient [Pa^{-1}]
M	Plastic modulus [MPa]

S	Cross section area of the specimen [mm^2]
SD	Standard Deviation
t	Time test [s]
T_0	Specimen temperature [K]
T_{exp}	Absolute experimental temperature of the specimen surface [K]
ΔT	Absolute temperature variation [K]
ΔT_s	Surface temperature variation of the specimen under static tensile test [K]
w	Amplitude of the micro fracture [mm]
v^*	Speed of sound in the material [m/s]
γ	Gruneisen parameter
ν	Poisson ratio
ρ_m	Mobile dislocation density [kg/m^3]
σ	Normal stress [MPa]
$\sigma_{eqv\ FEM}$	von Mises equivalent stress from FEM [MPa]
σ_L, σ_{cL}	Critical Stress, concrete Critical Stress [MPa]
σ_m	Average stress in the cross-section (load/area) [MPa]
σ_y	Yield strength of material [MPa]
χ	Thermal diffusivity [m^2/s]

7.1. Introduction

Several bridges and civil structures disasters, like Genova Morandi's viaduct, alert that the cyclical creep may have been an additional cause of the catastrophic collapse of these structures.

Fatigue phenomena on civil structures, subjected to dynamic loads over time (atmospheric phenomena, alternate loads and vibrations induced by vehicular traffic) lead to dangerous cracking, limiting the life of the structures. Indeed, during the design phase it is necessary to know not only the breaking limit of the concrete, but also the value of the "Critical Stress", lower than ultimate stress, for which irreversible cracking phenomena begins.

It is also known that the fatigue characterization of the concrete and of the pre-compressed concrete is not easy to perform due to the cost over time and to the necessary equipment for significant fatigue tests.

In the last thirty years, many studies have shown that the temperature variation of a mechanical component under stress is a good parameter for estimate the energetic release, hence the residual fatigue life of the material [19,20,86]. Different papers showed as the thermal analysis applied to steel specimens [3,69,142], to composite specimens [126,127,132], to welding joints [53] permit to estimate the fatigue limit of the materials in easy and rapid way.

Indeed, according to the thermo-elastic theory, under adiabatic conditions, there is a direct link between the applied stress and the temperature of the material.

In monoaxial tests, it is possible to define three phases of the temperature variation on the specimen surface in relation to the applied stress (section 2.4, Figure 2.4):

- a first phase where there is a linear correspondence between the applied load and temperature;
- a second phase where it is possible to observe the loss of linearity with a change of the slope in the temperature-stress (or deformation) curve;
- a third phase in which there is a sudden increase in temperature up to the specimen breakage.

The transition from the first to the second phase gives information about Critical Stress: this stress, if applied in a cyclical way, will lead to failure. The concrete life is affected by different factors, such as geometric ones, temperature variations, environmental and atmospheric effects and vibration phenomena. Therefore, as for aeronautical structures, it is necessary to define more accurate and programmed controls for some specific components during the design phase. The Italian technical construction code (NTC 2018) [145] defines the Ultimate Serviceability Limit (SLU) as the overload and breakage condition for a structure, even for fatigue damage. The same code defines the Serviceability Limit State (SLS) as the concrete limit stress state which produces crack, excessive deformation and fatigue damage that may locally affect the structural integrity. No information is given about the concrete strength under cyclic loads, except for bridges.

In the present chapter, a procedure to estimate the Critical Stress of the concrete in laboratories is proposed. Although it is lower than the ultimate stress, it must be taken into consideration during the design phase.

Furthermore, finite element analyses (FEA) were performed to qualitatively compare the stress maps (numerical) with the related surface temperature maps (experimental). Finally, a careful image analysis procedure has been carried out with the Matlab® software.

7.2. Materials and Methods

The 14 specimens were concrete cube of 15 cm side; the mix design per cubic meter is:

- inert for 1820 daN (4-16 size for 25%, 0-4 size for 65%, 0-2 size for 10%);
- cement CEM I 52.5 R for 410 daN; water for 172 litres;
- additive MAPEI "Dynamon NSG 1022" for 3.5 litres;
- density of the concrete 2404 kg / m^3;
- class of consistency S4 with slamp tests 210 cm.

The tests were made with the CONTROLS C7600 machine with full scale of 5.000 kN. The applied uniaxial compression stress rate was 1 MPa/s. The tests were carried out in load control at constant speed (N/s). The thermal images were acquired by FLIR SC300 IR.

Figure 7.1 shows a concrete specimen loaded at left side and thermal image of the specimen surface at the beginning of the test at right side. In the image at right side the analysed zones (square) and the reference temperature of the tests (image zero) are indicated. The maximum value of temperature within the five detection areas was recorded during the execution of the tests with an acquisition frequency of 10 Hz.

In order to correlate the thermal images with the stress map of the specimen, a static finite element analysis was conducted using Ansys® APDL. A cubic concrete specimen (Figure 7.2a) with the same geometry of the ones adopted for experimental tests was modelled. As in the experimental tests, the specimen was bonded with two rigid plates and the uniaxial load was applied on it through the rigid top plate.

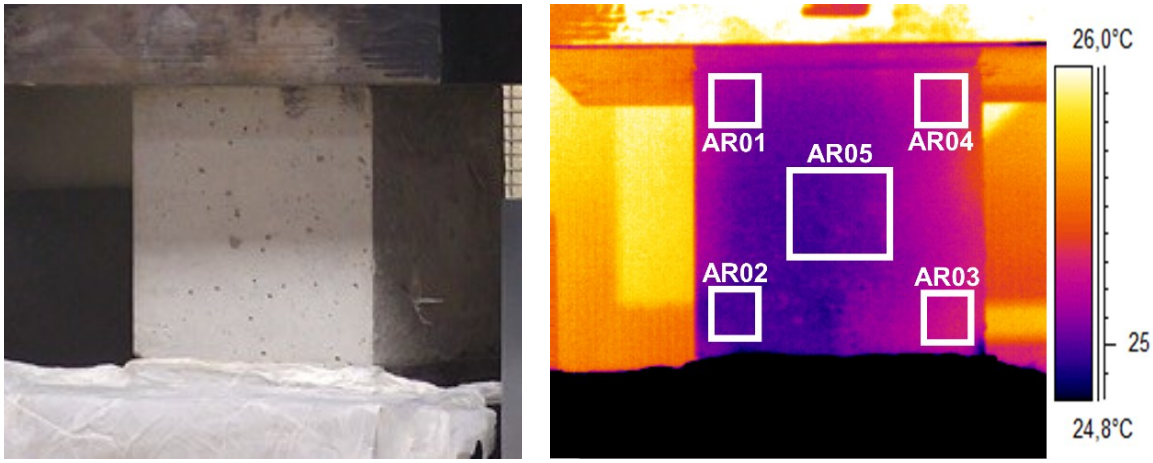

(a) (b)

Figure 7.1: a) adopted specimen; b) Thermal image of one face at the beginning of the test with the analysed areas (square)

The concrete specimen was modelled with hexa SOLID186 element type and the material characteristics of high strength concrete (E= 30 GPa, ν= 0,2) with linear elastic behavior were used. The contact zones between the plates of the test machine and the specimen were modelled as a surface-to-surface contact using CONTA174 elements for the specimen surfaces and TARGE170 for the rigid plates. In the FE analysis a "rough" contact model was taken into account since, as observed by Dai and Lam [146] on compressive tests of short concrete-filled elliptical steel columns, a large friction model between the plates and the surface of the specimen seems to adequately predict the contact behavior in tangential direction.

The rigid top plate was loaded at its pilot node and was fixed in all its d.o.f. except in the vertical displacement direction, while the bottom rigid plate was totally fixed (all the six d.o.f. are blocked) through its pilot node.

A convergence analysis (Figure 7.2b) on the vertical displacement of the central node of the specimen was conducted with different lengths of the finite elements, ranging from 5 mm to 25 mm. In order to obtain a better resolution of the stress field on the external specimen surface, 31.114 finite elements of 5 mm size were chosen for an appropriate comparison with the thermal images.

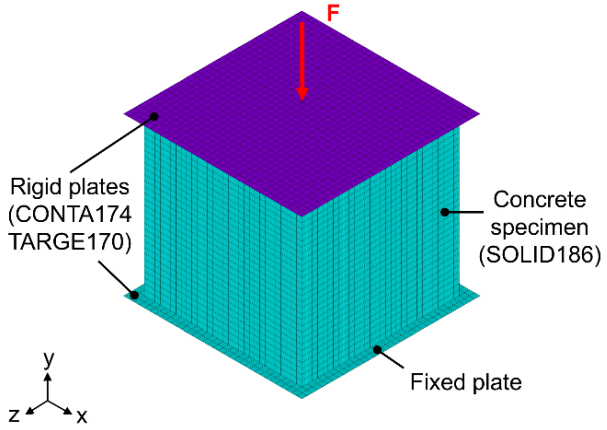

(a)

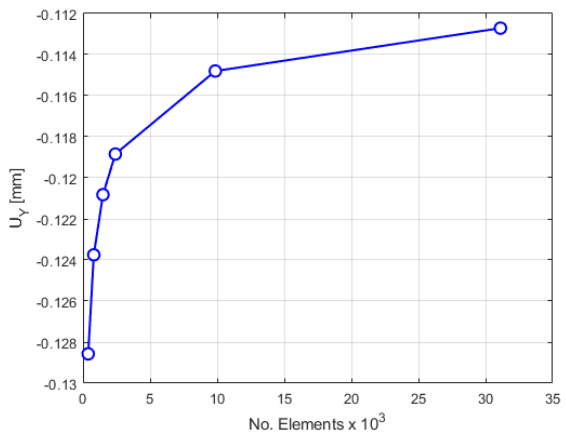

(b)

Figure 7.2: a) Finite element model of the cubic concrete specimen and b) convergence analysis on the vertical displacement of the specimen central node.

For a better presentation of the results, the image analysis of the acquired thermal maps has been carried out, adopting a procedure developed in Matlab®, as follows:

- Subtraction of the ambient temperature in order to emphasize the difference in temperature of the sample surface. The ambient temperature was detected as the average temperature inside a rectangular area outside the sample but with the same reflectivity.
- Noise reduction by Gaussian filter with SD= 8. The Gaussian filter replaces the value of each pixel with the weighted average value of the contiguous pixels. In this way the thermal map is smoother and less influenced by noise and anisotropies.
- Displaying by means of isotherm contours. The contours highlight better the different thermal areas and help to better understand the behavior of the specimen.

In Figure 7.3, an example of image analysis of the specimen surface temperature has been reported for a determined load condition.

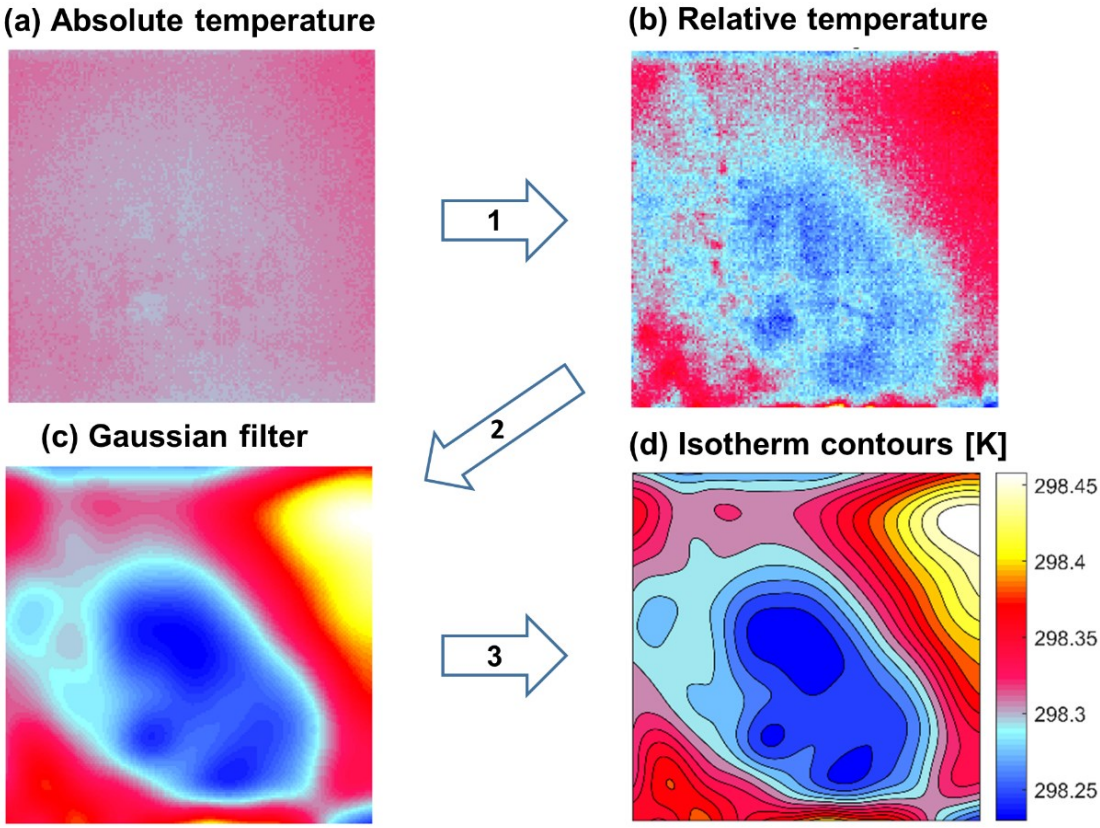

Figure 7.3: Thermal image processing steps: a) absolute temperature detected by IR camera; b) the ambient temperature is subtracted; c) noise reduction by means of a Gaussian filter (SD=8); d) the isotherm contours are plotted.

It is evident how the image processing allows to clearly improve the ability to distinguish the colder areas from the warmer ones. Furthermore, the 3D surface mapping help to clearly render the heat distribution on the external surface of the specimen, as in Figure 7.4Figure 7.5. The 3D surface of the equivalent stress on the external surface of the sample, as predicted by the FEA, is reported in Figure 7.. It shows the expected hourglass shape.

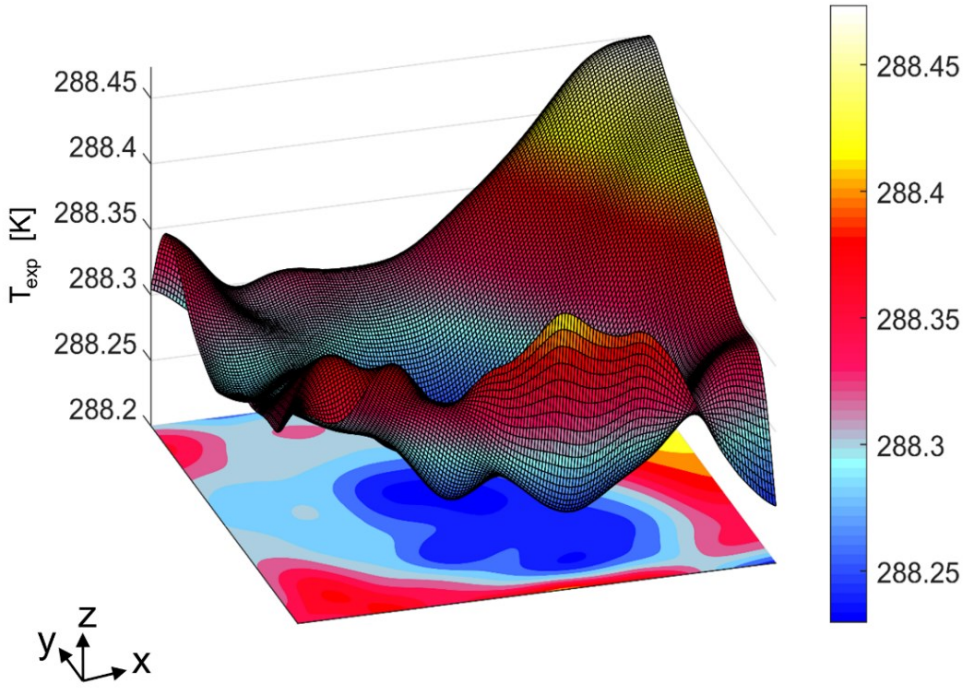

Figure 7.4: 3D rendering of the experimental thermal map on the specimen surface.

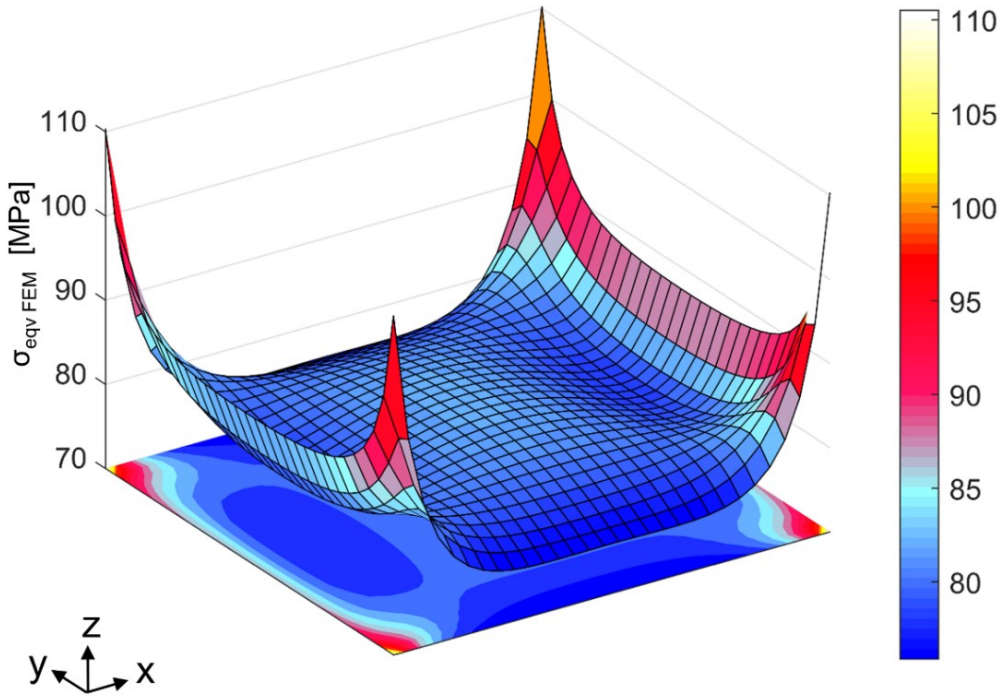

Figure 7.5: 3D rendering of the Equivalent stresses estimated by FEM on the specimen surface.

7.3. Results and analysis

A thermal analysis on concrete specimens during classic compressive static test was performed. The temperature vs. time vs. stress diagrams shown:

- A linear trend typical of the thermoelastic phase. At this stage, there are no microcracks and, therefore, the second term of equation (2.66) is not relevant.
- A second phase in which the points are well interpolated by means of a second straight line with a different slope.

The intersection of the two lines defines the Critical Stress; where micro-faults begin to appear in the internal structure of the concrete sample. In fact, the heat is released by plastic deformations. In the analytical model, the contribution of the second term of equation (2.66) increases more and more due to the effect of the applied compressive mean stress (σ_m) with a clearly visible temperature variation that continues until the specimen fails.

Figures 9.6-9 show the temperature recorded in characteristic points of the specimen surface during the loading phase.

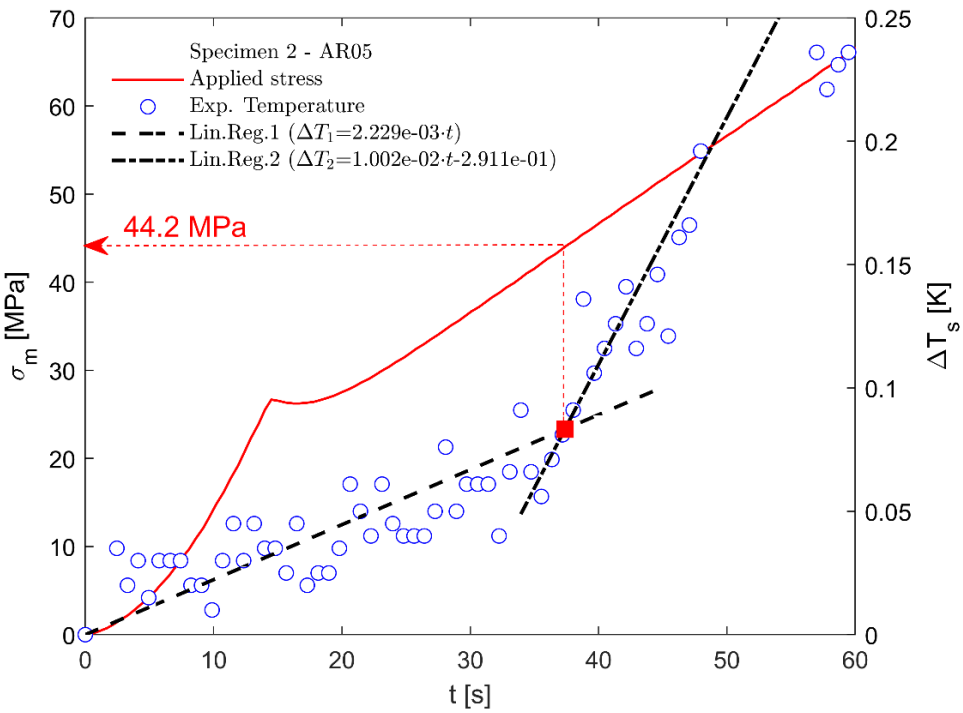

Figure 7.6: ΔT vs time curve (blue points) and stress vs time curve (red line) for area AR05 of Specimen 2.

In Figure 7.6, related to second tested specimen, the temperature data for the center (AR05, area no. 5 of Figure 7.1b) of specimen surface is reported. The intersection of the two straight lines (in black) define the Critical Stress for the concrete σ_{cL} at 44.2 MPa.

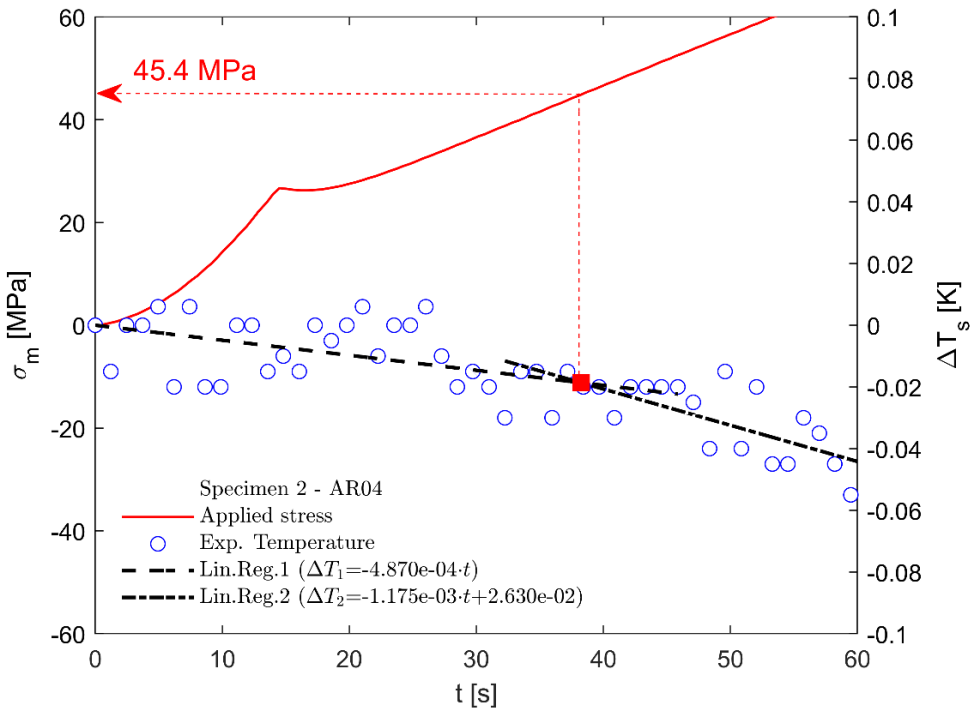

Figure 7.7: ΔT vs time curve (blue points) and stress vs time curve (red line) for area AR04 of Specimen 2.

In Figure 7.7, the data for the area located in the upper right corner (AR04, area no. 4 of the specimen of Figure 7.1) are reported. The corner area AR04 shows a different trend compared to the central area AR05 for the same concrete specimen; in fact, the temperature drops continuously. For area AR04, the change in slope is much less noticeable than in area AR05.

These behaviors are perfectly congruent with the stresses in the two examined areas: compressive stress for the central area AR05 and tensile stress for the upper right corner area AR04. The next two figures (Figure 7.8 and Figure 7.9) are related to a different area of the test performed on specimen no. 11. Also in this case, the previously seen phenomena are shown again.

It can be summarized that in all tests, a temperature trend similar to the one already described was observed. In particular, the temperate trend of area AR05 was used to determine the Critical Stress on the stress-time diagram.

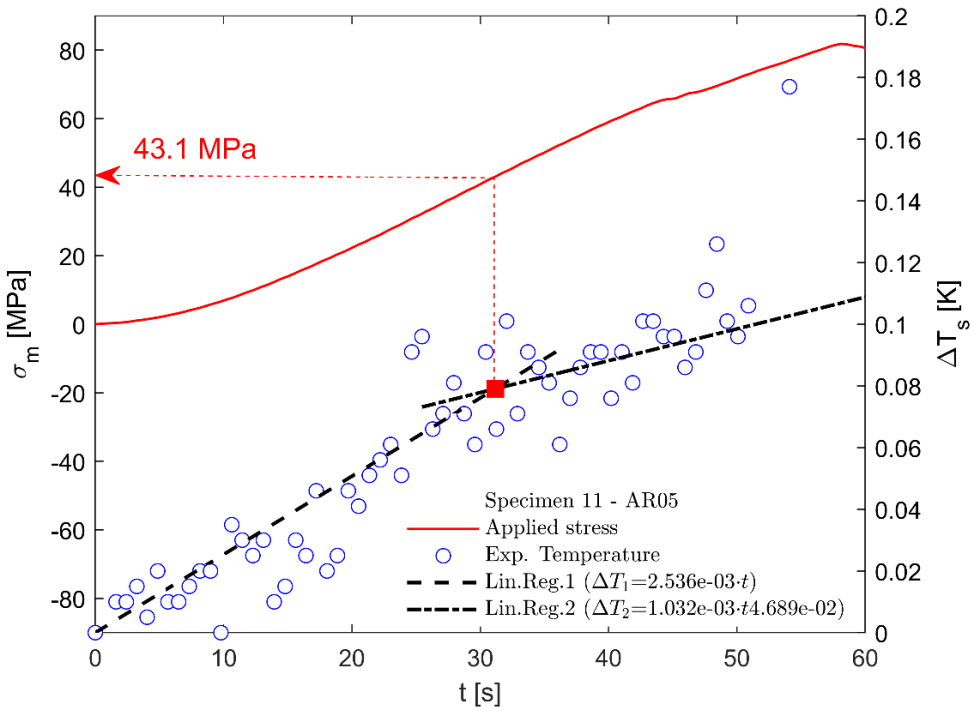

Figure 7.8: ΔT vs time curve (blue points) and stress vs time curve (red line) for area AR05 of Specimen 11.

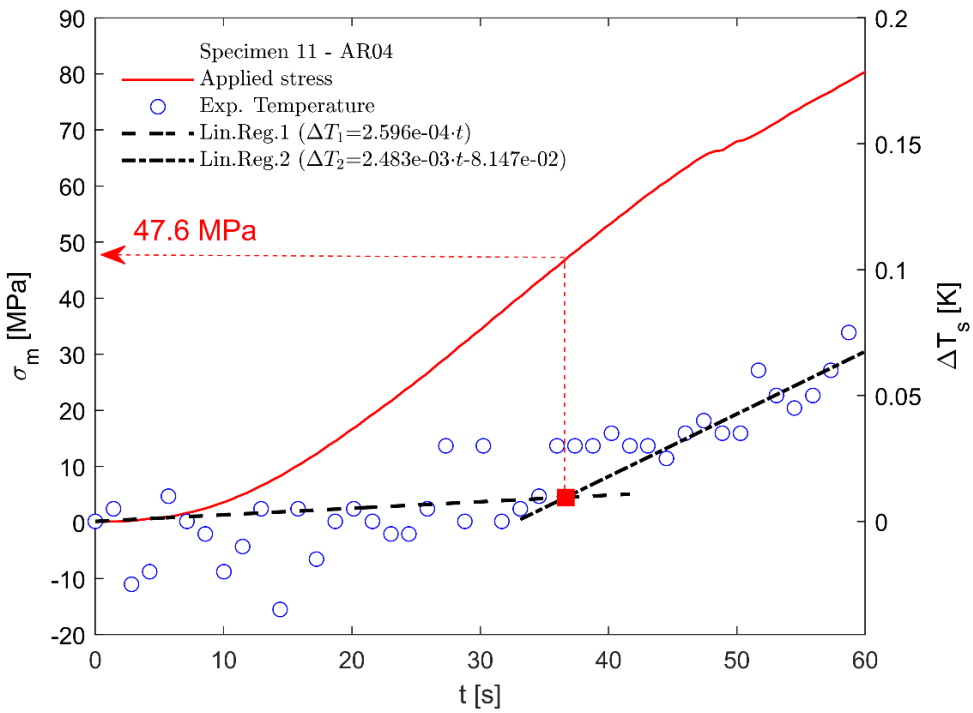

Figure 7.9: ΔT vs time curve (blue points) and stress vs time curve (red line) for area AR04 of Specimen 11.

Figure 7.10 shows a comparison of the picture taken after the breakage (a), the original IR image (b) and the processed IR image (c) recorded immediately before the breakage of the specimen no. 14. It is possible to observe the distribution of temperatures, linked to the stresses. In the centre of the specimen it is completely different from the four corner areas (AR01-04). This is due to the plate of the testing machine that activate a distorted tensional state. The value of the critical load at the corner, related to the intersections point of two temperature interpolating straight lines, is about 1000 kN, despite the plate effect on the corner areas. This value is practically comparable with the one recorded on the central area AR05.

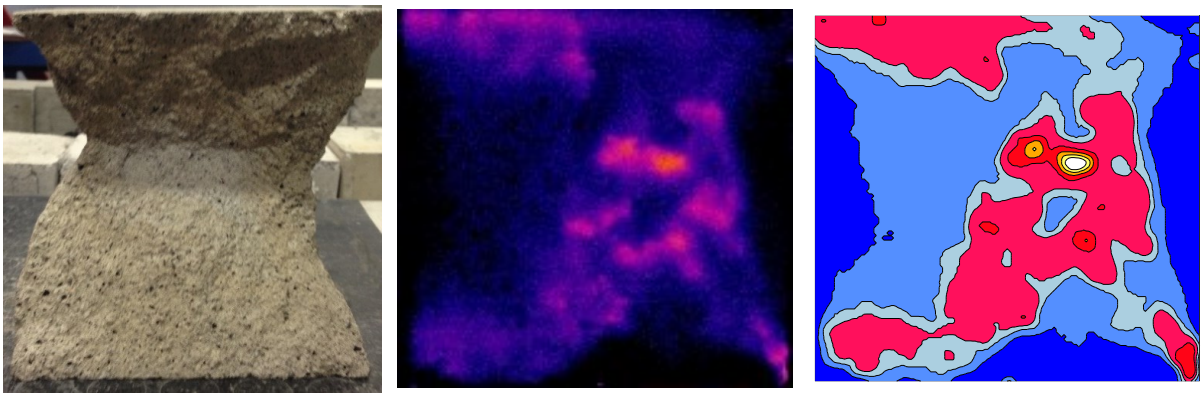

(a) (b) (c)

Figure 7.10: a) picture after the breakage of the specimen; b) original IR image and c) processed IR image before of the breakage.

The temperature variation of the central area AR05 of all samples was examined to determine the Critical Stress (σ_{cL}) and reported in Table 7.1. The first column shows the number of the specimen, the second column shows the value of the cubic compressive strength of concrete at 28 days R_c [MPa] of the specimen, the third column reports the Critical Stress σ_{cL} [MPa] referring to the central area and to the up right corner area. In the fourth column is reported their ratio $r = \sigma_{cL}/R_c$. both for the central area and the up right corner area.

Table 7.1: cubic strength Rc and Critical Stress σ_{cL} of the concrete.

Specimen no.	Strength R_c [MPa]	Concrete Critical Stress σ_{cL} [MPa]		$r= \sigma_{cL}/ R_c$	
		at the Center	at the Corner	at the Center	at the Corner
1	82	45	43	0.55	0.52
2	77	54	46	0.70	0.60
3	88	68	58	0.77	0.66
4	79	51	46	0.64	0.58
5	84	47	53	0.55	0.63
6	79	47	44	0.59	0.56
7	84	43	44	0.51	0.53
8	73	52	53	0.72	0.73
9	101	60	38	0.60	0.38
10	80	51	53	0.64	0.67
11	89	49	36	0.55	0.40
12	84	47	42	0.55	0.50
13	82	31	40	0.38	0.49
14	82	53	42	0.65	0.51
Average	83.3	49.8	45.7	0.60	0.554
Standard Deviation (SD)	6.51	8.42	6.56	0.0982	0.0996
Characteristic value $R_{ck}=(R_{cm}-1,64xSD)$	72.62	35.99	34.94		

In summary, the thermoelastic effect (first phase) of concrete is perfectly visible and the cubic Critical Stress can be determined from the ΔT vs time curves ($\sigma_{cL}\approx$ 36 MPa). This cubic Critical Stress is slightly less than the Italian code compressive stress limit ($\sigma_{c,max}$= 0.60xR_{ck}= 43,57 MPa) at the limit state serviceability (SLS) for the load characteristic combination (Italian code NTC 2018 - paragraph 4.1.2.2.5.1). This small difference in values suggests to investigate the effects of cyclical loads (wind effect for instance) also on the durability of civil structures.

In order to correlate the thermal images with the internal stress of the cubic concrete specimen, a finite element analysis was conducted with a load equal to the previously found critical load of about 1000 kN. The equivalent Von Mises stresses on the external surface of the cubic specimen,

calculated by the FE analysis (on right) and compared with the thermal map (on left), is reported in Figure 7.11. The values of the stress agree with the ones found experimentally and reported in Figure 7.11b (about 50 MPa, central area), therefore the finite element model is well calibrated.

In both the images reported in Figure 7.11 it is possible to highlight: the corner area (1) in which there are both the maximum of temperature and stress; the central area (2) in which there are the relative minimum values of the temperature and the relative maximum of the equivalent stress; the lateral area (3) in which there are the relative maximum of temperature and the relative minimum of stress; the contact area with the plates (4) in which there is the negative peak of temperature, due to the heat dissipation caused by the steel plates and the local contact stresses.

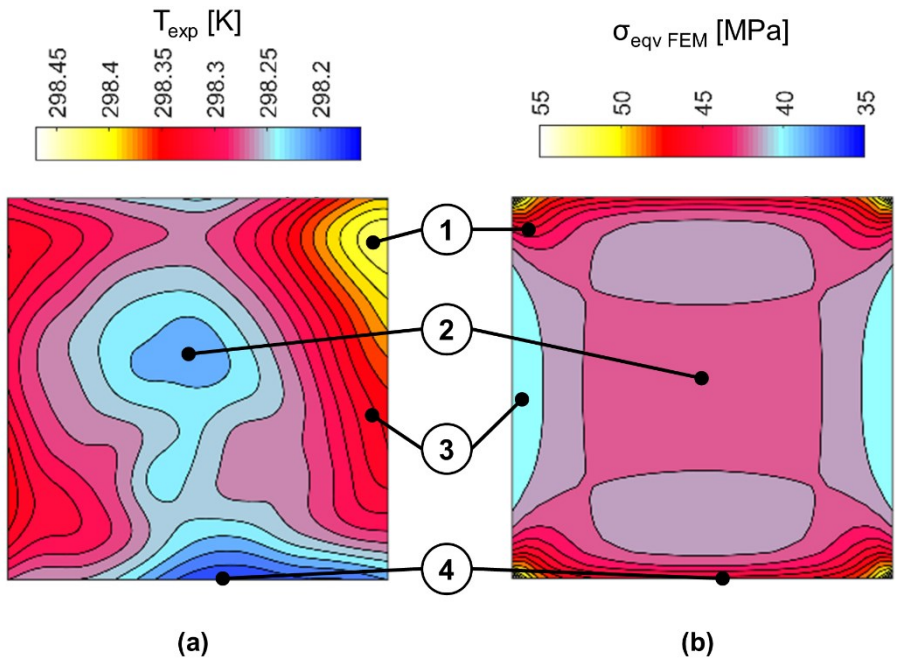

Figure 7.11: a) Thermal map and b) FEM Equivalent von Mises Stress for the critical load (1000 kN).

Basically, the two colormaps have a roughly mirrored behaviour. This is due to the fact that where there is an increase of the stresses, due to an expansion of the material, there is a consequent lowering of the temperature. This behaviour is more evident on a median horizontal section, in which the curve temperature and the correspondent equivalent stress curve appear almost reflected (Figure 7.12).

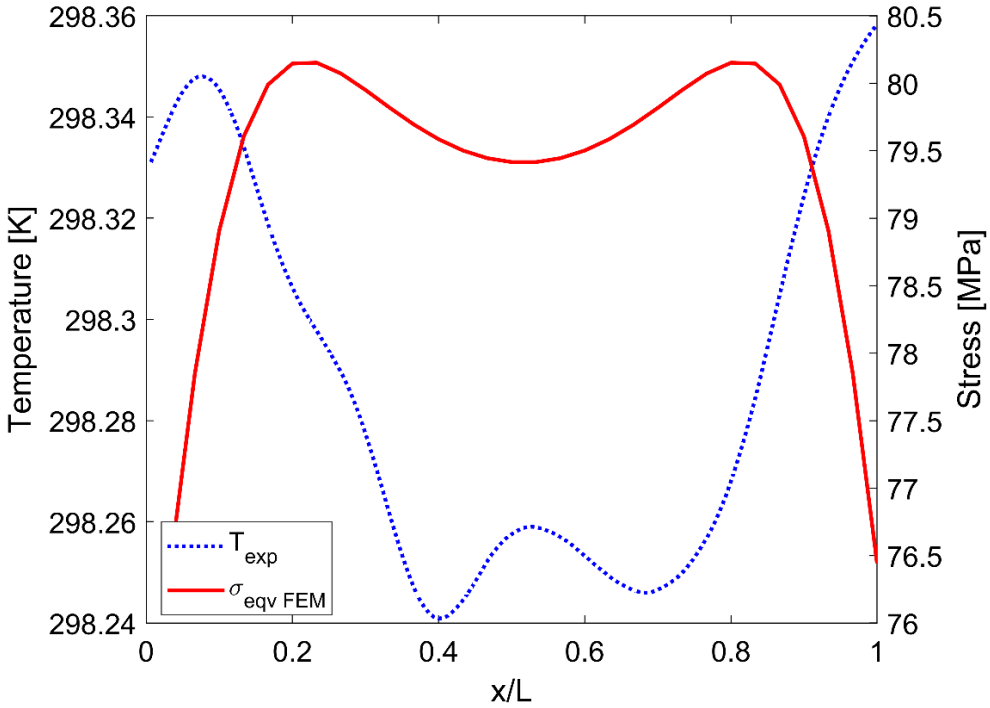

Figure 7.12: Experimental temperature and FEM equivalent von Mises stress curves on a median horizontal section of the specimen.

The examination of the thermal images of all the specimens shows the possibility to identify the lines and the areas in which the concrete material shall begin to fail locally.

In Figure 7.13, the stress distributions of four different load levels (500, 1000, 1500 and 1900 kN) calculated by FEM are compared with the experimental IR images of a specimen at the same load levels. The colormaps of temperature and the equivalent stress at the four different load conditions are reported using the same colorbar. The load equal to 1900 kN corresponds to the failure start. In all the maps it is possible to observe the expected hourglass shape, due to the freedom of expansion of the lateral specimen surfaces and to the constraints of the plates of the machine.

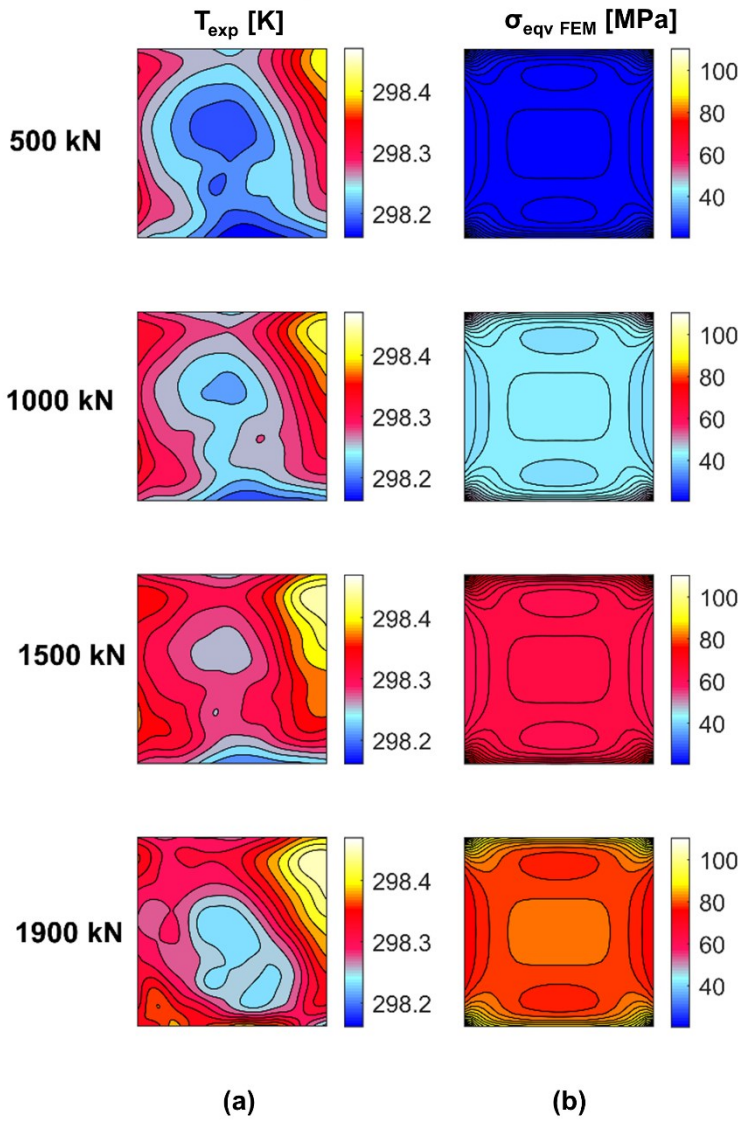

Figure 7.13: Comparison between a) experimental thermal and b) equivalent stress distribution on the specimen.

For loads much lower than the ultimate load of the material (500 and 1000 kN), it is difficult to identify the possible failure area, while the temperature line become more marked close to the ultimate load. The temperature gives indications about the possible beginning of cracking within the concrete specimen as is well shown for 1500 and 1900 kN loads. In particular, for loads close to the concrete ultimate load it is easy to identify the path along which the specimen should break. The stress maps reported in Figure 7.11 and Figure 7.13 show the usually hourglass shape, as it was observed in the concrete specimens after the breakage (Figure 7.10a).

7.4. Conclusion

In order to identify the Critical Stress value σ_{cL} , coinciding with the first local plasticization (not visible to human eye), a test campaign was performed on 14 samples of high strength concrete under classic uniaxial static compression tests using the thermographic technique.

The examination of the heat maps developed for four different load levels and of the related stress maps obtained through FEM confirms the validity of the proposed procedure. According to an experimental protocol, already adopted for other materials by Risitano et al. [3,69], the Critical Stress σ_{cL} (load/area of the cross section) can be defined.

The results of the research shown:

- The thermal analysis permits to identify the stress that produces the first local cracking in the specimen. Load different and lower (50% -70%) from the breaking load R_{ck}.
- The loss of linearity in the temperature - stress (strain) diagram, permits to associate the Critical Stress of concrete to the stress value that defines the beginning of fatigue phenomena.

On the basis of the results, it is possible to state also:

- The Italian code NTC 2018 (paragraph 4.1.2.2.5.1) for concrete, which identifies for the Serviceability State Limit (SLS) the limit compressive stress $\sigma_c \leq (0.45 \text{ to } 0.60)\ f_{ck}$, seems to be adequate.
- The procedure adopted permits, by means of static uniaxial compression test, to define in a more accurate way the allowable stress in the legal field (0.45 to 0.60 f_{ck}).
- A suitable protocol test may be adopted, both in the testing stage and in the working stage, as non-destructive method to determine the Critical Stress of the concrete specimen or structure components.

The proposed method can be very useful in the pre-project phase in which the designer, with easy compression tests, can know the value of the allowable compressive stresses for the load combination at serviceability state limit (SLS).

8. HIGH-DENSITY POLYETHYLENE

Risitano G, Guglielmino E, Santonocito D. Energetic approach for the fatigue assessment of PE100. Procedia Struct Integr 2020;26:306–12. doi:10.1016/j.prostr.2020.06.039.

Risitano G, Guglielmino E, Santonocito D. Evaluation of mechanical properties of polyethylene for pipes by energy approach during tensile and fatigue tests. Procedia Struct. Integr., vol. 13, Elsevier B.V.; 2018, p. 1663–9. doi:10.1016/j.prostr.2018.12.348.

Highlights

Since its introduction in pipe applications more than 40 years ago, polyethylene (PE) has been taking a growing place in gas and water distribution due to its low cost, lightness and good corrosion resistance. Besides, long-term properties have been steadily rising due to the development of novel PE-based materials. The present highest standard is the PE100 class.

Several laboratory tests are used to extract design data for long-term failure-type prediction based on stress and time to failure relationship. It remains difficult to assess the relation between creep and fatigue loadings on the one side. On the other side, the manufacturing process of the test specimens influences considerably the obtained performance for viscoelastic materials subjected to working conditions.

In present chapter, the mechanical properties of high-density polyethylene (HDPE), PE 100 class, for pipes were investigated using experimental techniques. Thermographic technique was used during the static tests in order to identify the maximum stress zone and also during the fatigue tests to study the temperature evolution of the specimen. The aim of this study is the application of the Thermographic Methods for the fatigue assessment of PE100.

The author would like to thanks Plastitalia S.p.a for the support on this research activity.

Nomenclature

c	specific heat capacity at costant pressure [kJ/(kg.K)]
f	frequency [Hz]
K_m	thermoelastic coefficient [MPa-1]
N	number of cycles
N_f	number of cycle to failure

R	stress ratio
T	surface temperature [K]
T_0	initial temperature [K]
α	thermal linear expansion coefficient [K-1]
ε	strain
ρ	density [kg/m^3]
σ	stress [MPa]
σ_1	uniaxial stress [MPa]
σ_{max}	maximum stress during fatigue test [MPa]
ΔT	temperature increment during static test [K]
ΔT_d	temperature increment during fatigue test [K]
ΔT_{stab}	stabilization temperature during TM test [K]
ΔT_1	estimated value of temperature for the first set of temperature data [K]
ΔT_2	estimated value of temperature for the second set of temperature data [K]

8.1. Introduction

Since its introduction in pipe applications more than 40 years ago, polyethylene (PE) has been taking a growing place in gas and water distribution due to its low cost, lightness and good corrosion resistance. Besides, long-term properties have been steadily rising due to the development of new PE based materials. Lifetime prediction of polymeric materials has been the subject of numerous studies[147–150]. The present highest standard is PE 100 class (ISO 12162), high-density polyethylene (HDPE), which means that pipes made from such materials should withstand a hoop stress of 10 MPa for 50 years at room temperature including a 1.25 safety factor.

The use of HDPE in applications requiring a long service lifetime such as for pressurized pipes for water and gas, has dramatically increased in the last years. For the new generation of pipe materials, a lifetime as long as 100 years is expected under normal operation conditions. To ensure proper performance over such a long time, precisely predicting the behavior of the HDPE pipes under the respective storage conditions is very important. Such information is usually

acquired using accelerated laboratory aging procedures, one of which is the hydrostatic pressure test, the most frequently and widely used method. Accelerated stress cracking test are also commonly performed in surfactant environment in order to reduce test time, but transposition of the results for predicting life time of pipes in natural conditions is not straightforward.

Deveci et al. in [151] discussed correlations of molecular weight, molecular weight distribution, short chain branching and rheological properties of different polyethylene materials with their slow crack growth resistances obtained from the strain hardening and crack round bar tests and their correlations with notched pipe tests.

In [152], an experimental analysis for determining the fatigue strength of HDPE-100 under cyclic loading is presented. The curve of cumulative fatigue damage versus number of cycles (D-N) was deduced from stiffness degradation. Based on the three stage damage trend, the remaining fatigue life is numerically predicted by considering a double term power damage accumulation model. This model is found to be accurate, both in modeling the rapid damage growth in the early life and near the end of the fatigue life. Numerical results illustrate that the proposed model is capable of accurately fitting several different sets of experimental data.

The traditional methods of fatigue assessment of metallic and composite materials are extremely time consuming. In order to overcome the above-mentioned problems, an innovative approach for fatigue assessment of materials and structures has been proposed by La Rosa and Risitano [2]: the Thermographic Method (TM). The Thermographic Method, based on thermographic analyses, allows the rapid determination of the fatigue limit. A review of the scientific results in literature, related to the application of the thermographic techniques to composite materials have been presented by Vergani et al. [134].

An innovative approach to determinate the fatigue limit during tensile static test has been proposed by Clienti et al. [86] for plastic material and by Risitano and Risitano [3] for metallic material. In [86], authors suggest that during quasi-static tensile tests the area, where first irreversible plasticization occurred, is detectable by the analysis of the T vs σ curve considering the temperature change of the curve slope. This variation identifies the transition zone between thermoelastic and thermoplastic behaviour, or in other words, the beginning of irreversible micro-plasticization. The authors have suggested that in that transition zone, there is the damage limit of material. This damage limit must be understood as the macroscopic stress value that would cause the material to break if subjected to cyclic loading at any load ratio. Then, it is very

close to the traditional fatigue limit. This approach, called Static Thermographic Method (STM), correlated the first deviation from linearity of the temperature surface of the material during tensile test to the fatigue limit. This was observed for basalt fibre reinforced composites by Colombo et al. [126] and glass fiber reinforced composites by Crupi et al. [54,132].

This chapter investigates static and fatigue behavior for a high-density polyethylene (HDPE), PE 100 class. The aim of this study is to apply for the first time both the TM and STM for the fatigue assessment of HDPE comparing the results with the results obtained by the traditional procedure, obviously taking into account that the polyethylene has different and more complex fatigue mechanisms respect to metallic materials.

8.2. Materials and Methods

The material under study was a high density polyethylene, PE, commercially named PE100. Table 8.1 shows the mechanical properties of the material by producer datasheet. Table 8.2 shows the values elaborated on 10 specimens by authors.

Table 8.1: Mechanical properties of PE 100 by datasheet.

Tensile Stress at Yield σ_y [MPa]	Tensile Modulus E [MPa]	Tensile Strain at break ε_f [%]	Density ρ [kg/m^3]
25	1100	>600%	948
ISO 527-2 (50 mm/min)	ISO 527-2 (1 mm/min)	ISO 527-2	ISO 1872-2/ISO 1183

Table 8.2: Mechanical properties of PE100 elaborated on 10 specimens by the authors.

Tensile Stress at Yield σ_y [MPa]	Tensile Modulus E [MPa]	Density ρ [kg/m^3]
25.9±1.9	861±91	948
ISO 527-2 (50 mm/min)	ISO 527-2 (1 mm/min)	

Dog bone specimens were injection molded (type 1A of the ISO 527-2:1993 standard) (Figure 8.1a). The static tests were carried out using an ITALSIGMA's 25 kN servo-hydraulic load machine at a crosshead rate equal to 5 mm/min with constant temperature and relative humidity (23 °C and 50% RH). The tensile tests were carried out on 10 specimens and for 3 of them the superficial temperature trend was monitored with the infrared camera FLIR A40 (Figure 8.1b).

Eleven specimens, investigated under fatigue loading, have the same geometry of those used for the static tests and are made with the same technological process. For all the fatigue tests, the following parameters were used: stress ratio R= 0.1; test frequency f= 5 Hz.

Fatigue tests were performed at constant temperature and relative humidity (23 °C and 50% RH). As previously mentioned, during all the tests the surface temperature of the specimen was monitored with an IR camera. Two types of tests were performed. One series of fatigue tests (8 specimens) were carried out with a constant stress amplitude until failure. The other series of tests (3 specimens) were carried out with increasing stress step until failure: for two tests, eleven 10.000 cycles loading step from 10 MPa to 20 MPa were used; while for the other test, nine 10.000 cycles loading step from 12 MPa to 20 MPa were used. The specimen fails when it reaches an elongation equal to the elastic limit elongation of the material. This value was obtained considering the maximum stress achieved by the specimens during the previous static tests and it is equal to 6.9 mm.

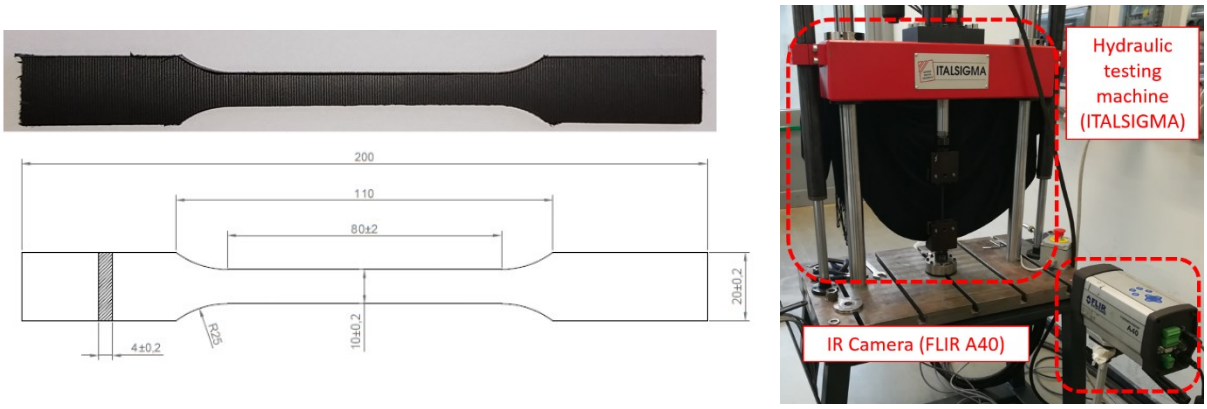

(a) (b)

Figure 8.1: a) Stardard ISO 527-2: 1993 specimen; b) Experimental setup.

8.3. Results and discussions

8.3.1. Static tensile tests

Static traction tests were performed on three PE100 specimens under displacement control, with a crosshead speed of 5 mm/min. The IR camera allows the assessment of the specimen's surface temperature evolution during static tensile tests. The applied stress, evaluated as the ratio between the force and the nominal cross section area of the specimen, is reported versus the superficial temperature variation, estimated as the difference between the instantaneous

temperature and the initial temperature of the surface recorded at time zero ($\Delta T = T_i - T_0$) (Figure 8.2).

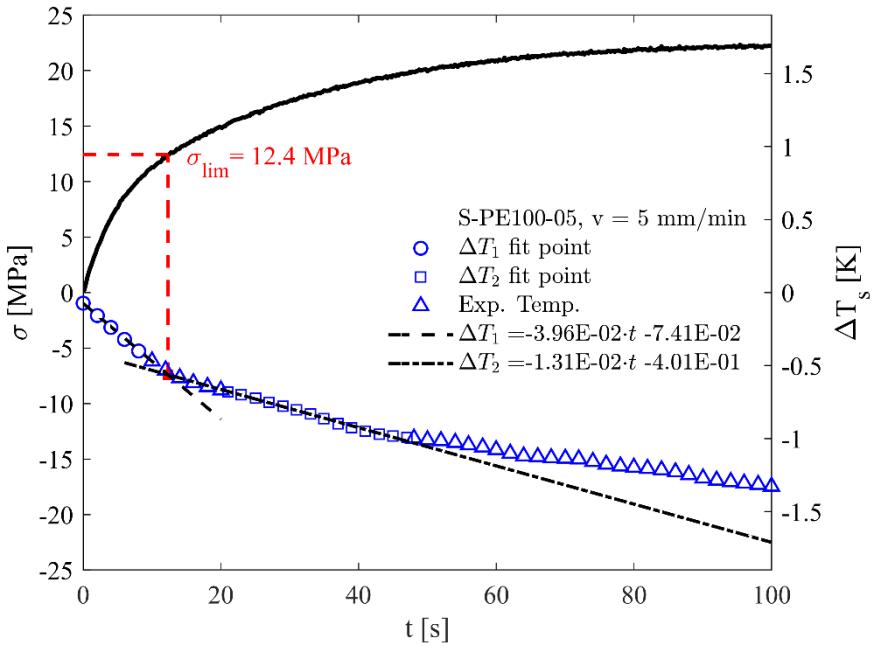

(a)

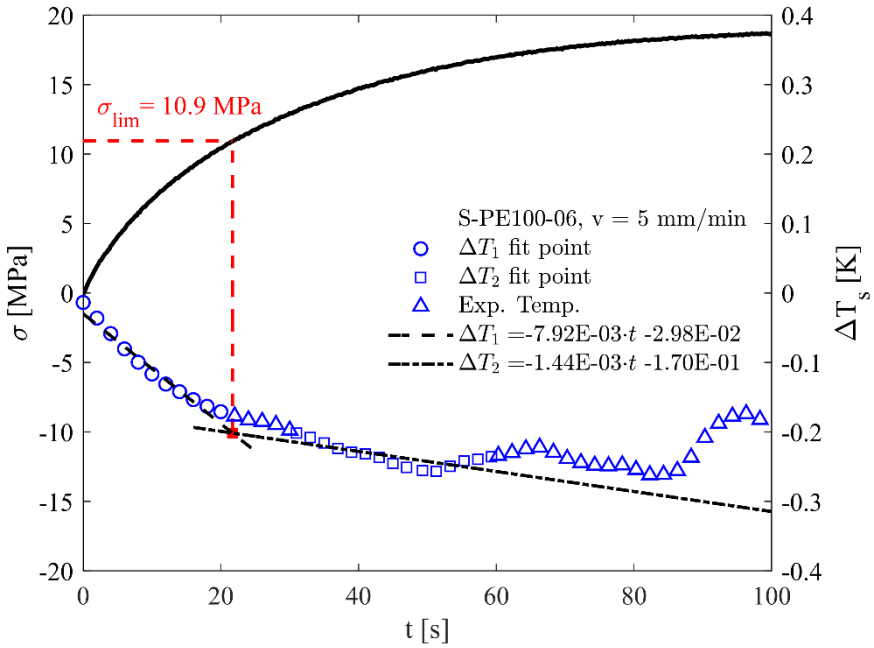

(b)

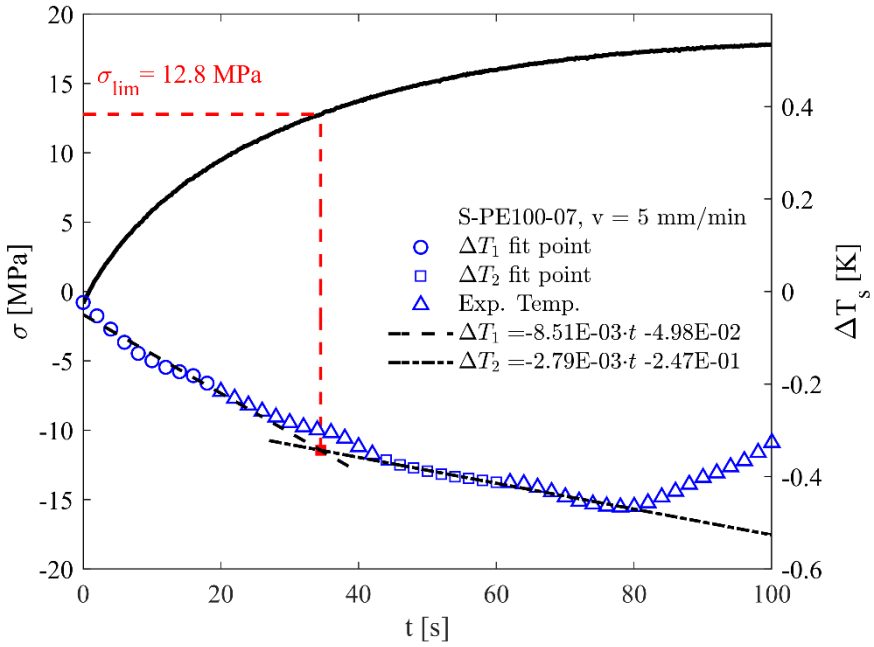

(c)

Figure 8.2: Temperature evolution vs. applied stress during static tensile test on PE100 specimens.

The temperature data has been filtered with a *rlowess* filter, with a data span of 5%, in order to reduce the outliers and highlight the thermoelastic trend. In the initial part of the ΔT-t curve it is possible to clearly distinguish the linear trend of the temperature, then it deviates from the linearity reaching a zero-derivative region, suddenly it experiences a rapid increment. It is possible to make two linear regression lines, the former for the first linear phase (early stage of the temperature signal, ΔT_1 fit point series) and the latter for the second phase (last stage before the sudden increase in the temperature signal, ΔT_2 fit point series). An intermediate set of temperature values between the ΔT_1 and ΔT_2 fit point series has not been taken into account in the evaluation of the two regression lines (Experimental Temperature series). Knowing the regression lines equations, it is possible to determine the intersection point of the two straight lines. The corresponding value of the applied stress, namely limit stress σ_{lim}, has an average value for the three tests of 12.0±1.0 MPa. It could be related to the macroscopic stress that introduces the first irreversible plasticization phenomena in the material.

8.3.2. Fatigue tests

Fatigue tests at constant amplitude values of the stress range were carried out until failure at a stress ratio R= 0.1. The temperature of the specimen surface was detected by an IR camera during each fatigue test. Figure 8.3 shows the typical ΔT vs N curve, during a fatigue test at σ_{max}= 17

MPa, showing the three phases of TM: an initial rapid linear increment (phase I), an another linear increment with lower slope (phase II) and a sudden increase just before the specimen failure (phase III). The three different phases of TM are also evident, for the same specimen, in the thermal image sequence of Figure 8.4.

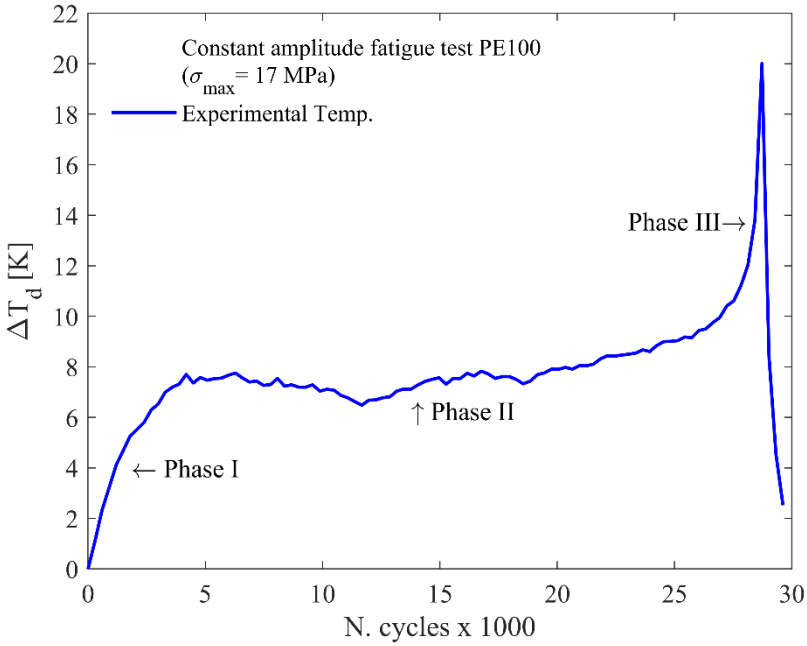

Figure 8.3: Temperature trend during a constant amplitude fatigue test on PE100.

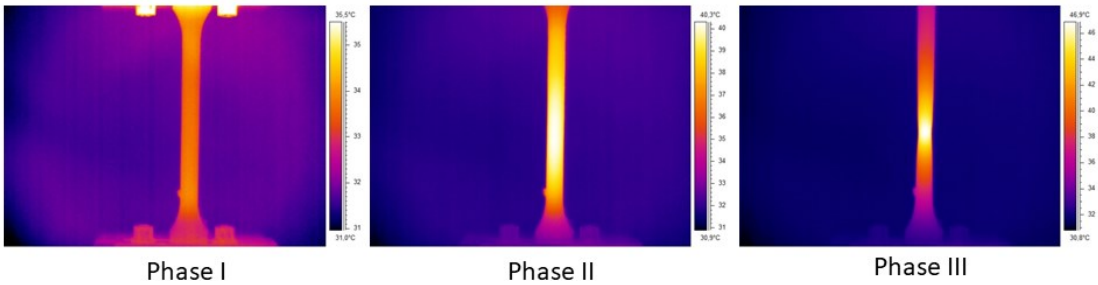

Figure 8.4: Temperature evolution during a constant amplitude fatigue test assessed by infrared camera.

A second series of fatigue test has been performed adopting a stepwise increase of the maximum applied stress from 10 MPa to 18 MPa, with a test frequency of 5 Hz and stress ratio R= 0.1. In Figure 8.5 is reported the typical trend of such a kind of fatigue test. As the stress increases, the superficial temperature detected by the infrared camera increases, then it reaches a stabilization phase. This trend is repeated for each stress level till the specimen failure. Figure 8.6 shows the fatigue limit predicted by the TM using the stabilization temperature applied to all

the eleven fatigue tests (constant amplitude and stepwise). As recommended in [17], two distinct linear regressions have been drawn; the x coordinate of the point in common to the two straight lines is the fatigue limit. It is very interesting to note that the fatigue strength is 11.32 MPa.

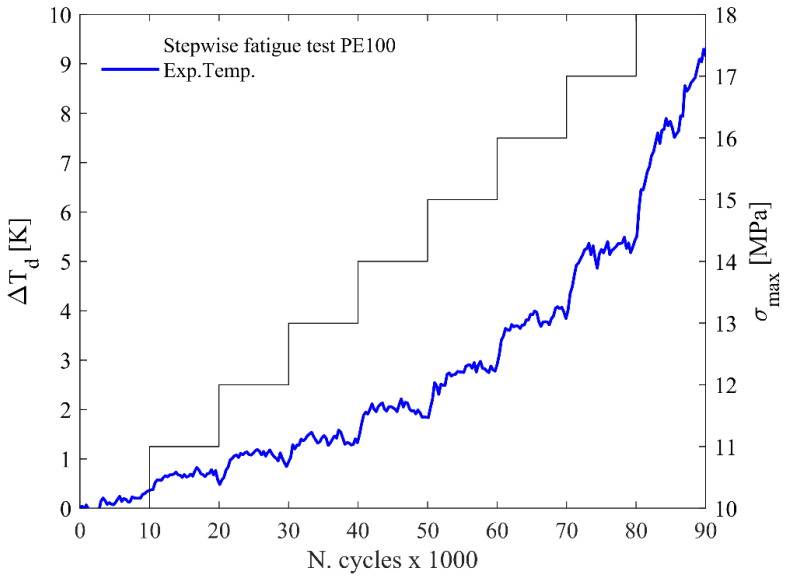

Figure 8.5: Temperature trend during a stepwise fatigue test on PE100.

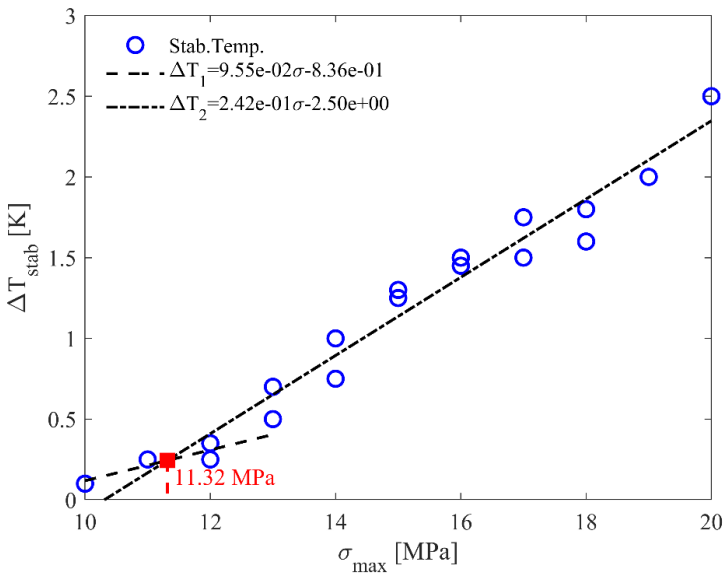

Figure 8.6: Fatigue limit assessed by means of the TM (constant amplitude and stepwise tests).

In Figure 8.7 are reported in a bi-log S-N plot the fatigue strength of the constant amplitude tests. Two tests per stress level have been performed, adopting a number of cycle for run out of N_A= 1x10^6. The set of data shows an inverse slope k= 7.23 and the fatigue limit with a 50%

probability of survival evaluated at N_A is equal to 11.4 MPa. In the same plot is reported the scatter band with one standard deviation for the limit stress assessed by STM.

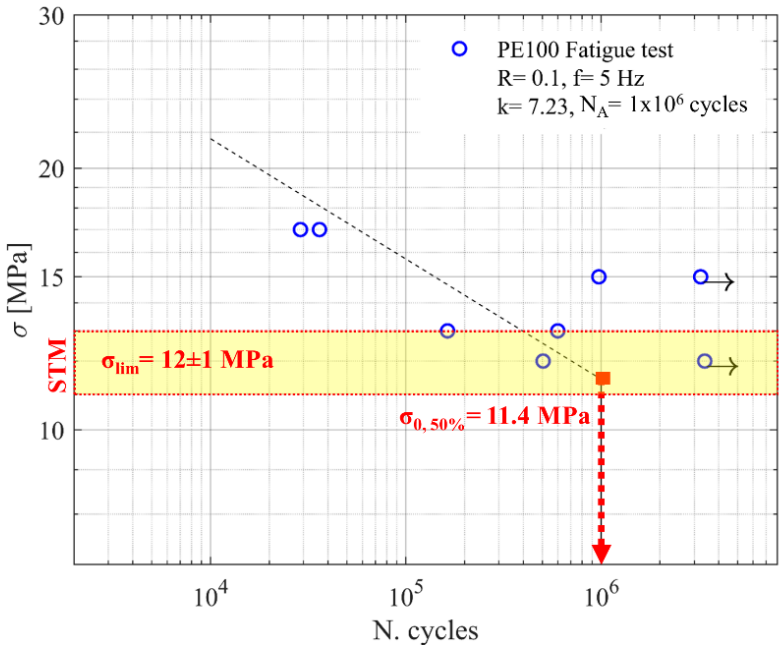

Figure 8.7: Comparison between the limit stress and the traditional fatigue tests.

As is possible to note, both failure and run out tests falls within the limit stress scatter band assessed by means of the STM. Also the fatigue limit estimated by traditional fatigue tests and TM, fall within the previous scatter band, hence is possible to establish a direct relation between the fatigue limit of the material and the limit stress evaluated adopting the STM. This value, if cyclically applied to the material, will lead to local plasticization phenomena, hence to fatigue failure. The STM could provide a good estimation of the fatigue limit adopting a limited number of specimens and a short amount of time, approximately 5 minutes per test, compared to the traditional fatigue test procedure, which requires a large amount of specimens and a long test time, especially for those materials that cannot be tested at higher frequencies (i.e. plastic and composite materials) due to the self-heating phenomena [25].

8.4. Conclusion

In this chapter the energetic release during tensile tests on high-density polyethylene (PE100) specimens has been evaluated. The mechanical properties of the material have been assessed and compared to datasheet values showing good agreement. The IR camera allowed the application of the Static Thermographic Method, monitoring the specimen's surface temperature during static tensile tests. The average value of the limit stress has been evaluated as the stress level at which the temperature deviates from its linear trend, obtaining an average value of 12.0±1.0 MPa on three tests. This value has been compared with the fatigue limit estimated by Thermographic Method (11.32 MPa) and traditional fatigue tests showing a direct relation with the fatigue limit of the material with 50% probability of survival (11.4 MPa).

The Static Thermographic Method could be adopted as a fast test procedure able to predict the fatigue properties of the materials from a uniaxial static test in a very short amount of time and with a very limited number of specimens.

9. 3D-PRINTED POLYAMIDE-12

Santonocito D. Evaluation of fatigue properties of 3D-printed Polyamide-12 by means of energy approach during tensile tests. Procedia Struct Integr 2020;25:355–63. doi:10.1016/j.prostr.2020.04.040.

Highlights

Rapid prototyping and Additive Manufacturing are experiencing a continuous and rapid growth in different industrial fields, ranging from automotive to biomedical applications. They allow the creation of a wide range of devices in a short time with several materials, such as polymers and metals. On the other hand, the manufacturing process considerably affects the performance of the obtained 3D-printed materials and different laboratory tests are required in order to assess the mechanical properties, especially the fatigue behavior, of these materials. The aim of this chapter is to apply, for the first time on 3D-printed materials, the Static Thermographic Method for the fatigue assessment of Polyamide-12.

The tests were performed on specimen made of Polyamide-12 printed with the Multijet Fusion (MJF™) printing system. A first series of static tensile tests was performed on three specimens with constant displacement rate. The superficial temperature was monitored by means of an infrared camera and the limit stress was evaluated. A second series of fatigue tests with constant amplitude and fully reversed load was performed on seven specimens and compared with the limit stress showing good agreement. An optical analysis of the fracture surfaces was performed on both the static and fatigue tested specimens.

The present work is the result of the collaboration between the Engineering Department of the University of Messina and the rapid-prototyping company Skorpion Engineering.

Nomenclature

c	specific heat capacity of the material [J/kg.K]
E	Young's Modulus [MPa]
K_m	thermoelastic coefficient [MPa^{-1}]
R	stress ratio

t	test time [s]
T, T_i	instantaneous value of temperature [K]
T_0	initial value of temperature estimated at time zero [K]
v	displacement velocity [mm/min]
α	thermal diffusivity of the material [m^2/s]
ΔT_s	absolute surface temperature variation during a static tensile test [K]
ΔT_1, ΔT_2	estimated value of temperature for the first and second set of temperature data [K]
ε, ε_f	strain, strain at failure
ε_1, ε_2	strain level for elastic modulus linear regression
ρ	density of the material [kg/m^3]
σ, σ_1	stress level, uniaxial stress [MPa]
σ_D	critical macro stress that produces irreversible micro-plasticity [MPa]
σ_{lim}	fatigue limit estimated with the Static Thermographic Method [MPa]
σ_U	ultimate tensile strength [MPa]

9.1. Introduction

Additive Manufacturing (AM) is spreading in several industrial fields [153] such as automotive [154], aerospace and aeronautics [155] and biomedical [156,157]. Combined with topology optimization it allows the creation of many devices with a variety of shape and functional design unattainable through traditional mechanical process [158–160]. Rapid prototyping enables the creation of final products directly from the CAD file, requiring design strategy in order to avoid the physical testing, adopting advanced simulation, structural optimization and failure prevention methods [114]. On the other hand, AM materials presents several issues due to the uncertainty of their mechanical performances.

Many authors have investigated the mechanical properties of AM materials, both polymers [161,162] and metals [163,164]. Especially the fatigue properties require a huge amount of time and a large number of specimens in order to be assessed, hence the infrared thermography (IR) could be a valid aid in the investigation of these properties. It has been applied on different

materials subjected to several loading conditions: notched and plain steel specimens under static and fatigue tests [3,68,69], laminated composites under tensile static loading [134], polyethylene under static and fatigue loading [137], short glass fiber-reinforced polyamide composites under static and fatigue loading [132], steels under high cycle [44,50,64,142] and very high cycle fatigue regimes [10,12].

In 2000, La Rosa and Risitano, proposed the Thermographic Method (TM) as an innovative approach based on thermographic analyses of the temperature evolution during the fatigue tests in order to predict the fatigue limit and the S-N curve [46]. In 2013, Risitano and Risitano proposed the Static Thermographic Method (STM) as a rapid procedure to derive the fatigue limit of the material evaluating the temperature evolution during a static tensile test.

The aim of this research activity is the application of the STM during static tensile tests for the first time on a 3D-printed plastic material. Tensile tests were carried out and IR thermography has been adopted during all the static tests in order to evaluate the energetic release of the material. This research activity is part of the collaboration between the Department of Engineering of the University of Messina and the rapid-prototyping company Skorpion Engineering.

9.2. Materials and Methods

Static tensile test were performed on specimen made of 3D-printed Polyamide-12, according to the geometry prescribed by the ASTM D638 standard, with a nominal cross section of 13 mm x 7 mm (Figure 9.1a). The specimens were realised with a HP Jet Fusion 3D 4200 printer, along the XY plane, adopting the polymeric powder HP 3D High Reusability PA12, with a powder melting point (DSC) of 187°C, particle size of 60 µm and bulk density 0.425 g/cm^3. The printer adopts the Multijet Fusion (MJF™) printing system: it is a powder-based technology without the adoption of a laser source. The powder bed is preheated uniformly and a first layer of liquid fusion agents is deposited on the printing plane, later a second layer with detailing agents is deposited in the points where the material need to be melted. A source of infrared energy, usually planar lamps, pass over the surface of the bed allowing the powder fusion. The process continues, layer by layer, up to the completion of the component. The specimens were printed adopting the "Fast" printing profile, which ensure a rapid printing process, but with lower mechanical properties compared to the "Mechanical" profile.

The tests were performed with a servo-hydraulic load machine ITALSIGMA 25 kN with a crosshead rate equal to 5 mm/min, at constant temperature and relative humidity (23°C and 50% RH) (Figure 9.1b). The tensile tests were carried out on three specimens and an infrared camera FLIR A40, with a sample rate of 1 image per second, was adopted to monitoring the specimen's surface temperature. Longitudinal displacements of the specimen were assessed by means of a Digital Image Correlation system GOM Aramis 3D 12M. The specimen surfaces were coated with high emissivity black paint on one side while with a speckle pattern on the other side.

A series of fatigue tests at constant amplitude was performed on seven specimens of the same geometry of the previous ones, with a stress ratio R= 0.1 and a test frequency f= 3 Hz. After the tests, the fracture surfaces of the specimens were analysed adopting a high definition optical microscope LEICA.

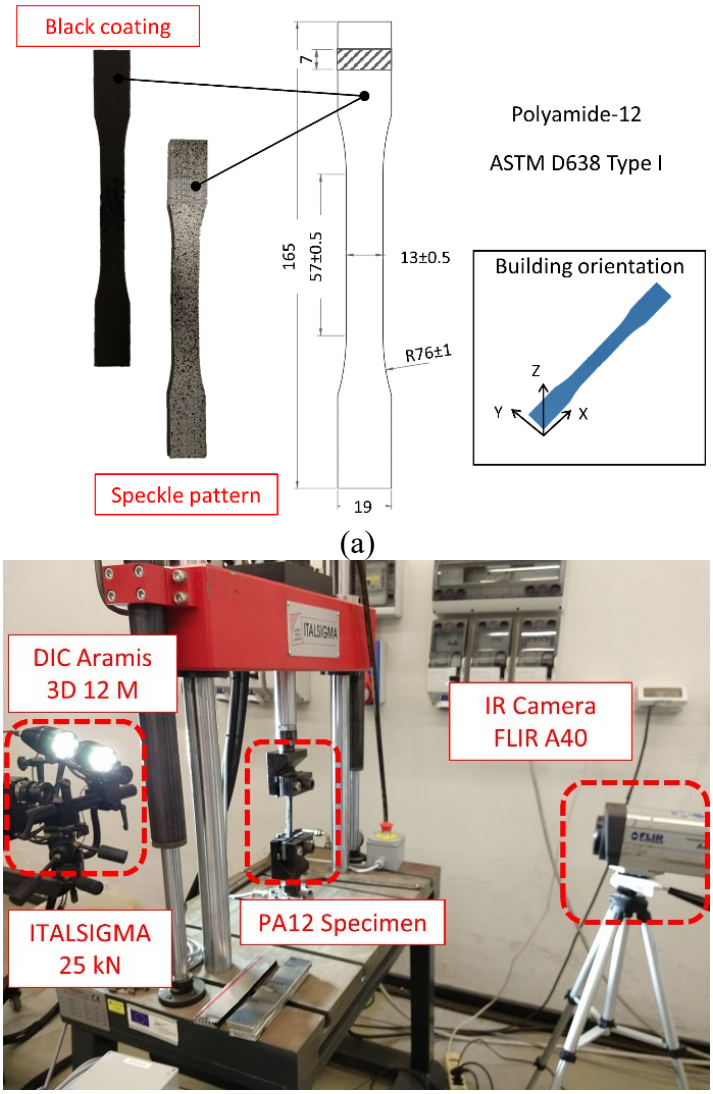

Figure 9.1: a) Specimen geometry and building characteristics; b) experimental setup.

9.3. Results and discussions

9.3.1. Mechanical properties

Static traction tests were performed on three specimens under displacement control, with a velocity of 5 mm/min. The DIC was adopted in order to assess the local displacement on the specimens while the IR camera was adopted to monitor the superficial temperature evolution. In Figure 9.2 are reported the engineering curves for the three tested specimens. The stress is evaluated as the ratio between the force and the nominal cross section area of the specimen, while the strain as the ratio of the distance variation of two spot over their initial distance (L_0= 10 mm). The Young's Modulus has been evaluated as the linear regression of the stress vs strain between ε_1=0.0005 and ε_2=0.0025.

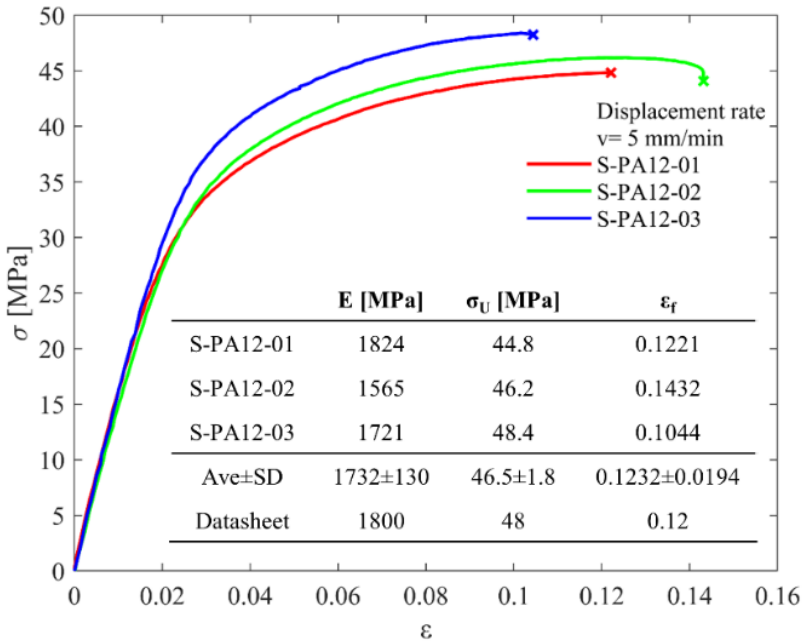

	E [MPa]	σ_U [MPa]	ε_f
S-PA12-01	1824	44.8	0.1221
S-PA12-02	1565	46.2	0.1432
S-PA12-03	1721	48.4	0.1044
Ave±SD	1732±130	46.5±1.8	0.1232±0.0194
Datasheet	1800	48	0.12

Figure 9.2: Engineering curve and mechanical properties for PA12.

As observed by Stoia et al. (2019) for SLS 3D-printed PA2200, this kind of material exhibit a linear elastic behavior followed by a smooth hardening until failure, and, in addition, it is not possible to assess a yield point. Considering the values of the mechanical properties for PA12 Type I specimens printed with "Fast" profile along XY direction, as reported by the manufacturer datasheet, it is possible to note how they fall within the range of the average and one standard deviation for the three tests. The mechanical properties are also in agreement with the ones found by Lammens et al. [165] for Selective Laser Sintering PA12 specimens, tested at 5 mm/min. For

PA12 specimens obtained by MJF™ system, O'Connor et al. [162] found lower values of the elastic modulus (E= ~1240 MPa) and higher elongation at break (ε_f= ~0.19), while Morales-Planas et al. [166] a lower elongation at break (ε_f= ~0.05).

9.3.2. Static Thermographic Method and Fatigue Limit

During static tensile tests, the evolution of the specimen's surface temperature has been evaluated by means of an IR camera. The applied stress is reported versus the specimen's surface temperature variation, estimated as the difference between the instantaneous temperature and the initial temperature of the surface recorded at time zero ($\Delta T = T_i - T_0$) (Figure 9.3).

The temperature data has been filtered with a *rlowess* filter, with a data span of 10%, in order to reduce the outliers and highlight the thermoelastic trend. In the initial part of the ΔT-t curve it is possible to clearly distinguish the linear trend of the temperature, then it deviates from the linearity reaching a plateau region, suddenly it experiences a rapid increment. It is possible to draw two linear regression line, the former for the first linear phase (early stage of the temperature signal, ΔT_1 fit point series) and the latter for the second phase (last stage before the sudden increase in the temperature signal, ΔT_2 fit point series), not taking into account the temperature values near the slope change (Experimental Temperature series).

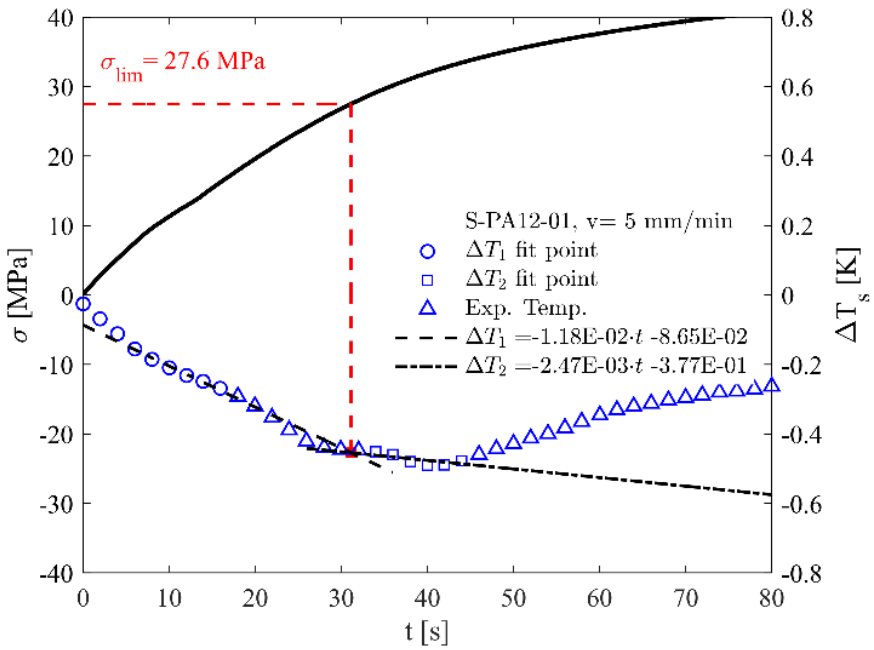

(a)

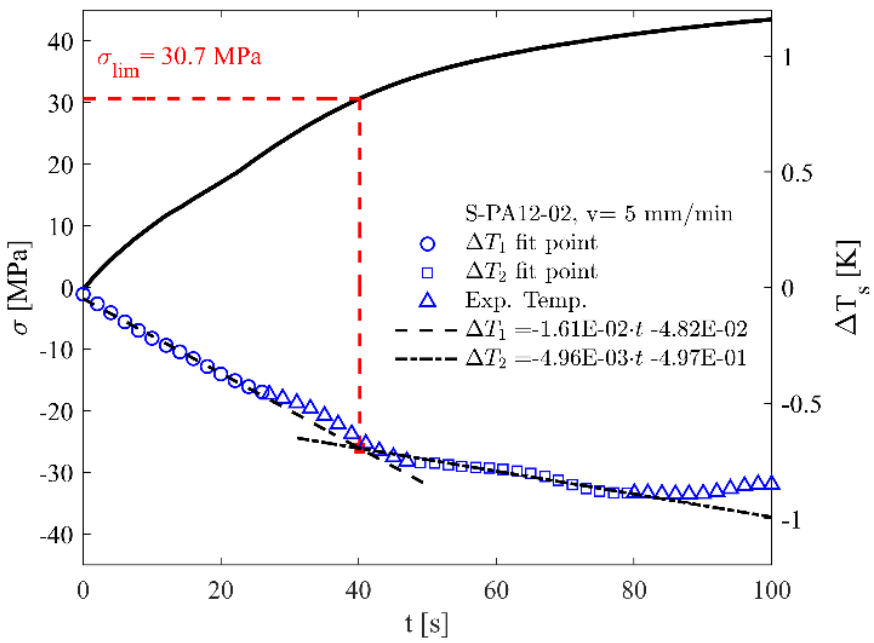

(b)

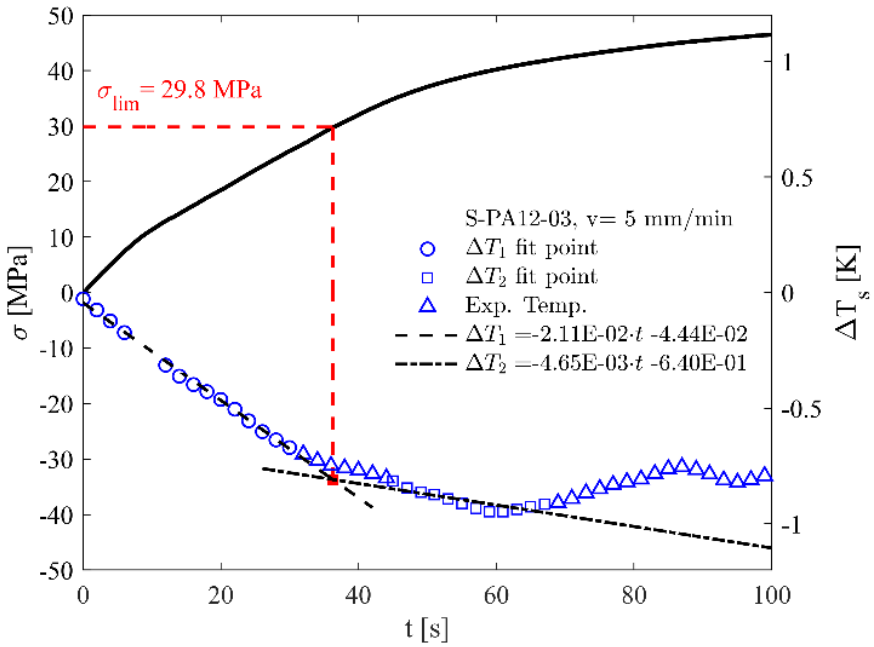

(c)

Figure 9.3: Temperature evolution vs. applied stress during static tensile test on PA12 specimens.

Solving the system of equations, it is possible to determine the intersection point of the two straight lines. The corresponding value of the applied stress, namely σ_{lim}, could be related to the macroscopic stress that introduces the first plasticization phenomena in the material. For the three static tensile tests an average value of 29.4±1.6 MPa has been found for the limit stress.

Useful information can be also retrieved observing the temperature trend. In particular, it is possible to define a yielding stress in correspondence of the temperature zero-derivative flex region, in the transition point between Phase II and Phase III. This stress can be thought as the macroscopic stress at which the majority of the material crystals are under plastic condition.

A series of fatigue tests has been carried out with constant stress amplitude, equal to 28 MPa and 30 MPa. In Figure 9.4 are reported in a S-N plot the test results, adopting a number of cycle for run out of $N_A = 2x10^6$. In the same plot are reported the average value and the scatter band with one standard deviation for the limit stress assessed by STM. As is possible to note, both failure and run out tests falls within the scatter band; hence the stress value assessed by means of the STM could be related with the fatigue limit of the material. However, several traditional fatigue tests have to be carried out to obtain the S-N curve and the fatigue limit of the material.

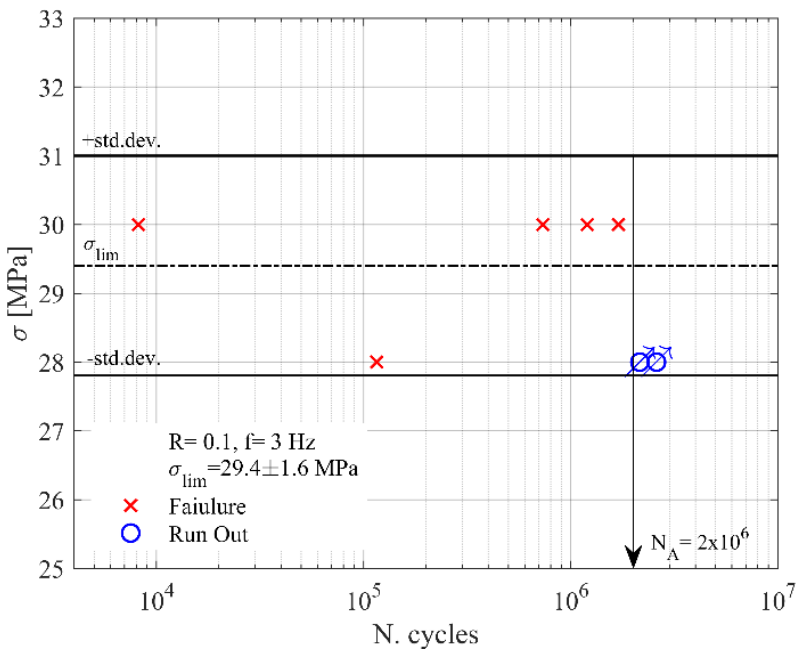

Figure 9.4: Comparison between the limit stress and the traditional fatigue tests.

9.3.3. Fracture surfaces

After static and fatigue tests the fracture surfaces have been evaluated through an optical microscope. In Figure 9.5, are reported the fracture surfaces of a sample per test typology; the other samples exhibit the same behavior. As regard to the static tests (Figure 9.5a), the fracture surfaces show the classical aspect of a ductile failure, with small plastic deformation. In all of the static fracture surfaces are clearly visible a series of defects due to the lack of powder melting.

In particular, defects with a diameter of about 1 mm has been found surrounded by non-melted powder where it is possible to distinguish the different layers.

Fatigue fracture surfaces show a smoother profile, typical of a brittle failure (Figure 9.5b). The surface appears darker than the static case and this could be addressed to the increase in specimen's temperature due to the fatigue tests frequency [25]. Defects due to the lack of powder melting, with an average diameter of 0.3 mm, have been found. Also in this case, the different layers of material could be observed near the circular defects area, with an average length of the cracks equal to 0.6 mm. From the analysis of the fracture surfaces it is evident how the printing process affects the mechanical properties of the materials both under static and fatigue tests [167].

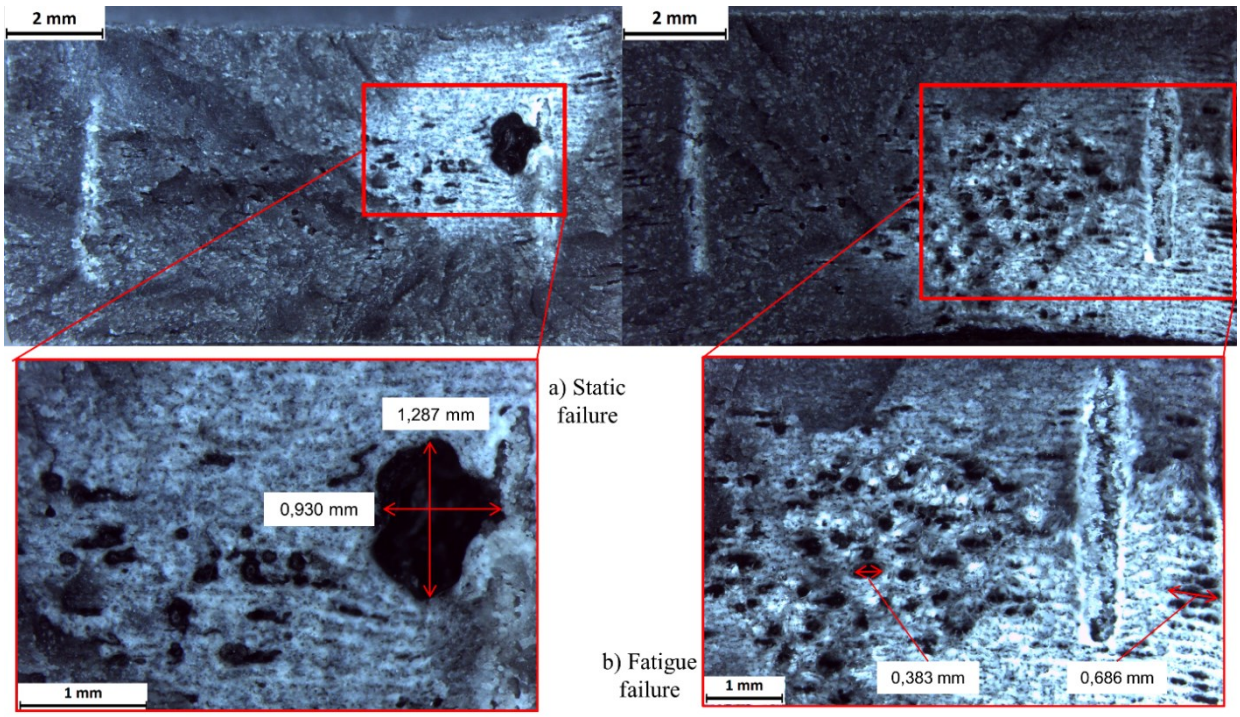

Figure 9.5: Fracture surfaces for: a) static tensile tests; b) fatigue tests.

9.4. Conclusion

In this chapter the energetic release during tensile tests on 3D printed polyamide-12 specimens has been evaluated. The mechanical properties of the material have been assessed and compared to other authors and datasheet values showing good agreement. During the same tensile tests, the IR camera allowed the application of the Static Thermographic Method, monitoring the specimen's surface temperature. The average value of the limit stress has been evaluated as the

stress level at which the temperature deviates from its linear trend, obtaining a value of 29.4±1.6 MPa. This value has been compared with traditional fatigue test showing a relation with the fatigue limit of the material. Micrographic analysis of the fracture surfaces have been performed showing how the printing process severally affects the mechanical properties of the material under static and fatigue loading.

The Static Thermographic Method could be adopted in rapid prototyping process as a fast test procedure able to predict the fatigue properties of the 3D-printed materials from a conventional static test in a very short amount of time and with a limited number of specimens.

10. COMPOSITE MATERIAL PA66GF35

Santonocito D. Numerical and experimental evaluation of the energetic release during tensile tests on short fiber reinforced composite material. Under review (presented at national machine design conference AIAS2020, Juniores Session)

Highlights

In this chapter, a simple numerical model is presented in order to evaluate the energetic release of short fiber composite PA66GF35 under static tensile tests. The micro-mechanical behavior of the fiber-matrix system was taken into account, as well as the fiber distribution and orientation. Numerical simulation at macro scale level were carried out to predict the temperature evolution of the material under monotonic load.

Experimental validation was performed on dog-bone specimens monitoring the surface temperature with an infrared camera. A deviation from the linearity of the thermoelastic effect has been noticed for a stress level below the yielding strength of the material.

The analysis of the temperature trend evolution may be a useful aid in order to identify damage initiation within the material that would lead to failure, especially under fatigue load, even adopting a simple and rapid static tensile test.

Nomenclature

c	specific heat capacity of the material [J/kg.K]
d_f	diameter of the fiber [μm]
E	Young's Modulus [MPa]
$I_{1\sigma}$	First stress invariant [MPa]
K_m	thermoelastic coefficient [Pa^{-1}]
l_f	fiber length [μm]
L	matrix cylinder length [μm]
S	matrix cylinder diameter [μm]

t	test time [s]
T, T_i	instantaneous value of temperature [K]
T_0	initial value of temperature estimated at time zero [K]
W_p	Plastic work per volume unit [Nmm/mm^3]
α	linear expansion coefficent [K^{-1}]
ΔT_s	absolute surface temperature variation during a static tensile test [K]
ΔT_1	estimated value of temperature for the first set of temperature data [K]
ΔT_2	estimated value of temperature for the second set of temperature data [K]
ε, ε_f, $\bar{\varepsilon}$	strain, strain at failure, average strain
ρ	density of the material [kg/m^3]
ν	Poisson coefficient
σ, $\bar{\sigma}$	stress level, average stress [MPa]
σ_y	yielding stress [MPa]
σ_R	ultimate stress [MPa]
$\sigma_{lim\ Exp}$, $\sigma_{lim\ FEM}$	limit stress estimated with the Static Thermographic Method [MPa] experimental, simulated

10.1. Introduction

In the recent years, infrared thermography has been adopted to monitor the fatigue behavior of several class of materials [136,137,142], even composite material [132,168]. In 2013, Risitano and Risitano [3] proposed the Static Thermographic Method (STM) as an innovative test procedure able to estimate the onset of damage processes within the material evaluating the energetic release during a static tensile tests. The macroscopic stress level at which a deviation from the linearity of the thermoelastic trend is observed correspond to the stress that introduce in the material irreversible damage. Clienti et al. [86] for the first time observed such behavior and correlates it to the fatigue limit of plastic materials. The same behavior has been observed also in basalt fiber composites [126] and glass fiber reinforced materials [169].

It is difficult to model the internal micro structure of the materials, especially for metals, and correlate it to the macroscopic behavior; but, on the other hand, the internal structure of composite material is well known. The material under study is a composite material of the class PA66GF35, which has been investigated by several authors in literature. Sato et al. [170] analyzed the damage evolution on this class of composite under static and fatigue tests and proposed a micro failure model. Bernasconi et al. [171] analyzed the influence of the fiber orientation on the fatigue behavior of short glass fiber reinforced PA6 composites. De Monte et al. [172] studied the influence of the temperature and thickness of specimens retrieved at several orientations respect the Mold Flow Direction (MFD). Adopting the infrared thermography, Belmonte et al. [173] studied the damage mechanism on plain and notched specimens of reinforced polyamide. Several authors have focused their study on modelling the fiber-matrix interaction of composites material [174]. Horst et al. [175] created a finite element model to investigate the stresses at fiber and matrix interface of glass fiber reinforced polyamide composites and compared it to experimental results.

In this chapter, a first attempt to understand the link between the internal micro structure and its micro failure mechanism on the overall energetic release of a composite material is performed. Numerical simulations are carried out in order to predict the onset of damage within the material while the STM is applied on dog-bone specimens in order to verify the damage model.

10.2. Materials and Methods

The material under study was a composite obtained by injection molding process of the type PA66GF35. In this kind of material, the matrix phase in composed by aliphatic polyamide 66 while the fiber is made of glass and it is dispersed in the matrix with a weight percentage of 35%. Three specimens of the Type 1A according to ISO527 standard where retrieved from a plate along the mold flow direction (MFD, 0° orientation) (Figure 10.1a). The specimens were subjected to natural ageing at room temperature for about 4 years. In Table 10.1 are reported the mechanical properties as declared by the manufacturer. The specimens were tested under displacement control, with a crosshead speed of 5 mm/min, adopting a servo-hydraulic test machine ITALSIGMA 25kN (Figure 10.1b). During the tests the superficial temperature was monitored with an infrared camera FLIR A40 with a sample rate of 1 image per second. The superficial strains were assessed by means of a stereo cameras Digital Image Correlation (DIC)

system, with a resolution of 4000 x 3000 pixels and focal length of 50 mm. The system accuracy for the strain measurement is up to 0.01%, and the images were acquired at 1 Hz.

Table 10.1: PA66GF35 mechanical and thermal properties as declared by the manufacturer.

Tensile Strength	Tensile Modulus	Fiber length	Fiber Diameter	Density	Specific heat	Linear expansion coefficient
σ_R [MPa]	E [GPa]	l_f [μm]	d_f [μm]	ρ [kg/m^3]	c [J/kg.K]	α [K^{-1}]
150÷210	8.7÷11.4	280	10	1410	1670	2.5 x 10^{-5}

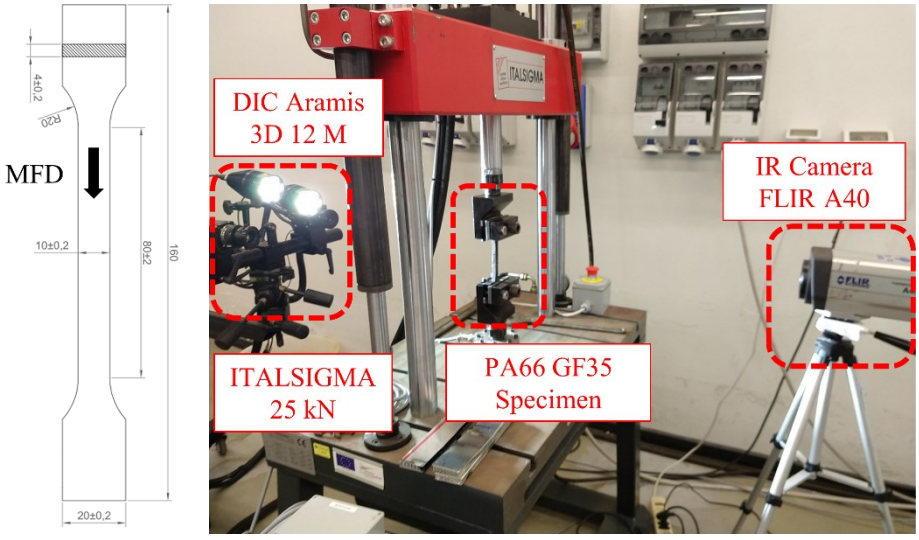

(a) (b)

Figure 10.1: a) specimen geometry according to ISO527; b) Experimental setup.

In order to assess the micro failure behavior of the composite, a 2D finite element model was created with Ansys APDL. The material properties of the fiber and matrix adopted are reported in Table 10.2. The fiber-matrix system was modelled as a cylinder (fiber) within another one (matrix) taking into account the volume percentage of the fiber respect to the matrix ($V_f = ld^2/LS^2$) [176]. The geometrical characteristics of the model are reported in Figure 10.2, were a total number of 6900 PLANE183 elements were adopted. Axial symmetry boundary condition was adopted for the system, while the bottom elements were fixed and a displacement for the top ones was imposed in order to achieve the 3% of strain. As regards the right matrix elements, in order to avoid the formation of internal cracks, the displacement along the x direction were coupled together and equal to the matrix node far away from the fiber tip [175].

Table 10.2: Material properties of fiber and mantrix for FE model.

	Mechanical behaviour	E [GPa]	σ_y [MPa]	ν	ρ [kg/m^3]
Fiber (Glass)	Linear elastic	72	-	0.22	2.54
Matrix (PA66)	Von Mises Yielding	3.1	51	0.4	1.16

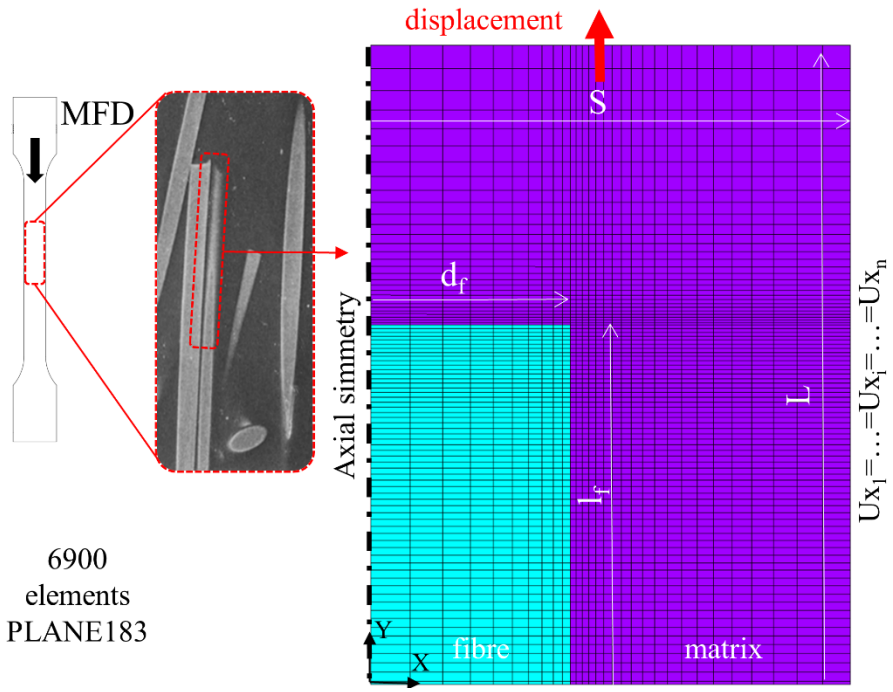

Figure 10.2: Micro mechanical Finite Element model.

The stress-strain behavior was evaluated with the same procedure proposed by several authors [176,177], where the stress and strain are estimated as average values over the element volumes according to the following equations:

$$\bar{\sigma} = \frac{1}{V}\sum_{k=1}^{N} V_k \sigma_{ij}^k \qquad \bar{\varepsilon} = \frac{1}{V}\sum_{k=1}^{N} V_k \varepsilon_{ij}^k \tag{10.1}$$

A 3D macro mechanical model of the Type 1A specimens were also modelled adopting 1/8th of the geometry (Figure 10.3), in order to apply the temperature model developed in section 2.4.2.

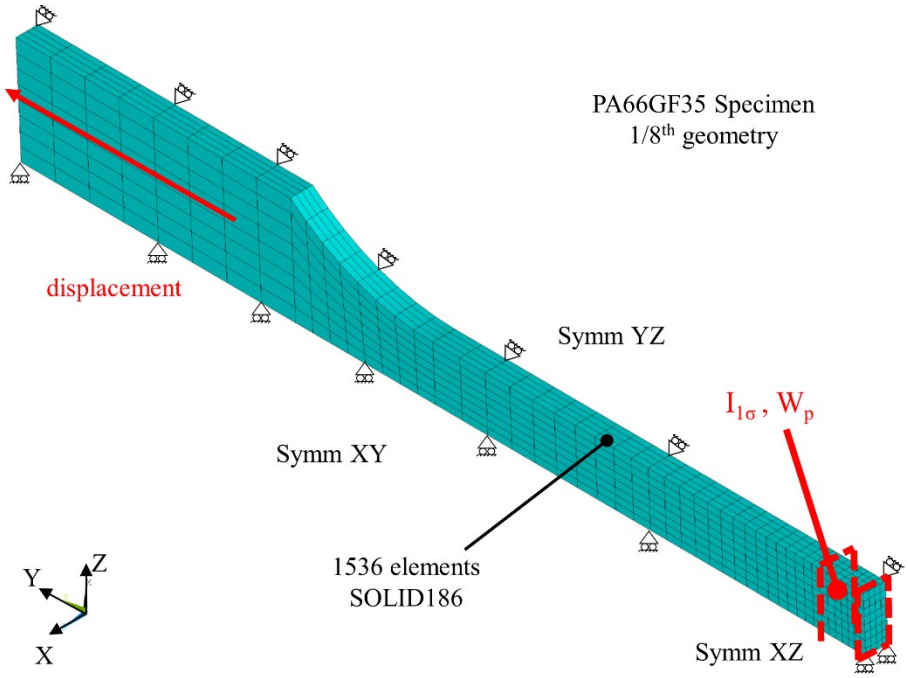

Figure 10.3: Macro mechanical Finite Element model of the PA66GF35 Type 1A specimen.

Hexahedral 20-node SOLID186 elements were adopted and after a calibration procedure, a total number of 1536 elements were chosen. In order to emulate the static traction tests, an imposed displacement to the grip nodes was applied. The composite material was modelled as a homogeneous isotropic material with elasto-plastic behavior. The engineering curve coming from the DIC system was adopted and it was corrected taking into account the damage mechanisms assessed by the micro mechanical FE model. As regard the fiber orientation, the injection molding process creates a typical sandwich structure, where the fibers in the shell regions (near the mold walls) are directed along the MFD, while in the core region they are almost perpendicular to the MFD. Since it was observed by several authors that the core region is about the 5% of the specimen thickness [178,179], taking into account the small thickness of the adopted specimens, the core region was neglected and all the fibers within the composite were considered aligned to the MFD and hence to the load direction. The first stress invariant and the plastic work per volume unit of a volume of about 2 mm region of the specimens reduced section were retrieved.

10.3. Results and discussions

10.3.1. Experimental test

Static tensile tests were performed on three specimens adopting a crosshead velocity of 5 mm/min. The crosshead velocity has to be choose properly in order to assure adiabatic test conditions, i.e. the specimens are not allowed to exchange heat with the environment. The superficial temperature trend was monitored with an infrared camera and the obtained temperature signal was filtered with a *rlowess* filter, with a data span of 10%, in order to reduce the outliers and highlights the thermoelastic trend. In Figure 10.4, the nominal stress versus the specimen's surface temperature variation, estimated as the difference between the instantaneous temperature and the initial temperature of the surface recorded at time zero ($\Delta T = T_i - T_0$) are reported.

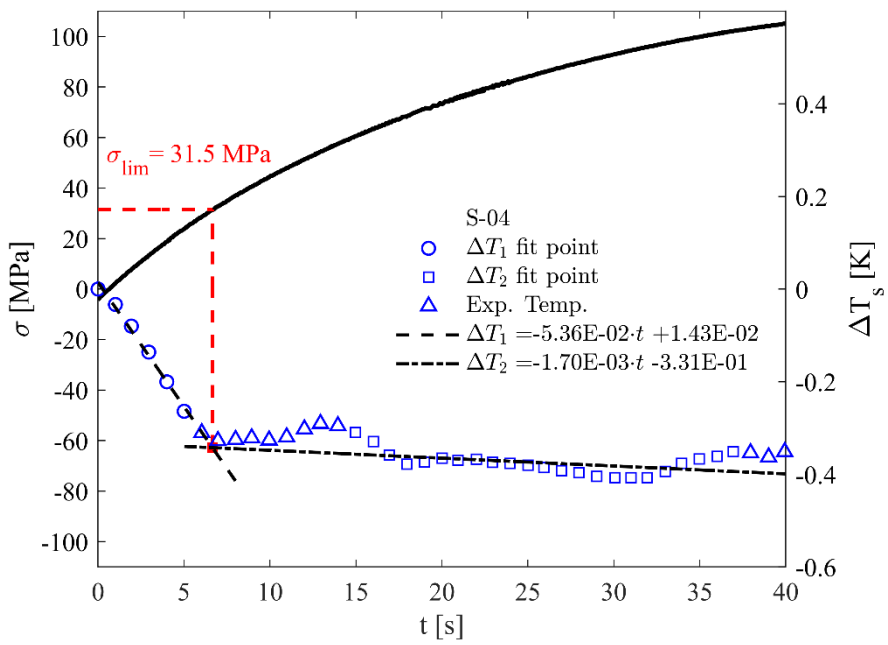

Figure 10.4: Experimental temperature trend vs. stress level during a static tensile test on PA66GF35 Type 1A ISO527 specimen.

In the initial part of the ΔT-t curve it is possible to clearly distinguish the linear trend of the temperature, then it deviates from the linearity reaching a plateau region. It is possible to draw two linear regression line, the former for the first linear phase (early stage of the temperature signal, ΔT_1 fit point series) and the latter for the second phase (last stage before the sudden increase in the temperature signal, ΔT_2 fit point series), not taking into account the temperature values near the slope change (Experimental Temperature series). Solving the system of

equations, it is possible to determine the intersection point of the two straight lines. The corresponding value of the applied stress could be related to the macroscopic stress that leads to irreversible damage phenomena in the material. The limit stress has been evaluated on three tests, obtaining a value equals to 34.1±3.8 MPa.

10.3.2. Micro failure within the material

Prior to modelling the micro mechanical failure of the composite material it is important to observe the damage evolution during a static traction test. Sato et al. [170] observed the progression of the damage within a composite with PA66 matrix and dispersed glass fibers during static tensile and fatigue tests adopting the SEM technique. They observed as the fiber tip does not contribute to the load transfer between the fiber and the matrix, hence the matrix can be thought as not bonded with the fiber ends. For low stress levels, micro voids at fiber end regions are observed and, as the load increases, interfacial micro failure of the matrix along the fiber length arises. Then the micro cracks propagate within the matrix up to reach a very large plastic deformation with catastrophic failure of the whole composite. From the micro mechanical FE model the stress-strain curve has been evaluated, as well as the plasticity evolution within the matrix phase. As done by Kang et al.[176] for metal matrix composite material, in Figure 10.5 are reported the engineering stress-strain curve obtained from the micro mechanical FE model up to 1.7% of strain (for higher deformation, FE values were not reliable) and from the static traction test performed on a specimen, assessed with DIC method. The experimental PA66GF35 curve exhibits, for the same strain level, higher stress values compared to the FE curve. The estimated elastic modulus (29.7 GPa, according to ISO527 standard) is considerably higher compared to the manufacturer data. On the other hand, the estimated elastic modulus of the FE curve (11.3 GPa) is almost near the upper bound value of the range declared by the manufacturer. The differences in the mechanical behavior of the experimental and simulated stress-strain curve may be due to not have taken into account, in the FE model, the viscoplastic behavior of the matrix and to the excessive ageing of the tested specimens. In the same figure are reported some images extracted from the FE model with the representation of the “stress ratio” parameter, i.e. the level of plasticity of one element, as estimated by the ANSYS software (blue=fully elastic, red=fully plastic). As the strain level increases, the plastic area in the matrix increases. For a strain level of about ε= 0.002, the fiber matrix debonding region reaches the 5% of the fiber length. Such a strain level can be considered as the limit strain level where irreversible micro failure arises within the material. For higher strain levels, the plastic area increases in a similar way as observed by Sato et al.

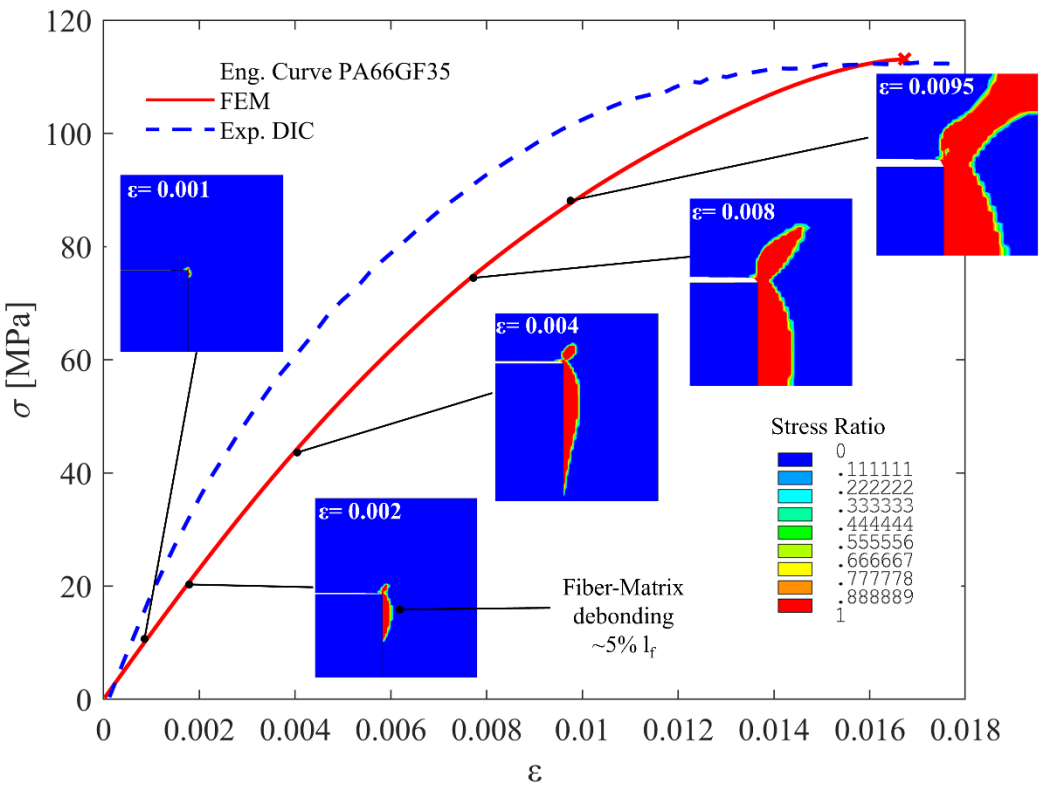

Figure 10.5: Comparison between Experimental and Numerical (FE) engineering curve for PA66GF35. Evolution of the plasticization within the matrix.

10.3.3. Predicting the temperature evolution

From the micro mechanical FE model, the minimum strain level at which damage begin within the composite material has been assessed; hence, in order to model the overall plastic behavior of the specimen, the experimental stress-strain curve of the material has been redefined considering the material as isotropic elastic till ε= 0.002, then it has been considered as a plastic material adopting an isotropic multilinear plasticity model. The core region generated by the injection molding process (fiber aligned perpendicularly to the MFD) has been neglected, considering its small presence in the specimen volume, while the overall specimen has been considered as oriented along the MFD. A displacement on the grip section nodes has been imposed and the first stress invariant and the plastic work per unit of volume have been evaluated from the finite element simulation of the specimen. Due to the ageing of the material under study, the thermoelastic constant K_m has been directly evaluated from experimental data performing a linear regression of the relative temperature variation versus the stress. In Figure 10.6 are

reported the experimental filtered temperature and the numerical prediction of the temperature according to the model presented in section 2.4.2. By observing the experimental trend, the three different phases are evident. In the first phase the temperature trend is perfectly linear, then for a stress level of 31.5 MPa it deviates from the linearity reaching a plateau region where it is almost flat. When the stress level is equal to 95 MPa, a very high further temperature increment is experienced till the specimen failure. The temperature trend predicted by the FE simulation adopting the corrected stress-strain curve for the same specimen of the experimental test, perfectly follow the linear trend of the experimental temperature up to the stress level of 32.7 MPa, where the specimen experiences the first micro failure. From that point, the temperature slightly increases and, in the third phase, it experiences the same asymptotical increase of the experimental trend. The limit stress assessed by the FE simulation is in good agreement with the experimental value. The knowledge of the micro failure within the material has allowed a good prediction of the macro failure of the composite material analyzing the energetic release.

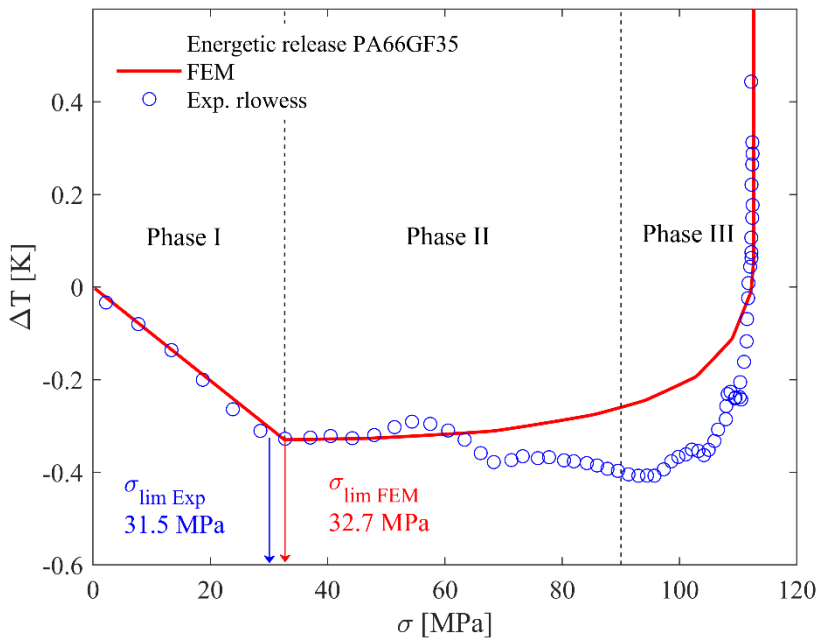

Figure 10.6: Energetic release of PA66GF35. Comparison between experimental and simulated temperature trend.

10.4. Conclusion

Understanding the internal micro structure of the material and the micro failure mechanism under static loads is fundamental in order to predict failures. In this chapter, moving from the observation of the micro damage mechanism of a PA66GF35 composite material, a finite

element simulation has been carried out in order to assess the strain level at which irreversible damage begin within the material. This information has allowed to redefine the stress-strain curve of the material assessed experimentally, taking into account the plastic behavior of the material. Numerical simulation has been carried out at macroscopic scale in order to predict the energetic release of the material. The simulated temperature trend has been compared with the experimental ones, performed on the same specimen geometry, showing good agreement between the limit stresses, i.e. the stress level at which the temperature trend deviates from the linearity. The adoption of the Static Thermographic Method could be a useful aid in order to identify, with a rapid test procedure, the onset of irreversible micro damage within the material that lead to the failure of the structure.

11. LOCAL APPROACHES FOR WELDED STRUCTURES

Highlights

In this chapter, several local approaches are applied to welded joints in order to synthetize the fatigue data. The local approaches based S-N curve are compared with the nominal stress based S-N curve in terms of statistical data dispersions. The local approaches allow to obtain a good synthesis of the fatigue data despite the different geometries, the thickness and the load conditions.

This activity is part of the training that the authors performed at the University of Padova in 2019. The authors would like to thanks Prof. Giovanni Meneghetti and Prof. Alberto Campagnolo for the support.

Nomenclature

a	load carrying plate thickness [mm]
b	welding bead height [mm]
E	Young's modulus [MPa]
N	number of cycles
R_0	control volume radius [mm]
r	radial coordinate [mm]
t	transverse plate thickness [mm]
T_K, T_W, T_σ	scatter index
W	averaged Strain Energy Density [Nmm/mm^3]
2α	opening angle of V-notch [deg]
$\Delta\sigma_{nom}$, $\Delta\sigma_{eq,peak}$	nominal tensile stress [MPa]
ΔK_1	NSIF-based fatigue strength of welded joints [MPamm$^{0.326}$]

θ	angular coordinate [deg]
λ_1, λ_2	mode I and II Williams' eigenvalues for stress distribution at V-notches
ν	Poisson's ratio
$\sigma_{\theta\theta}$, σ_{rr}, $\tau_{r\theta}$	stresses in the bisector polar coordinate system [MPa]

11.1. Introduction

The fatigue assessment of mechanical components requires a huge amount of time to be performed. In addition, the geometry of the tested component and its loading conditions can determine several fatigue strengths for the same component and different parameters may play a fundamental role in the fatigue life, assuming that it is a problem linked to the local stress field near notches.

In the last twenty years several methods to overcome such problems have been proposed. In 1998, Lazzarin and Tovo [95] proposed the Notched Stress Intensity Factor (NSIF) for the assessment of the welded joints, considered as mechanical components with several notch types. In 2005, Livieri and Lazzarin [5] proposed to evaluate the strain energy density (SED) over a control volume and compare it with a critical value which causes the failure of the components. Meneghetti and Lazzarin [115] in 2007 evaluated the elastic peak stress at notch tips in order to assess in a rapid way, thanks to a calibrated mesh, the NSIF values. Starting from the SED formulation, the equivalent peak stress parameter (Peak Stress Method, PSM) has been proposed as a criterion to synthetize the fatigue data of welded components.

In this chapter, several local approaches are adopted in order to estimate the fatigue life of two different class of welded joints, cruciform and T, under traction and bending fatigue loading conditions. The fatigue curves of the components are reformulated in terms of NSIF, SED and Equivalent Peak Stress and compared to the nominal stress fatigue curve.

11.2. Materials and Methods

Numerical finite element simulations were carried out on four different geometries of welded joints, both cruciform and T, whose characteristics are reported in Table 11.1. The joint geometries are taken from the experimental works of Maddox and Gurney, where they were tested under tensile and bending fatigue loading adopting a stress ratio R= 0 and the nominal

stress reported in the same table with the relative number of cycles to failure. All the fatigue failures occurred at toe region. In the same table are also reported the calibration coefficient K_{FE}^* for the application of the PSM as evaluated in [115]. How it is possible to observe, they are within the proposed average value with scatter band of 1.38±5%.

Table 11.1: Welded joint geometries from [115].

Series	Joint geometry	a [mm]	t [mm]	b [mm]	Load type	K_I^V/σ_g [$mm^{0.326}$]	σ_{peak}/σ_g	K_{FE}*	N [cycles]	$\Delta\sigma_{nom}$ [MPa]
1 (Maddox 1987)	Cruciform-nlc	13	10	8	T	2.633	1.870	1.408	192000	200
									507000	140
									2937000	100
									4297000	80
12 (Gurney 1991)	Cruciform-nlc	100	220	15	T	5.704	4.222	1.351	109000	150
									224000	120
									322000	100
									1153000	65
									2147000	55
16 (Gurney 1991)	Cruciform-nlc	100	13	8	B	3.051	2.131	1.432	120000	260
									200000	220
									302000	180
									744000	140
									1180000	120
									2158000	110
23 (Gurney 1997)	T-nlc	6	6	6	B	1.793	1.272	1.410	135000	300
									237000	260
									407000	200
									573000	190
									665000	180
									1525000	160
									1534000	150
									2601000	140

After that the geometry of the welded joints was recreated adopting Ansys APDL, taking advantage of their symmetries, two meshes were adopted. The first mesh (Figure 11.1) was modelled adopting a control volume at the welding bead toe point, that can be considered as a sharp V-notch with opening angle of $2\alpha = 135°$. A mapped mesh with element dimensions of the order of 10^{-5} mm was created within the control volume of radius $R_c = 0.28$ mm. Despite the SED method is well suited to adopt a low number of elements within the control volume, this one was modelled in such way in order to estimate the NSIF according to Gross and Mendelson definition (equation (3.5)). Outside of the control volume a free mesh with element size reported in Table 11.2 were created. The nominal stress was applied on the right side of the joint as a constant

value over the thickness a of the joint with symmetric boundary conditions, if under the traction test condition (T); while it was applied as a triangular gradient over the half thickness of the joint (0 MPa up to $\Delta\sigma_{nom}$) and with antisymmetric condition, under the bending test condition (B). The second kind of mesh (Figure 11.2) was made adopting the free mesher, with an average element size of 1 mm, in order to apply the PSM. The same boundary conditions of the first FE model were applied to that model. For both the models, the quad 4-node element PLANE182 with "simple enhanced strain" formulation was adopted and the material properties of structural steel (E= 206 GPa, ν= 0.33) were implemented. The dimensions of the different FE model are reported in Table 11.2.

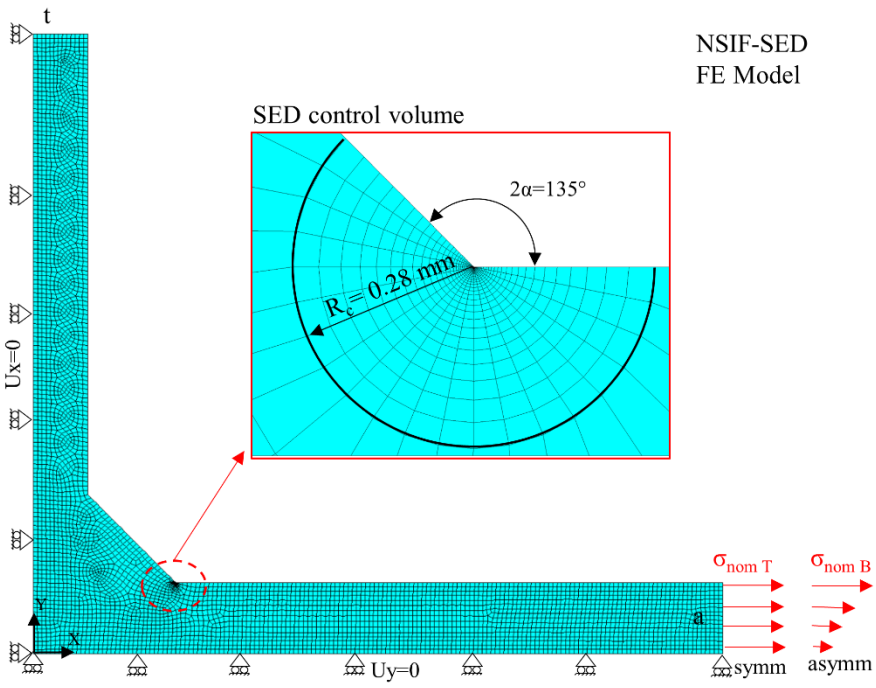

Figure 11.1: FE model for the estimation of the NSIF and SED.

For the estimation of the NSIF, the stress field $\sigma_{\theta\theta}$ along a path of the opening angle bisector was retrieved (Figure 3.1). For the SED estimation, the strain energy of all the elements within the control volume was retrieved, summed and averaged over the entire control volume. Lastly, for the PSM evaluation, the maximum elastic stress $\sigma_{\theta\theta max}(r=0, \theta=0)$ was estimated.

Table 11.2: FE model dimensions.

Series	FEM NSIF-SED	FEM PSM

	No. Elements	Element size [mm]	No. Elements	Element size [mm]
1 (Maddox 1987)	5553	0.4	722	1
12 (Gurney 1991)	20601	0.8	11913	1
16 (Gurney 1991)	6297	0.8	3469	1
23 (Gurney 1997)	4617	0.4	521	1

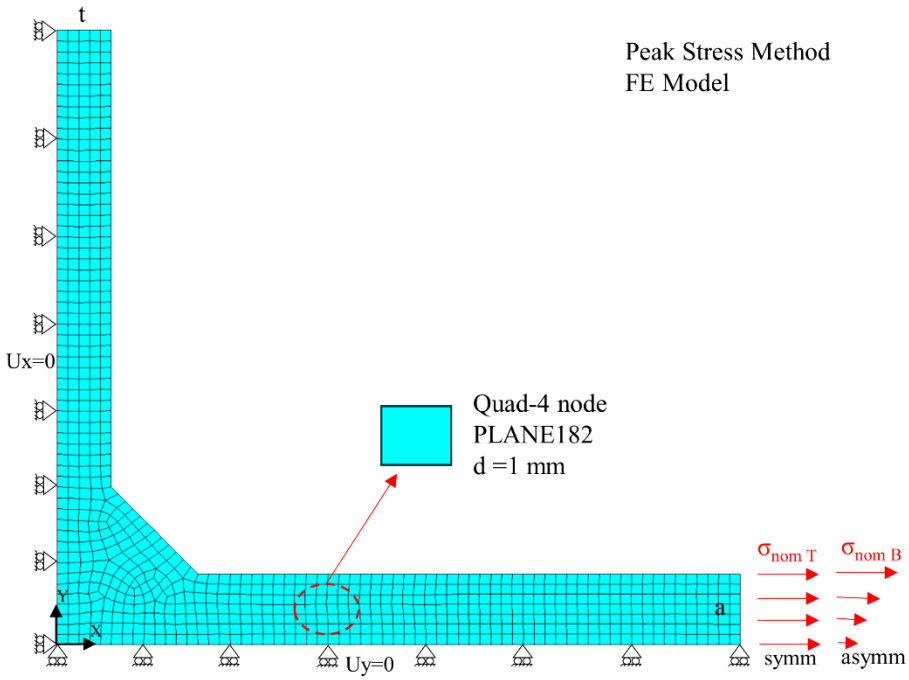

Figure 11.2: FE model for the estimation of the PSM.

11.3. Results and discussions

The fatigue data from Table 11.1 are reported in the bi-log S-N graph of Figure 11.3. According to the standards, the inverse slope was fixed to k= 3. The scatter band for a probability of survival (PS) of 97.7% has been evaluated and the scatter index T_σ, estimated as the ratio between the lower PS value (184 MPa) over the maximum PS value (28 MPa) at a run-out number of cycles equal to $5x10^6$, is equal to 6.59. This is a high value, due to the great differences between the several welded joints geometries tested and their loading conditions.

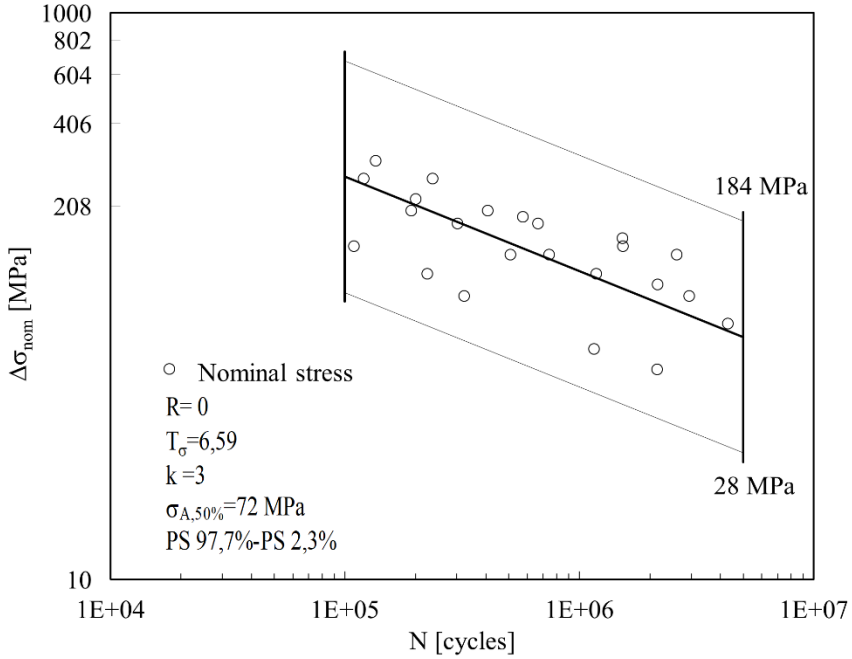

Figure 11.3: Nominal stress based S-N curve for welded joints.

From the finite element model of the welded joints geometries, during the post processing phase, the stress field along the bisector path has been retrieved and plotted versus the radial coordinate r in the bi-log graph of Figure 11.3. As an example, two nominal stress level for two different geometries have been reported. The power law regression has been performed and reported in the same graph. As it is possible to note, the exponent of the power law is equal to the Williams eigenvalue for mode I, which describes the singularity grade of the stress field around the notch tip. The other geometries for several nominal stress values exhibits the same trend and all the power law exponents are equal to the Williams eigenvalues.

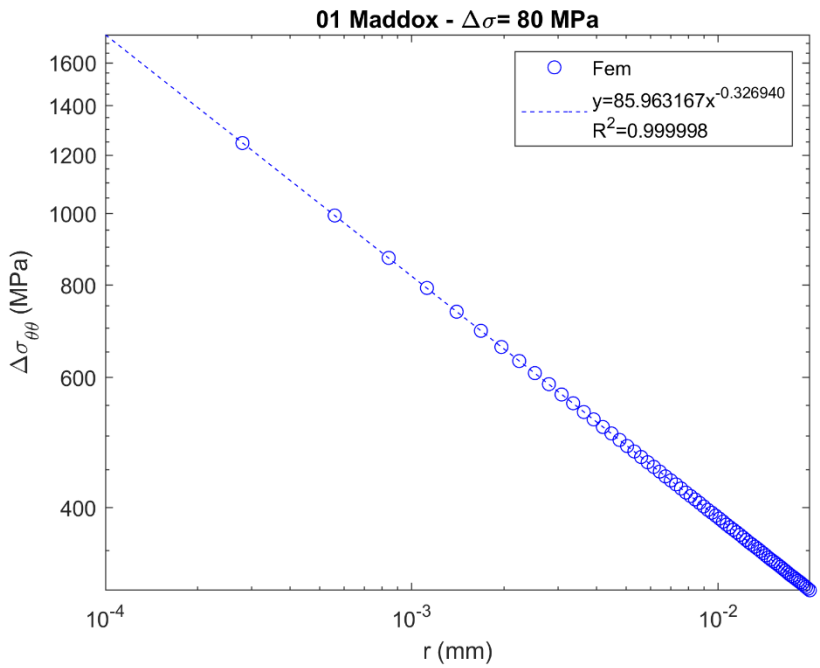

(a)

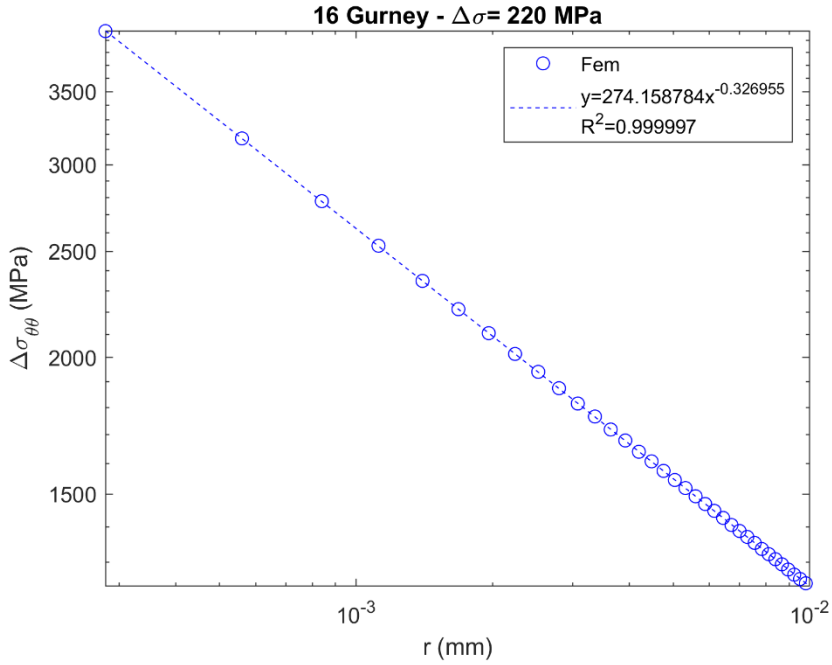

(b)

Figure 11.4: Stress fields along the opening angle bisector path form the notch tip.

In Figure 11.5 are reported the mode I NSIF values, estimated by the Gross and Mendelson definitions, versus the radial coordinate in a bi-log plot. Power law regressions have been performed and the ΔK_I values have been estimated as the power law coefficients, given the singularity of the stress field.

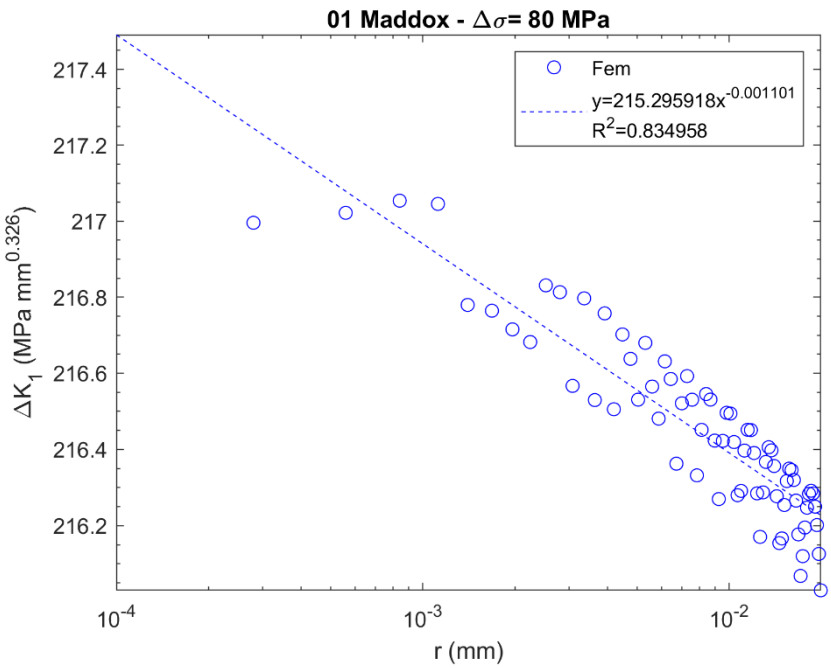

(a)

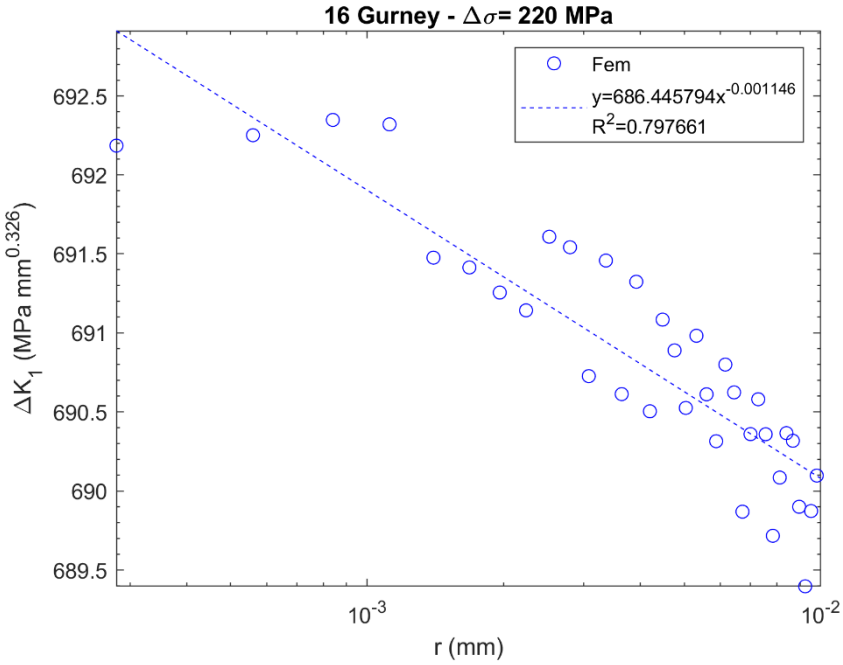

(b)

Figure 11.5: Mode I NSIF estimation by power law regressions.

The S-N curve in terms of mode I NSIF has been reported in Figure 11.6, after that all the experimental test of Table 11.1 have been elaborated in terms of the ΔK_1 value retrieved from the numerical simulations.

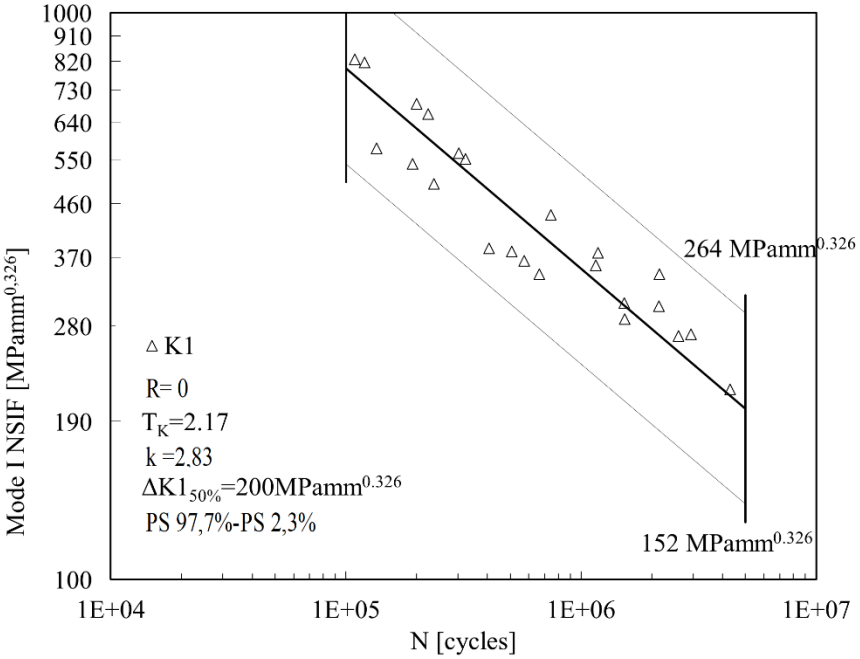

Figure 11.6: NSIF based S-N curve for welded joints.

The inverse slope of the S-N curve is equal to 2.83 and the scatter index for a PS of 97.7% is equal to T_K= 2.17; a lower value compared to the nominal stress scatter index. This is due to the ability of the NSIF to synthetize with a unique parameter, depending of the notch characteristics, the fatigue strength of very different geometries. The scatter index is higher compared to the value proposed in literature, but still acceptable [115].

Evaluating the average strain energy density over a control volume it is possible to overcome the limits of the NSIF approach, where it is not possible to compare with a unique parameter the fatigue failure danger from different notch types (e.g. toe and root failures). In Figure 11.7 the S-N curve in terms of SED has been reported. The inverse slope of the SED based S-N curve is equal to 1.43 and the scatter index evaluated in terms of SED ($T_W=T_\sigma^{0.5}$) for the PS of 97.7% is equal to 2.14. this value is lower compared to the nominal stress approach and quite similar to the NSIF value.

By adopting the PSM approach, the S-N curve for the welded joints has been elaborated and reported in Figure 11.8. The inverse slope is equal to k= 2.96, a value near the nominal stress approach and the ones proposed by the standards. The scatter index evaluated for a PS of 97.7% is equal to 1.9 (the same proposed in literature [115]), a value lower compared to the other local approaches. Hence also the PSM, as well as the other local approaches, is able to synthetize the

fatigue data of mechanical components regardless the whole geometry and the loading condition, but considering only the local stress field or energy configuration near a notch region.

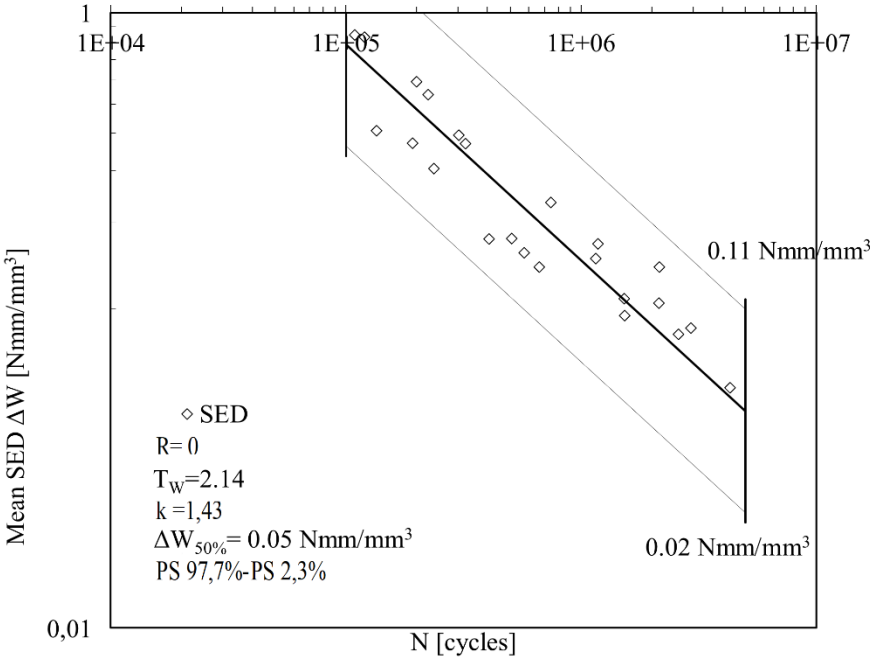

Figure 11.7: SED based S-N curve for welded joints.

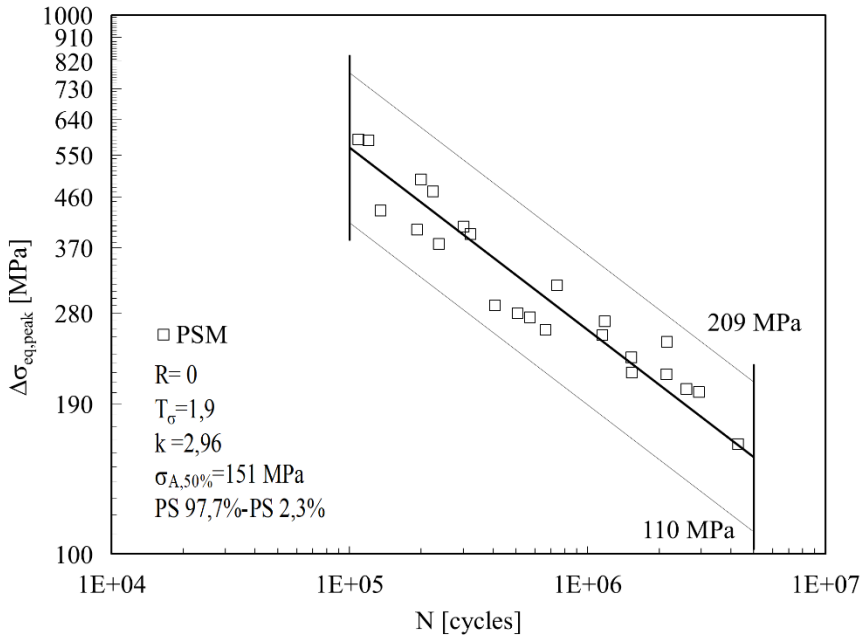

Figure 11.8: PSM based S-N curve for welded joints.

11.4. Conclusion

In this chapter several local approaches are adopted in order to estimate the fatigue life of welded joints. The experimental fatigue data of several class of cruciform and T joints under tensile and bending load conditions have been elaborated in order to obtain the S-N curve in terms of Notched Stress Intensity Factor (NSIF), Strain Energy Density (SED) over a control volume and Peak Stress Method approaches. These parameters have been obtained by means of linear elastic finite elements simulations.

The S-N curves based on local approaches have been compared to the nominal stress based ones. In terms of scatter index, the nominal stress approach shows a high data dispersions and the designer must adopt a specific S-N curve for each welded joint geometries and loading conditions. On the other hand, the local approaches are able to synthetize the fatigue data of several welded joint geometries under different loading conditions adopting only one S-N curve.

12. FATIGUE ASSESSMENT OF WELDED JOINT BY MEANS OF SED APPROACH AND COMPARISON WITH STANDARDS

Foti P, Santonocito D, Ferro P, Risitano G, Berto F. Fatigue assessment of common welded joints by means of the Strain Energy Density method. Under submission.

Highlights

The main aim of the present chapter is to investigate the effects of different parameters on the fatigue strength of cruciform and T-welded joints through an energetic approach based on the Strain Energy Density failure criteria.

The parameters taken into account in the present chapter for investigate the fatigue strength are the scale effect, the lack of welding bead penetration and the welding bead height.

The results of the numerical analysis carried out have been also compared with the fatigue strength predicted by the most known design guidance for the fatigue assessment of steel welded joints: Eurocode 3; British Standard; International Institute of Welding; Det Norske Veritas – Germanischer Lloyd (DNV-GL). These are among the most known standards for the fatigue assessment of steel welded joints.

From the comparison carried out is evident that the standards present some differences about the characterization of the details; besides it is not always clear. The standards do not consider each of the parameters taken into account in the present chapter that, instead, have an important role on the fatigue strength of the detail analysed and should not be neglected as shown through the numerical analysis carried out.

This research activity is part of the collaboration between the University of Messina and the Norwegian University of Science and Technology NTNU.

Nomenclature

a	load carrying welding throat [mm]

$2a, 2a_{int}$	lack of penetration, critical lack of penetration [mm]
$\bar{a}$	S-N curve constant according to DNV-GL standard
E	Young's modulus [MPa]
e_1, e_2, e_3	mode I, II and III functions of 2α in the SED expressions for sharp V-notches
F	remote applied force [N]
FAT	classes the permissible values of the nominal stress ranges at 2 million of cycles
$f_{(t)}$	scale factor according to BS and IIW standards
h	welding bead height [mm]
I_1, I_2	mode I and II functions in the SED expression for sharp V-notches
K^n_1, K^n_2	mode I and II notch stress intensity factors of a sharp V-notch.
K_{IC}	material toughness
k_s	scale factor
k	scale parameter
L	transverse plate thickness with bead height
L_{E3}	transverse plate thickness
l	welding length
m	inverse slope of FAT classes, power law regression exponent
N	number of cycles
n	scale exponent
R_0	control volume radius
r	radial coordinate
SED	strain energy density
t, t_{ref}, t_{eff}	plate thickness, reference plate thickness, effective plate thickness (DNV-GL)
$\widetilde{W}$	averaged Strain Energy Density
W_c	critical strain energy
2α	opening angle of V-notch
γ	supplementary angle of α

$\Delta\sigma_a$	fatigue strength of the butt ground welded joints
$\Delta\sigma_i$	nominal tensile stress
ΔK_{1A}^N	NSIF-based fatigue strength of welded joints
ΔW_i	critical value of the mean SED at working condition i
ΔW_L	critical value of the SED that corresponds to the fatigue limit
θ	angular coordinate
λ_1, λ_2	mode I and II Williams' eigenvalues for stress distribution at V-notches
ν	Poisson's ratio
σ_{ij}	ij component of the stress tensor
σ_t	maximum tensile stress
$\tilde{\sigma}_{ij}$	angular stress functions
σ_w	stress at welding throat
$\sigma_{\theta\theta}$, σ_{rr}, $\tau_{r\theta}$	stresses in polar coordinate system
χ_1, χ_2	auxiliary parameters, function of the opening angle

12.1. Introduction

The presence of a geometrical discontinuities in a component involve a localized stress concentration that could lead to the generation of a crack, affecting the assessed fatigue life of such a component.

Fatigue is the progressive structural damage due to the application of cyclic loads with variable-amplitude and, dealing with welded components, the problem is even more complex due to the welding process itself that involves many other defects and imperfections in addition to the geometrical discontinuity due to the welding.

Since it is impossible to obtain mechanical components without the presence of intrinsic defect in the material and of geometrical discontinuities, their effects on the assessed fatigue life of a component must be evaluated through specific, fast and reliable experimental [53,142] and numerical methods [180]to prevents fracture.

Even if the fracture mechanics have already shown that fatigue has a local nature, most of the standards [181–185] for fatigue assessment take mainly into account global design methods such as the nominal stress approach or the hot-spot approach [186,187] and in some cases they report some local methods only as a possibility for fatigue design without giving any data about the fatigue strength of the details analyzed through these others methods.

The nominal stress method considers external loads or nominal stresses in the critical cross-section and compares them with the S-N curves that correlate the fatigue strength, expressed by the amplitude of the nominal stress or also by the remotely applied loads, versus the number of cycles. As a matter of fact, the fatigue behavior of a component is given considering the influence of all peculiarities of a welded joint only in a statistical way; besides, considering how the experimental data are summarized, the fatigue strength suggested could only be used rigorously only dealing with details analyzed with the fatigue tests.

In order to generalize the method, the standards assume that the Wöhler curves of the component have the same inverse slope in a bi-logarithmic diagram and define the so-called FAT classes, whose value is given on the base of the shape, the loading conditions and the most relevant geometrical parameters of the detail considered (Figure 12.1).

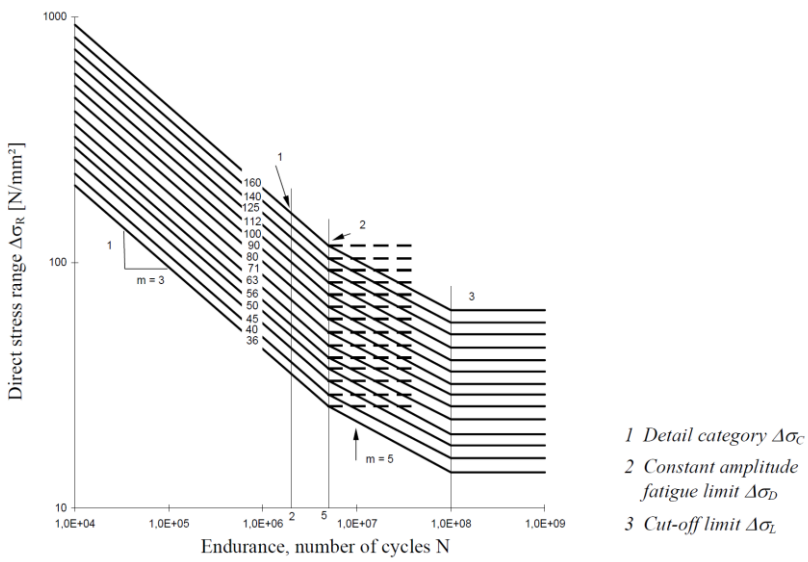

Figure 12.1: S-N curves of different FAT classes for fatigue assessment of welded joints, according to the Eurocode 3

As an alternative to the nominal stress approach, most of the standards suggest also the structural stress approach [181–185] whose main advantage is that only one FAT class must be

used depending on the type of weld. However, as discussed by Lazzarin et al. [188], this method has also some drawbacks; indeed, its application is limited to components whose failure is due to the weld toe and the determination of the structural stress, possible through different techniques, requires a certain expertise also because different structural stress approaches could be considered [189].

The difficulties in performing a more precise fatigue assessment make the methods discussed above widely appreciated even if they usually lead to an excessive conservative design as shown in Figure 12.2 where are reported the failure probability for many common standards. For the standards considered in the present chapter (Eurocode 3, British Standard, International Institute of Welding, DNV-GL) the failure probability is 2.3%.

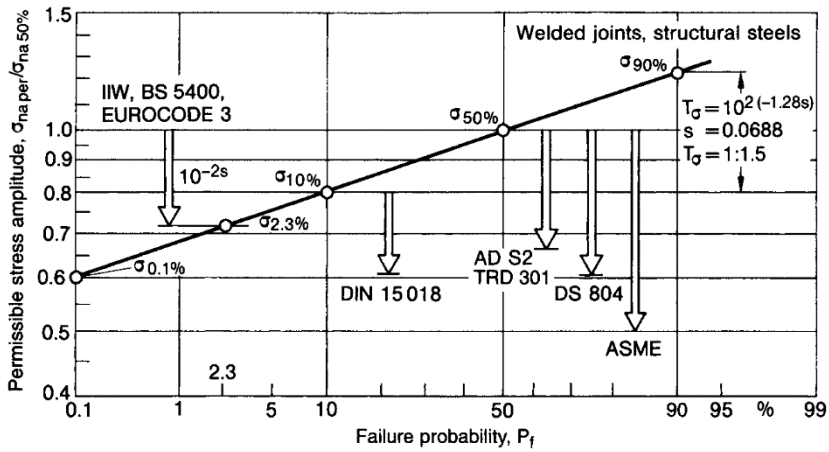

Figure 12.2: Failure probability for different standards [189].

Besides, it must be pointed out that the experimental validation of these methods is based on tests carried out on geometries and loading conditions rarely encountered also in common mechanical applications whose assessment, in this regard, lacks a statistical validation.

A more precise fatigue assessment can be carried out through the local approaches, although they require more expertise in their application.

Each of these methods is distinguished by the local parameter chosen to determine the fatigue strength [189]. As well as the methods suggested from the standards, also these methods neglect some welding peculiarities or deal with them in a statistical way but, even with these simplifications, they are able to give a more realistic evaluation of the fatigue strength and overcomes some problems of the global methods thanks to the possibility to consider the fatigue

strength found for a detail equal to that of any other components that presents locally a similar condition.

The main aim of the present chapter is to point out the discrepancies between the various standards dealing with two of the most common and tested welded joints, the cruciform and T joints, and to show the advantages that the application of a local method could lead dealing with the fatigue assessment of mechanical components.

In the present chapter we consider the local approach called Strain Energy Density (SED) method whose basic concepts are explained in section 3.2.

12.2. Fatigue assessment of Cruciform and T-joint by Standards

All the standards suggest, as principal fatigue assessment method, the nominal stress approach [182–185]. In the subparagraphs of section 3 we explain how the various standards, taken into account in the present chapter, treat the problem of fatigue with regard to cruciform and T-joints underlining the peculiarities of each method in suggesting the fatigue class of the detail with varying its principal geometrical parameters. The Figure 12.3 shows the geometrical parameters of the joints considered.

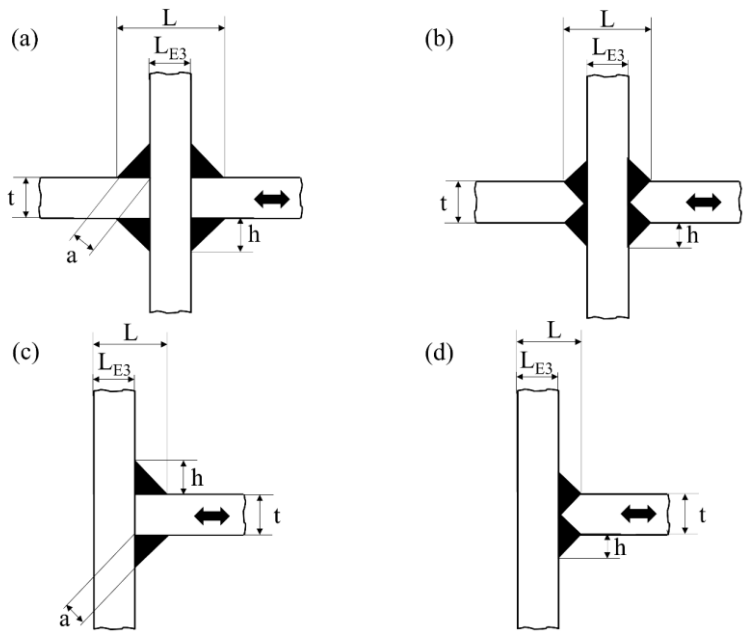

Figure 12.3: Main geometrical parameters for Cruciform joint with a) incomplete and b) complete penetration and for T-joint with c) incomplete and d) complete penetration.

12.2.1. Fatigue assessment by Eurocode 3

Among the European standards, the Eurocodes define the standards for constructions. The Eurocode 3 (EU3) in its ninth section deals with the assessment of fatigue resistance of members, connections and joints subjected to fatigue loading. Other standards, such as the British Standard [184], remands to the Eurocode for the fatigue assessment of steel building and civil engineering structures.

Dealing with welded joints, in general, the Eurocode 3 distinguishes several details reporting their geometrical shape and loading conditions: for each detail classified, it defines the FAT class for a set of its geometrical parameters and gives some simple rules to obtain the FAT class for any other set of geometrical parameters. In general, the reference case, for which the standard gives the FAT class, has a value of 25 mm for the principal geometrical parameter. The standard does not consider post fabrication treatments to improve the fatigue strength besides the stress relief. The data provided must be applied to structures under normal atmospheric conditions with enough corrosion protection and regular maintenance.

In order to evaluate the FAT class for a set of geometrical parameters different from the reference case, the standard suggests, in general, using the rule of the scale effect multiplying the FAT class reported for a correcting factor k_s evaluable as:

$$k_s = \left(\frac{t_{ref}}{t}\right)^n \tag{12.1}$$

where n is equal to 0.2 or 0.25 depending on the detail. Following the rule of the scale effect, for a detail with a principal geometrical parameter minor than 25 mm, the designer should expect a higher fatigue strength for the detail. This possibility is not excluded by the standard but, on the other hand, it states also that this must be proved by the designer himself through experimental tests carried out according to EN 1990.

In order to have a classification as simple as possible, the standard makes also the assumption that the Wöhler curve has, for every welded detail, an inverse slope of m= 3 between $1 \cdot 10^4$ and $5 \cdot 10^6$ cycles and an inverse slope of m= 5 between $5 \cdot 10^6$ and $1 \cdot 10^8$ cycles, as it is possible to see from Figure 12.1.

As regard cruciform and T-joints, the Eurocode 3 reports in a table the FAT classes for different sets of the ranges of their main geometrical parameters. For these joints the standard does not suggest the use of the scale effect law. In particular, the geometrical parameters used by the standard are the intermediate plate thickness L_{E3} and the attached load carrying plate thickness t reported in Figure 12.3.

The standard establishes also some requirements to use the FAT classes reported in its text. The joint must be inspected and found free from discontinuities and misalignments outside the tolerance of EN 1090. The misalignment of the load-carrying plates, for example, should not exceed 15% of the thickness of the intermediate plate.

As regard the same detail with partial penetration the standard requires also a double assessment. In this case both the weld root and toe must be verified. The weld toe assessment must follow the FAT classes established for the full penetration joint while for the weld root the FAT class suggested is of 36 MPa evaluating $\Delta\sigma_W$ as:

$$\sigma_w = F / \sum (a \cdot l) \tag{12.2}$$

Where l is the weld length and a the load carrying weld throat as shown in Figure 12.4.

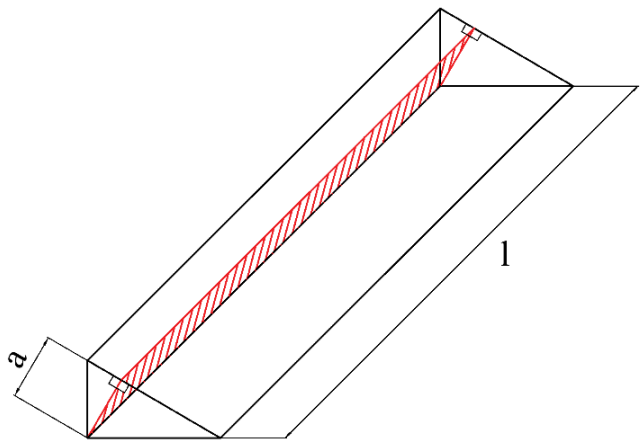

Figure 12.4: Welding beam parameters for incomplete penetration joints.

12.2.2. Fatigue assessment by British Standard and International Institute of Welding

Through [182] and [184], the International Institute of Welding (IIW) and the British Standard (BS) give the recommendations for the assessment of fatigue damage in welded components.

Differently from the Eurocode 3, the IIW standard gives also some data for the fatigue assessment of welded joints through local methods such as the threshold stress intensity factor range ΔK_{th} both for steel and aluminum.

As regards the nominal stress method, dealing with welded joints, the standards follow the methodology already explained for the Eurocode 3, classifying the details according to their shape and loading condition.

However, differently from the Eurocode 3, the BS and the IIW distinguish several cases for the S-N curve slope and the numbers of cycles to reach the constant amplitude fatigue limit (CALF) depending on the loading type but also on the application. In particular, for components that have to work in the field of very high cycle fatigue, such as rotating welded machine parts, the standard suggests for N> $1 \cdot 10^7$ a slope m=22 taking into consideration those experimental data that have pointed out that a CALF does not exist.

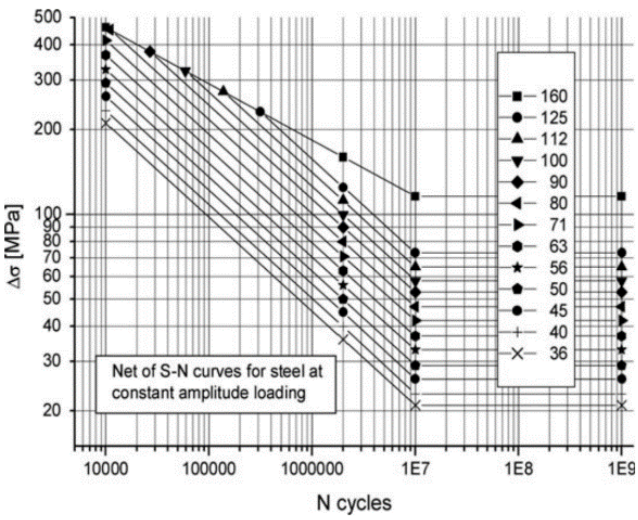

(a)

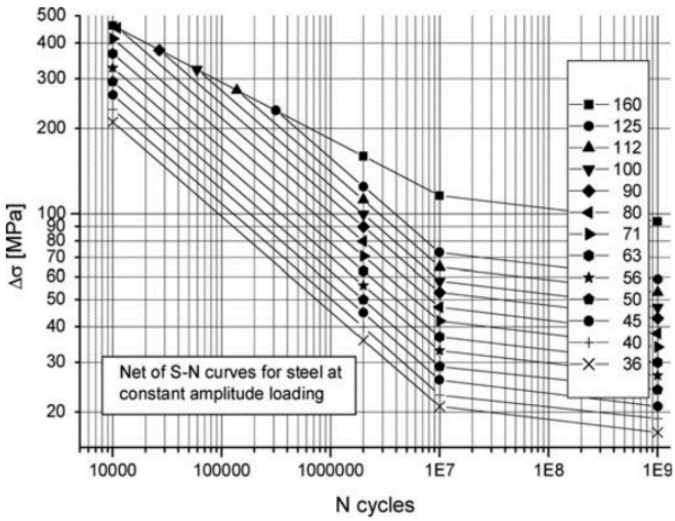

(b)

Figure 12.5: Fatigue resistance S-N curves for a) normal application and b) very high cycles applications according to IIW.

The standards underline also that the fatigue data provided must be considered valid only for those welded components that satisfy the quality parameter of the welding procedures and for welding procedures.

As regard the scale effect, the lower fatigue strength for thicker members is taken into consideration by multiplying the FAT class of the structural detail (for cruciform joints 68 MPa for BS; 71 MPa for IIW) by the thickness reduction factor $f_{(t)}$:

$$f_{(t)} = \left(\frac{t_{ref}}{t_{eff}}\right)^n \tag{12.3}$$

Where the reference thickness t_{ref}= 25mm. As regards the determination of t_{eff}, the BS and IIW rules to determine it are reported in equation (12.4):

$$if \quad \frac{L}{t} < 2 \quad then \quad t_{eff} = t \tag{12.4}$$

$$if \quad \frac{L}{t} \geq 2 \quad then \quad t_{eff} = \max[0.5 \cdot L; t]$$

Where L and t are the parameters reported in Figure 12.3.

Different correction exponents depending on the kind of joint analysed and on the welding condition (as welded or toe grounded) are suggested by this standard. For the joints analyzed in the present chapter, considered in as welded condition, the n exponent suggested is 0.25 for BS and 0.3 for IIW.

The IIW, for both the cruciform and the T-joint, distinguishes three different cases: full penetration; partial penetration with potential failure from weld toe; lack of penetration with potential failure from weld root with a/t≤1/3.

For the last two cases the standard expects the verification of both root and toe to establish which is the critical point of the welding.

As regard the assessment of the welding with lack of penetration the verification must be done through the stress evaluated in the weld throat according to equation (12.2) and Figure 12.4.

12.2.3. Fatigue assessment by DNV-GL

The DNV-GL standard [185] deals with the fatigue design of offshore steel structures. As regards the nominal stress method, dealing with welded joints, the standard follows the methodology already explained for the Eurocode 3, classifying the details according to their shape and loading condition. For each detail classified, the standard indicates, for a set of its geometrical parameters, which fatigue master curve must be used for its assessment. The standard tabulates the coefficients needed to define the fatigue master curve that has in general a bi-linear trend in a double logarithmic diagram.

In order to evaluate the FAT class for a set of geometrical parameters different from the reference case, similar to the other standards, the DNV-GL suggests, in general, using the rule of the scale effect, reported in equation (12.5), adjusting the reference fatigue master curve through the effective thickness of the component according to the following equation:

$$\log N = \log \bar{a} - m \log \left[\Delta\sigma \left(\frac{t_{eff}}{t_{ref}} \right)^k \right] \tag{12.5}$$

Where the reference thickness is equal to t_{ref}= 25mm and the parameters $\bar{a}$, m and k are tabulated by the standard. Different correction exponents, k, depending on the kind of joint analysed are suggested by this standard. For the joints analyzed in the present chapter the exponent suggested is 0.20 for t≤ 25 mm, 0.25 for t> 25 mm both in full and in partial penetration condition.

As regards the parameter t_{eff} in equation (12.5) the standard rules to determine it are reported in the following equation:

$$t_{eff} = \min\big((14\,mm + 0.66 \cdot L), t\big) \tag{12.6}$$

where L and t are the parameters reported in Figure 12.3.

For both the cruciform and the T-joint, the standard distinguishes three different cases to be assessed following the same procedure explained in section 12.2.2: full penetration; partial penetration with potential failure from weld toe; lack of penetration with potential failure from weld root.

As regards the partial penetration welds that are affected by competing failure from weld toe and root, differently from the other standards taken into account in the present chapter, the DNV-GL standard in its section 2.8 deals with the penetration effect on cruciform joints, even if its contribution remains still very limited. The equi-probability failure curve from toe and root regions are reported in a welding beam height vs. lack of penetration graph, normalized respect to the plate thickness (Figure 2.15 of the standard), reported here in Figure 12.6.

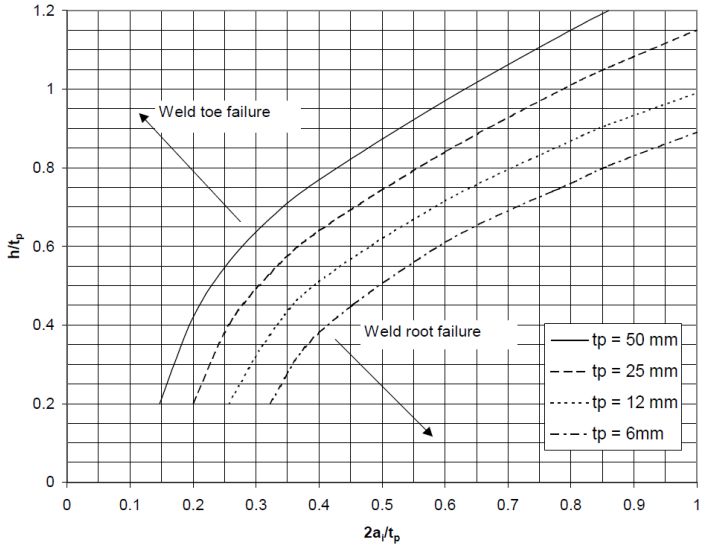

Figure 12.6: Probability curves of root failure equal to toe failure with geometrical parameters describing the welded joint according to DNV-GL.

12.3. Finite elements modelling

Due to the large number of simulations, a parametric 2-D finite element model was created adopting Ansys APDL. Dealing with welded joints it is important to make some considerations about the shape of the welding. Indeed, the weld bead geometry cannot be precisely defined because of the bead shape and the toe radius that vary with the welding process itself and its technical parameters. Anyway, the conventional welding techniques result in very small value for the toe radius ranging from 0.2 mm to 0.8 mm and in a typical opening angle of $2\alpha = 135°$. Considering the typical ranges of the geometrical parameters of a real steel welded joint it is allowed to simplify the model describing the welding as an ideally sharp V-notch. Other geometrical parameters taken into account in the model were the thickness t, the transverse thickness L_{E3}, the weld bead height h and the lack of penetration 2a. In order to minimize the computational time and complexity of the system, the symmetries of the details were considered, modelling only a quarter of the geometry for the cruciform joint (Figure 12.7). The system was modelled under plain strain condition adopting quadrilateral 8-node elements of the type PLANE183.

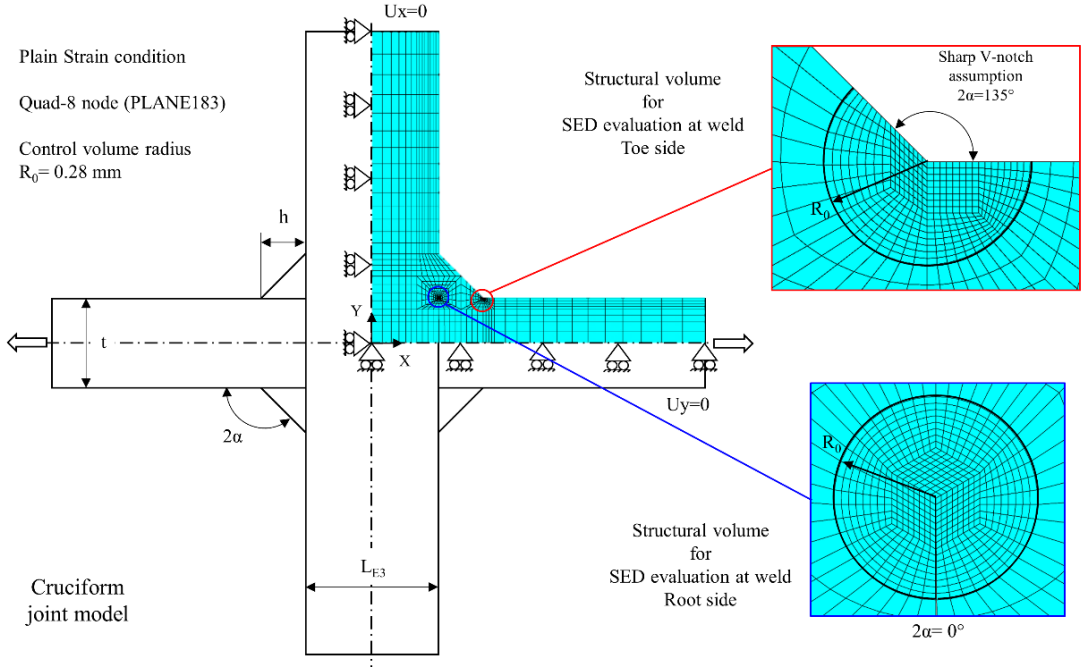

Figure 12.7: Parametric finite element model

According to the SED approach, a control volume was built in correspondence of the toe and root regions adopting a radius R_0= 0.28 mm, determined through equation (3.31) using data taken by literature [190], and with material properties typical for structural steel (E= 206 GPa, ν= 0.3). A mapped mesh was built and after a convergence analysis a number of 96 elements for the control volume was adopted as a good trade-off between results accuracy and computational time. In Table 12.1 are reported the SED values evaluated at the toe region for a specified geometry. It is possible to predict with a good precision the SED value even with a low number of elements inside the control volume due to the fact that it is derived directly from the nodal displacements [191]. As the FE model is parametric, it was possible to perform a sensitivity analysis of the geometrical parameter on the SED values estimated at toe and root regions. The L_{E3}, t and h values were varied in several ways, as well as the lack of penetration of the welding 2a. The same results obtained for cruciform joints can be applied also to T-joints.

Table 12.1: Convergence analysis on the SED value.

No.FE Rc	ΔW_{toe} [Nmm/mm^3]	Δ [%]
6	0.039579	1.85
24	0.040351	-0.06
96	0.040299	0.06
384	0.040310	0.04
1536	0.040320	0.01
6144	0.040325	ref.

12.4. Results and discussions

12.4.1. Main geometry effect

A first series of FE simulations has been carried out on the cruciform joint geometry considering two limit conditions: full penetration (FP), 2a= 0, and incomplete penetration (IP), 2a= t. In the first condition, the welding bead has completely penetrated inside the plate thickness, ensuring the safer working condition, i.e. the macro-crack in the root region it is not present. In the latter condition, the welding bead has not penetrated inside the plates, hence it is the most dangerous working condition. In this case, both the toe and root regions have to be considered for the evaluation of the SED. The transverse plate thickness L_{E3} and the plate thickness t were varied, fixing one of them and changing the other one. The SED vs. L_{E3} and SED vs. t curves were fitted with power laws, respectively $\Delta W= c \cdot t^m$ and $\Delta W= c \cdot L_{E3}^m$. In Figure 12.8 are reported the SED curves, evaluated at toe region, for the full penetration condition. Generally, the higher the plate thickness t, the higher the SED value. As is possible to see in Figure 12.8a, the SED value slightly change with L_{E3} up to a value of 160 mm, then it became almost constant. As regard the plate thickness t (Figure 12.8b), the SED value severally increases as t increases. Also here, the higher the transverse plate thickness, the higher the SED value, up to L= 80 mm; after, the trend slightly change from each other. For the full penetration working condition, the SED value at toe region is more sensitive to the plate thickness t.

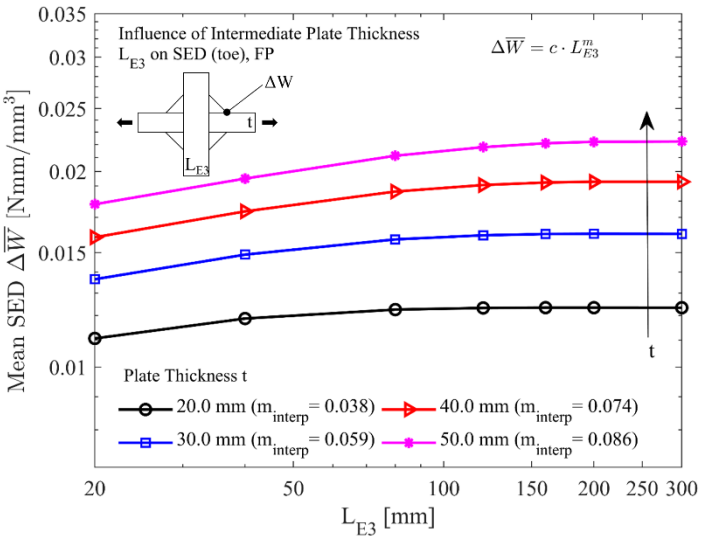

(a)

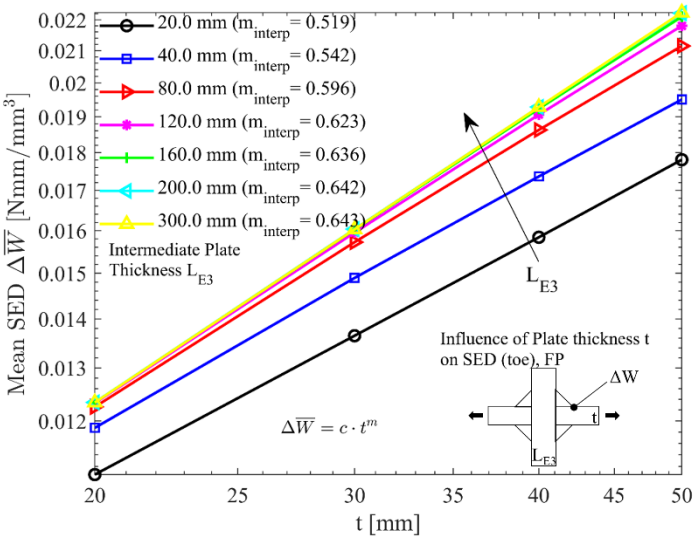

(b)

Figure 12.8: Effect of the geometry on the SED value of cruciform joints with full penetration.

In Figure 12.9, the SED trend for the incomplete penetration working condition are reported. For the root region (Figure 12.9a, b), the SED shows a very slight decrease with the transverse plate thickness L_{E3}, while it is more sensitive to the plate thickness t where it exhibit an increasing trend. Regarding to the toe region (Figure 12.9c, d), a similar behavior is shown. The plate

thickness t is the more critical geometrical parameter for the SED estimated at root, with a quasi linear increase (m~ 1), and toe regions (m~ 0.675).

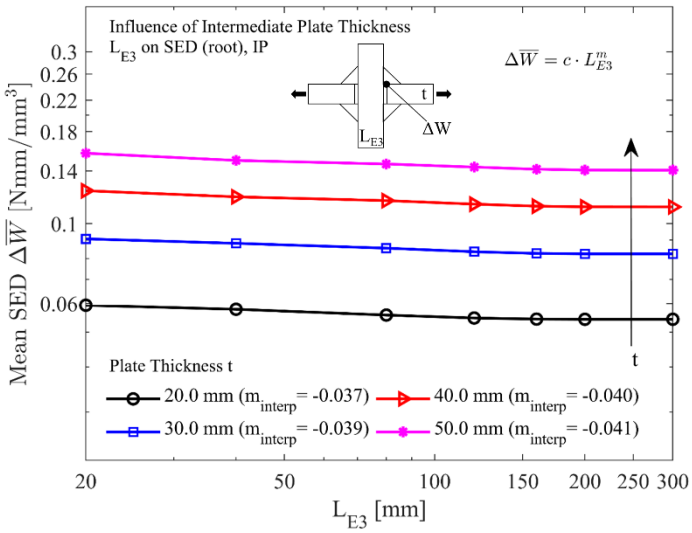

(a)

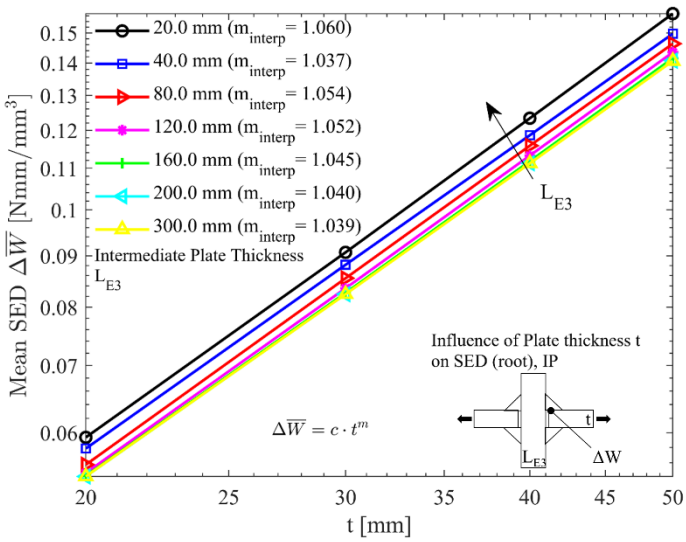

(b)

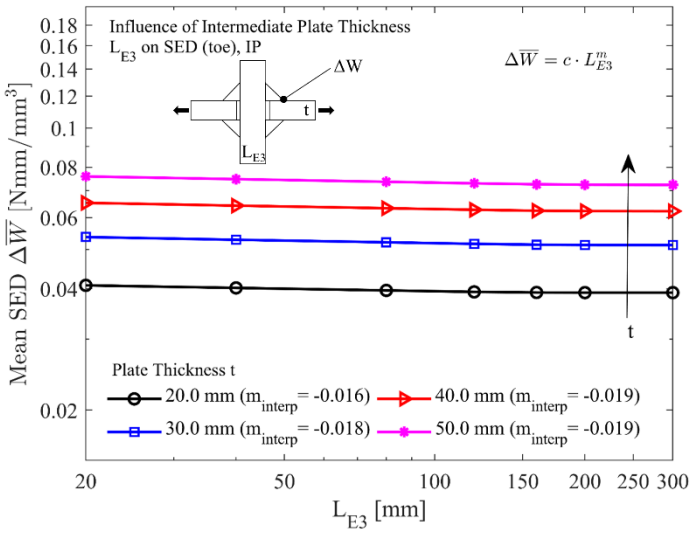

(c)

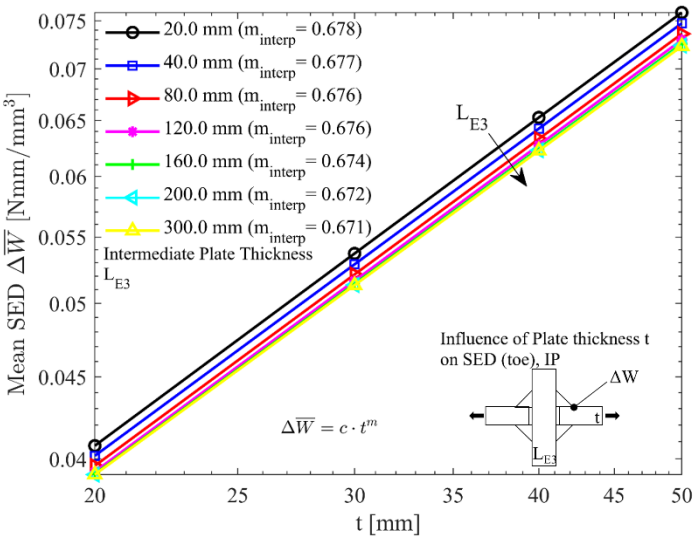

(d)

Figure 12.9: Effect of the geometry on the SED value of cruciform joints with incomplete penetration.

12.4.2. Scale effect

A second series of simulations was carried out on cruciform joint geometries with different t/L_{E3} ratio, varying the dimension of t and L_{E3} according to a scale parameter k (= 1, 2, 4, 8, 16). The mean SED value has been reported vs. the plate thickness t. A logarithmic interpolation on the curve has been performed according to the scale effect equation, evaluating the λ_1 parameters. In Figure 12.10 the SED trend evaluated at the toe and root regions in full penetration and incomplete penetration configuration for two different geometries have been reported. For the SED trend at toe and root region, a value of the λ_1 parameters respectively of 0.673 and 0.499 has been obtained.

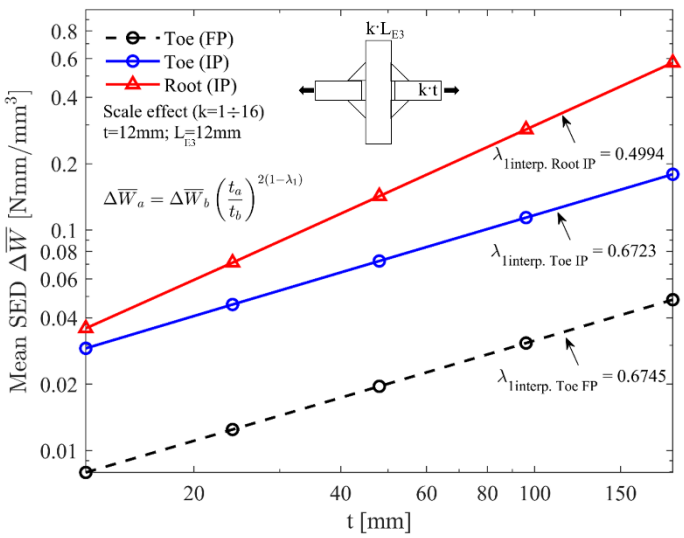

(a)

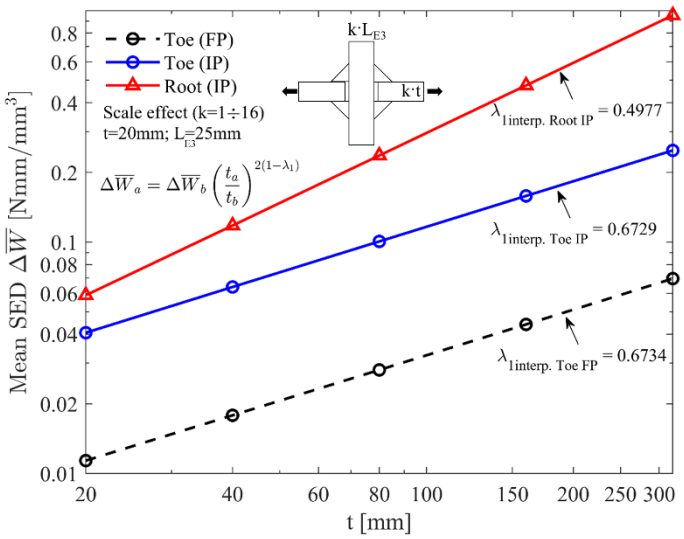

(b)

Figure 12.10: Scale effect on SED of different cruciform joint geometries.

In Table 12.2, the values of the λ_1 parameters for several cruciform joint geometric configuration of t and L_{E3}, with different t/L_{E3} ratio, have been reported. They are in good agreement with the mode I Williams' eigenvalues for a notch opening angle of 2α= 135° (toe region) and 2α= 0° (root region). Therefore, the SED approach is able to catch the scale effect on the joint geometries. The adoption of the Williams' eigenvalues for the scale effect also in the nominal stress method could lead to a better representation of the joints fatigue life.

Table 12.2: Estimated values of the λ_1 parameters under scale effect for different geometric configurations.

t/L_{E3}	Full Penetration (FP)	Incomplete Penetration (IP)	
	λ_1 interpolation Toe	λ_1 interpolation Toe	λ_1 interpolation Root
0.5	0.6747	0.6720	0.4994
0.8	0.6734	0.6729	0.4977
1	0.6745	0.6723	0.4994
1.2	0.6738	0.6728	0.4983
1.5	0.6743	0.6726	0.4995

12.4.3. Full, partial and incomplete penetration

In order to assess the effect of the lack of penetration on SED, a series of FE simulations were carried out varying the 2a parameter on different cruciform joints configurations. In Figure 12.11 the SED trend at toe and root regions for two geometries have been reported vs. the lack of penetration 2a expressed as percentage of the plate thickness t. For lower values of the lack of penetration, the SED evaluated at toe region shows higher value compared to the SED at root region.

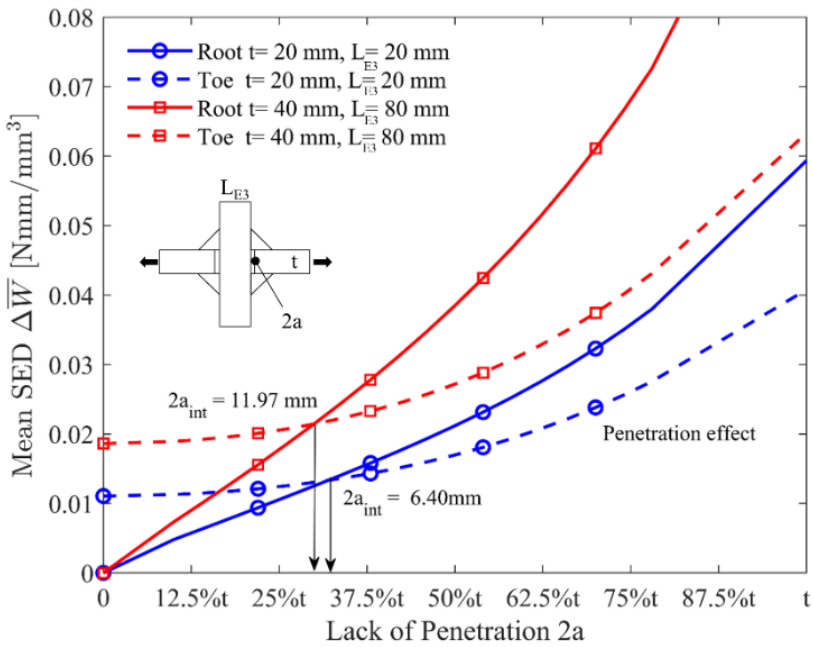

Figure 12.11: Effect of the lack of penetration 2a on SED.

As the lack of penetration increases, the SED values at toe and root region became equal, then the root SED shows higher value compared to the toe SED. The lack of penetration value corresponding to intersection of the two SED values, is indicated as $2a_{int}$ and it changes with the geometries.

Table 12.3: Critical values of SED and fatigue limit for partial penetration cruciform joints.

L_{E3} [mm]	t [mm]	$2a_{int}$ [mm]	2a/t [%]	ΔW_{root} IP [Nmm/mm^3]	ΔW_{toe} FP [Nmm/mm^3]	$\Delta W_{intersection}$ PP [Nmm/mm^3]	$\Delta\sigma_{L\ root}$ IP [MPa]	$\Delta\sigma_{L\ toe}$ FP [MPa]	$\Delta\sigma_{L\ int}$ PP [MPa]
20	20	6.40	31.99	0.0594	0.0111	0.0133	29.66	68.68	62.56
	30	7.04	23.46	0.0907	0.0136	0.0154	23.99	61.84	58.29
	40	7.73	19.32	0.1234	0.0158	0.0173	20.57	57.41	54.87
	50	8.46	16.91	0.1568	0.0178	0.0192	18.25	54.14	52.14
40	20	8.11	40.54	0.0579	0.0119	0.0153	30.04	66.30	58.44
	30	8.91	29.72	0.0882	0.0149	0.0173	24.33	59.20	54.93
	40	9.55	23.89	0.1187	0.0174	0.0193	20.97	54.83	51.97
	50	10.12	20.23	0.1497	0.0195	0.0212	18.67	51.73	49.61
80	20	9.44	47.21	0.0558	0.0123	0.0168	30.60	65.26	55.71
	30	10.88	36.27	0.0855	0.0157	0.0191	24.71	57.62	52.22
	40	11.97	29.93	0.1158	0.0186	0.0214	21.23	52.94	49.36
	50	12.82	25.63	0.1464	0.0211	0.0235	18.89	49.68	47.09
120	20	9.94	49.68	0.0547	0.0123	0.0174	30.89	65.07	54.84
	30	11.74	39.13	0.0835	0.0160	0.0199	25.00	57.21	51.24
	40	13.19	32.98	0.1132	0.0191	0.0224	21.47	52.33	48.27
	50	14.34	28.68	0.1435	0.0218	0.0247	19.07	48.93	45.96
160	20	10.11	50.55	0.0543	0.0123	0.0175	30.99	65.04	54.56
	30	12.12	40.41	0.0827	0.0160	0.0202	25.13	57.08	50.84
	40	13.82	34.56	0.1118	0.0192	0.0229	21.61	52.10	47.78
	50	15.23	30.45	0.1416	0.0221	0.0253	19.20	48.60	45.40
200	20	10.14	50.71	0.0543	0.0123	0.0176	31.01	65.04	54.51
	30	12.23	40.78	0.0824	0.0160	0.0203	25.17	57.06	50.74
	40	14.07	35.18	0.1113	0.0193	0.0230	21.66	52.03	47.61
	50	15.65	31.29	0.1408	0.0222	0.0256	19.26	48.47	45.15
300	20	10.14	50.68	0.0543	0.0123	0.0176	31.01	65.05	54.53
	30	12.24	40.82	0.0824	0.0160	0.0203	25.17	57.07	50.74
	40	14.13	35.34	0.1112	0.0193	0.0231	21.66	52.03	47.57
	50	15.80	31.61	0.1407	0.0222	0.0257	19.26	48.44	45.09

In Table 12.3, for different geometric configurations the intersection values of the lack of penetration $2a_{int}$, of the SED evaluated at root and toe region respectively for IP and FP configuration, and of the critical SED for partial penetration joints, as well as their corresponding fatigue limit in terms of nominal applied stress level have been reported. Generally, increasing the plate thickness t and the transverse plate thickness L_{E3} dimensions increases the SED value and, hence, reduces the nominal stress level. It would be better, for the cruciform joint, to maintain the lack of penetration of the welding bead lower than the $2a_{int}$ value in order to have fatigue failure only at toe region, a simpler region to inspect compared to the root.

Simulations have been carried out on cruciform geometries where three values of t and L_{E3} were combined. The lack of penetration 2a and welding beam height h values have been adopted in order to obtain a joint geometrical configuration that, according to the DNV-GL standard, correspond to the equi-probability conditions for the fatigue failure from toe and root regions. The SED values at toe and root regions were evaluated and compared between them.

Table 12.4: Effect of the penetration. Comparison with standard.

L_{E3} [mm]	t [mm]	h/t	2a/t	ΔW_{root} [Nmm/mm^3]	ΔW_{toe} [Nmm/mm^3]	$\Delta_{root-toe}$ [%]
12	12	0.4	0.34	0.0098	0.0098	-0.45
		0.5	0.40	0.0104	0.0105	-1.58
		0.6	0.48	0.0111	0.0112	-1.01
	25	0.4	0.26	0.0158	0.0131	16.74
		0.5	0.30	0.0162	0.0142	11.99
		0.6	0.36	0.0169	0.0152	9.95
	50	0.4	0.20	0.0228	0.0175	22.92
		0.5	0.22	0.0224	0.0192	14.43
		0.6	0.28	0.0247	0.0211	14.56
25	12	0.4	0.34	0.0086	0.0104	-20.64
		0.5	0.40	0.0093	0.0109	-17.64
		0.6	0.48	0.0100	0.0114	-13.11
	25	0.4	0.26	0.0147	0.0143	2.76
		0.5	0.30	0.0154	0.0151	2.31
		0.6	0.36	0.0166	0.0158	4.58
	50	0.4	0.20	0.0242	0.0193	20.28
		0.5	0.22	0.0240	0.0205	14.37
		0.6	0.28	0.0266	0.0221	16.72
50	12	0.4	0.34	0.0079	0.0107	-35.14
		0.5	0.40	0.0085	0.0111	-30.30
		0.6	0.48	0.0092	0.0114	-24.03
	25	0.4	0.26	0.0129	0.0153	-18.58
		0.5	0.30	0.0137	0.0158	-15.61
		0.6	0.36	0.0148	0.0163	-9.69
	50	0.4	0.20	0.0220	0.0212	3.48
		0.5	0.22	0.0221	0.0220	0.49
		0.6	0.28	0.0253	0.0231	8.52

It is worth underlining that the standard does not specify some important geometrical parameters characterizing the welded joint, in particular the parameters L_{E3} and t in Table 12.4. For geometries where the plate thickness t is equal to the transverse plate thickness L_{E3}, the differences between the SED evaluated in the two regions is lower than 8.52% showing a very good agreement between the standard and the SED method. Considering that the standard does not give precise indication about these parameters the assumption L_{E3}= t seems reasonable for

the diagram reported in Figure 12.6. Generally, the bigger the dimensions of the joint, the bigger the relative difference of the SED values.

12.4.4. Welding Bead Height

Even if the effect of the welding bead height has been analysed [111,192,193], revealing possible beneficial effect on the fatigue class of welded joints, the standards taken into account in the present work do not consider the effect of the welding bead height (like the Eurocode 3). At least they take it into account without distinguish between the welding bead height and the plate thickness, considering directly the parameter L reported in Figure 12.3. The influence of the welding bead height h on the fatigue strength of the joint analysed has been evaluated though the SED method by means of FE simulations on incomplete penetration geometries, where the h/t ratio has been varied maintaining the plate thickness t and transverse plate thickness L_{E3} fixed (Table 12.5). The same behavior is exhibited by the same scaled geometry. The h/t ratio equal to 0.5 has been taken as the reference value. For lower values of the h/t ratio the fatigue life is severally reduced, up to -41% and -46% respectively for the root and toe region. An increase of the welding beam height has a beneficial effect on the fatigue life of the joint.

Table 12.5: SED vs. welding bead height.

h/t	ΔW_{root} [Nmm/mm^3]	ΔW_{toe} [Nmm/mm^3]	$\Delta\sigma_{L\ root}$ [MPa]	$\Delta\sigma_{L\ toe}$ [MPa]	Δ_{root}	Δ_{toe}
0.2	0.1687	0.1401	17.59	19.30	-41	-46
0.3	0.1083	0.0825	21.96	25.15	-26	-30
0.4	0.0777	0.0558	25.92	30.59	-13	-15
0.5	0.0594	0.0408	29.66	35.78	ref	ref
0.6	0.0472	0.0316	33.26	40.64	12	14

12.4.5. Comparison between the Standards and the SED Method

In this section a comparison between the FAT classes suggested by the standards and the estimations by the SED method are presented for the joint class considered. The comparison is made considering different values of the parameters L_{E3} and t (Figure 12.3), in the ranges suggested by the Eurocode 3 and considering a welding bead height equal to h= 0.5t . The full penetration condition for cruciform joints has been taken into account and the FAT classes proposed by the standards are reported in Table 12.6 with also the proposed FAT classes by SED approach and their relative variances. Even if the standards define the FAT classes with different probability of survival (PS 95% Eurocode 3 and IIW; PS 97.7% BS and DNV-GL) and considering the usual scatter of fatigue tests, the difference in terms of stress is less than 2% and

may be neglected in several areas of applications [182]. For smaller values of L_{E3} and t, generally the FAT classes proposed by the Eurocode 3 are higher compared to the SED method, but they are also higher compared to the other three standards.

Table 12.6: FAT classes comparison between the different standards and the SED method for full penetration cruciform joints.

L_{E3} [mm]	t [mm]	EU3 PS=95% [MPa]	BS PS=97.7% [MPa]	IIW PS=95% [MPa]	DNV-GL PS=97.7% [MPa]	SED $\Delta\sigma_L$ [MPa]	$\Delta_{SED-EU3}$ [%]	Δ_{SED-BS} [%]	$\Delta_{SED-IIW}$ [%]	$\Delta_{SED-DNV\ GL}$ [%]
20	20	80	68.00	71.00	62.97	68.68	-16.5	1.0	-3.4	8.3
	30	80	64.97	67.22	60.63	61.84	-29.4	-5.1	-8.7	2.0
	40	80	60.46	61.66	58.67	57.41	-39.3	-5.3	-7.4	-2.2
	50	80	57.18	57.67	57.00	54.14	-47.8	-5.6	-6.5	-5.3
40	20	80	64.97	67.22	58.67	66.30	-20.7	2.0	-1.4	11.5
	30	80	62.51	64.18	57.00	59.20	-35.1	-5.6	-8.4	3.7
	40	80	60.46	61.66	55.53	54.83	-45.9	-10.3	-12.5	-1.3
	50	80	57.18	57.67	54.24	51.73	-54.6	-10.5	-11.5	-4.8
80	20	71	57.18	57.67	53.08	65.26	-8.8	12.4	11.6	18.7
	30	71	55.83	56.04	52.04	57.62	-23.2	3.1	2.7	9.7
	40	71	54.63	54.60	51.10	52.94	-34.1	-3.2	-3.1	3.5
	50	71	53.55	53.30	50.23	49.68	-42.9	-7.8	-7.3	-1.1
120	20	56	52.57	52.13	49.43	65.07	13.9	19.2	19.9	24.0
	30	56	51.67	51.06	48.69	57.21	2.1	9.7	10.7	14.9
	40	56	50.84	50.09	48.01	52.33	-7.0	2.8	4.3	8.3
	50	56	50.08	49.18	47.37	48.93	-14.4	-2.3	-0.5	3.2
160	20	56	49.37	48.35	46.77	65.04	13.9	24.1	25.7	28.1
	30	50	48.70	47.57	46.20	57.08	12.4	14.7	16.7	19.1
	40	50	48.08	46.84	45.67	52.10	4.0	7.7	10.1	12.3
	50	50	47.50	46.16	45.17	48.60	-2.9	2.3	5.0	7.1
200	20	56	46.95	45.52	44.69	65.04	13.9	27.8	30.0	31.3
	30	50	46.43	44.92	44.24	57.06	12.4	18.6	21.3	22.5
	40	45	45.94	44.35	43.81	52.03	13.5	11.7	14.8	15.8
	50	45	45.47	43.81	43.40	48.47	7.2	6.2	9.6	10.5
300	20	56	42.75	40.68	40.98	65.05	13.9	34.3	37.5	37.0
	30	50	42.43	40.31	40.69	57.07	12.4	25.7	29.4	28.7
	40	45	42.11	39.95	40.40	52.03	13.5	19.1	23.2	22.3
	50	40	41.81	39.60	40.13	48.44	17.4	13.7	18.3	17.2

The FAT classes proposed by the Eurocode 3 standard for L_{E3} values in the range 20÷80 mm are more conservative compared to the SED method. This can lead to an over dimensioning of the joints. On the other hand, for $L_{E3} \geq 120$ mm, the SED FAT classes are higher compared to the relative Eurocode 3 classes. Lower differences are reported increasing the t values. The British Standard shows relative variations compared to the SED method within about the absolute 10%

range for $L_{E3} \leq 40$ mm. As the L_{E3} values increases, the relative variations increase but, as the t values increases, it shows a decreasing trend. The same behavior of the British Standard is exhibited by the IIW standard. The DNV-GL standard has relative variations within the 11.5% range for $L_{E3} \leq 40$ mm, then it increases with the same trend of BS and IIW standard. For $L_{E3} \geq 120$ mm, the SED FAT classes show higher values compared to the other standards classes, especially for lower t values.

12.5. Conclusion

In the present work a comparison between several standards (Eurocode 3, BS, IIW and DNV-GL) for the fatigue design of welded joints, which adopt the nominal stress approach, and the Strain Energy Density method has been carried out. Finite element simulations have been performed on several cruciform joint geometries in order to obtain the SED value averaged over a control volume in critical areas. The main outcomes are the following:

- The influence of the cruciform joint main geometrical parameters on fatigue life has been assessed, showing how the plate thickness t severally affect it compared to the transverse plate thickness L_{E3}.
- The scale effect for this joint class can be predicted adopting the mode I Williams' eigenvalues for typical toe (2a= 135°) and root (2a= 0°) notch configurations.
- The influence of the welding bead penetration on the joint fatigue life has been assessed through the SED method, where the standards provide incomplete, or do not provide at all, information. The method is able to individuate the critical values of lack of penetration where the root failure is more critical compared to toe failure.
- The welding bead height influence on the fatigue life of the joint has been investigated showing how an increase of its dimension is beneficial for fatigue life.
- A comparison of the FAT classes indicated by the standards and the SED method has been carried out showing how the standards overestimates or underestimate the fatigue strength of the welded joint considered, given the fact that they neglect some parameters that instead reveal an important influence on the fatigue life.

The SED method allows the designer, adopting finite element simulations, to assess in an easy way the critical areas of the welded joints under study regardless particular effects, such as scale effect or lack of penetration, that are already taken into account within this energetic approach.

CONCLUDING REMARKS

The work presented in this Ph.D. thesis is the synthesis of the intense activity research, performed over a period of three years, in the field of rapid fatigue assessment of materials adopting energy based approaches.

Most of the research activities have been presented in international and national conferences and published in peer reviewed journals.

The main aim of the research activities performed has been the application of the Risitano Thermographic Method (TM) and the Static Thermographic Method (STM), as well as the averaged Strain Energy Density approach on several materials and mechanical components.

The adoption of the Infrared thermography, to monitor the specimen surface temperature during a fatigue test, can reduce of several order of magnitude the test time to derive the fatigue limit and the S-N curve of the material. In particular, by side of the Thermographic Method, the Static Thermographic Method allows to derive in a rapid way the fatigue limit of the material evaluating the first deviation from the linearity of the thermoelastic effect.

The Static Thermographic Method has been applied on several materials. On plain structural steel specimens, as well as on notched specimens of medium carbon steel, it has been compared to TM and traditional fatigue tests showing good agreement. On plain specimens of C45 medium carbon steel, it has been compared with several other energetic methods, within a round robin activity of several Italian Universities, showing its ability to predict a reliable value of the fatigue limit. The monitoring of high strength concrete specimens under static compression test by means of the STM has allowed to detect the beginning of microfailure mechanism within the material. The STM has been also applied on plastic materials, such as high-density polyethylene, ad 3D printed material PA12. A link between the internal microstructure of the material, its microfailure mechanism and its macroscopic energetic release has been developed on composite material PA66GF35.

Within the local approaches, the Strain Energy Density approach allows to synthetize the results of fatigue data of notched components adopting a single design curve. This aspect is particularly useful when dealing with notched mechanical components, such as welded joints, whose design is defined by standards that do not take into account several parameters which may affect the fatigue life of the component.

The development and application of energy based approaches is still under growth. A future perspective may be the link between the experimental energetic release, both under fatigue and static tests assessed by means of TM and STM approaches, with the evaluation of local energy configuration by SED approach.

Energy based method can be adopted in the industrial field where there is the necessity to assess the fatigue properties in a rapid way, especially dealing with 3D printed devices, saving time and material, hence cost.

LIST OF PUBBLICATIONS

1. Corigliano, P, Cucinotta, F, Guglielmino, E, Risitano, G, **Santonocito, D**. Fatigue assessment of a marine structural steel and comparison with thermographic method and static thermographic method. Fatigue Fract Eng Mater Struct. 2020; 43: 734– 743. https://doi.org/10.1111/ffe.13158
2. Puleio F, Rizzo G, Nicita F, **Santonocito D** et al. Chemical and mechanical roughening treatments of a supra-nano composite resin surface: SEM and topographic analysis. Appl Sci 2020;10:1–9. doi:10.3390/app10134457.
3. Foti P, **Santonocito D**, Ferro P, Risitano G, Berto F. Determination of Fatigue Limit by Static Thermographic Method and Classic Thermographic Method on Notched Specimens. Procedia Struct Integr 2020;26:166–74. doi:10.1016/j.prostr.2020.06.020.
4. Risitano G, Guglielmino E, **Santonocito D**. Energetic approach for the fatigue assessment of PE100. Procedia Struct Integr 2020;26:306–12. doi:10.1016/j.prostr.2020.06.039.
5. **Santonocito D.**, Evaluation of fatigue properties of 3D-printed Polyamide-12 by means of energy approach during tensile tests, Procedia Structural Integrity, Volume 25, 2020, Pages 355-363, ISSN 2452-3216, https://doi.org/10.1016/j.prostr.2020.04.040.
6. Cervino, G.; Montanari, M.; **Santonocito, D.**; Nicita, F.; Baldari, R.; De Angelis, C.; Storni, G.; Fiorillo, L. Comparison of Two Low-Profile Prosthetic Retention System Interfaces: Preliminary Data of an In Vitro Study. Prosthesis 2019, 1, 54-60.
7. Cicciù, M.; Cervino, G.; Terranova, A.; Risitano, G.; Raffaele, M.; Cucinotta, F.; **Santonocito, D**.; Fiorillo, L. Prosthetic and Mechanical Parameters of the Facial Bone under the Load of Different Dental Implant Shapes: A Parametric Study. Prosthesis 2019, 1, 41-53.
8. Guglielmino E., Risitano G., **Santonocito D.**, A new approach to the analysis of fatigue parameters by thermal variations during tensile tests on steel, Procedia Structural Integrity, Volume 24, 2019, Pages 651-657, ISSN 2452-3216, https://doi.org/10.1016/j.prostr.2020.02.057.

9. P. Corigliano, F. Cucinotta, E. Guglielmino, G. Risitano, **D. Santonocito**, Thermographic analysis during tensile tests and fatigue assessment of S355 steel, Procedia Structural Integrity, Volume 18, 2019, Pages 280-286, ISSN 2452-3216, https://doi.org/10.1016/j.prostr.2019.08.165.
10. G. Cervino, L. Fiorillo, G. Iannello, **D. Santonocito**, G. Risitano, M. Cicciù, Sandblasted and Acid Etched Titanium Dental Implant Surfaces Systematic Review and Confocal Microscopy Evaluation, Materials 2019, 12(11), 1763 , https://doi.org/10.3390/ma12111763.
11. C. Barone, R. Casati, L. Dusini, F. Gerbino, E. Guglielmino, G. Risitano, **D. Santonocito**, Fatigue life evaluation of car front halfshaft, Procedia Structural Integrity, Volume 12, 2018, Pages 3-8, ISSN 2452-3216, doi: https://doi.org/10.1016/j.prostr.2018.11.112.
12. G. Risitano, E. Guglielmino, **D. Santonocito**, Evaluation of mechanical properties of polyethylene for pipes by energy approach during tensile and fatigue tests, Procedia Structural Integrity, Volume 13, 2018, Pages 1663-1669, ISSN 2452-3216, doi: https://doi.org/10.1016/j.prostr.2018.12.348.
13. Cucinotta F., Guglielmino E., Longo G., Risitano G., **Santonocito D.**, Sfravara F. (2019) Topology Optimization Additive Manufacturing-Oriented for a Biomedical Application. In: Cavas-Martínez F.,Eynard B., Fernández Cañavate F., Fernández-Pacheco D., Morer P., Nigrelli V. (eds) Advances on Mechanics, Design Engineering and Manufacturing II. Lecture Notes in Mechanical Engineering. Springer, Cham doi: https://doi.org/10.1007/978-3-030-12346-8_18

ACKNOWLEDGMENTS

I would like to express my sincere gratitude to Prof. Giacomo Risitano, “Sensei” Giacomo, for his deep esteem and trust in my person. All my scientific growth, but also personal growth, would never be possible without is support as scientist and, mainly, as human being.

Besides my advisor, I would like to thanks also Prof. Filippo Berto for his continuous support in my research activity and availability to host me at NTNU, where I met many colleagues and friends.

My sincere gratitude to Prof. Giovanni Meneghetti and, in a special way, to Prof. Alberto Campagnolo for having me at University of Padova.

My appreciation also to Prof. Esteban Codina Macia for having me at UPC and to support me in a research activity still under development.

At last but not least, my sincere gratitude to all the “guys” of the seventh floor of the Department of Engineering of the University of Messina, that made my days better.

REFERENCES

[1] Khonsari MM, Amiri M. Introduction to thermodynamics of mechanical fatigue. CRC press; 2012.

[2] La Rosa G, Risitano A. Thermographic methodology for rapid determination of the fatigue limit of materials and mechanical components. Int J Fatigue 2000;22:65–73. doi:10.1016/S0142-1123(99)00088-2.

[3] Risitano A, Risitano G. Determining fatigue limits with thermal analysis of static traction tests. Fatigue Fract Eng Mater Struct 2013;36:631–9. doi:10.1111/ffe.12030.

[4] Audenino AL, Goglio L, Rossetto M. Metodi sperimentali per la progettazione. Libreria editrice universitaria Levrotto & Bella; 1997.

[5] Livieri P, Lazzarin P. Fatigue strength of steel and aluminium welded joints based on generalised stress intensity factors and local strain energy values. Int J Fract 2005;133:247–76. doi:10.1007/s10704-005-4043-3.

[6] Mughrabi H. Cyclic slip irreversibilities and the evolution of fatigue damage. Metall Mater Trans B Process Metall Mater Process Sci 2009;40:431–53. doi:10.1007/s11663-009-9240-4.

[7] Wöhler A. Über die festigkeitsversuche mit eisen und stahl. Ernst & Korn; 1870.

[8] Bathias C, Paris PC. Gigacycle fatigue in mechanical practice. vol. 185. CRC Press; 2004.

[9] Nishijima S, Kanazawa K. Stepwise S-N curve and fish-eye failure in gigacycle fatigue. Fatigue Fract Eng Mater Struct 1999;22:601–7. doi:10.1046/j.1460-2695.1999.00206.x.

[10] Crupi V, Epasto G, Guglielmino E, Risitano G. Thermographic method for very high cycle fatigue design in transportation engineering. Proc Inst Mech Eng Part C J Mech Eng Sci 2015;229:1260–70. doi:10.1177/0954406214562463.

[11] Crupi V, Epasto G, Guglielmino E, Risitano G. Analysis of temperature and fracture surface of AISI4140 steel in very high cycle fatigue regime. Theor Appl Fract Mech 2015;80:22–30. doi:10.1016/j.tafmec.2015.07.007.

[12] Plekhov O, Naimark O, Semenova I, Polyakov A, Valiev R. Experimental study of thermodynamic and fatigue properties of submicrocrystalline titanium under high cyclic and gigacyclic fatigue regimes. Proc Inst Mech Eng Part C J Mech Eng Sci 2015;229:1271–9. doi:10.1177/0954406214563738.

[13] Goodman J. Mechanics applied to engineering. Longmans, Green; 1919.

[14] Gerber H. Bestimmung der zulässigen spannungen in eisen-constructionen. Wolf; 1874.

[15] Soderberg CR. Factor of safety and working stress. Trans Am Soc Mech Eng 1939;52:13–28.

[16] Palmgren A. Die lebensdauer von kugellargern. Zeitshrift Des Vereines Duetsher Ingenieure 1924;68:339.

[17] Miner MA, others. Cumulative fatigue damage. J Appl Mech 1945;12:A159--A164.

[18] Manson SS. Fatigue : A Complex Subject-Some Simple Approximations some approximations useful in design are outlined and their application illustrated. Exp Mech 1965;5:193–226. doi:https://doi.org/10.1007/BF02321056.

[19] Risitano A, Risitano G. Cumulative damage evaluation in multiple cycle fatigue tests taking into account energy parameters. Int J Fatigue 2013;48:214–22. doi:10.1016/j.ijfatigue.2012.10.020.

[20] Risitano A, Risitano G. Cumulative damage evaluation of steel using infrared thermography. Theor Appl Fract Mech 2010;54:82–90. doi:10.1016/j.tafmec.2010.10.002.

[21] Karolczuk A, Macha E. A review of critical plane orientations in multiaxial fatigue failure criteria of metallic materials. Int J Fract 2005;134:267–304. doi:10.1007/s10704-005-1088-2.

[22] Stanfield G. Discussion on the strength of metals under combined alternating stresses.

Proc Inst Mech Eng 1935;131:93.

[23] Socie DF, Marquis GB. Multiaxial fatigue. Society of Automotive Engineers Warrendale, PA; 2000.

[24] Stephens RI, Fatemi A, Stephens RR, Fuchs HO. Metal fatigue in engineering. John Wiley & Sons; 2000.

[25] Hülsbusch D, Kohl A, Striemann P, Niedermeier M, Walther F. Development of an energy-based approach for optimized frequency selection for fatigue testing on polymers – Exemplified on polyamide 6. Polym Test 2019:106260. doi:10.1016/j.polymertesting.2019.106260.

[26] Eshelby JD. Dislocations as a cause of mechanical damping in metals. Collect Work J D Eshelby 2007:3–23. doi:10.1007/1-4020-4499-2_1.

[27] Zener C. Internal friction in solids. J Appl Phys 1986;60:1888–95. doi:10.1063/1.337237.

[28] Morrow J. Cyclic plastic strain energy and fatigue of metals. Intern. Frict. damping, Cycl. Plast., ASTM International; 1965.

[29] Kaleta J, Blotny R, Harig H. Energy stored in a specimen under fatigue limit loading conditions. J Test Eval 1991;19:326–33.

[30] Hodowany J. On the conversion of plastic work into heat. California Institute of Technology, 1997.

[31] Kapoor R, Nemat-Nasser S. Determination of temperature rise during high strain rate deformation. Mech Mater 1998;27:1–12. doi:10.1016/S0167-6636(97)00036-7.

[32] Geraci A, La Rosa G, Risitano A. L'infrarosso termico nelle applicazioni meccaniche. CRES Symp. Catania Italy, 1984, p. 8–9.

[33] Curti G, La Rosa G, Orlando M, Risitano A. Analisi tramite infrarosso termico della temperatura limite in prove di fatica. Proc XIV Convegno Naz AIAS 1986:211–20.

[34] Geraci A, La Rosa G, Risitano A. Influence of frequency and cumulative damage on the determination of fatigue limit of materials using the thermal infrared methodology. XV Symp Mech Eksp 1992:63–6.

[35] Geraci AL, Guglielmino E, La Rosa G, Roccati G. Notch sensitivity in specimens with blind hole under fatigue test. Third Int. Conf. SPT, Vienna, 1989, p. 10–2.

[36] Guglielmino E, La Rosa G, Olivieri SM, La Pasta A. Analisi mediante techniche termografiche del comportamento a fatica di giunti di testa con saldatura laser. Proc. XXII AIAS Congr. Forli, 1993, p. 301–7.

[37] Geraci A, La Rosa G, Risitano A. On the new methodology for the determination of the fatigue limit of materials using thermal infrared techniques. Risk minimization by Exp. Mech., 1992.

[38] Fracchia R, Pozzati M, Goria CA. Valutazione rapida del limite di fatica di bielle motore in ghisa. Congr. FAST, Milano, 1997, p. 1037–44.

[39] La Rosa G, Risitano A. Application of a new methodology to determine the fatigue limit using thermal infrared techniques. 17th Symp. Exp. Mech. Warsaw, 1996, p. 498–503.

[40] Geraci AL, La Rosa G, Risitano A, Grech M. Determination of the fatigue limit of an austempered ductile iron using thermal infrared imagry. Digit. Photogramm. Remote Sensing'95, vol. 2646, 1995, p. 306–17.

[41] Fargione G, Geraci A, La Rosa G, Risitano A, Grench M. Determinazione del limite di fatica in materiali sottoposti a differenti trattamenti termici mediante considerazioni energetiche. XXVI Convegno Naz AIAS, Catania 1997:1–12.

[42] Guglielmino E, Guglielmino ID, La Rosa G, Pasta A. Analysis of laminate composite under cyclic testing using thermal infrared imagery. Int. Conf. Mater. Eng. Gall., 1996, p. 899–906.

[43] La Rosa G, Perrone S, Quaresimin M. Determinazione della resistenza a fatica di materiali compositi con tecniche termografiche. 27th Natl. Congr. AIAS, 1998.

[44] Curà F, Curti G, Sesana R. A new iteration method for the thermographic determination of fatigue limit in steels. Int J Fatigue 2005;27:453–9. doi:10.1016/j.ijfatigue.2003.12.009.

[45] Fargione G, Tringale D, Guglielmino E, Risitano G. Fatigue characterization of mechanical components in service. Frat Ed Integrita Strutt 2013;26:143–55.

doi:10.3221/igf-esis.26.14.

[46] Fargione G, Geraci A, La Rosa G, Risitano A. Rapid determination of the fatigue curve by the thermographic method. Int J Fatigue 2002;24:11–9. doi:10.1016/S0142-1123(01)00107-4.

[47] Palumbo D, Galietti U. Characterisation of steel welded joints by infrared thermographic methods. Quant Infrared Thermogr J 2014;11:29–42. doi:10.1080/17686733.2013.874220.

[48] Galietti U, Palumbo D, De Finis R, Ancona F. Fatigue limit evaluation of martensitic steels with thermal methods 2014. doi:10.21611/qirt.2014.105.

[49] Amiri M, Khonsari MM. Life prediction of metals undergoing fatigue load based on temperature evolution. Mater Sci Eng A 2010;527:1555–9. doi:10.1016/j.msea.2009.10.025.

[50] Amiri M, Khonsari MM. Rapid determination of fatigue failure based on temperature evolution: Fully reversed bending load. Int J Fatigue 2010;32:382–9. doi:10.1016/j.ijfatigue.2009.07.015.

[51] Risitano A, La Rosa G, Geraci A, Guglielmino E. The choice of thermal analysis to evaluate the monoaxial fatigue strength on materials and mechanical components. Proc Inst Mech Eng Part C J Mech Eng Sci 2015;229:1315–26. doi:10.1177/0954406215572429.

[52] Biot M, Crupi V, Marinò A, Risitano G. Thermographic method for fatigue prediction of friction stir welded light alloy panels in shipbuilding. Proc 7th Symp High Speed Mar Veh 2005 Conf HSMV 2005 2005;2005:81–8.

[53] Corigliano P, Epasto G, Guglielmino E, Risitano G. Fatigue analysis of marine welded joints by means of DIC and IR images during static and fatigue tests. Eng Fract Mech 2017;183:26–38. doi:10.1016/j.engfracmech.2017.06.012.

[54] Crupi V, Guglielmino E, Scappaticci L, Risitano G. Fatigue assessment by energy approach during tensile and fatigue tests on PPGF35. Procedia Struct Integr 2017;3:424–31. doi:10.1016/j.prostr.2017.04.068.

[55] Lipski A. Rapid Determination of the S - N Curve for Steel by means of the Thermographic Method 2016;2016:1–9.

[56] Lipski A, Boroński D. Use of thermography for the analysis of strength properties of mini-specimens. Mater Sci Forum 2012;726:156–61. doi:10.4028/www.scientific.net/MSF.726.156.

[57] Li XD, Zhang H, Wu DL, Liu X, Liu JY. Adopting lock-in infrared thermography technique for rapid determination of fatigue limit of aluminum alloy riveted component and affection to determined result caused by initial stress. Int J Fatigue 2012;36:18–23. doi:10.1016/j.ijfatigue.2011.09.005.

[58] Wang XG, Crupi V, Guo XL, Zhao YG. Quantitative Thermographic Methodology for fatigue assessment and stress measurement. Int J Fatigue 2010;32:1970–6. doi:10.1016/j.ijfatigue.2010.07.004.

[59] Germain P, Suquet P, Nguyen QS. Continuum thermodynamics. ATJAM 1983;50:1010–20.

[60] Lemaitre J, Chaboche J-L. Mechanics of solid materials. Cambridge university press; 1994.

[61] Chrysochoos A, Berthel B, Latourte F, Galtier A, Pagano S, Wattrisse B. Local energy analysis of high-cycle fatigue using digital image correlation and infrared thermography. J Strain Anal Eng Des 2008;43:411–21. doi:10.1243/03093247JSA374.

[62] Meneghetti G, Ricotta M. The heat energy dissipated in the material structural volume to correlate the fatigue crack growth rate in stainless steel specimens. Int J Fatigue 2018;115:107–19. doi:10.1016/j.ijfatigue.2018.07.037.

[63] Rousselier G. Dissipation in porous metal plasticity and ductile fracture. J Mech Phys Solids 2001;49:1727–46. doi:10.1016/S0022-5096(01)00013-8.

[64] Meneghetti G, Ricotta M, Atzori B. A synthesis of the push-pull fatigue behaviour of plain and notched stainless steel specimens by using the specific heat loss. Fatigue Fract Eng Mater Struct 2013;36:1306–22. doi:10.1111/ffe.12071.

[65] Feltner CE, Morrow JD. Microplastic strain hysteresis energy as a criterion for fatigue

fracture 1961.

[66] Halford GR. The energy required for fatigue(Plastic strain hystersis energy required for fatigue in ferrous and nonferrous metals). J Mater 1966;1:3–18.

[67] Meneghetti G. Analysis of the fatigue strength of a stainless steel based on the energy dissipation. Int J Fatigue 2007;29:81–94. doi:10.1016/j.ijfatigue.2006.02.043.

[68] Rigon D, Ricotta M, Meneghetti G. Analysis of dissipated energy and temperature fields at severe notches of AISI 304L stainless steel specimens. Frat Ed Integrita Strutt 2019;13:334–47. doi:10.3221/IGF-ESIS.47.25.

[69] Ricotta M, Meneghetti G, Atzori B, Risitano G, Risitano A. Comparison of Experimental Thermal Methods for the Fatigue Limit Evaluation of a Stainless Steel. Metals (Basel) 2019;9:677. doi:10.3390/met9060677.

[70] Thomson W. XV. On the Dynamical Theory of Heat, with numerical results deduced from Mr Joule's Equivalent of a Thermal Unit, and M. Regnault's Observations on Steam. Trans R Soc Edinburgh 1853;20:261–88. doi:10.1017/S0080456800033172.

[71] Nowacki W. Thermoelasticity. Elsevier; 2013.

[72] Jones R, Tay TE, Williams JF. Thermomechanical behaviour of composites. Comput Mech 1989;5:255–61. doi:10.1007/BF01046942.

[73] Potter RT, Greaves LJ. The Application Of Thermoelastic Stress Analysis Techniques To Fibre Composites. In: Vukobratovich D, editor. Optomech. Syst. Eng., vol. 0817, SPIE; 1987, p. 134. doi:10.1117/12.967419.

[74] Rogers G, Mayhew Y. Engineering thermodynamics work and heat transfer. Prentice-Hall; 1992.

[75] Renton JD. Applied elasticity: matrix and tensor analysis of elastic continua. Elsevier; 2002.

[76] Caglioti G, Ferro Milone A, Società italiana di fisica. Mechanical and thermal behaviour of metallic materials : Varenna on Lake Como, Villa Monastero, 30th June - 10th July 1981. North-Holland Pub. Co; 1982.

[77] Melvin AD, Lucia AC, Solomos GP, Volta G, Emmony D. Thermal emission measurements from creep damaged specimens of AISI 316L and Alloy 800H. Proc 9th Int Conf Exp Mech Vol 2, Pages 765-773 1990;2:765–73.

[78] Melvin AD, Lucia AC, Solomos GP. The thermal response to deformation to fracture of a carbon/epoxy composite laminate. Compos Sci Technol 1993;46:345–51. doi:10.1016/0266-3538(93)90180-O.

[79] Brown N. Observations of microplasticity 1968.

[80] ARSENAULT RJ. MICROPLASTICITY OF BCC METALS AND SOLID SOLUTIONS IN TERMS OF THE DOUBLE-KINK MECHANISM 1968.

[81] BEGHI M, BOTTANI CE, Caglioti G. Irreversible thermodynamics of metals under stress 1986.

[82] Chrysochoos A, Louche H. Infrared image processing to analyze the calorific effects accompanying strain localization. Int J Eng Sci 2000;38:1759–88. doi:10.1016/S0020-7225(00)00002-1.

[83] Plekhov OA, Naimark OB. Theoretical and experimental study of energy dissipation in the course of strain localization in iron. J Appl Mech Tech Phys 2009;50:127–36. doi:10.1007/s10808-009-0018-x.

[84] Geraci A, La Rosa G, Risitano A. Correlation between thermal variation in static test and elastic limit of material using infrared imagery. 7th Int. Conf. Mech. Behav. Mater. Hague May, 1995.

[85] Risitano A, Corallo D, Risitano G, Sirugo A. Determinazione del limite di fatica mediante prove quasi-statiche. Proc XXXIX Convegno Naz AIAS 2010.

[86] Clienti C, Fargione G, La Rosa G, Risitano A, Risitano G. A first approach to the analysis of fatigue parameters by thermal variations in static tests on plastics. Eng Fract Mech 2010;77:2158–67. doi:10.1016/j.engfracmech.2010.04.028.

[87] Jiang L, Wang H, Liaw PK, Brooks CR, Klarstrom DL. Temperature evolution during low-cycle fatigue of ULTIMET® alloy: Experiment and modeling. Mech Mater 2004;36:73–84. doi:10.1016/S0167-6636(03)00032-2.

[88] LY HA, INOUE H, IRIE Y. Numerical Simulation on Rapid Evaluation of Fatigue Limit through Temperature Evolution. J Solid Mech Mater Eng 2011;5:459–75. doi:10.1299/jmmp.5.459.

[89] Pitarresi G, Patterson EA. A review of the general theory of thermoelastic stress analysis. J Strain Anal Eng Des 2003;38:405–17. doi:10.1243/03093240360713469.

[90] Biot MA. Thermoelasticity and irreversible thermodynamics. J Appl Phys 1956;27:240–53. doi:10.1063/1.1722351.

[91] Rittel D, Zhang LH, Osovski S. The dependence of the Taylor–Quinney coefficient on the dynamic loading mode. J Mech Phys Solids 2017;107:96–114. doi:10.1016/j.jmps.2017.06.016.

[92] Smith RA, Miller KJ. Prediction of fatigue regimes in notched components. Int J Mech Sci 1978;20:201–6. doi:10.1016/0020-7403(78)90082-6.

[93] Williams ML. Stress Singularities Resulting From Various Boundary Conditions in Angular Corners of Plates in Extension. J Appl Mech 1952;19:526–8.

[94] Gross B, Mendelson A. Plane elastostatic analysis of V-notched plates. Int J Fract Mech 1972;8:267–76. doi:10.1007/BF00186126.

[95] Lazzarin P, Tovo R. A notch intensity factor approach to the stress analysis of welds. Fatigue Fract Eng Mater Struct 1998;21:1089–103. doi:10.1046/j.1460-2695.1998.00097.x.

[96] Lazzarin P, Livieri P, Berto F, Zappalorto M. Local strain energy density and fatigue strength of welded joints under uniaxial and multiaxial loading. Eng Fract Mech 2008;75:1875–89. doi:10.1016/J.ENGFRACMECH.2006.10.019.

[97] Lazzarin P, Zambardi R. A finite-volume-energy based approach to predict the static and fatigue behavior of components with sharp V-shaped notches. Int J Fract 2001;112:275–98. doi:10.1023/A:1013595930617.

[98] Lazzarin P, Zambardi R. The equivalent strain energy density approach re-formulated and applied to sharp V-shaped notches under localized and generalized plasticity. Fatigue Fract Eng Mater Struct 2002;25:917–28. doi:10.1046/j.1460-2695.2002.00543.x.

[99] Beltrami E. Sulle condizioni di resistenza dei corpi elastici. Nuovo Cim 1885;18:145–55. doi:10.1007/BF02824697.

[100] Neuber H. Theory of notch stresses: principles for exact calculation of strength with reference to structural form and material. vol. 4547. USAEC Office of Technical Information; 1961.

[101] Erdogan F, Sih GC. On the crack extension in plates under plane loading and transverse shear. J Fluids Eng Trans ASME 1963;85:519–25. doi:10.1115/1.3656897.

[102] Sih GC. Strain-energy-density factor applied to mixed mode crack problems. Int J Fract 1974;10:305–21. doi:10.1007/BF00035493.

[103] Sih GC. Surface layer energy and strain energy density for a blunted crack or notch. Prospect Fract Mech Noordhoff Int Publ Leyden, Netherlands 1974, 85-102 1974.

[104] Sih GC, Sih GC. A special theory of crack propagation. Mech Fract Initiat Propag 1991;1:1–22. doi:10.1007/978-94-011-3734-8_1.

[105] Molski K, Glinka G. A method of elastic-plastic stress and strain calculation at a notch root. Mater Sci Eng 1981;50:93–100. doi:10.1016/0025-5416(81)90089-6.

[106] Berto F, Elices M, Lazzarin P, Zappalorto M. Fracture behaviour of notched round bars made of PMMA subjected to torsion at room temperature. Eng Fract Mech 2012;90:143–60. doi:10.1016/j.engfracmech.2012.05.001.

[107] Berto F, Cendon DA, Lazzarin P, Elices M. Fracture behaviour of notched round bars made of PMMA subjected to torsion at -60°C. Eng Fract Mech 2013;102:271–87. doi:10.1016/j.engfracmech.2013.02.011.

[108] Berto F, Lazzarin P. Recent developments in brittle and quasi-brittle failure assessment of engineering materials by means of local approaches. Mater Sci Eng R Reports 2014;75:1–48. doi:10.1016/j.mser.2013.11.001.

[109] Filippi S, Lazzarin P, Tovo R. Developments of some explicit formulas useful to describe elastic stress fields ahead of notches in plates. Int J Solids Struct 2002;39:4543–65. doi:10.1016/S0020-7683(02)00342-6.

[110] Lazzarin P, Berto F. Some expressions for the strain energy in a finite volume surrounding the root of blunt V-notches. Int J Fract 2005;135:161–85. doi:10.1007/s10704-005-3943-6.

[111] Foti P, Filippi S, Berto F. Fatigue assessment of welded joints by means of the strain energy density method: Numerical predictions and comparison with eurocode 3. Frat Ed Integrita Strutt 2019;13:104–25. doi:10.3221/IGF-ESIS.47.09.

[112] Gómez FJ, Elices M, Berto F, Lazzarin P. Fracture of U-notched specimens under mixed mode: Experimental results and numerical predictions. Eng Fract Mech 2009;76:236–49. doi:10.1016/j.engfracmech.2008.10.001.

[113] Gómez FJ, Elices M, Berto F, Lazzarin P. A generalised notch stress intensity factor for U-notched components loaded under mixed mode. Eng Fract Mech 2008;75:4819–33. doi:10.1016/j.engfracmech.2008.07.001.

[114] Berto F, Razavi SMJ, Torgersen J. Frontiers of fracture and fatigue: Some recent applications of the local strain energy density. Frat Ed Integrita Strutt 2018;12:1–32. doi:10.3221/IGF-ESIS.43.01.

[115] Meneghetti G, Lazzarin P. Significance of the elastic peak stress evaluated by FE analyses at the point of singularity of sharp V-notched components. Fatigue Fract Eng Mater Struct 2007;30:95–106. doi:10.1111/j.1460-2695.2006.01084.x.

[116] Nisitani H, Teranishi T. KI of a circumferential crack emanating from an ellipsoidal cavity obtained by the crack tip stress method in FEM. Eng Fract Mech 2004;71:579–85. doi:10.1016/S0013-7944(03)00035-3.

[117] Meneghetti G. Simplified evaluation of the local stress field in fillet welded joints. Riv Ital Della Saldatura 2002;4:499–505.

[118] Meneghetti G, Campagnolo A, Avalle M, Castagnetti D, Colussi M, Corigliano P, et al. Rapid evaluation of notch stress intensity factors using the peak stress method: Comparison of commercial finite element codes for a range of mesh patterns. Fatigue Fract Eng Mater Struct 2018;41:1044–63. doi:10.1111/ffe.12751.

[119] Meneghetti G, Campagnolo A. State-of-the-art review of peak stress method for fatigue

strength assessment of welded joints. Int J Fatigue 2020;139:105705. doi:10.1016/j.ijfatigue.2020.105705.

[120] Meneghetti G, Campagnolo A, Babini V, Riboli M, Spagnoli A. Multiaxial fatigue assessment of welded steel details according to the peak stress method: Industrial case studies. Int J Fatigue 2019;125:362–80. doi:10.1016/j.ijfatigue.2019.04.014.

[121] Campagnolo A, Vormwald M, Shams E, Meneghetti G. Multiaxial fatigue assessment of tube-tube steel joints with weld ends using the peak stress method. Int J Fatigue 2020;135:105495. doi:10.1016/j.ijfatigue.2020.105495.

[122] Meneghetti G, Lazzarin P. The peak stress method for fatigue strength assessment of welded joints with weld toe or weld root failures. Weld World 2011;55:22–9. doi:10.1007/BF03321304.

[123] Meneghetti G. The use of peak stresses for fatigue strength assessments of welded lap joints and cover plates with toe and root failures. Eng Fract Mech 2012;89:40–51. doi:10.1016/j.engfracmech.2012.04.007.

[124] Risitano G, Clienti C. Experimental study to verify the fatigue limit found by thermal analysis of specimen surface in mono axial traction test. Key Eng Mater 2012;488–489:795–8. doi:10.4028/www.scientific.net/KEM.488-489.795.

[125] Risitano A, Fargione G, Guglielmino E. Definition of the linearity loss of the surface temperature in static tensile tests. Frat Ed Integrita Strutt 2014;30:201–10. doi:10.3221/IGF-ESIS.30.26.

[126] Colombo C, Vergani L, Burman M. Static and fatigue characterisation of new basalt fibre reinforced composites. Compos Struct 2012;94:1165–74. doi:10.1016/j.compstruct.2011.10.007.

[127] Palumbo D, De Finis R, Demelio PG, Galietti U. Early detection of damage mechanisms in composites during fatigue tests. Conf. Proc. Soc. Exp. Mech. Ser., vol. 8, Springer, Cham; 2017, p. 133–41. doi:10.1007/978-3-319-42195-7_19.

[128] Corigliano P, Crupi V, Epasto G, Guglielmino E, Risitano G. Fatigue Assessment by Thermal Analysis during Tensile Tests on Steel. Procedia Eng 2015;109:210–8.

doi:10.1016/j.proeng.2015.06.215.

[129] Hayabusa K, Inaba K, Ikeda H, Kishimoto K. Estimation of Fatigue Limits from Temperature Data Measured by IR Thermography. Exp Mech 2017;57:185–94. doi:10.1007/s11340-016-0221-7.

[130] Dulieu-Barton JM, Stanley P. Development and applications of thermoelastic stress analysis. J Strain Anal Eng Des 1998;33:93–104. doi:10.1243/0309324981512841.

[131] Gigliotti M, Pannier Y, Minervino M, Lafarie-Frenot MC, Corigliano P. The effect of a thermo-oxidative environment on the behaviour of multistable [0/90] unsymmetric composite plates. Compos Struct 2013;106:863–72. doi:10.1016/J.COMPSTRUCT.2013.07.016.

[132] Crupi V, Guglielmino E, Risitano G, Tavilla F. Experimental analyses of SFRP material under static and fatigue loading by means of thermographic and DIC techniques. Compos Part B Eng 2015;77:268–77. doi:10.1016/j.compositesb.2015.03.052.

[133] Corigliano P, Crupi V, Guglielmino E. Non linear finite element simulation of explosive welded joints of dissimilar metals for shipbuilding applications. Ocean Eng 2018;160:346–53. doi:10.1016/J.OCEANENG.2018.04.070.

[134] Vergani L, Colombo C, Libonati F. A review of thermographic techniques for damage investigation in composites. Frat Ed Integrita Strutt 2014;8:1–12. doi:10.3221/IGF-ESIS.27.01.

[135] Wang XG, Crupi V, Guo XL, Guglielmino E. A thermography-based approach for structural analysis and fatigue evaluation. Proc Inst Mech Eng Part C J Mech Eng Sci 2011;226:1173–85. doi:10.1177/0954406211421998.

[136] Rigon D, Ricotta M, Meneghetti G. An analysis of the specific heat loss at the tip of severely notched stainless steel specimens to correlate the fatigue strength. Theor Appl Fract Mech 2017;92:240–51. doi:10.1016/j.tafmec.2017.09.003.

[137] Risitano G, Guglielmino E, Santonocito D. Evaluation of mechanical properties of polyethylene for pipes by energy approach during tensile and fatigue tests. Procedia Struct. Integr., vol. 13, Elsevier B.V.; 2018, p. 1663–9. doi:10.1016/j.prostr.2018.12.348.

[138] Colombo C, Vergani L. Thermographic applications for the rapid estimation of fatigue limit. Procedia Struct Integr 2019;24:658–66. doi:10.1016/j.prostr.2020.02.058.

[139] Szala G, Ligaj B. Application of hybrid method in calculation of fatigue life for C45 steel (1045 steel) structural components. Int J Fatigue 2016;91:39–49. doi:10.1016/j.ijfatigue.2016.05.015.

[140] Curà F, Gallinatti AE. Fatigue damage identification by means of modal parameters. Procedia Eng., vol. 10, Elsevier B.V.; 2011, p. 1697–702. doi:10.1016/j.proeng.2011.04.283.

[141] Plekhov O, Naimark O, Semenova I, Polyakov A, Valiev R. Experimental study of thermodynamic and fatigue properties of submicrocrystalline titanium under high cyclic and gigacyclic fatigue regimes. Proc Inst Mech Eng Part C J Mech Eng Sci 2014;229:1271–9. doi:10.1177/0954406214563738.

[142] Corigliano P, Cucinotta F, Guglielmino E, Risitano G, Santonocito D. Fatigue assessment of a marine structural steel and comparison with Thermographic Method and Static Thermographic Method. Fatigue Fract Eng Mater Struct 2020;43:734–43. doi:10.1111/ffe.13158.

[143] Palumbo D, De Finis R, Demelio PG, Galietti U. Early Detection of Damage Mechanisms in Composites During Fatigue Tests. In: Zehnder AT, Carroll J, Hazeli K, Berke RB, Pataky G, Cavalli M, et al., editors. Fract. Fatigue, Fail. Damage Evol. Vol. 8, Cham: Springer International Publishing; 2017, p. 133–41.

[144] Santonocito D. Evaluation of fatigue properties of 3D-printed Polyamide-12 by means of energy approach during tensile tests. Procedia Struct Integr 2020;25:355–63. doi:10.1016/j.prostr.2020.04.040.

[145] Norme Tecniche per le Costruzioni (NTC 2018). Italy: Gazzetta Ufficiale n.42 del 20/02/2018, Supplemento ordinario n.8; 2018.

[146] Dai X, Lam D. Numerical modelling of the axial compressive behaviour of short concrete-filled elliptical steel columns. J Constr Steel Res 2010;66:931–42. doi:10.1016/j.jcsr.2010.02.003.

[147] Langlois V, Audouin L, Verdu J, Courtois P. Thermooxidative aging of crosslinked linear polyethylene: Stabilizer consumption and lifetime prediction. Polym Degrad Stab 1993;40:399–409. doi:10.1016/0141-3910(93)90150-H.

[148] Gugumus F. Effect of temperature on the lifetime of stabilized and unstabilized PP films. Polym Degrad Stab 1999;63:41–52. doi:10.1016/S0141-3910(98)00059-7.

[149] Gillen KT, Bernstein R, Clough RL, Celina M. Lifetime predictions for semi-crystalline cable insulation materials: I. Mechanical properties and oxygen consumption measurements on EPR materials. Polym Degrad Stab 2006;91:2146–56. doi:10.1016/j.polymdegradstab.2006.01.009.

[150] Celina M, Gillen KT, Assink RA. Accelerated aging and lifetime prediction: Review of non-Arrhenius behaviour due to two competing processes. Polym Degrad Stab 2005;90:395–404. doi:10.1016/j.polymdegradstab.2005.05.004.

[151] Deveci S, Fang D. Correlation of molecular parameters, strain hardening modulus and cyclic fatigue test performances of polyethylene materials for pressure pipe applications. Polym Test 2017;62:246–53. doi:10.1016/j.polymertesting.2017.07.007.

[152] Djebli A, Bendouba M, Aid A, Talha A, Benseddiq N, Benguediab M. Experimental Analysis and Damage Modeling of High-Density Polyethylene under Fatigue Loading. Acta Mech Solida Sin 2016;29:133–44. doi:10.1016/S0894-9166(16)30102-1.

[153] Ngo TD, Kashani A, Imbalzano G, Nguyen KTQ, Hui D. Additive manufacturing (3D printing): A review of materials, methods, applications and challenges. Compos Part B Eng 2018;143:172–96. doi:10.1016/j.compositesb.2018.02.012.

[154] Schmitt M, Mehta RM, Kim IY. Additive manufacturing experimental infill testing and optimization for automotive lightweighting. SAE Tech Pap 2019;2019-April:1–8. doi:10.4271/2019-01-1275.

[155] Singamneni S, Lv Y, Hewitt A, Chalk R, Thomas W, Jordison D. Additive Manufacturing for the Aircraft Industry : A Review Journal of Aeronautics & Aerospace Additive Manufacturing for the Aircraft Industry : A Review. J Aeronaut Aerosp Eng 2019;8:0–13. doi:10.4172/2329-6542.1000214.

[156] Revilla-León M, Özcan M. Additive Manufacturing Technologies Used for Processing Polymers: Current Status and Potential Application in Prosthetic Dentistry. J Prosthodont 2019;28:146–58. doi:10.1111/jopr.12801.

[157] Coulter FB, Schaffner M, Faber JA, Rafsanjani A, Smith R, Appa H, et al. Bioinspired Heart Valve Prosthesis Made by Silicone Additive Manufacturing. Matter 2019;1:266–79. doi:10.1016/j.matt.2019.05.013.

[158] Dapogny C, Estevez R, Faure A, Michailidis G. Shape and topology optimization considering anisotropic features induced by additive manufacturing processes. Comput Methods Appl Mech Eng 2019;344:626–65. doi:10.1016/j.cma.2018.09.036.

[159] Cucinotta F, Guglielmino E, Longo G, Risitano G, Santonocito D, Sfravara F. Topology optimization additive manufacturing-oriented for a biomedical application. vol. 1. Springer International Publishing; 2019. doi:10.1007/978-3-030-12346-8_18.

[160] Cucinotta F, Raffaele M, Salmeri F. A Topology Optimization of a Motorsport Safety Device. In: Rizzi C, Andrisano AO, Leali F, Gherardini F, Pini F, Vergnano A, editors. Des. Tools Methods Ind. Eng., Cham: Springer International Publishing; 2020, p. 400–9.

[161] Stoia DI, Mar L, Linul E. Correlations between Process Parameters and Outcome Properties of Laser-Sintered Polyamide 2019.

[162] O'Connor HJ, Dickson AN, Dowling DP. Evaluation of the mechanical performance of polymer parts fabricated using a production scale multi jet fusion printing process. Addit Manuf 2018;22:381–7. doi:10.1016/j.addma.2018.05.035.

[163] Meneghetti G, Rigon D, Gennari C. An analysis of defects influence on axial fatigue strength of maraging steel specimens produced by additive manufacturing. Int J Fatigue 2019;118:54–64. doi:10.1016/j.ijfatigue.2018.08.034.

[164] Razavi SMJ, Ferro P, Berto F, Torgersen J. Fatigue strength of blunt V-notched specimens produced by selective laser melting of Ti-6Al-4V. Theor Appl Fract Mech 2018;97:376–84. doi:10.1016/j.tafmec.2017.06.021.

[165] Lammens N, Kersemans M, De Baere I, Van Paepegem W. On the visco-elasto-plastic response of additively manufactured polyamide-12 (PA-12) through selective laser

sintering. Polym Test 2017;57:149–55. doi:10.1016/j.polymertesting.2016.11.032.

[166] Morales-Planas S, Minguella-Canela J, Lluma-Fuentes J, Travieso-Rodriguez JA, García-Granada AA. Multi Jet Fusion PA12 manufacturing parameters for watertightness, strength and tolerances. Materials (Basel) 2018;11:1–11. doi:10.3390/ma11081472.

[167] Wang X, Zhao L, Fuh JYH, Lee HP. Effect of porosity on mechanical properties of 3D printed polymers: Experiments and micromechanical modeling based on X-ray computed tomography analysis. Polymers (Basel) 2019;11. doi:10.3390/polym11071154.

[168] Colombo C, Libonati F, Vergani L. Fatigue damage in GFRP. Int J Struct Integr 2012;3:424–40. doi:10.1108/17579861211281218.

[169] Harizi W, Chaki S, Bourse G, Ourak M. Mechanical damage assessment of Glass Fiber-Reinforced Polymer composites using passive infrared thermography. Compos Part B Eng 2014;59:74–9. doi:10.1016/j.compositesb.2013.11.021.

[170] Sato N, Kurauchi T, Sato S, Kamigaito O. Microfailure behaviour of randomly dispersed short fibre reinforced thermoplastic composites obtained by direct SEM observation. J Mater Sci 1991;26:3891–8. doi:10.1007/BF01184987.

[171] Bernasconi A, Davoli P, Basile A, Filippi A. Effect of fibre orientation on the fatigue behaviour of a short glass fibre reinforced polyamide-6. Int J Fatigue 2007;29:199–208. doi:10.1016/j.ijfatigue.2006.04.001.

[172] De Monte M, Moosbrugger E, Quaresimin M. Influence of temperature and thickness on the off-axis behaviour of short glass fibre reinforced polyamide 6.6 - Cyclic loading. Compos Part A Appl Sci Manuf 2010;41:1368–79. doi:10.1016/j.compositesa.2010.02.004.

[173] Belmonte E, De Monte M, Hoffmann CJ, Quaresimin M. Damage mechanisms in a short glass fiber reinforced polyamide under fatigue loading. Int J Fatigue 2017;94:145–57. doi:10.1016/j.ijfatigue.2016.09.008.

[174] Goh KL, Aspden RM, Hukins DWL. Review: Finite element analysis of stress transfer in short-fibre composite materials. Compos Sci Technol 2004;64:1091–100. doi:10.1016/j.compscitech.2003.11.003.

[175] Horst JJ, Salienko N V., Spoormaker JL. Fibre-matrix debonding stress analysis for short fibre-reinforced materials with matrix plasticity, finite element modelling and experimental verification. Compos Part A Appl Sci Manuf 1998;29:525–31. doi:10.1016/S1359-835X(97)00125-5.

[176] Kang GZ, Gao Q. Tensile properties of randomly oriented short δ-Al2O3 fiber reinforced aluminum alloy composites: II. Finite element analysis for stress transfer, elastic modulus and stress-strain curve. Compos - Part A Appl Sci Manuf 2002;33:657–67. doi:10.1016/S1359-835X(02)00006-4.

[177] Houshyar S, Shanks RA, Hodzic A. Modelling of polypropylene fibre-matrix composites using finite element analysis. Express Polym Lett 2009;3:2–12. doi:10.3144/expresspolymlett.2009.2.

[178] Arif MF, Meraghni F, Chemisky Y, Despringre N, Robert G. In situ damage mechanisms investigation of PA66/GF30 composite: Effect of relative humidity. Compos Part B Eng 2014;58:487–95. doi:10.1016/j.compositesb.2013.11.001.

[179] De Monte M, Moosbrugger E, Quaresimin M. Influence of temperature and thickness on the off-axis behaviour of short glass fibre reinforced polyamide 6.6 - Cyclic loading. Compos Part A Appl Sci Manuf 2010;41:1368–79. doi:10.1016/j.compositesa.2010.02.004.

[180] Kang G, Luo H. Review on fatigue life prediction models of welded joint. Acta Mech Sin Xuebao 2020;36:701–26. doi:10.1007/s10409-020-00957-0.

[181] Fricke W. IIW guideline for the assessment of weld root fatigue. Weld World 2013;57:753–91. doi:10.1007/s40194-013-0066-y.

[182] Hobbacher A. Recommendations for Fatigue Design of Welded Joints and Components. 2016. doi:10.1007/978-3-319-23757-2.

[183] 1993-1-3:2009 BE. Eurocode 3: Design of steel structures - Part 1-9: Fatigue. Eurocode 3 Des. steel Struct. - Part 1-9 Fatigue, vol. 7, 2011.

[184] British Standards Institution. BSI Standards Publication Guide to fatigue design and assessment of steel products 2014.

[185] Der Norske Veritas. DNVGL-RP-C203. Fatigue Design of Offshore Steel Structures. Recomm Pract 2016:176.

[186] Niemi E, Fricke W, Maddox SJ. The Structural Hot-Spot Stress Approach to Fatigue Analysis, Singapore: 2018, p. 5–12. doi:10.1007/978-981-10-5568-3_2.

[187] Fricke W, Remes H, Feltz O, Lillemäe I, Tchuindjang D, Reinert T, et al. Fatigue strength of laser-welded thin-plate ship structures based on nominal and structural hot-spot stress approach. Ships Offshore Struct 2015;10:39–44. doi:10.1080/17445302.2013.850208.

[188] Lazzarin P, Livieri P, Berto F, Zappalorto M. Local strain energy density and fatigue strength of welded joints under uniaxial and multiaxial loading. Eng Fract Mech 2008;75:1875–89. doi:10.1016/J.ENGFRACMECH.2006.10.019.

[189] Radaj D, Sonsino CM, Fricke W. Fatigue Assessment of Welded Joints by Local Approaches: Second Edition. 2006. doi:10.1533/9781845691882.

[190] Berto F, Lazzarin P. Recent developments in brittle and quasi-brittle failure assessment of engineering materials by means of local approaches. Mater Sci Eng R Reports 2014;75:1–48. doi:10.1016/j.mser.2013.11.001.

[191] Foti P, Berto F. Strain energy density evaluation with free coarse mesh model. Mater Des Process Commun 2019:1–4. doi:10.1002/mdp2.116.

[192] Atzori B, Demelio G, Rossi B. Effetto delle dimensioni del cordone di saldatura sulla resistenza a fatica dei giunti a croce. Riv Ital Della Saldatura 2009;61:447–55. doi:10.3221/IGF-ESIS.09.03.

[193] Balasubramanian V, Guha B. Effect of weld size on fatigue crack growth behaviour of cruciform joints by strain energy density factor approach. Theor Appl Fract Mech 1999;31:141–8. doi:10.1016/S0167-8442(99)00008-7.